INVESTIGATION OF POLAR AND MAGNETIC ORDERING IN TRANSITION METAL OXIDE THIN FILM HETEROSTRUCTURES

Thesis by

Rajesh Mandal
Registration ID: 20142027

In partial fulfillment of the requirements
for the degree of

Doctor of Philosophy (PhD)

Department of Physics

Indian Institute of Science Education and Research
Pune, India

November 2020

CERTIFICATE

This is to certify that the work incorporated in the thesis entitled ***Investigation of polar and magnetic ordering in Transition Metal Oxide thin film heterostructures***" submitted by Rajesh Mandal was carried out by the candidate under our supervision. To the best of our knowledge, the work presented here or any part of it has not been included in any other thesis submitted previously for the award of any degree or diploma from any other university or institution.

Dr. Shouvik Datta
Thesis Supervisor

Prof. Satischandra Ogale
Thesis Co-Supervisor

Date: 30^{th} November, 2020
Place: Pune, India

DECLARATION

I declare that this written submission represents my ideas in my own words and where others ideas have been included, I have adequately cited and referenced the original sources. I also declare that I have adhered to all principles of academic honesty and integrity and have not misrepresented or fabricated or falsified any idea/data/fact/source in my submission. I understand that violation of the above will be cause for disciplinary action by the institute and can also evoke penal action from the sources which have thus not been properly cited or from whom proper permission has not been taken when needed.

Rajesh Mandal
ID: 20142027

Date: 30^{th} November, 2020
Place: Pune, India

Dedicated to my beloved grandparents...

ACKNOWLEDGEMENTS

At the beginning I would like to thank myself for completing this thesis along with travelling to more than 50 places in 19 countries all over the world and making an amazing group of international friends. This thesis would not have been possible without the contribution of many amazing individuals who have helped me grow professionally and personally. I am grateful to them for their warm support. I sincerely wish a happy and cheerful life to all of them.

First I wish to thank my supervisor Dr. Shouvik Datta for giving me the most important thing as PhD student which is freedom in pursuing a designed research problem.I am deeply motivated with his encouragement and joy in doing basic science. I wish to thank my co-supervisor Prof. Satishchandra Ogale for giving me everything that I needed to become a successful Research Scholar. His appetite for hard work and pursuit of excellence in fundamental research has always inspired me. I feel very fortunate to work with such an amazing dynamic person. My interest in the field of Oxide Thin Films would not be possible to grow without his continuous guidance. My sincere thanks goes to my RAC members Dr. Mukul Kabir and Dr. Surjeet Singh for continuous evaluation.

This thesis would not have been possible without my national and international collaborators. I would like to thank my national collaborators Dr. Ram Janay Choudhary, Dr. Rajeev Rawat, Malvika Tripathi, Supriyo Majumder and Mohit Chandra from UGC-DAE-CSR,Indore, Dr. Mukul Kabir, Dr. Sunil Nair, Dr. Rohit Babar and Avirup De from IISER,Pune for their continuous support in experiments and useful scientific discussions. I would like to thank my international collaborators Prof. Vasily Moshnyaga and Dr. Vladimir Roddatis from Georg-August-Universität Göttingen, Göttingen, Germany, Prof. Philipp Gegenwart from Universität Augsburg, Augsburg, Germany. I sincerely thank my friends Dr. Abhijit Biswas from Rice University, USA and Dr. Soumendra Nath Panja from University of St Andrews, UK for all the motivations,inspirations and scientific discussions in Oxide research.

I wish to acknowledge IISER Pune for my doctoral fellowship, European Union for awarding Erasmus Plus PhD exchange fellowship to Georg-August-Universität Göttingen,Germany, 1st Physikalisches Institut, Georg-August-Universität Göttingen for funding as a guest researcher, Infosys Foundation for conference travel grant.

I am thankful to all of my past and present lab members and colleagues in both Department of Physics, IISER Pune and 1st Physikalisches Institut, Georg-August-Universität Göttingen for making my lab life awesome. Specially I would like to mention about Vishal, Aniruddha, Kingshuk, Divya, Swati, Shrreya, Swathi, Prachi, Apurva, Philipp,

Vitaly, Henrike and Sebastian. I wish to thank all of my Integrated PhD batchmates of the year 2014 at IISER Pune. I wish to thank my friends Amit, Milan, Jyotirmoy, Rupak, Korak, Debesh, Anweshi, Arnab, Sohom, Tathagata, Dipti, Swagata, Minal, Malvika, Ruby, Vikhyat, Arnab, Sofia, Samuli, Irina, Andrea, Milike, Flavien, Paolo, Telesia, Chamila, Yeimar, Junko, Emine, Büsra and Sanem for making my life beautiful.

I would like to thank all the administrative staffs at IISER Pune for making my academic life easy and smooth. Specially I want to thank Tushar Kurulkar, Sayalee Damle, Prabhakar Anagare, Dhanashree Sheth, Sneha Chordiya and Priyadarshini Tamhane.

At the end I am fortunate to have the support of my parents and maternal uncles. Without them it was impossible to continue my academic journey from a lower middle class farmer family in rural India.

SYNOPSIS

With the discovery of high - T_c superconductors, diversity in research interest among Oxide materials has been grown exponentially in last 30 years. With the observation of novel and emergent multi - functionalities, the field of Oxides become a major area of research in the field of condensed matter physics. Starting from binary to ternary oxides with spinel or perovskite structures, Oxides become an important playground of interesting fundamental many - body physics due to the presence of strongly correlated electronic and magnetic states. The hunch for developing new devices using the wide - spread functionalities of Oxides has given the birth of new technological field called Oxide Electronics. Over the past two decades, research in oxide thin films has been boosted with the invention of new deposition techniques to make ultra thin single crystalline films, ideal for not only the tunability of existing fundamental properties but also designing a platform for novel phenomena that are unforeseeable in bulk materials. The major advantage of thin film is to design novel structure and functionality of the material that are inaccessible in it's bulk from with the help of reduced dimensionality and strain engineering with substrates. The first approach was for a homoepitaxy (growth of same material as in substrate) and reproduction of the existing bulk structure of materials. Later, heterostructures and superlattices have been explored widely in terms of lattice modulation, interface engineering and doping. Perovskite Oxides have been proved to be very important platform in this context due to the smooth hierarchy in the lattice mismatch in a wide range of crystal structures. Designing novel polar and magnetic ordering in oxide thin films and heterostructures by strain engineering is going to be the key focus of this thesis. We have grown and investigated functional properties of a perovskite ($TbMnO_3$), a double perovskite (Tb_2CoMnO_6) and a perovskite heterostructure ($BaTiO_3$ - $SrIrO_3$) in order to contribute a little to this field.

Chapter 1: gives the basic concepts of describing a condensed matter system mainly strongly correlated oxides. Basic tools and mechanism for the physical phenomena relevant to this thesis will be briefly introduced. Firstly, a short review will be provided about the basic electronic structure of the Transition Metal Oxides. Importance of the chemical environments and strong interactions among the various degrees of freedom namely charge, spin, lattice and orbital in determining many emergent properties in oxides will be addressed. With a special focus on the perovskite structure, we will then introduce the detail mechanisms of magnetic and polar ordering in a wide range of oxides. All relevant models and mechanisms explaining the long - range magnetic ordering and ferroelectricity will be introduced with a brief discussion on the important theories and observations on the coupling between these two order parameters. Finally, the importance of oxides thin films will be discussed in the context of tuning and designing novel magnetic and polar

ordering via strain engineering along with the motivation as well as scope of this thesis.

Chapter 2: deals with the details about the growth of magnetic and ferroelectric Oxide thin films. We will first discuss the principles of growth of thin films in general; later highlights will be on oxide films. Then the detail role of substrates in terms of epitaxial relationship will be introduced. Thereafter, the modern available deposition techniques will be discussed. At the end, we will come to the detail growth methods intensively used in this thesis namely Pulsed Laser Deposition (PLD) and Metal-organic Aerosol Deposition (MAD) techniques for the deposition of Oxides.

Chapter 3: gives the brief overview of the major measurement techniques that have been intensively used in this thesis. Firstly, we will review the detail measurement techniques for investigation of crystal and electronic structures of thin films. Focus will be on X-ray Diffraction (XRD), X-ray Photoelectron Spectroscopy (XPS), Raman Spectroscopy and Transmission Electron Microscopy (TEM) along with Electron Energy Loss Spectroscopy (EELS). Optical Ellipsometry and Reflection High Energy Electron Diffraction (RHEED) will be discussed as in - situ monitoring techniques for thin film growth. Basic principles and measurement procedures for Magnetic Measurements using conventional SQUID and home built set up for Dielectric Spectroscopy and Resistivity will also be discussed briefly.

Chapter 4: presents the growth of high quality epitaxial strain stabilized hexagonal phase of $TbMnO_3$ films on YSZ(111) substrate and their structural transformations are analyzed by means of various ex- and in-situ characterization techniques. A temperature dependent Raman spectroscopy revealed a structural phase transition from $P6_3cm$ to $P6_3/mcm$ structure at ferroelectric $T_C \sim 800$ K. Optical ellipsometry, confirming a phase transition at 800 K, indicates a change of charge transfer from oxygen to Mn at the structural phase transition. In - situ transmission electron microscopy (TEM) of the lamella samples displayed an irreversible $P6_3cm$ to $P6_3/mcm$ transformation and vanishing of ferroelectric domains already at 410 K. Concurrently, the room temperature TEM of h - $TbMnO_3$ films after the temperature cycling (300K-1300K-300K) revealed an inhomogeneous microstructure, containing both ferroelectric and paraelectric nanodomains with $P6_3cm$ and $P6_3/mcm$ structure, respectively. We point out a strong influence of stress relaxation, induced by the sample geometry as well as by temperature cycling, onto the structure and ferroelectricity in h-$TbMnO_3$ thin films.

Chapter 5: describes Magneto-Dielectric properties of partially B-site ordered monoclinic Tb_2CoMnO_6 double perovskite thin film epitaxially grown on Nb:$SrTiO_3$(001) substrates by metalorganic aerosol deposition(MAD) technique.Transmission electron microscopy and electron energy loss spectroscopy mapping shows the presence and distribution of both Co^{2+} and Co^{3+} ions in the film, evidencing a partial B-site disorder, which was further confirmed by the observation of reduced saturation magnetization at low

temperatures. The ferromagnetic Curie temperature, T_C = 110 K, is slightly higher as compared to the bulk value (100 K), probably due to an in plane biaxial tensile strain. Temperature dependent dielectric study reveals an unexpected high temperature dipolar relaxor-glass-like transition at a temperature $T^* \sim 190$ K > T_C, which depends on the applied frequency and indicates a superparaelectric behavior.Two different dielectric relaxation peaks have been observed; they merge at T^* where likely a coupling between the disorder-induced short range charge-spin interactions results in a 4% magneto-dielectric coupling.

Chapter 6: presents the growth of 3d-5d based relaxed $BaTiO_3/SrIrO_3$ heterostructures, to obtain emergent phenomena arising from the interfacial coupling between B-site (Ti^{4+}; $3d^0$ and Ir^{4+}; $5d^5$) cations. Parent $BaTiO_3$ film shows weak ferromagnetic ordering at T_C $\sim$ 136 K, due to the oxygen vacancies, in contrast of paramagnetic nature in strong spin-orbit coupled $SrIrO_3$ film. Interestingly, in $BaTiO_3/SrIrO_3$ heterostructure we observed magnetic ordering at $T_C \sim 160$ K. X-ray photoelectron spectroscopy of O 1s and Ti 2p reveals the presence of oxygen vacancies and Ti^{3+} states in BaTiO3/SrIrO3, similar to the parent $BaTiO_3$. However, significant changes in Ir 4f spectrum line shape with coverage has been observed in $BaTiO_3/SrIrO_3$, in contrast of parent $SrIrO_3$. Therefore, this remarkable enhancement in T_C is attributed with the interfacial charge transfer process and the presence of strong spin-orbit coupling.

Chapter 7: summarizes the conclusions of the works completed presented in this thesis, along with possible methods and avenues for the scope of future work are pointed out.

Appendix A: presents $(B_XC_YN_Z)/Al_2O_3$, a 2D material - Oxide hybrid heterostructure. Boron carbonitride ($B_XC_YN_Z$) represents an interesting family of materials containing all light elements and two dimensional graphene like hybrid layers.In this work, we have grown thin films of this compound using Pulsed Laser Deposition (PLD) method, and investigated their magnetic and transport properties along with the detailed electronic structure by using various spectroscopic techniques. In depth analysis of the typical role of dopants and defects, especially the prevalent nitrogen defects, is elucidated using Density Functional Theory (DFT) calculations to understand the experimental observations. A dramatic crossover in the transport mechanism of charge carriers is observed in this system with the change in doping level of specific nitrogen defects. A robust and high saturation magnetization is achieved in BCN films, which is higher by almost hundred times as compared to that in similarly grown undoped carbon film.

Table of Contents

CHAPTER 1

Introduction

Current chapter deals with the basic concepts of describing a condensed matter system, mainly strongly correlated oxides. Basic tools and mechanisms for the physical phenomena relevant to this thesis are briefly introduced. Firstly, a short review is provided about the basic electronic structure of the Transition Metal Oxides. Importance of the chemical environments and strong interaction among the various degrees of freedom namely charge, spin, lattice and orbital in determining many emergent properties in oxides are discussed. With a special focus on the perovskite structure, we introduce the detailed mechanisms of magnetic and polar ordering in a wide range of oxides. All relevant models and mechanisms explaining the long range magnetic ordering and ferroelectricity are introduced with a brief discussion on the important theories and observations on the coupling between these two order parameters. Finally, the importance of oxides thin films is discussed in the context of inducing and tuning novel magnetic and polar ordering via strain engineering along with the motivation as well as scope of this thesis.

1.1 Basic Concepts

1.1.1 Why Transition Metal Oxides?

Transition metal Oxides (TMO) have attracted the condensed matter physics community from a long time in history, due to it's rich crystal structure, an wide range of novel physical properties and as a potential candidate for the next generation devices and technology. Over past 30 years, research in oxides has been boosted due to the invention of new deposition techniques to make ultra-thin single crystalline films, ideal for not only the tunability of existing physical properties but also designing a platform for novel phenomena that are absent and impossible in bulk materials [1]. The rich physical properties present in complex oxides are the manifestation of the strong electron-electron correlation and interaction among degrees of freedom, namely Spin, Charge, Lattice and Orbitals in the wide range of complex crystal structures [2]. Starting form binary oxides to complex ternary oxides, the correlated electronic structure, chemical states and bonding environment always gives the opportunity to explore novel and intrinsic physics as Metal-Insulator Transition [3], High T_C superconductor [4], Colossal Magneto-Resistance [5], Magnetism, Ferroelectricity, Multiferroics [1] and many interesting transport phenomena [6]. Most common types of crystal structures for ternary oxides have been presented in Figure 1.1. One of the most studied structure is the perovskite (AMO_3) that will be the primary focus of this thesis. The most important aspect of studying perovskite structure is the tuning and engineering of their chemical environment and electronic structures with alternating or replacing A and M site cations with other cations having different size/valency. That could change and induce many unexpected physical properties with the strong interplay between different degrees of freedom in the system.

1.1.2 Environments and origin of crystal fields

Most common Perovskite oxides (AMO_3) have the cubic unit-cell consisting of MO_6 octahedra at the center and corners are shared with A cation [7]. Here M is generally the transition metal ions and A is a cation from another group in periodic table (most commonly the Rare Earth ions). d orbitals of the transition metal ion overlaps with the oxygen p orbitals during the formation of the octahedra. This local environment where d orbitals are placed surrounded with negatively charged oxygen p orbitals, gives rise of the so called crystal field [8]. Size and direction of the d orbitals are crucial to understand this phenomenon. The five d orbitals are categorized according to the pointing directions. If we use a Cartesian coordinate system then d_{xy}, d_{yz} and d_{xz} lies in between the respective axes as denoted. On the other hand, d_{z^2} points towards z axis and $d_{x^2-y^2}$ points in both x and y axis. The first three orbitals are named as t_{2g} and rest two are named as e_g orbitals. In an octahedral environment, where any of oxygen p_x, p_y and p_z orbitals approach the d

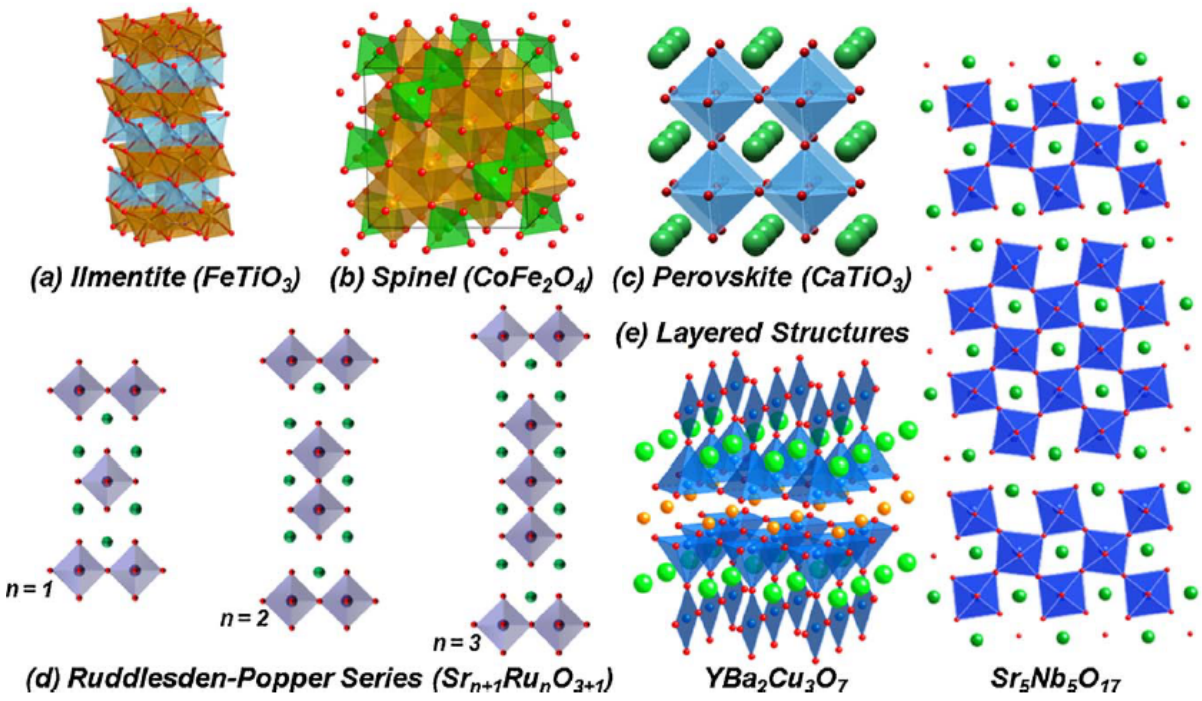

Fig. 1.1 Examples of ternary oxide crystal structures including (a) ilmentite, (b) spinel, (c) perovskite, and derivatives of the perovskite such as (d) the RuddlesdenPopper series and (e) layered perovskites. Adapted from Ref.[1] with the permission of Elsevier

orbital, e_g orbitals will feel much more coulombic repulsion than the t_{2g} orbitals, due to the symmetry. Consequently, the e_g orbitals will be uplifted to higher energy states and t_{2g} orbitals will be lowered in energy, breaking the degeneracy of ground state as shown in Figure 1.2 . This redistribution of the ground state energy will be definitely different for the various environments (tetrahedral or polyhedral for example). The strength of this crystal field also will depend on the size of the d orbitals. For example, due to the extended nature of 4d and 5d orbitals, they will feel less coulombic repulsion than the 3d orbitals. Distribution of electronic as well as spin states will also highly depend on the competition between the crystal field energy and the electron-electron coulombic repulsion or the pairing energy. Depending on their relative strengths, ground state could be either high spin or low spin state. In case of 3d ions, crystal field energy is significantly higher than spin-orbit interaction strength and this leads to the quenching of the orbital angular momentum. With the violation of Hund's rule, J will no longer be a good quantum number and effective moment will solely depends on its spin moment. For 4d and 5d case, where crystal field energy and spin-orbit interaction strength are comparable, electronic and magnetic ground states will be again redistributed, as observed in case of Ruthenates and Iridates [223].

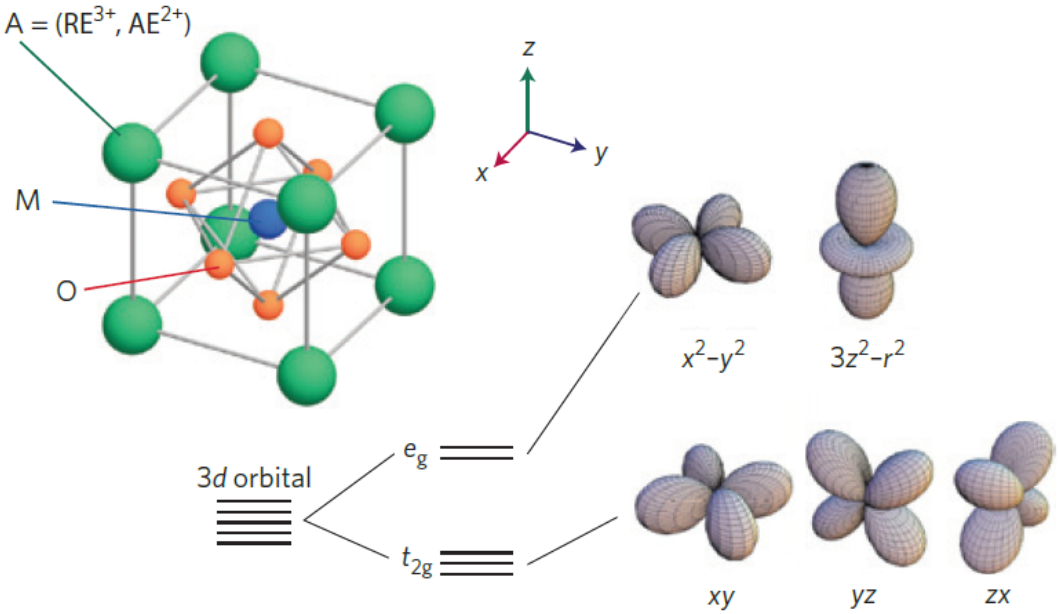

Fig. 1.2 Cubic perovskite system and the redistribution of the ground states of 3d orbitals due to crystal field splitting. Adapted from Ref.[2] with the permission of Springer Nature

1.1.3 Strong Electronic Correlation

Along with the crystal field splitting, strong electron-electron interaction present in the transition metal oxides is equally responsible for the wide range of interesting and novel phenomena as stated in previous sections. In condensed matter physics, the very first successful attempt to calculate electronic structure and explain the physical properties was the tight binding model. The band theory along with it successfully had explained the existence of metallic and insulating state in solids. Real problem started while explaining the band structure of some transition metal oxides, for example NiO [3]. The band theory predicts it as a metal but experiment shows it as an insulator. Electron-Electron coulombic repulsion that resists the double occupancy of electrons in single orbital was ignored in previous theoretical models. This on site coulomb repulsion (U) was first successfully included in a model proposed by John Hubbard that could resolve that existing puzzle and open up the possibility of realization of physically acceptable ground states [10, 11, 12]. In a very simple framework the model could be explained by two simple terms. (1) The hopping term (t) that is the kinetic energy of the electron moving from one atomic site to another site and (2) the Coulomb repulsion or the potential energy term (U) that challenge the electron motion. The competition between these two terms will decide the final electronic arrangement along with the spin ground state. If we remove the repulsion term U then it will automatically reduce to the tight binding model with a

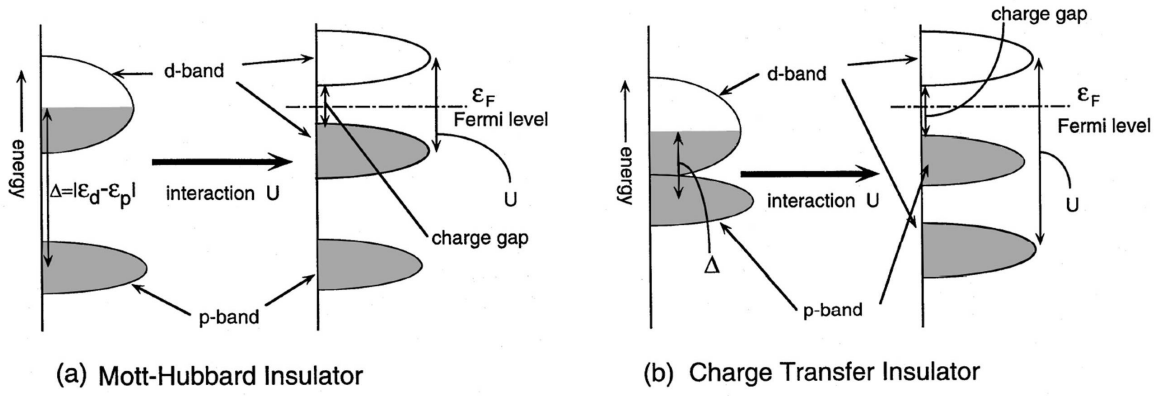

Fig. 1.3 Schematic band diagram showing the characteristic bands and corresponding energies in (a) Mott-Hubbard Insulator and (b) Charge-transfer Insulator. Adapted from Ref.[3] with the permission of American Physical Society

metallic ground state. Mathematically, the Hubbard Hamiltonian of a system with fixed n number of electrons could be written as following:

$$\mathcal{H} = -t \sum_{<i,j>,\sigma} (C^{\dagger}_{\sigma i} C_{\sigma j} + C^{\dagger}_{\sigma j} C_{\sigma i}) + U \sum_i n_{+i} n_{-i} \qquad (1.1)$$

Here the first term is the hopping or kinetic term and the second is the on-site Coulomb repulsion. The creation operator $C^{\dagger}_{\sigma i}$ creates an electron at i^{th} site and $C_{\sigma j}$ annihilate the other at j^{th} site. σ is the electron spin that could be either up (+) or down (-). $< i, j >$ denotes the nearest neighbour hopping. $C^{\dagger}_{\sigma i} C_{\sigma i}$ is denoted as number operator $n_{\sigma i}$.The summation i over all sites adds an interaction energy U, whenever a double occupancy is found and it's zero for a vacant site or single occupancy.

Application of Hubbard model in transition metal oxides leads to very promising and interesting results. Here the hopping term could be redefined as charge transfer energy Δ that is the difference between the energy of the transition metal d orbital (ε_d) to the ligand oxygen p (ε_p) orbital. $\mid \varepsilon_d - \varepsilon_p \mid$ defines the energy needed to transfer a charge (electron/hole) from d to p orbital for hybridization. When an on site Coulomb repulsion (U) is applied to this system , two different scenarios can occur as presented in Figure 1.3. (1) $\Delta >$ U: on site electron-electron repulsion splits the half filled d band into a fully filled Lower Hubbard Band (LHB) and an empty Upper Hubbard Band (UHB), with a band gap as shown in Figure 1.3 (a). This causes an insulating ground state, named as Mott-Hubbard Insulator. Most common oxides of this type are $LaTiO_3$ and Cr_2O_3. Metallic ground state could only exist if the band width is much larger than U. (2) $\Delta <$ U: in this case the p band is very close to the d band due to strong covalent bond. By applying large value of U, the LHB is pushed away bellow p band so that any added holes

always goes to the p band and the insulating ground state is always determined with p-d charge transfer as shown in Figure 1.3 (b). This is called Charge-Transfer type Insulator [13, 14]. Most common examples are CuO and NiO.

1.2 Magnetic ordering in Oxides

Magnetism is undoubtedly one of the oldest physical phenomena that had been noticed in materials like Iron Oxide. Net magnetic moment possessed by a material is given by the combined moment of the electron spin (S) and orbital angular momentum (L). A material with long range magnetic ordering, undergoes a phase transition from its high temperature paramagnetic (randomly oriented moments with no net magnetic moment) phase to the low temperature long range ordered phase, at a certain temperature specific to the material. For a ferromagnetic transition it is the Curie Temperature (T_C) and for an antiferromagnetic transition it is the Neel Temperature (T_N). Bellow this transition temperature the spontaneous magnetic ordering occurs. Interesting thing about a ferromagnet is that the spontaneous magnetization could be switched by applying an external applied magnetic field. To understand the microscopic mechanism of long range ordering, magnetic exchange interaction has been proved to be the strongest tool. The origin could be understood from basic quantum mechanical wave function overlapping of simple two electron system. One dimensional spin chain with nearest neighbour interaction had been studied first as a model system to understand long range ordering with exchange interaction. It's also called as Heisenberg Model [15] with the following Hamiltonian.

$$\mathcal{H} = -\sum_{i,j} J_{ij} \mathrm{S}_i \cdot \mathrm{S}_j \tag{1.2}$$

Where J is the strength of the exchange (exchange integral) and summed over all the neighbouring spin sites. Value and sign of J will decide the characteristics of the interaction. This has successfully explained the existence of antiferromagnetic ground state of 1 dimensional spin chains. Heisenberg Model can also be deduced from the above mentioned Hubbard Model in strong U limit [3]. The experimental results of the macroscopic magnetization in wide range of ferro and antiferromagnetic materials are successfully explained and analysed with Weiss Model with an extra term in the Hamiltonian as $g\mu_B \sum_j S_j \cdot B$. This term is called as Zeeman term, explaining the interaction of individual spins with external applied magnetic field B where g is the g factor and μ_B is the Bohr magneton. Taking an approximation of effective molecular field produced by all the neighbour spins, it has explained almost all the types of long range ordering in solids [8]. In all the above discussions we have only considered spin only moment and inclusion of orbital moment has been done in revised models later on. Magnetism in oxides is not very simple to model as an indirect exchange occurs between the moments on the sites of transition metal ions (M) via non magnetic oxygen ions (O) in M -O- M chains. Though calculation

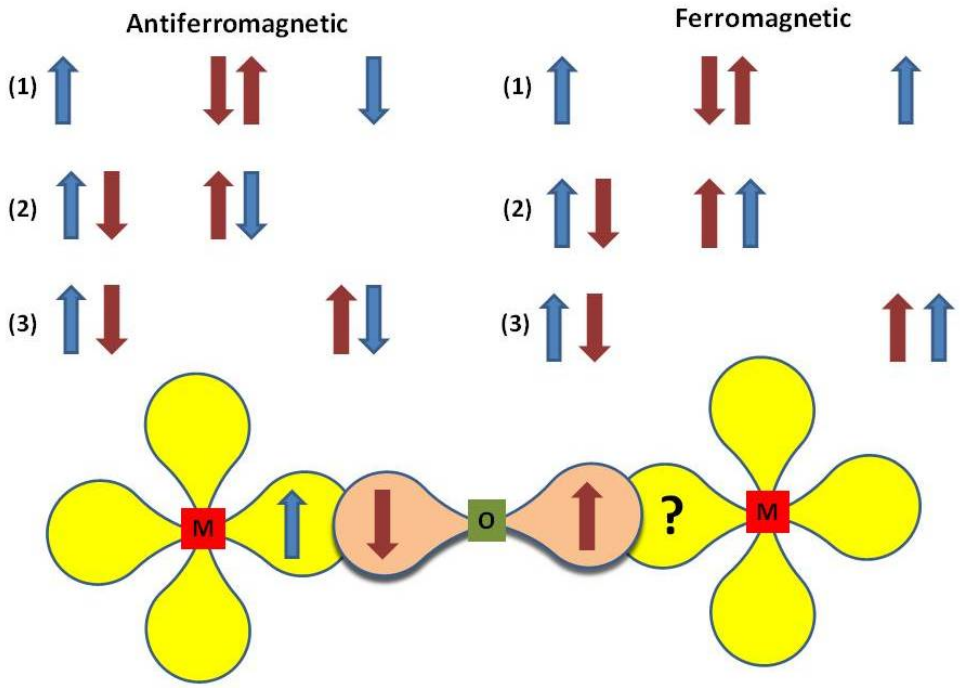

Fig. 1.4 Schematic cartoon for the simple superexchange interaction in a M -O- M 1D spin chain showing the favourable antiferromagnetic ground state

of the exchange integral is very complex, qualitatively the mechanism could be explained and results could be predicted with some empirical rules. The most common exchange interactions relevant to this thesis are discussed in the following sections.

1.2.1 Superexchange interactions

Superexchange interaction [16] is the heart of the magnetic interaction in most of magnetic insulating oxides. As said, the detail calculation of the exchange integral and determining the ground state is not easy due to the complexity of the system. But qualitatively a simple superexchange mechanism is easily understandable. It's an indirect interactions between the electrons of transition metal d orbitals via oxygen 2p electrons. A simple schematic diagram has been presented in Figure 1.4. Here two e_g $d_{x^2-y^2}$ orbitals are overlapped with oxygen p_x orbital in a M -O- M bond angle of 180°. Each $d_{x^2-y^2}$ orbital has one and p_x has a pair of electrons. There could be two different scenarios (Antiferromagnetic and Ferromagnetic) for the ground state as shown in Figure 1.4. For the antiferromagnetic case the electrons are allowed to delocalize themselves in three different ways as shown. For a ferromagnetic ordering these three delocalizations are forbidden due to the same spin state in a single orbital. As discussed in Hubbard Model, an electronic ordering always tries to minimize it's coulombic repulsion. In this case we can see that an antiferromagnetic ground state always has a kinetic benefit for the electron delocalization and minimization of electrostatic repulsion. The observation of antiferromagnetic ordering in $LaMnO_3$ could

be well explained with this simple model. Here Mn^{3+} has four d electrons in high spin state with a single electron in e_g $d_{x^2-y^2}$ orbital. These e_g electrons interact antiferromagnetically with the neighbouring sites in chain [17]. Many complex situations can arise depending on the nature of d and p orbital involved, the bonding angle, degree of bonding or overlapping and the filling of the involved d orbitals. These results could be summarized in some empirical rules called Goodenough-Kanamori rules [18, 19, 20, 21]. It says (1) Exchange interaction between two partially/half filled orbitals with 180° overlapping is strong and antiferromagnetic, (2) if the overlapping is in 90° with same condition then the interaction is weak and ferromagnetic, and (3) interaction between a half filled and a vacant (or doubly occupied) orbital is weak and ferromagnetic due to an energetic advantage of hopping of electrons on to the unoccupied orbital.

1.2.2 Double exchange interactions

Double exchange interaction could be explained as a essential extrapolation of a ferromagnetic superexchange interaction (Goodenough-Kanamori third rule) in an extended manner. This mechanism occurs in a system of mixed valence magnetic ions, for example of the mixture of Mn^{3+} ($t_{2g}^3 e_g^1$) and Mn^{4+} ($t_{2g}^3 e_g^0$). Both Mn^{3+} and Mn^{4+} are in high spin states in the chain of alternate ions. We can see a possibility of hopping the e_g electron of Mn^{3+} to the vacant e_g orbital of the Mn^{4+}. This hopping is only possible if the t_{2g} electrons of both ions have the same spin alignment, as hopping does not allow a spin flipping. According to the Hund's first rule, both single center e_g and t_{2g} electrons have to be with the same spin orientation to maintain the high spin state. So an antiferromagnetic arrangement of the t_{2g} in the neighbouring sites restrict the hopping of e_g electrons. Now as discussed in the previous sections, electron delocalization is always preferred to minimize the coulomb electrostatic repulsion, hopping of the e_g electrons in the chain gives the system a kinetic preference. So a ferromagnetic ordering will be preferred and due to the electrons hopping in the extended chain, the system becomes metallic. The most popular example of double exchange is the mixed valence manganites such as $La_{1-x}Sr_xMnO_3$ [3]. Parent compound $LaMnO_3$ has only Mn^{3+} ions and is an antiferromagnetic insulator as discussed previously. With the optimum doping of divalent Sr^{2+} ions (x= 0.175), Mn^{4+} concentration in the system and it suddenly becomes a metallic ferromagnet.

1.2.3 Anisotropic exchange

Till now we have only encountered the interactions that take place in the plane of the spins from the Heisenberg Model and the dot product of the spins. In the previous models what we have ignored is the Spin-Orbit coupling. Incorporation of the relativistic Spin-Orbit coupling in the superexchange model introduces a new kind of exchange interaction that is not isotropic. This interaction has been phenomenologically introduced by Dzialoshin-

ski [22] and later a detail theory was developed by Toru Moriya [23], and is known as Dzyaloshinskii-Moriya interaction (DMI). The expression for this exchange interaction is written as Hamiltonian $\mathcal{H} = \sum_{i,j} D_{ij} \cdot [S_i \times S_j]$ where D_{ij} is a constant vector. The value and direction of this vector will depend on the symmetry of the placement of spins S_i and S_j. D_{ij} can lie either parallel or perpendicular to the line connecting the spins and have a non zero value only if the center of that line does not possess an inversion symmetry. The interaction is in such a way, that it always tries to orient the spins at 90° in a plane perpendicular to the D vector. In many systems, it results a canting of spins. One of the interesting examples is $\alpha - Fe_2O_3$, where DM interaction causes a canting of spins in the trigonal lattice resulting a net magnetic moment and weak ferromagnetism [23] in the antiferromagnetic chain. This interaction is also responsible for the stabilization of many non colinear spin textures like magnetic skyrmions [24] and presence of net magnetic ordering in ferroelectric materials making them as potential multiferroics (coexistence of both polar and magnetic ordering in a single material) such as $BiFeO_3$ [25].

1.3 Polar ordering in Oxides

Ferroelectricity is also considered as one of the oldest and fundamental physical phenomena in solid state physics. As we know electron has charge (-e) along with it's spin degrees of freedom. An electrical dipole is composed of two opposite charges separated by a certain distance. In a normal dielectric medium these unit of tiny dipoles could be created with an application of external electric field, with the separation of charges along the direction of the electric field. There could be materials with the presence of permanent dipoles and they become ordered bellow a certain temperature, called as ferroelectric curie temperature (T_C) and gives a spontaneous polarization (P) similar as a ferromagnet where spins are the responsible for spontaneous magnetization (M), as discussed in previous sections. The direction of the polarization could be switched from -P to +P according to the direction of the external electric field [26]. Bellow the ferroelectric T_C the coulombic dipole-dipole interaction is responsible for the long range ordering of the dipoles causing the spontaneous polarization. Ferroelectricity was first discovered in Rochelle salt ($NaKC_4H_4O_6$, $4H_2O$) in seventeenth century and polarization switching along with the curie temperature was first measured around 1921 by Valasek [27]. Ferroelectricity in perovskite oxides are mostly due to the noncentrosymmetric distortion of the unit cell along with the offcentering of the metal and oxygen ions, causing permanent dipoles in the system. The major and relevant mechanisms that cause ferroelectricity in oxides are discussed as follows.

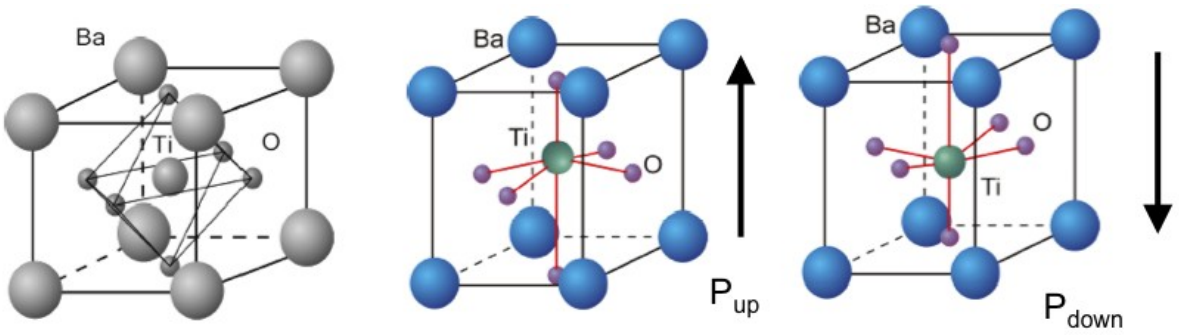

Fig. 1.5 Unit cell of the perovskite $BaTiO_3$. High temperature paraelectric cubic phase (left one). Room temperature ferroelectric and tetragonal phases, showing up and down polarization directions (middle and right one). Adapted from Ref. [28] with the terms & conditions of AAAS

1.3.1 Displacive Transition

Typically, most common displacive class of ferroelectric perovskite oxides (AMO_3) contains a Transition Metal Oxide ion with a vacant d orbital, i.e. a formal configuration d^0 at the M site such as Ti^{4+}, Zr^{4+} or W^{6+}. In the centrosymmetric cubic phase, the net center of both the positive and the negative ions are merged, giving no net dipole moment in the paraelectric phase as in the case of $BaTiO_3$ [28]. Though the long range dipole-dipole interaction always promotes a offcentering of charges and bond distortion, the short range local coulomb repulsion tries to minimize itself in a nonpolar cubic phase. So the emergence of the ferroelectricity will primarily depend on the balance between these two forces. Bellow T_C, the d^0 orbital rehybridizes with one or more than one oxygen p orbital creating a noncentrosymmetric octahedral distortion as shown in Figure 1.5. That distortion minimizes the overall energy of the system creating a permanent dipole moment in certain direction. The lowering of the energy due to the mixing of the orbitals is larger than the local coulomb repulsion resisting the offcentering. This change in the chemical bonds that stabilize a distorted structure over a centrosymmetric one could be well explained by so called second-order JahnTeller effects [29, 30]. This theory explains the emergence of very low frequency phonon mode called as soft phonon mode that is one of the key signatures of displacive ferroelectricity.

1.3.2 Geometrical Ferroelectricity

Hexagonal perovskite Manganites ($RMnO_3$; R is a rare earth ion) belong to this class of ferroelectric oxides. In the rare earth series, in periodic table, the atomic radii decreases along the right of the row from La to Lu ions. When the R site is occupied with a rare earth ion with bigger ionic radii (La, Ce, Pr or Nd), the perovskite takes an orthorhombic structure due to the large Jahn-Teller distortion in the cubic phase with the Mn^{3+}

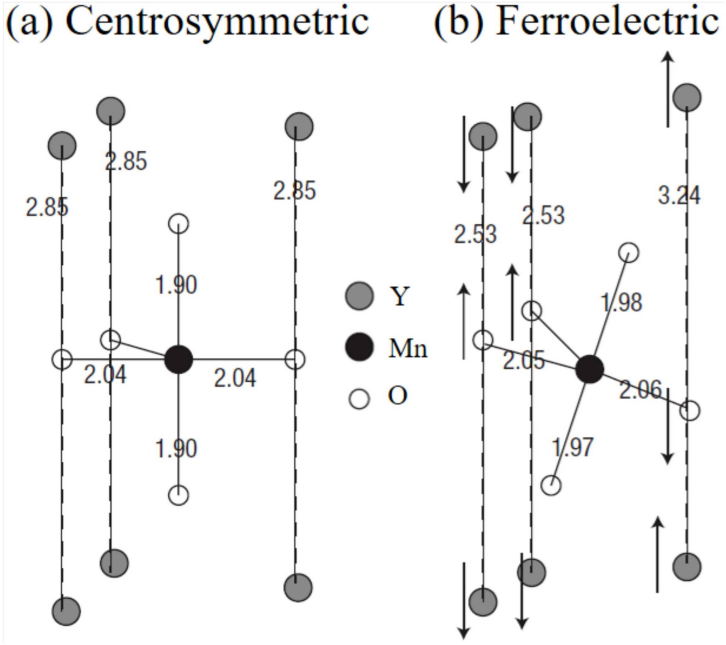

Fig. 1.6 Schematic of the rotation of the MnO_5 polyhedra from para to ferroelectric phase. The numbers denote the bond length in Å, whereas the arrow indicates the atomic displacement with respect to the centrosymmetric paraelectric phase.Adapted from Ref.[32] with the permission of Springer Nature

ion in the octahedral environment. Taking the smaller atomic radii (Y, Dy, Er or Lu), the structure takes a hexagonal phase for stabilization. Unlike the cubic symmetry with MnO_6 octahedra, the hexagonal manganites unit cells are composed of a MnO_5 trigonal bypyramid or polyhedra. The crystal field splitting varies drastically from an octahedral environment. Here two degenerate e_g orbitals (e_{1g}^2 & e_{2g}^2) with two-fold degeneracy and a single e_{1g}^0 orbital in the absence of the Jahn-Teller distortion has been observed. Taking the case of $YMnO_3$ as the most celebrated hexagonal manganite, it undergoes a phase transition from a paraelectric hexagonal $P6_3/mmc$ phase to another hexagonal $P6_3cm$ phase having a ferroelectric ordering with a T_C around 950 K [31]. This noncentrosymmetric distortion of the unit cell is a result of the buckling of the MnO_5 polyhedra. Due to this buckling, the inversion symmetry of the mirror plane perpendicular to the hexagonal c axis is lost, resulting an asymmetric change in the Y-O bond along the c direction, as shown in Figure 1.6. It has been theoretically found that above distortion in the centrosymmetric structure does not change any bonding environment or coordination inside MnO_5 polyhedra and no rehybridization is taking place with offcentering of Mn ions unlike the case of displacive transition discussed previously [32, 33]. The whole mechanism which is driven from a geometrical instability thus put these group of materials in the class of improper ferroelectrics. The hexagonal ferrites ($RFeO_3$) also belong to this class of ferroelectric oxides. Further details about Geometrical Ferroelectricity will be discussed

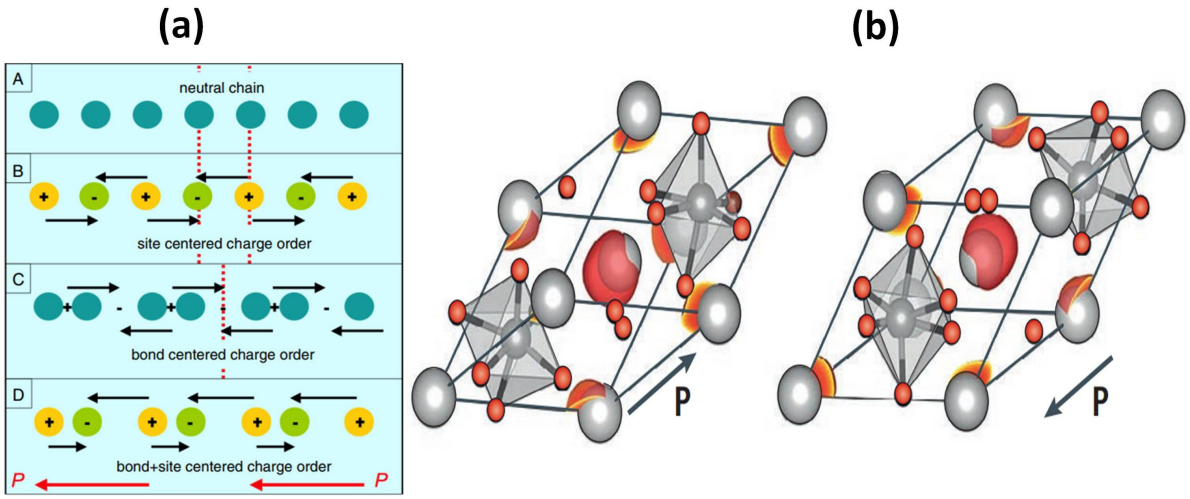

Fig. 1.7 (a) Schematic diagram of the 1D chain showing different types of charge ordering and the emergence of non zero polarization with the direction indicated with arrows. Adapted from Ref.[34] with the permission of IOP Publishing. (b) Structure of $BiFeO_3$ showing the electron lone pair (red) of the Bi^{3+} ion (grey). The electron cloud is shifted to FeO_6 octahedra generating a spontaneous polarization in [111] direction. Adapted from Ref.[37] with the permission of Springer Nature.

later in Chapter 4.

1.3.3 Charge ordering and lone pair mechanism

As permanent electric dipoles are the basic ingredients of ferroelectricity, it is natural that ordering of electrical charges in certain manner sometime triggers the presence of spontaneous polarization in the crystal structure [34]. The simplest model of a 1D chain has been presented in Figure 1.7(a) to show the emergence of non zero polarization due to charge ordering. Firstly, it could be a chain of neutral atoms with no dipole moment. Secondly, the positive and negatively charged ions can order themselves in alternate sites. In this site centered case, alternate and opposite dipoles appears that cancel each other with no net dipole moment. Thirdly, the atoms can arrange with alternative inequivalent bonds. In this case also spatial inversion symmetry is not broken and the system is non polar. Finally, it could be a cite centered as well as bond centered simultaneously. In this case the scenario will be changed completely. We can see clear broken inversion symmetry due to the combination of both site centered and dimerized bonds with a net and non zero dipole moment. Fe_3O_4 [35] and $LuFe_2O_4$ [36] are the most interesting examples of this class of ferroelectric oxides with a charge ordering of Fe^{2+} and Fe^{3+} ions.

Lone pair driven ferroelectricity has been found in perovskite oxides containing A site cation with a $6s^2$ lone pair such as Bi^{3+} [37]. It was proposed long back that a lone

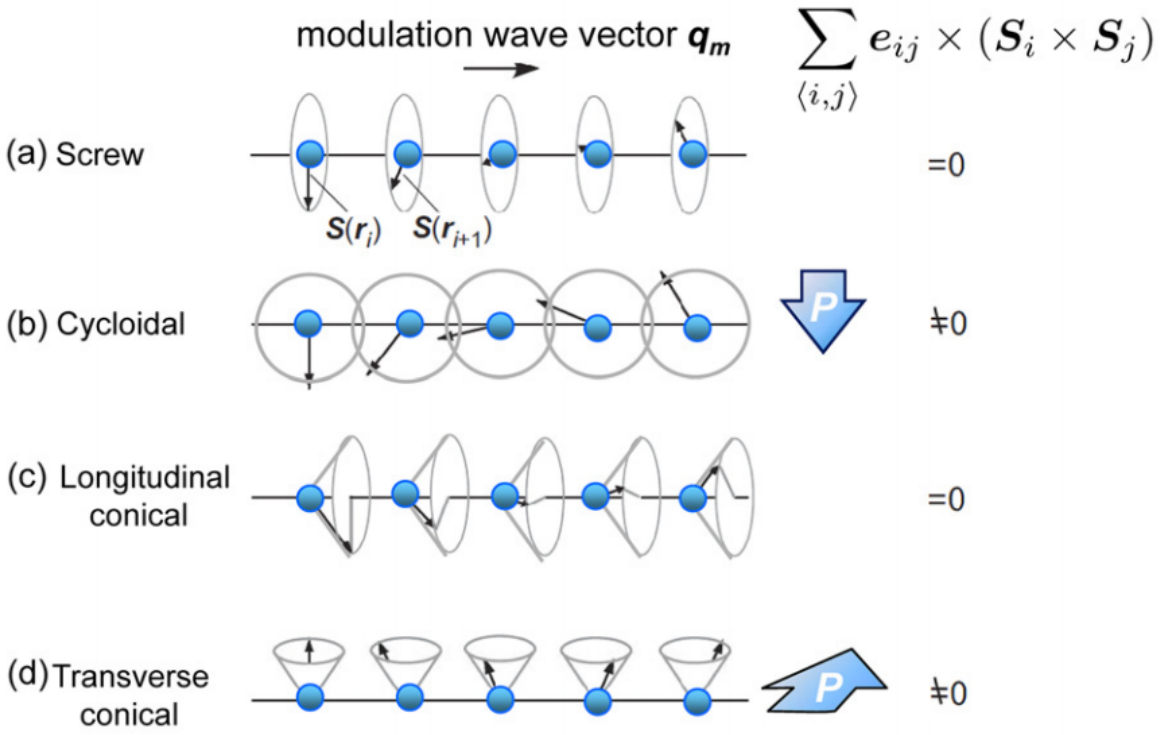

Fig. 1.8 Schematic cartoon for different types of spiral magnetic structure on a 1D array of magnetic spins S(r). The calculated directions of spontaneous polarization P calculated from the spin-current model or inverse DM model are also indicated in the respective structures. Adapted from Ref.[42] with the permission of IOP Publishing.

pair can't have a character of pure s orbital and always tries to admix itself with a p orbital [38]. The tendency of stereochemical activity of the lone pair results a broken spatial inversion symmetry. Taking the example of $BiFeO_3$ as shown in Figure 1.7 (b), the $6s^2$ lone pair of Bi^{3+} ion always pushes itself toward the oxygen anion of FeO_6 octahedra, resulting an offcentering of the Bi^{3+} ion along with the electron cloud from a pure spherical shape to lobe shape. This offcentering is further stabilizes itself with the electron transfer from 6p orbital and appearance of switchable spontaneous polarization along [111] direction. Similar class of materials that do not have a lone pair in the A site for example $LaMnO_3$, does not have ferroelectric ordering but $BiMnO_3$ is a ferroelectric with a transition temperature about 800 K [39].

1.3.4 Coupled polar and magnetic ordering

In the most important class of improper ferroelectric oxides, magnetic ordering in the structure itself is able to break the spatial inversion symmetry and can generate spontaneous polarization. This class of materials are categorized as Type II multiferroics [37], where a considerable amount of magneto-electric coupling is present. There are many interesting mechanisms that are responsible for this phenomena and all of them are not

in the scope of this thesis. Primarily, we will focus and briefly review the most important and intensely studied mechanism that is the non-colinear spin arrangement in inverse Dzyaloshinskii-Moriya (DM) interaction and spin current model. DM interaction originates from the relativistic spin-orbit coupling promoting a canting and non-colinear arrangement of spins as discussed in Section 1.2.3. In the inverse DM interaction, the competition between AFM/FM interaction due to the geometric frustration in the structure leads to the non-colinear spin configuration and the spin structure stabilizes itself via the offcentering in the ion chain, breaking the spatial inversion symmetry. Thus it generates a spontaneous macroscopic polarization [40, 41]. A detail mathematical model describing the emergence of polarization due to non-colinear spin configuration has been developed as the spin current model. A spin current is realized as a flow between the canted spins S_i and S_j in a modulating spin structure in particular direction q_m called as modulation wave vector. Different types of spin currents have been shown in Figure 1.8. The detail calculation shows that the induced macroscopic polarization P could be expressed as $P = \eta \sum_{i,j} e_{ij} \times [S_i \times S_j]$, where η is a coupling constant depends on the strength of spin orbit coupling and e_{ij} is a vector directed towards the line connecting S_i and S_j [42]. One of the most interesting examples of this class of ferroelectric oxides is orthorhombic $TbMnO_3$ [43]. Bellow the ferroelectric T_C, Mn^{3+} spins arrange in cycloidal spin arrangement that triggers a spontaneous polarization in the plane of the spiral. The switching of the modulation wave vector has also been observed with the polarization reversal on applied electrical field in the polarized neutron scattering experiment [44].

1.4 Importance of Oxide Thin Films

Field of oxide thin films or Oxide Electronics has gained a huge importance in last three decades with the advancement of new deposition techniques and the control over thin film growth [45]. An epitaxial oxide thin film is basically an extended single crystal of the desired material on a preferable single crystalline oxide substrate. The details of the thin film growth mechanisms and techniques used in this thesis will be discussed in Chapter 2. The major advantage was to design novel structure and functionality of the material that are inaccessible in it's bilk from with the help of reduced dimensionality and strain engineering with substrates [1]. The wide range of substrates that are generally used for the gradual tuning of oxide functionality with the imposed strain has been shown in Figure 1.9. The first approach was for a homoepitaxy (growth of same material as in substrate) and reproduction of the existing bulk structure of materials. Later heterostructures and superlattices [46] have bees explored widely in terms of lattice modulation, interface engineering and doping. Perovskite Oxides have been proved to be very important platform in this context due to the sooth hierarchy in the lattice mismatch in a wide range of crystal structures. Ground breaking discovery like the two dimensional gas in the interface of

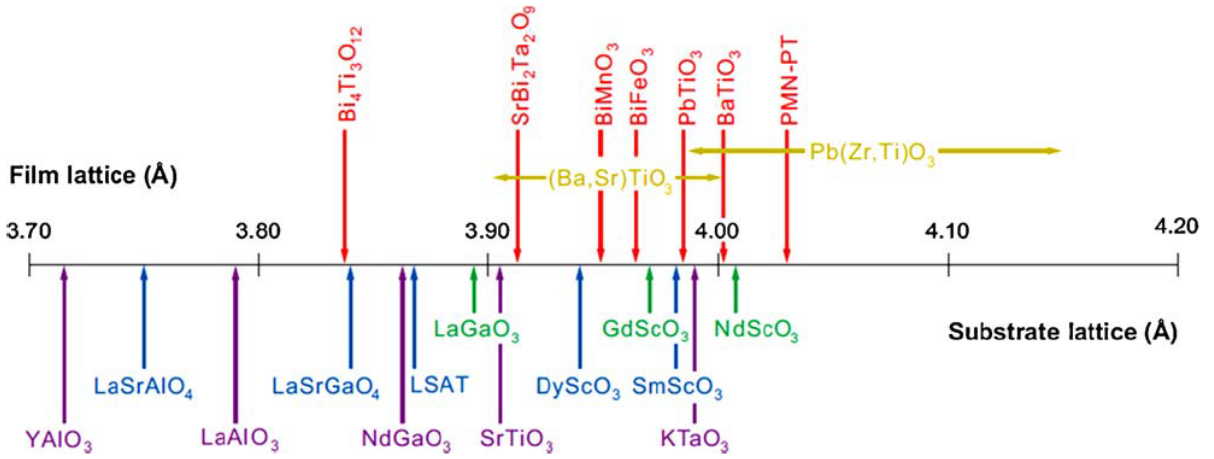

Fig. 1.9 pseudo-tetragonal or pseudo-cubic a-axis lattice constants of some ferroelectric perovskites of current interest along with the commercially available substrates. Adapted from Ref.[49] with the permission of Annual Reviews.

$LaAlO_3/SrTiO_3$ heterostructures [47] and superconductivity in $Nd_{0.8}Sr_{0.2}NiO_2$ thin film [48] in last year have pushed the field a step ahead in terms of fundamental research. In the following section we will primarily survey about the recent developments in the magnetic and ferroelectric oxide thin films in terms of technological as well as fundamental point of view that are in the scope of this thesis.

1.4.1 Modulating polar & magnetic ordering

Thin films & Heterostructures: Thin films of ferroelectric oxides got importance from the beginning of this century. The major concerns and challenges were the sustainability of the ferroelectricity in ultra-thin films [50], along with the manipulation of the parameters like ferroelectric T_C, spontaneous polarization or applied voltage with strain engineering [49]. The very first breakthrough was the observation of room temperature ferroelectricity in $SrTiO_3$ thin film, which is generally paraelectric in any temperature. Epitaxial strain had enhanced the ferroelectric T_C hundred times, which was not previously possible with chemical doping in bulk samples [51]. Conventional ferroelectric oxide that was firstly explored as thin film was $BaTiO_3$. The ferroelectric transition temperature as well as the remnant polarization were dramatically enhanced with respect to the bulk single crystal depending on the compressive strain imposed by different rare earth oxide scandate substrate as shown in Figure 1.10 [52]. The most celebrated ferroelectric perovskite oxide thin film that has been widely studied is $BiFeO_3$ as an effective magnetoelectric multiferroic thin film. A coupling between it's lone pair driven ferroelectricity and canted antiferromagnetic order has been observed in thin films that is absent in the bulk crystal [25]. Study of ferroelectric domains in ultra-thin single crystalline films is

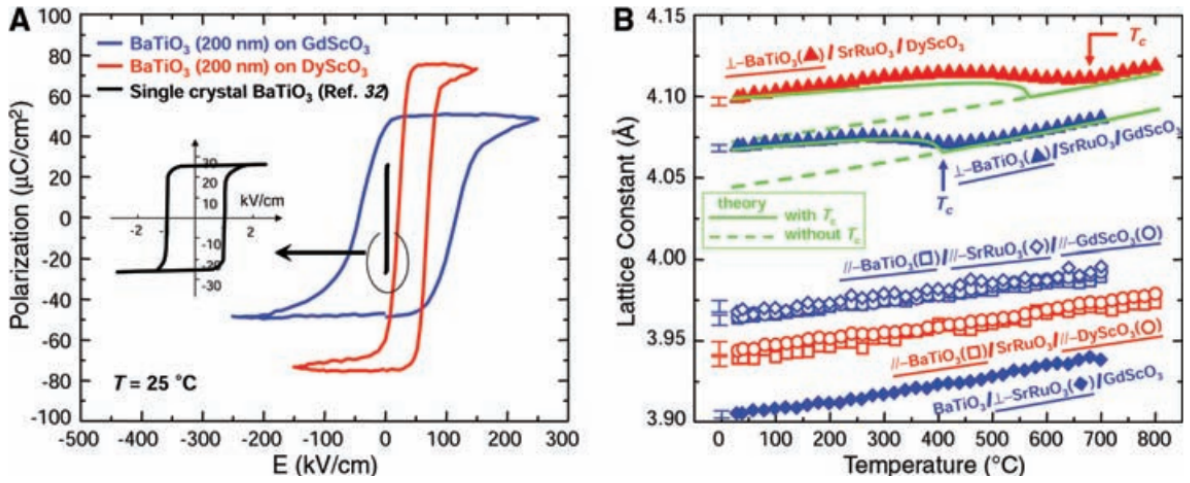

Fig. 1.10 (A) Polarization-electric field hysteresis loops for strained $BaTiO_3$ thin film capacitors with $SrRuO_3$ top and bottom electrodes grown on $DyScO_3$ and $GdScO_3$ substrates. The inset shows the hysteresis loop of an unstrained bulk $BaTiO_3$ single crystal for comparison.(B) Temperature dependence of the in-plane and out-of-plane lattice parameters of these same strained $SrRuO_3/BaTiO_3/SrRuO_3$ capacitor structures. Adapted from Ref. [52] with the terms & conditions of AAAS

also of rapidly growing interest among researchers. $Pb(Zr_xTi_{1-x})O_3$ [53, 54] and $BiFeO_3$ have been studied widely in this context. The complex domain structures of $BiFeO_3$ and switching with electric field (commonly 71° and 109°) on different substrate plane and orientations have been studied rigorously for last fifteen years [55, 56, 57, 58, 59]. Thin films of both orthogonal & hexagonal rare earth manganites have been also intensively explored, as will be discussed in detail in Chapter 4. Recently, a novel rhombohedral phase of $Hf_{0.5}Zr_{0.5}O_2$ has been epitaxially stabilized on [001] oriented $La_{0.7}Sr_{0.3}MnO_3/SrTiO_3$ with a high polarization value [60]. While talking about thin films of magnetic oxides, ferromagnetic Ferrites with spinel structures (Fe_3O_4, $NiFe_2O_4$, and $CoFe_2O_4$) had drawn the primary attention [61]. The most studied thin films of magnetic oxides are the mixed valance manganites due to the rich phase diagram consisted with magnetic and metal-insulator transition, charge ordering, colossal magnetoresistance (CMR) etc [62] for last 20 years. The structural and magnetic properties could be significantly modified with strain in thin films. Ferromagnetic and half metallic $La_{0.70}Sr_{0.30}MnO_3$ & $La_{0.67}Ca_{0.33}MnO_3$ were the most investigated manganites in this context. Switching and anisotropy of in-plane to out-of-plane magnetization has been well observed in $La_{0.70}Sr_{0.30}MnO_3$ on $SrTiO_3$ & $LaAlO_3$ depending on the applied strain (tensile & compressive) [63, 64]. Sometimes novel cationic A site ordering of La and Ca in $La_{0.67}Ca_{0.33}MnO_3$ thin film on MgO results unconventional rhombohedral phase that is unusual in bulk material [65]. A huge effort has been given in the oxide thin film community doing research on ferroelectric and magnetic oxide thin film is to make a ferromagnetic ferroelectric oxide with significant

magneto-electric coupling as most of the bulk multiforrics are antiferromagnets. The intensive study on $BiFeO_3$ [66], $BiMnO_3$ [67], h-$YMnO_3$ [68, 69] and $EuTiO_3$ [70] thin films are very intriguing in this respect. Artificially engineered ferromagnetic/ferroelectric heterostructures such as $BaTiO_3$-$CoFe_2O_4$ [71] or $BiFeO_3$-$La_{0.70}Sr_{0.30}MnO_3$ [72] has also been explored for years for optimization of electric field control of magnetization.

Superlattices: Modulation of polar and magnetic ordering in oxide multilayers or superlattices have been proved to be very powerful over years. Study of $LaMnO_3/SrMnO_3$ superlattice has been found to show interesting results. Both $LaMnO_3$ and $SrMnO_3$ are antiferromagnetic insulators as bulk parent compound. Interestingly, it has been found that the superlattice becomes a metallic ferromagnet with a repeat length of layers $\leq$ 2 u.c. With increasing the repeat distance the magnetic behaviour gradually becomes similar to parent $LaMnO_3$ but the electronic conductivity is controlled by the interface [73]. It was later found that a critical repeat distance triggers a metal-insulator transition [74] in the superlattice. In recent years, two remarkable discoveries have further pushed the effect of superlattice. First is the observation of polar vortex & antivortex pairs in $(SrTiO_3)_n/(PbTiO_3)_n$ superlattices on $DyScO_3$ substrate [75] as shown in Figure 1.11(a). Further development comes true last year with the observation of polar skyrmion for the first time, stabilized at room temperature [76]. Second is an artificially engineered superlattice $(LuFeO_3)_m/(LuFe_2O_4)_1$ as presented in Figure 1.11(b). This superlattice of geometrical ferroelectric ($LuFeO_3$) and ferrimagnetic ($LuFe_2O_4$) has been found to have strong ferromagnetic & ferroelectric ordering along with considerable magneto-electric coupling at room temperature [77].

1.4.2 Technological aspect & Device integration

Though there are plenty of applications of ferroelectric and ferromagnetic oxides, in this section we will primarily focus on the oxide thin films in the context of device science and technology. The most celebrated application of polar and magnetic ordering is in the nonvolatile Random Access Memory (RAM). It could be either a Ferroelectric Random Access Memory (FRAM) or Magnetoresistive Random Access Memory (MRAM). Nonvolatility, that is retaining data even when the power is off along with low power consumption are the advantage of them over traditional dielectric RAM. For a FRAM, a capacitor with the ferroelectric is used as memory unit cell. Positive and negative polarization (+P or -P) work as 0 and 1 binary bits. In contrast, in MRAM, the up and down spins acts as the bits. The major problem with FRAM is the destructive read process i.e. changing the stored data while reading it. Many different architectures for FRAM have been proposed and commercialized over years of development [78, 79]. Modern MRAM works on the principle of basic Magnetic Tunnel Junctions (MTJ). MTJ is composed of two ferromagnetic layers (one is fixed and other is free to switch) separated by a non magnetic barrier.

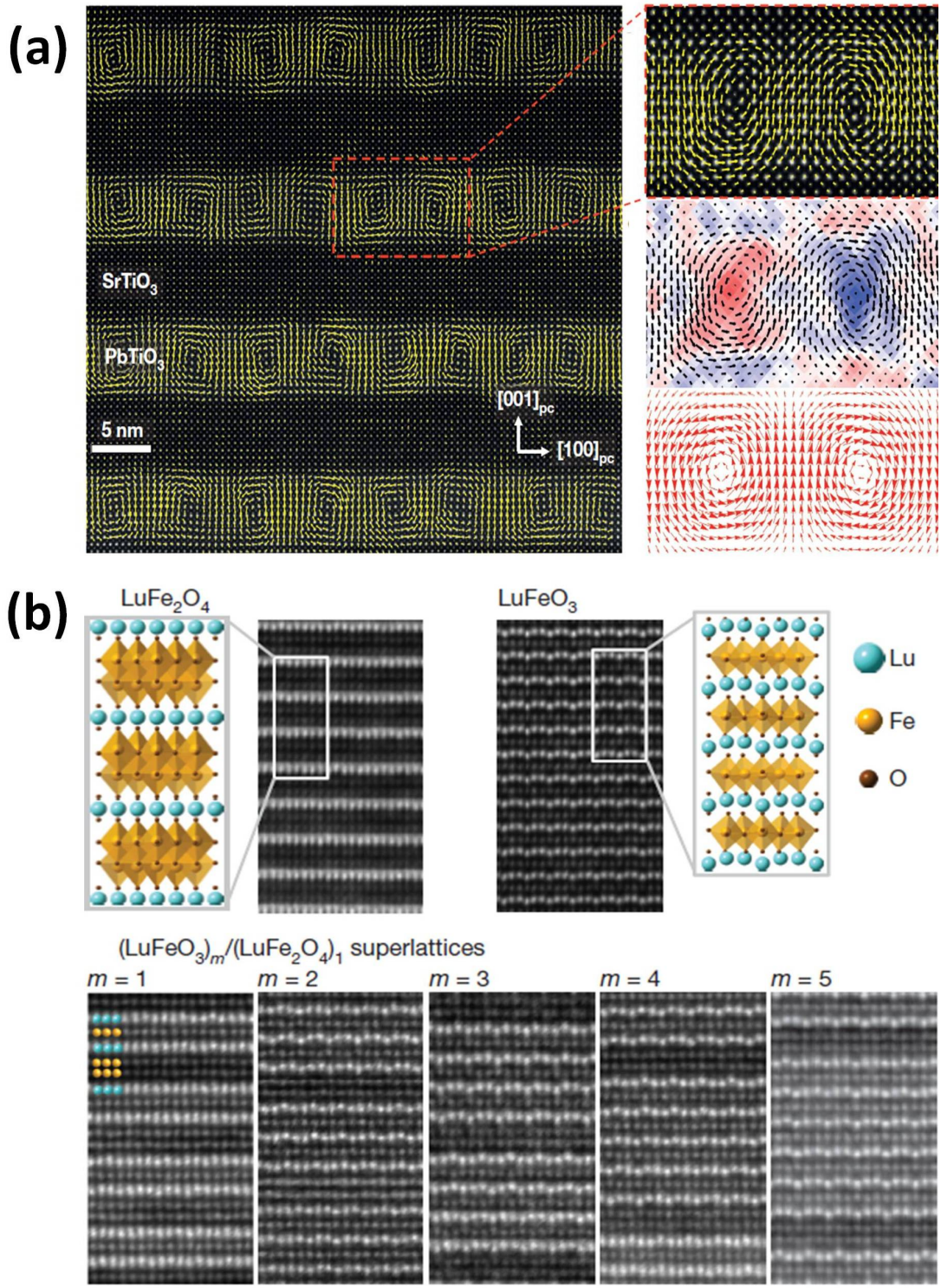

Fig. 1.11 (a) Observation of vortex-antivortex pair like polar domains in $(SrTiO_3)_n/(PbTiO_3)_n$ superlattices . The atomic polar displacement vectors has been presented as yellow arrows in HR-STEM images.(b) HAADF-STEM images of $(LuFeO_3)_m/(LuFe_2O_4)_1$ superlattice with different number of repeat unit cell(m) along with the parent individual structures. Adapted from Ref.[75] &[77] with the permission of Springer Nature

Depending on the spin orientation, the electrons scatter while flowing as current in the junction. This spin dependent scattering offers either low or high resistance of the MTJ depending on the parallel or anti-parallel spin configuration. The high and low resistance state work as 0 and 1 binary bits [80]. MTJ and MRAM also have been commercialized successfully. The current research focus to make a magneto-electric multiferroic RAM where 4 bits can be used simultaneously (two from polarizations, two from the spins). The technical problem of data reading in FRAM can be solved here to write with electric field and read magnetically. Ultra thin (2 nm) $La_{0.1}Bi_{0.9}MnO_3$ has been investigated as Multiferroic Tunnel Junction and 4 bit operation is well demonstrated by the group of Nobel laureate Dr. Albert Fert in 2007 [81]. Device optimization or the technology for commercialization is still under active research and development.

1.5 Motivation & Scope of this Thesis

Motivation of this thesis simply emerges from the rich literature and history of oxide thin film research. Gradual development in growth and characterization techniques, precise control over quality of single crystallinity and thickness make the field of Oxide Electronics an attractive playground for last two decades not only to explore fundamental physics but also for the pathway to device science. Inducing novel polar and magnetic ordering in some new strain stabilized engineered oxide thin films as well as heterostructures is going to be the key focus of this thesis. We have grown and investigated a perovskite, a double perovskite and a perovskite heterostructure in order to contribute a little to this field.

This Thesis presents:

- The detail mechanism and growth of the epitaxial oxide thin films heterostructure using low cost vacuum free technique Metal-organic Aerosol Deposition (MAD) assisted with optical ellipsometry along with conventional technique like Pulsed Laser Deposition (PLD) assisted with Reflection High Energy Electron Diffraction (RHEED). Both optical ellipsometry and high pressure RHEED have been used to monitor in-situ growth parameters and precise thickness of the film.

- A newly discovered hexagonal phase of conventional magneto-electric o-$TbMnO_3$. This hexagonal phase is strain stabilized in thin films and does possess geometrical ferroelectricity at room temperature. Our deposition technique and growth procedure results a way better growth than previous reports of this artificial metastable phase in terms of single crystalline quality as well as the sharpness of substrate-film interface of h-$TbMnO_3$/YSZ(111) films. Detail combined high temperature measurements such as Transmission Electron Microscopy, Raman Spectroscopy and Optical ellipsometry point out the ferroelectricity $T_C \sim 800$ K, for the first time.

- A first time growth of partially B-site ordered monoclinic epitaxial Tb_2CoMnO_6 double perovskite thin film on Nb:$SrTiO_3$ (001). Transmission electron microscopy and electron energy loss spectroscopy mapping shows the presence and distribution of both Co^{2+} and Co^{3+} ions in the film, evidencing a partial B-site disorder, which was further confirmed by the observation of reduced saturation magnetization at low temperatures. Temperature dependent dielectric measurements reveals an unexpected high temperature dipolar relaxor-glass-like transition at a temperature $T^* \sim 190$ K $> T_C$, which depends on the applied frequency and indicates a superparaelectric behaviour. Two different dielectric relaxation peaks have been observed; they merge at T^* where likely a coupling to the disorder-induced short range charge-spin correlations results in a 4% magneto-dielectric coupling.

- The growth of 3d-5d based relaxed $BaTiO_3/SrIrO_3$ heterostructures, to obtain emergent phenomena arising from the interfacial coupling between B-site (Ti^{4+}; $3d^0$ and Ir^{4+}; $5d^5$) cations. Parent $BaTiO_3$ film shows weak ferromagnetic ordering at $T_C \sim$ 136 K, due to the oxygen vacancies, in contrast of paramagnetic nature in strong spin-orbit coupled $SrIrO_3$ film. Interestingly, in $BaTiO_3/SrIrO_3$ heterostructure we observed magnetic ordering at $T_C \sim 160$ K. X-ray photoelectron spectroscopy of O 1s and Ti 2p reveals the presence of oxygen vacancies and Ti^{3+} states in $BaTiO_3/SrIrO_3$, similar to the parent $BaTiO_3$. However, significant changes in Ir 4f spectrum line shape with coverage has been observed in $BaTiO_3/SrIrO_3$, in contrast of parent $SrIrO_3$. Therefore, this remarkable enhancement in T_C is attributed with the interfacial charge transfer process and the presence of strong spin-orbit coupling. We establish the presence of two new plausible interactions in the system namely Ti^{4+} -O- Ir^{4+} and Ti^{3+} -O- Ir^{4+}.

CHAPTER 2

Growth of Oxide Thin Films

As discussed in the previous chapter, diversity in research interest among oxide materials has been grown exponentially in last 30 years. Due to the novel and emerging functionality, the field of oxides becomes a major area of research in the field of condensed matter physics. Starting from binary to ternary oxides with spinel or perovskite structures Oxides become an important playground of interesting fundamental many body physics due to the presence of strongly correlated electronic and magnetic states. The hunch for developing new devices using the broad functionalities of Oxides has given the birth of new technical field called Oxide Electronics.

The present chapter deals with the details of the growth of magnetic and ferroelectric Oxide thin films. We first discuss the principles of growth of thin films in general; later highlight the oxide films. Then the detailed role of substrates in terms of epitaxial relationship is introduced. Thereafter the modern available deposition techniques are discussed. At the end we present the detailed growth methods intensively used in this thesis namely Pulsed Laser Deposition (PLD) and Metal-organic Aerosol Deposition (MAD) techniques for the deposition of Oxides.

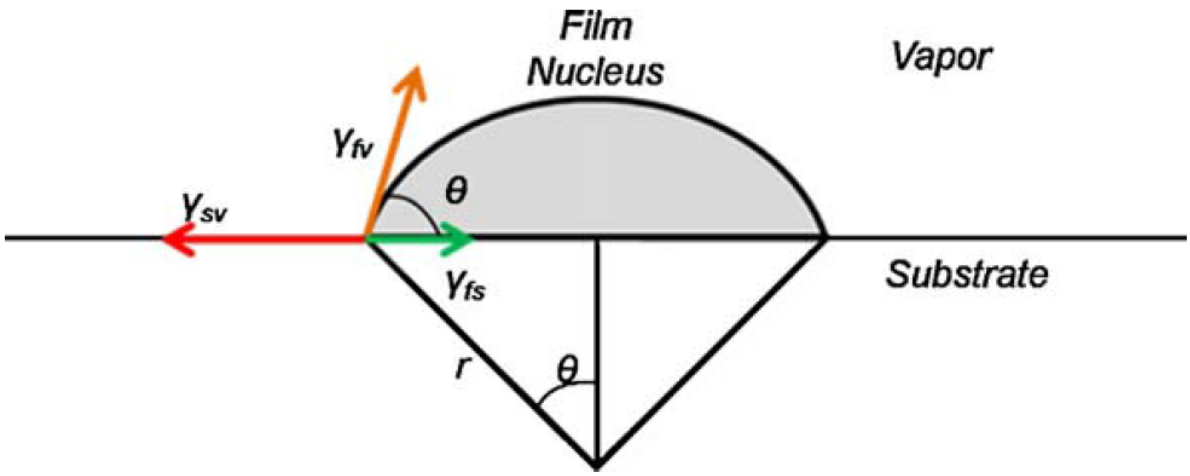

Fig. 2.1 Schematic representation of nucleation process during film growth with the primary components of surface tensions. Adapted from Ref.[1] with the permission of Elsevier

2.1 Principles of thin film growth

Although the process of thin film growth is quite complex from microscopic point of view, the key to entire mechanism mostly depends on local thermodynamics. As we know, any physical system wants to minimize its free energy for stabilization. Here during film growth the free energy is the surface energy which must be minimized for a stable film. Mostly, the mechanism of thin film or crystal growth is described in terms of thermodynamic model of nucleation. From the point of view of droplet theory and basic capillary action, vapor phase nucleation could be modeled on substrate surface. This method is well explained by L.W. Martin et al. [1] as depicted in Figure 2.1. The horizontal components of the of the interfacial surface tensions among the participating phases are stabilized in equilibrium with the Youngs equation, $\gamma_{sv} = \gamma_{fs}+\gamma_{fv}\cos\theta$. Here γ is the interfacial surface energy. s, v and f refers to the substrate, vapor and film respectively. θ is the contact angle. For an island type growth θ is always positive and for a layer by layer growth droplets are parallel to the substrate surface hence $\theta \sim 0$. So we have two distinct cases for the film formation. For the first case, $\gamma_{sv} < \gamma_{fs}+\gamma_{fv}$. In this case as we see during the growth island type growth is possible if surface tension of the substrate is less than that of the film and that explains the cluster growth of metal on non metallic substrate. On the other hand a layer by layer growth occurs when the vapour wets the substrate or substrate surface tension exceeds than that of the film. As film - substrate surface tension for different materials are hard to determine sometime, homoepitaxy could be understood in this scenario for the sake of simplicity.

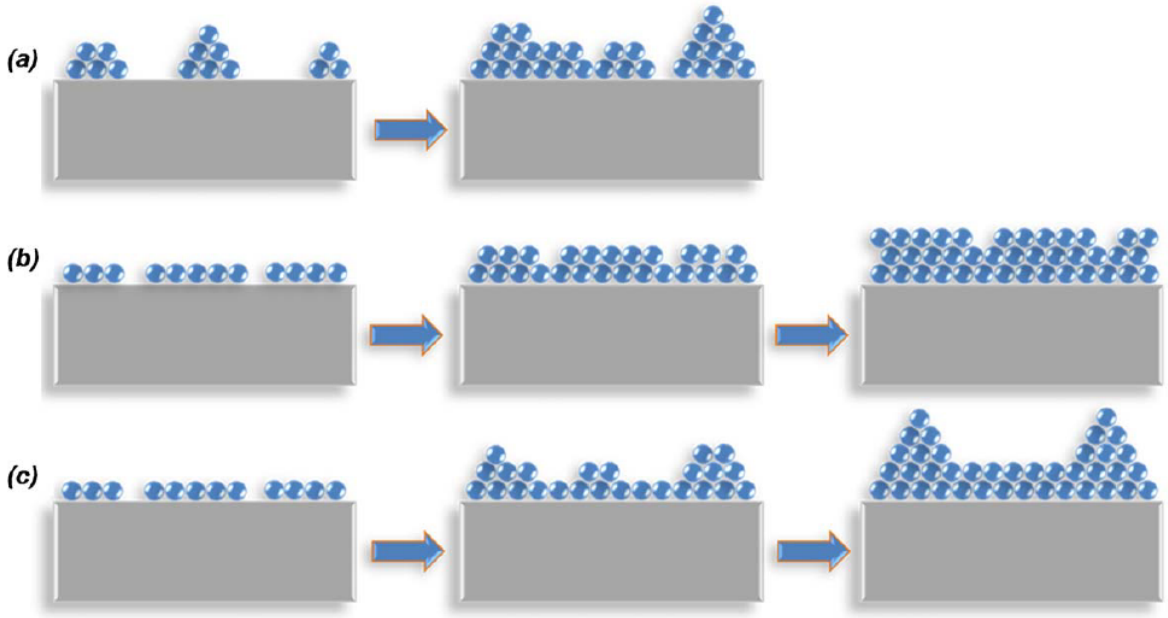

Fig. 2.2 Illustrations of the basic growth modes including (a) Volmer-Weber (island), (b) Frank-Van der Merwe (layer-by-layer) and (c) Stranski-Krastanov growth.Adapted from Ref.[1] with the permission of Elsevier

Depending on the above factors and local thermodynamics the growth mechanism could be categorized into three distinct types. (1) Frank-Van der Merwe or simply layer-by-layer growth. In this case as explained before thin film growth takes place as atomic layers. The atomic interaction between film and substrate atoms are much stronger than intra atomic interaction inside film and deposition takes place as planner sheets. Many oxide semiconductors are grown in this mode on oxide substrate. (2) Volmer-Weber or island growth. Due to the strong intra-atomic interactions, films start forming globules or small islands. This is very common during the growth of dissimilar materials. Mostly non oxides and metals grow in this mode on oxide substrate. (3) A mixture of layer by layer and island type growth named as Stranski-Krastanov growth. Here presence of competitive inter and intra atomic interaction leads to the mixed growth depending on the local dynamics. This has been observed in many metal-metal or metal-semiconductor heterostructure [82]. Schematic visualization of various growth process has been presented in Figure 2.2 [1, 82].

2.2 Role of substrate and strain

Epitaxial thin film growth can be understood as extending the crystal on the single crystalline substrate lattice. There could be two possible ways to achieve this. First is the homoepitaxy where substrate and film are chosen as same material. Due to the exact matching of the substrate - film lattice parameters, layer by layer epitaxial growth is very

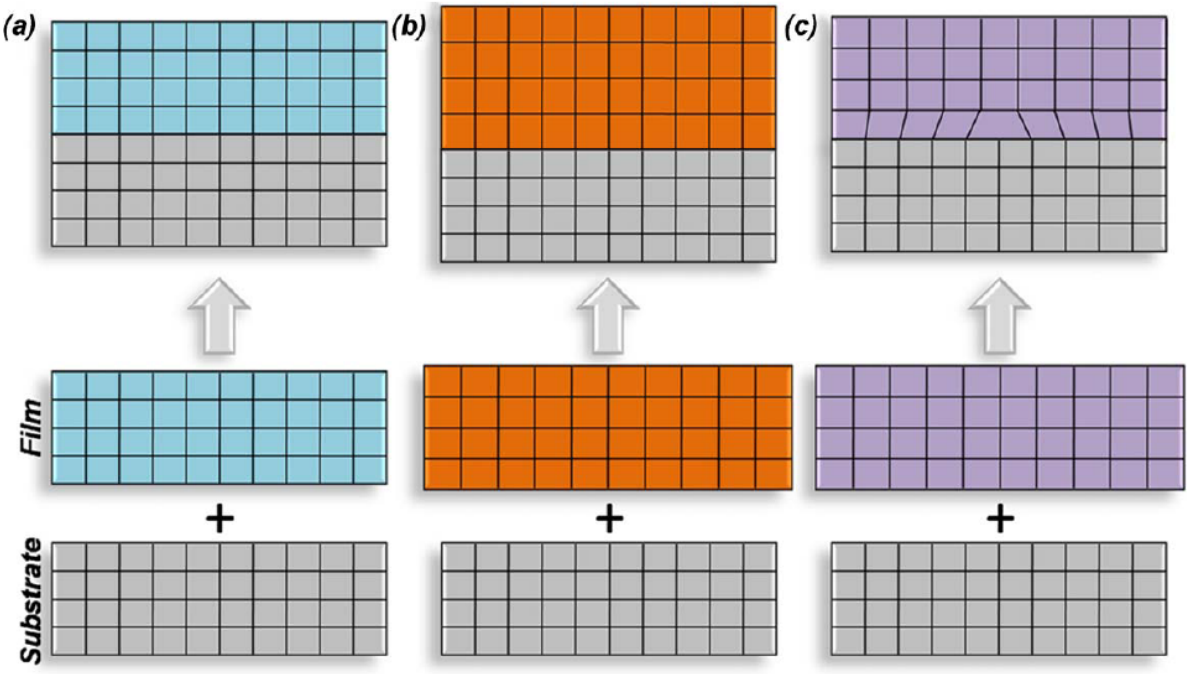

Fig. 2.3 Illustration of (a) nearly perfectly lattice matched homoepitaxial growth, (b) strained, and (c) relaxed heteroepitaxial film growth. Adapted from Ref.[1] with the permission of Elsevier

much favourable in this scenario. Second is the heteroepitaxy where the film is a different material than the substrate. The presence of the lattice mismatch between them triggers two different ways of the stabilization of the film. If the lattice mismatch is small then the film lattice tries to take the in plane lattice parameter of the substrate and stabilizes in a strained state. This accommodation of the strain results a reformed crystal structure with elongation or shortening of lattice parameter or octahedral rotation [83]. The epitaxial strain could be defined as the lattice mismatch f $\sim$ | c_f - c_s | /c_f . Where c_f and c_s are film and substrate lattice parameters respectively. The film stabilizes with a tensile strain if $c_s > c_f$ and with a compressive strain if $c_s < c_f$. Typically the epitaxial growth occurs when f < 0.1 and beyond that interfacial energy is reduced and epitaxy breaks. If the lattice mismatch is slightly larger than a strained state, the film become relaxed taking its original bulk lattice parameter. In this case the effect of substrate strain becomes effective for few layers in the interface. Beyond that the film results a quick relaxation with the formations of defects or dislocation. Strained state occurs when the the crystal structures are very similar for both film and the substrate materials. For example, perovskite on perovskite. Dissimilar structures lead to relaxed film most of the time. Sometime lattice mismatch f depends on the temperature and thermal expansion coefficients of film and substrate become crucial for the heteroepitaxy [84]. Figure 2.3 depicts the different ways of epitaxial growth [187].

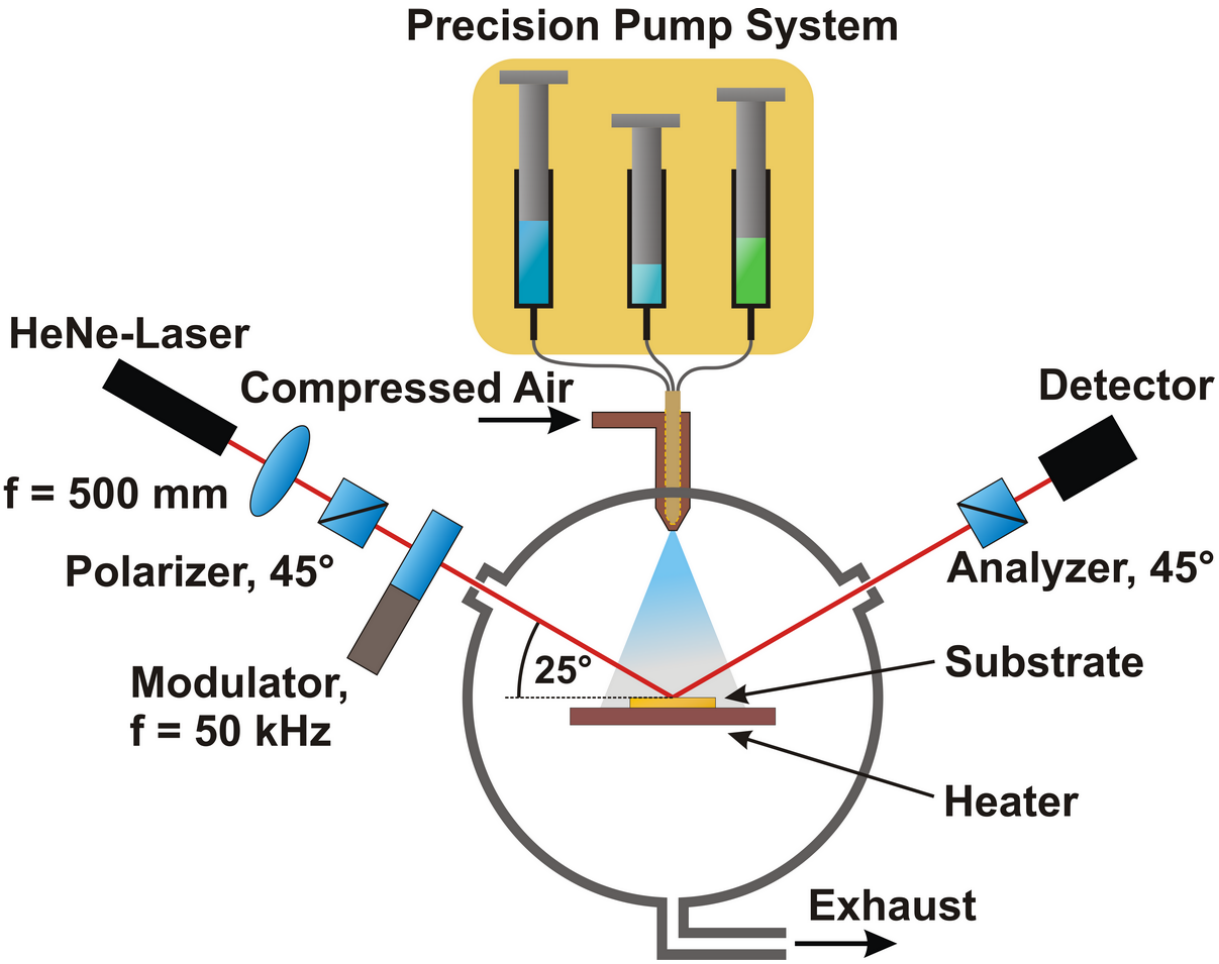

Fig. 2.4 Schematic structure of the MAD system with the deposition chamber and the arrangement of heater, nozzle and computerized syringe system. Adapted from https://www.uni-goettingen.de/en/39787.html with the permission of Prof. V. Moshnyaga

2.3 Deposition Techniques

Recent advancements on deposition methods have opened a new horizon in the research of oxide thin films. Growth techniques like Sputtering, Chemical Vapour Deposition (CVD), Laser Ablation specially Pulsed Laser Deposition (PLD), Aerosol Deposition, Molecular Beam Epitaxy (MBE) etc have been proved to be very powerful in terms of sample quality as well as growth of ultra-thin single crystalline oxide films. Here in this section two deposition techniques intensively used have been discussed as following.

2.3.1 Metalorganic Aerosol Deposition (MAD)

The thin films examined in Chapter 4 & 5 are produced using the so-called organometallic aerosol deposition (MAD)[85, 86], with which the most varied oxide layers such as mixed-

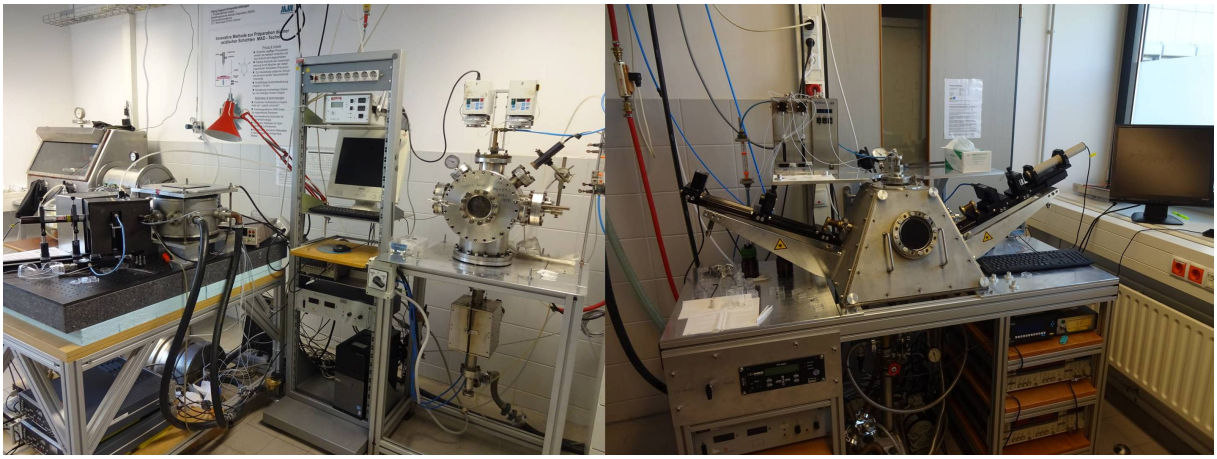

Fig. 2.5 The real set up for MAD (left) and LOMAD (right) used to grow films at I. Physikalisches Institut,Georg-August-Universität Göttingen, Germany

valent manganates [85, 86, 87], titanates [88], high-temperature Superconductor cuprates [89], ZnO [90] or double perovskites [91, 92, 93] in extremely high quality could be grown. This chemical deposition process is the basis organometallic precursors in the desired stoichiometric ratio and in the desired concentration in a polar, organic solvent (here dimethylformamide (DMF); chemical formula: C_3H_7NO) dissolved and then in ambient air via a computer-controlled dosing syringe system (type SyrDos 2 from HiTec Forceps) using compressed air (p $\approx$ 5 bar) and a pneumatic nozzle as an aerosol heated, crystalline substrate can be sprayed. The MAD system is shown schematically in Figure 2.4. The substrate itself is centred in front of the nozzle on a SiC heater, the temperature of which can be resistively controlled via a power source. Thus, layers with different substrate temperatures are produced. Depending on the oxide, these are in a range of T = 500 - 1200 °C. A water cooling, the compressed air and precise control of the current level via a computer protect the heater along with the substrate from rapid heating and cooling. The syringe system can be operated at different speeds (steps per second), which makes it possible to determine the deposition rate (in μl/s; typically 1 - 100 μl/s) and thus the growth rate of the layers (in nm/s) is here about 0.1 - 3 nm/s approximately. The growth of oxide layer on the substrate is based on the principle of chemical vapour deposition by a pyrolysis reaction, where the metal ions, the dissolved precursors from the droplets of the aerosol (a few μm droplet size) and the oxygen of the compressed air form the metal oxide layer, while the remaining solution components (the remaining solvent and organic residues of the precursor) burn to CO_2, H_2O and other components with the exhaust air from the deposition chamber. With the proportional dependence of the oxide layer thickness from the solution volume, the solution for an atomic monolayer (ML) of the oxide can be found. Approximately, $V_{ML} \approx$ 5 - 10 μl depending on the oxide, substrate, temperature and solution concentration. About the precision of the syringes of V $\approx$ 10 nl

[94] (the syringe volume is V = 500 μl per complete filling) the layer thickness can be up to 1/100 of a monolayer to be controlled. In addition, an optional growth control can be carried out for superlattice layers using an integrated ellipsometry measurement set up [89, 92, 95, 96]. Compared to molecular beam epitaxy (MBE), the pulsed laser deposition (PLD), sputtering or thermal evaporation, the MAD offers advantage that there is no ultra-high vacuum for the layer growth is needed. Furthermore, the growth parameters such as stoichiometry in the solution, the growth rate, the layer thickness and the growth temperature vary flexibly for each layer [85, 86]. By growing under ambient air (oxygen partial pressure p_{O2} = 0.21 mbar), film also becomes a stoichiometric one and oxygen deficiency due to oxygen vacancies in the oxide layer is avoided [86]. An aftercare heating in an oxygen atmosphere is therefore not necessary. However, that must be done for the pyrolysis reaction and the burning of the solvent a certain temperature is required, so that a deposition at about room temperature not possible. The interaction must also be carried out for metals with several oxidation levels of temperature and partial pressure of oxygen are taken into account at the MAD standard temperature (T = 1000 °C) to obtain the desired oxide [92, 97]. It is therefore necessary to expand the system so that the oxygen partial pressure during deposition to be able to influence. This enables the concept of oxygen-reduced MAD (LOMAD, Low Oxygen MAD) [92, 97, 98]. Another extension is that growth of micro structures with line widths below one micrometer by local heating the substrate using a position-controllable laser [99]. The detail growth of the films studied in this thesis has been presented in respective chapters.

2.3.2 Pulsed Laser Deposition (PLD)

The thin films examined in Chapter 6 & Appendix A are produced using Pulsed Laser Deposition (PLD) technique. Laser based ablation technique is one of the most celebrated and advanced methods in the community of Oxide thin film growth. Starting from 1980s with the discovery of high T_C cuprate superconductors and successful deposition of YBCO thin films [100] in 1987, pulsed laser deposition has drawn a significant attention for the development of oxide thin film based research. With various major modern advancements, PLD technique is now one of the most used methods to grow a wide range of semiconductors, insulators, superconductors, two dimensional and layered materials. The schematic diagram for a basic PLD system has been presented in Figure 2.6. Whole set up is primarily contained with an Excimer Laser, a deposition chamber and an automated target rotation control system. Pulsed Excimer Lasers are gas lasers containing mixture of a noble and a halide gas. Both of them don't react in their ground states but form bonding while in excited states. As the life time of this excited dimer state is very short, they quickly decay to their respective ground states with an emission in ultra violet range. Most common combination that are used in such lasers are ArF, KrCl, KrF, XeCl and XeF. A KrF laser has been used to grow all the films related to this thesis with a

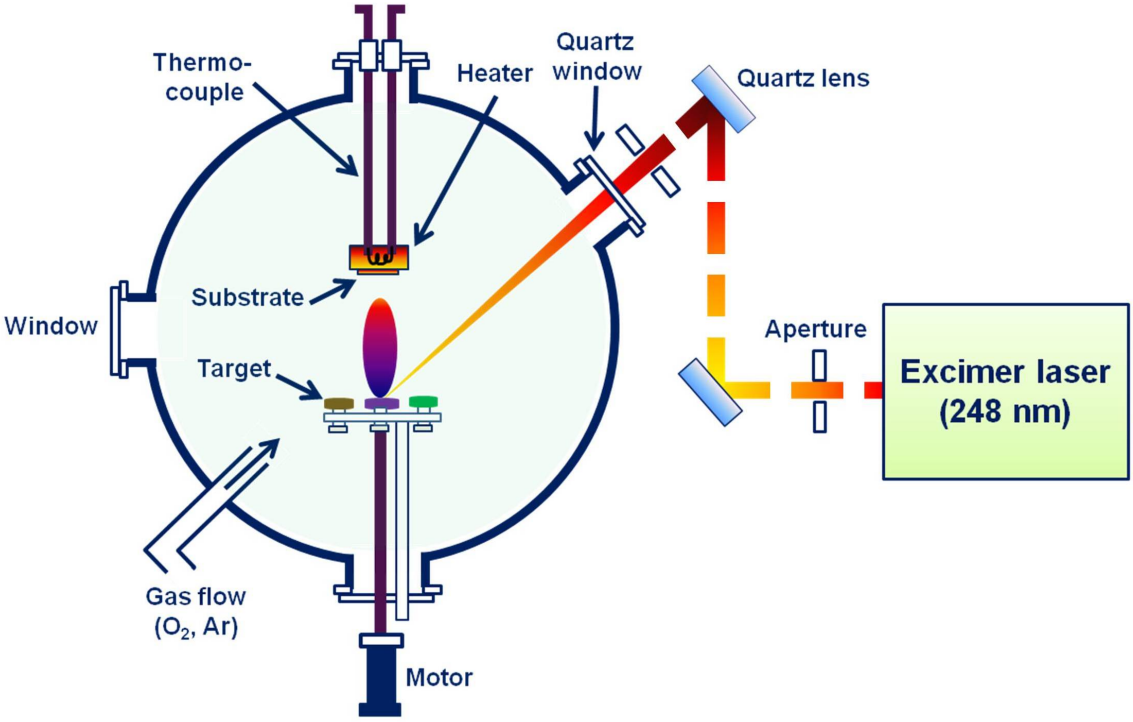

Fig. 2.6 Schematic structure of the PLD system with the deposition chamber and the arrangement of Laser, heater and computerized target system. Adapted from Ref.[101] with the permission of Dr. Abhijit Biswas

wavelength $\lambda = 248$ nm.

The deposition chamber that has been primarily installed and used at IISER, Pune is a steel vacuum chamber connected with gas controller, vacuum system and the automated target control system provided by Excel Instruments,Mumbai. Vacuum system consists of a rotary and a turbo pump by Pfeiffer Vacuum System. The lowest pressure inside the chamber that can be achieved is around 1×10^{-7} mbar. Substrate could be mounted on a heater as depicted in the schematic and the targets are placed in front of the heater. The programmable heater is made of stainless steel and the temperature of which can be resistively controlled via a power source. The highest temperature that could be achieved is around 800 °C. The target to heater distance is around 6 cm and targets could be rotated and changed automatically by an external software. The laser beam coming from the quartz window hits the target at an angle about 45°. Oxygen partial pressure could be manually controlled and adjusted with gas controller. Targets are made from the powder of the required materials/mixture of materials with proper stoichiometry prepared by standard solid state reaction method. Another advanced chamber that has been used

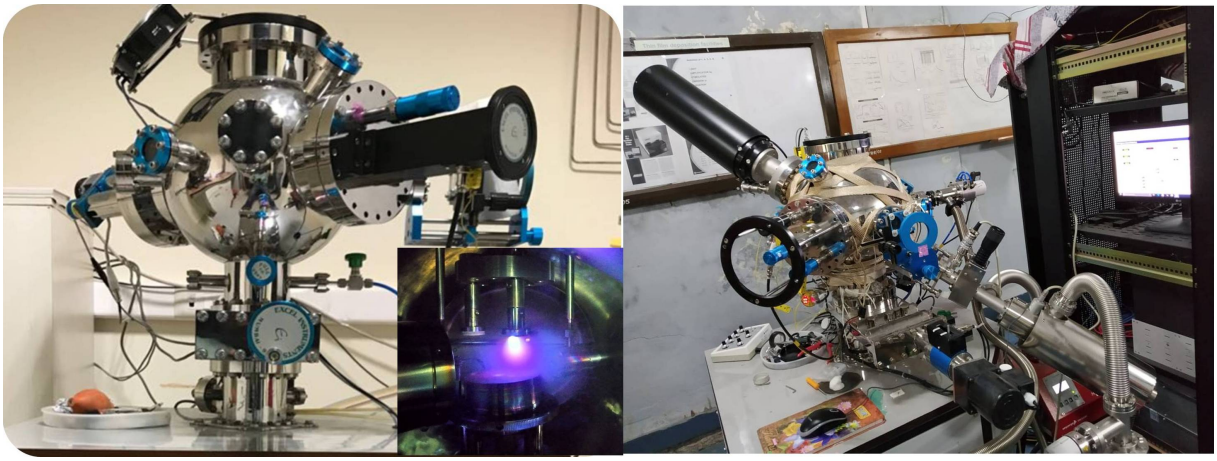

Fig. 2.7 The real set up for PLD (left) and RHEED assisted PLD (right) used to grow films at IISER Pune and UGC-DAE CSR Indore respectively. The real snapshot of the plasma plume during deposition (inset)

very shortly at UGC-DAE CSR Indore is equipped with Reflection High Energy Electron Diffraction (RHEED) [102] is used to monitor the in-situ layer by layer growth and the quality of thin film as shown in Figure 2.7. Here an incident high energy electron beam ($>$ 1 KeV) at low angle (1 - 4°) on the substrate surface is reflected to the detector. With growth of film layers on the substrate it creates diffraction pattern and oscillation of the RHEED intensity that can give us the quality of the growth and interface as well as the number of unit cell [103]. The technical details of RHEED have been discussed in chapter 3.

The most interesting and fundamental part of PLD process is the laser-material interaction and the creation of plasma plume. When a short duration high energy laser pulse is absorbed at the target surface within a very short area, it primarily cause an electronic excitation and thermal vibration. After that, thermal melting and evaporation starts with a highly directed plasma plume consisting of small chunks, atoms, molecules, highly energetic ions as well as electrons. All these phenomena occurs in a very short duration of time. Typically the pulse width of the lasers used in PLD is around 20 ns. This flush evaporation and creation of plasma depend on primarily three factors. They are incident photon energy, absorption depth of the photon on the target surface and the thermal diffusion length of the target material. For most oxide materials the absorption depth is approximately 100 nm for the UV wavelength range used for deposition. The thermal diffusion length ζ is defined as $2[\left(\frac{\kappa}{\rho c}\right)\Delta t]^{1/2}$, where κ is the thermal diffusivity, ρ is the mass density of the target, c is the specific heat and Δt is the pulse duration of the incident photon [1]. The real image of the plasma plume has been shown in Figure 2.7. After the creation of highly oriented plasma plume, all the energetic species reached the substrate placed perpendicular to the center of plume conic and growth starts. Though

the growth modes in thermodynamic equilibrium have been discussed previously, it could not be the ideal case for PLD process. Due to the limited amount of surface diffusion and fast process with the supersaturation of plasma,the deposited material will not have the enough time to minimize it's surface energy in an ideal thermodynamic equilibrium. Hence the kinetic effects have to be taken care of and it lead to the high nucleation rate along with different growth modes. Surface diffusion coefficient and the surface diffusion length are the most important kinetic parameters in this respect [103]. Another parameter which is very important for the PLD growth kinetics, is the laser fluence. It denotes the amount of energy dumped on the target surface per unit area. Simply it's the energy density of the laser pulse expressed in J/cm^2. Higher laser fluence increase the kinetic energy of the charged particles in the plasma plume and hence increase the surface diffusion length. For most of the oxide materials a laser fluence of 2-3 J/cm^2 is generally used. In reactive PLD process such as deposition of Oxides using O_2 partial pressure inside chamber,laser fluence highly affects the rate of O_2 incorporation and the stoichiometry of the film. In most cases, higher laser fluence combined with high substrate temperature prefer single crystalline pure phase films. In simple words higher laser energy density makes the ionic migration process from target to substrate faster and hence reduce the probability of ionic dissociation or forming any other impurity phases.

2.4 Conclusions

In summary detail mechanism of growing a thin film and role of substrate on the film quality have been intensively discussed in this chapter. Overview and the detail parameters of two growth techniques namely Metalorganic Aerosol Deposition (MAD) and Pulsed Laser Deposition (PLD) have been presented that are rigorously used in this thesis. There are few advantages as well as disadvantages of PLD over MAD. As an advantage PLD is an universal and popular technique that can be used to grow variety of other materials (nitrides, chalcogenides, carbides) other than oxides with suitable gas pressure or in vacuum. On the other hand MAD is a very limited and less popular technique that can be only used to grow oxides as the growth takes place in atmospheric oxygen pressure or controlled low oxygen pressure. As a disadvantage PLD is very expensive and complex technique than MAD which is much simpler. MAD grown oxide films are always oxygen stoichiometric and on the other hand PLD grown films are mostly oxygen deficient to a certain extent. To study oxygen vacancy in the film PLD and LOMAD could be equally useful.

CHAPTER 3

Experimental Techniques

The current chapter gives the brief overview of the major measurement techniques that have been extensively used in this thesis. Firstly, we review the detailed measurements for investigation of crystal and electronic structures of the thin films. Focus is on X-ray Diffraction (XRD), X-ray Photoelectron Spectroscopy (XPS), Raman Spectroscopy and Transmission Electron Microscopy (TEM) along with Electron Energy Loss Spectroscopy (EELS). Optical Ellipsometry and Reflection High Energy Electron Diffraction (RHEED) are also discussed as in-situ monitoring techniques for thin film growth. Basic principles and measurement procedures for Magnetic Measurements using conventional SQUID-VSM and home built set up for Dielectric Spectroscopy and Resistivity are also discussed briefly.

3.1 Structural Characterizations

3.1.1 X-ray Diffraction (XRD)

X-ray Diffraction is a non destructive technique to understand a crystal structure.The basic principle is very simple. X-ray that has a wavelength of same order as the spacing between atomic planes when passes through the crystal planes, get scattered elastically from the atomic electron cloud in different planes. The constructive interference between scattered beams gives the information about the atomic arrangement in the lattice. Quantitatively the spacing among the different parallel atomic planes can be evaluated from the Bragg's law [104] as given by the equation 2d sinθ = nλ. Here d is the inter planar distance, θ is the angle between the incident beam and the diffraction plane, n is an integer and λ is the wavelength of the x-ray. This equation simply defines the criteria for a constructive interference where the path difference between two beams 2d sinθ is an integer multiple of the wavelength λ as shown in Figure 3.1 (a) [105]. Bragg's law could be understood and derived in more generalised framework with wave vectors where the change in the respective wave vectors $\overrightarrow{\Delta k}$ ($\overrightarrow{k} - \overrightarrow{k'}$) and displacement vector $\overrightarrow{d}$ are related as $\overrightarrow{d} \cdot \overrightarrow{\Delta k} = 2n\pi$ for a constructive interference as depicted in Figure 3.1 (b) & (c). This generalised diffraction condition along with Bragg's law could also be well derived and represented with the framework of reciprocal space & Fourier analysis where construction of Ewald sphere and Laue equations are very fundamental [106]. Ewald sphere is a very simple construction to understand the diffraction pattern geometrically. The generalized diffraction condition can be written in 3 dimension with the components of the displacements vector. These three equations are Laue equations. Each Laue equations can be represented by a cone about the components of displacement vector. Geometrically the diffraction criteria is visualized with sphere in reciprocal space where all the three cones lie simultaneously. All the points on the sphere surface hence the planes satisfy the diffraction condition.

In practical scenario, there are many different geometry of the measurements along with specified type of samples. Samples could be in either form of powder, single crystal or thin films. Here we are fully concerned about the measurement of XRD in thin film samples. The schematic experimental set up has been shown in Figure 3.1 (d). Here the sample is placed on a goniometer stage. Diffraction conditions for different planes in a crystalline thin film could be achieved with the tuning of the angles ϕ, χ and ω. The most used geometry is Bragg-Brentano θ - 2θ geometry. Here the incident angle θ is moved in such a way that the coupled detector arm also moves to satisfy the Bragg's condition as in Figure 3.1 (a), while all the goniometer angles are fixed. In plane epitaxy is understood with a ϕ scan where sample is rotated along the ϕ axis for a particular θ - 2θ geometry. This scan could be symmetric (χ=0) or asymmetric ($\chi \neq 0$). The most detail

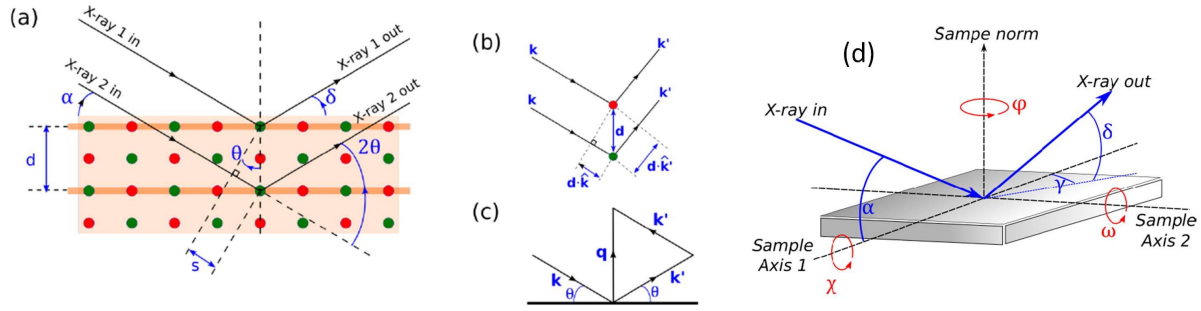

Fig. 3.1 (a) Criteria for a constructive interference in Bragg's angle θ, d is the inter planer spacing, s is the path difference between the rays, the coloured circles represent the atomic positions.(b) & (c) Generalised wave vector formalism for the Bragg's equation.(d) Detail arrangement of the axes and angles for a thin film XRD measurement set up equipped with a goniometer stage. Adapted from Ref.[105] with the terms & conditions of MDPI

measurement is a Reciprocal Space Map (RSM) where a series of θ - 2θ measurements are done for all the different planes with a gradual change in χ and other parameters remain fixed. RSM measurement is mainly used in case of epitaxial film to determine the in plane lattice parameter, substrate strain and crystalline quality. RSM is mostly carried out for a asymmetric plane that is accessed with tuning a non zero value of χ. Ideally for a particular plane there should be a sharp spot in the reciprocal space. In practical situation the spot is broadened due to the defects in the crystal. The extracted 2θ value from a asymmetric RSM spot is used to calculate in plane lattice parameter of substrate as well as film using the corresponding symmetry relations. Another important ans simple measurement is carried out is the Rocking Curve. Here we keep our detector in a fixed 2θ position for a plane of diffraction then the sample is moved around the position with changing θ.Thus we get a plot of intensity vs θ around a diffraction peak. The broadening of this curve gives an idea about the crystalline quality of the film. In depth analysis of the in-plane & out-of-plane strain, dislocations and tilting could be done with this as will be discussed in subsequent chapters.

3.1.2 X-ray Photoelectron Spectroscopy (XPS)

X-ray Photoelectron Spectroscopy is a surface probe spectroscopic technique that is widely used to analyse local electronic structure, bonding environment and chemical state of the elements in the sample. The basic principle is based on the famous photoelectric effect. When a high energy X-ray of particular wavelength λ falls on the surface of a sample, it kicks the core electrons of the elements present in the sample. The binding energy (E_B) of the ejected core electrons can be calculated as $E_B = E_\lambda$ - (E_K + W). Here E_λ is the energy

of the incident X-ray, E_K is the kinetic energy of the photo electron and W is the work function of the sample surface [107, 108]. The ejected core electrons encounter a number of inelastic scattering with the lattice (Phonon) as well as other electrons that causes the decay in the kinetic energy. So the count of the photoelectrons that are reaching the detector or energy analyser outside is very crucial and it depends on the inelastic mean free path of the photo electrons inside the sample. Thus sampling depth that is the maximum depth from where the kicked electrons are reaching the detector is very less, making XPS a surface probe technique. For most of the samples with a Al k_α X-ray source the sampling depth is approximately 3-10 nm but it could vary for specific samples.

The laboratory based experimental set up for XPS is shown in Figure 3.2 [109]. The major components are (1) a X-ray source. In most cases an Al or Mg source is used with their k_α lines of E_λ = 1253.6 & 1486.6 eV that are enough to probe core electrons of most of the elements. (2) An energy analyser of the ejected photo electrons. It is a hemispherical shaped electrostatic filter with a inner and an outer radii for the two concentric hemispheres. This two oppositely charged hemispheres make a circular trajectory of the electrons. There is also a negatively charged gate before the entrance of the hemispheres that set the energy of the incoming electrons and entering the analyser to a constant value E_0. Now depending on the elements for which the spectrum is to be recorded, E_0 could be set accordingly along with the +ve and -ve of the hemispheres for the detection in a specific energy window. Also a high vacuum system is necessary for the accuracy in the detection of electron count.

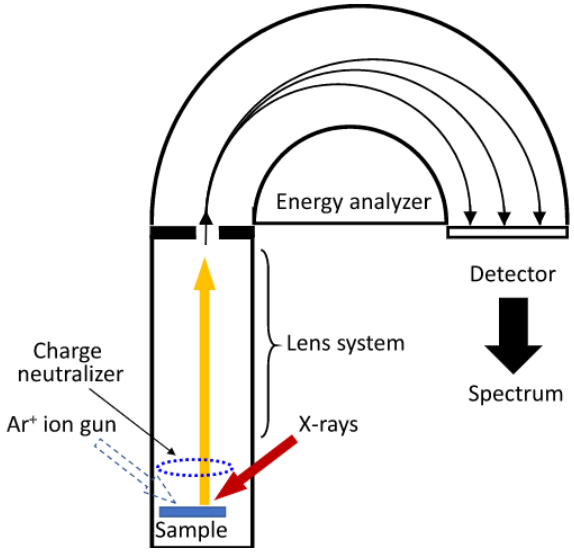

Fig. 3.2 The schematic experimental set up of the XPS spectrometer with the hemispherical electron energy analyser. Adapted from Ref.[109] under the creative commons license of Elsevier

The XPS spectra in real experiment is a series of peaks for different core electron for

the elements present in the sample in a wide range of calculated binding energy. Each element has their characteristic peaks for different core electron energies. The detail chemical state and local electronic structure are analysed with the peak positions and the shape of the peaks. For example a shift in the binding energy that is a chemical shift gives significant information about the oxidation states of the elements. The peak width and the broadening also used to quantify the distribution of the elements. The detail XPS study presented in Chapter 6 & Appendix A were analysed using XPSPEAK 4.1 software. The background was fitted with Shirley background and peaks were fitted with mix of Gaussian and Lorentzian function.

3.1.3 Raman Spectroscopy

Raman Spectroscopy is a widely used popular spectroscopic technique to analyse crystal structure, specifically the lattice vibration. This technique is based on the basic principle of Raman Scattering [110] in light-matter interaction. When an incident light wave interacts with a crystal lattice it can either scatters elastically or non elastically. In a elastic scattering also called as Rayleigh scattering, the energy of the scattered photon remains same as the incident photon. Raman scattering is an inelastic scattering where the energy of the scattered photons can be either lower or higher than the incident photon. Due to this inelastic scattering, the crystal lattice or molecule vibrates in some specific frequencies called the normal mode of phonon vibration. The energy of the scattered photon could be expressed as $h\nu_s = \mathrm{h}\nu_p \pm \mathrm{h}\nu_{osc}$.ν_s , ν_p and ν_{osc} are the frequencies of the scattered photon, incident photon and the quantum of the lattice vibration i.e. phonon. The scattering where the scattered photons gained the energy or have an energy higher than the incident one is called an anti-Stokes process and the opposite process where scattered frequency is lower than the incident one is called a Stokes process, as depicted in Figure 3.3 [111]. The semi classical theory of the Raman scattering is explained in the context of quantum mechanical description of harmonic oscillator. Transition among the quantized vibrational energy states according to the selection rules gives the characteristic stokes and anti-stokes lines.

In real experiment a high intensity laser source is used for incident or pump photon. Mostly visible lasers (blue, green or red) are used in most of the commercial Raman Spectrometers. Raman spectra is generally recorded in a confocal microscope with a backscattering geometry. The Rayleigh line is set as zero and the Raman peak intensities for Stokes and anti-Stokes scattering are plotted with the frequency difference $\Delta\nu$ with respect to the zero symmetrically on both sides of Rayleigh line. Each peak corresponds to a specific normal phonon mode for a particular crystal lattice. As Raman scattering is highly depended on the symmetry of the molecule or lattice, the polarization of the incident photon has an influence on the modes of vibration. Mathematically, the normal

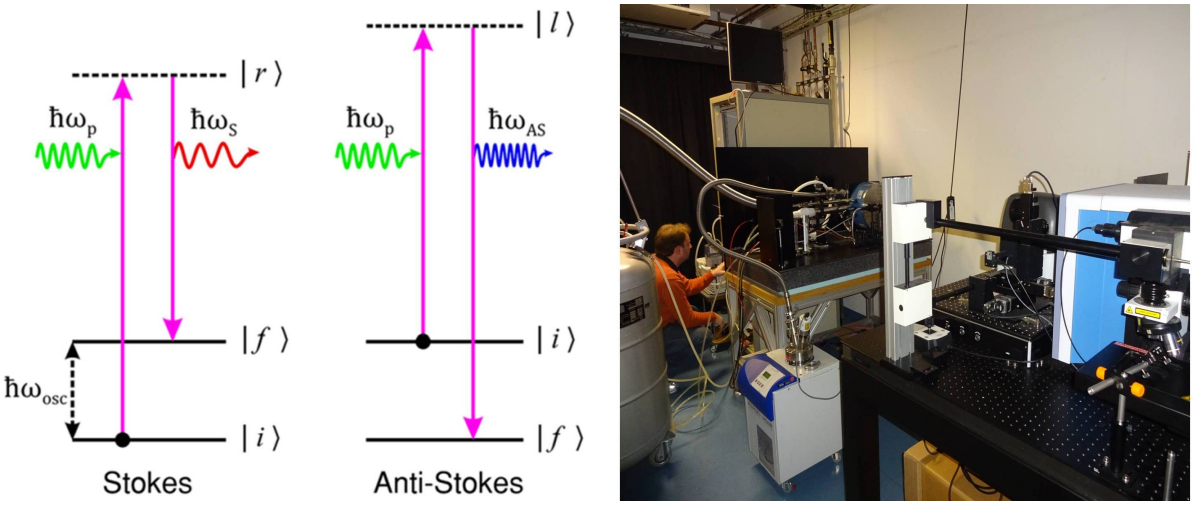

Fig. 3.3 (left) The schematic representation of the vibrational energy states and transition of the stokes and anti-stokes process. Adapted from Ref.[111] under the creative commons license of Springer Nature. (right) The Raman Spectrometer used in this thesis at I. Physikalisches Institut,Georg-August-Universität Göttingen, Germany

modes are expressed as a form of tensor depending on the plane of polarization of the incident light. Many times parallel and perpendicular polarization trigger separate modes of vibration that give very important information about the symmetry of the crystal. The broadening and shift of the peak positions are analysed to reveal crystalline quality and the presence of other interactions or contributions in the system such as electron-phonon interaction, spin-phonon interaction, lattice expansion/contraction or anharmonicity of the vibration [112]. The experimental details of polarization dependent & high temperature Raman spectra presented in Chapter 4 is given in the section 4.2.2.

3.1.4 Electron Energy Loss Spectroscopy (EELS)

Electron Energy Loss Spectroscopy is also a popular spectroscopic technique mainly used for element detection and to probe the local environment or chemical valance state. This technique is complementary to the X-ray Photoelectron Spectroscopy (XPS) and synchrotron based X-ray Absorption Near Edge Spectroscopy (XANES). Basic principle is based on the inelastic scattering of electrons [113]. When a beam of high energy electron passes through a sample, the incoming electrons inelastically scatter inside the sample in different mechanisms like electron-phonon interaction, transition of core electrons to outer shell, interaction with the free electrons or a removal of core electron i.e. ionization. Among all these processes, the ionization of the core shell is particularly important for EELS. In real EELS spectrum this ionization for specific elements are represented as different edges. EELS spectrum is plotted as scattered electron intensity vs the energy loss of the detected electrons. Within the full spectrum, all the ionization edges for different

elements present in the sample with the characteristic value of energy loss. The shape and the position of the edges gives the detail information about the relative concentration of the elements along with the local chemical environment.

In real experiment, an EELS measurement is attached with a Transmission Electron Microscopy (TEM) set up as will be discussed in next subsection. The transmitted electrons are detected and analysed with an electron detector. In many cases, EELS spectrum is recorded both in transmission or reflection geometry. The most important use of this technique in the context of thin film is the EELS mapping in high spacial atomic resolution. In an epitaxial oxide film, individual atoms of different elements in layers are mapped with high resolution in modern EELS mapping in selected area [114]. The recent development and advancement in Scanning Transmission Electron Microscopy (STEM) and High-angle annular dark field (HAADF) imaging makes the atomically resolved EELS mapping as one of the most powerful tool to probe the interfacial structure in oxide thin film heterostructures and superlattices. Both EELS spectra and selected area mapping has been proved as powerful evidence of partial B-site ordering in a double perovskite as presented in Chapter 5.

3.1.5 Transmission Electron Microscopy (TEM)

Transmission Electron Microscopy is one of the most used microscopic techniques in material science. An electron beam is transmitted through a thin prepared sample and the lattice structure is imaged due to the wave nature of electrons. TEM enables the imaging of the local structure and chemistry, where the spatial resolution is fractions of a lattice constant. For TEM investigations, firstly a lamella is prepared from the sample which represents a cross section through the heterostructure. The thickness of the lamella must be less than 100 nm so that the electron beam is not completely absorbed in the lamella and transmission of the electron beam is possible. Typically, the TEM lamella is produced by cutting the sample with a focused ion beam (FIB). Many times defects are produced specially in complex oxide thin films due to the bombarding with high-energy ions in vacuum. So many times ion etching (Ar ions) is used to the remove the first few layers with a grazing incidence and thus no defects are induced in deeper layers. Now the electron beam can transmit through the lamella and can interact inside the material. The transmitted and scattered electrons are detected with mainly two different modes and detectors. First is an Axial Bright Field Detector placed directly in the path of the transmitted electron beam. Both fully transmitted and scattered electrons are detected here and a bright low contrast image is produced. Second is an Annular Dark Field (ADF) Detector placed outside the direct transmitted beam. With the use of high-angle annular dark-field (HAADF) imaging where only scattered electrons are detected, high contrast atomically resolved image of the specimen is produced [115, 116]. The schematic diagram

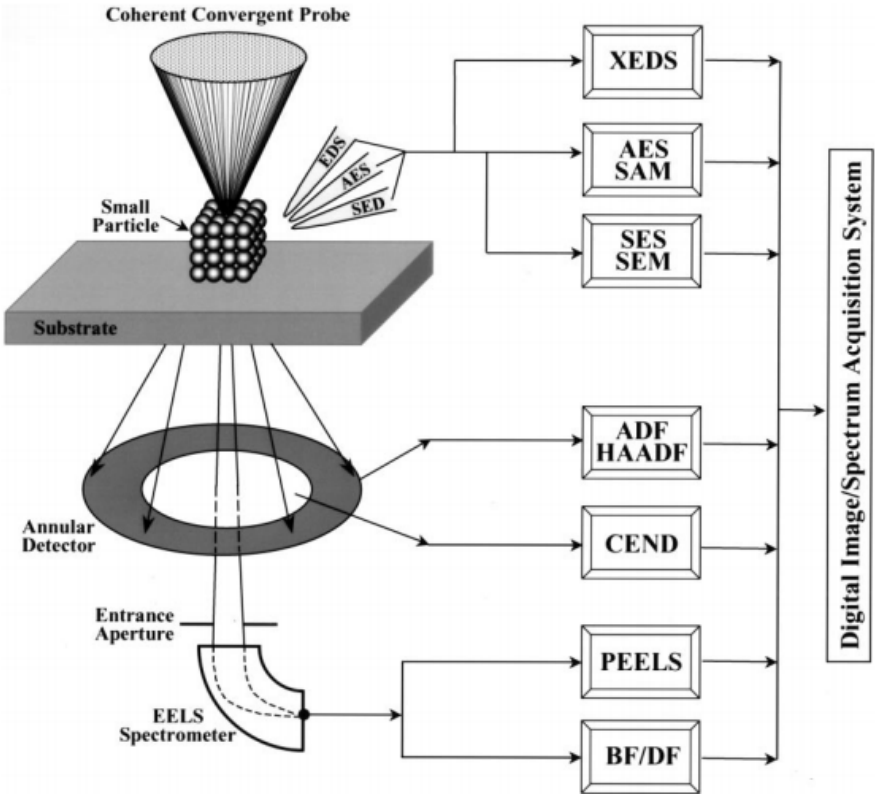

Fig. 3.4 The schematic diagram of a Scanning Transmission Electron Microscopy (STEM) set up equipped with HAADF detector and EELS mapping. Adapted from Ref.[116] with the permission of Oxford University Press.

of a scanning Transmission Electron Microscopy has been presented in Figure 3.4 [116].

Now in advanced TEM set up, the electron beam is used in a scanning mode (STEM) over the different parts of the sample for better signal and EELS mapping as discussed in previous section. Along with EELS, the STEM set up is also used to produce a Selected Area Electron Diffraction (SAED) pattern from the sample which is complementary to the X-ray Diffraction to analyse local symmetry and crystal structure of the specimen. The STEM images, SAED patterns EELS mapping presented in Chapter 4 & 5 are measured by Dr. Vladimir Roddatis in Institut für Materialphysik, Georg-August-Universität Göttingen, Göttingen, Germany. The experimental details are presented in the measurement sections of respective chapters.

3.2 Thin film monitoring

3.2.1 Optical Ellipsometry

Optical Ellipsometry is an useful technique to study the quality of a thin film. It is widely used to monitor the growth of a thin film, determination of the thickness and optical con-

stants such as refractive index. The basic principle is the change of the polarization state of light after reflection or transmission from a medium. In an ellipsometric measurement a light beam with a definite polarization is reflected from the thin film surface and the change in polarization for the reflected beam is detected. A standard ellipsometry set up installed inside the MAD chamber has been shown in Figure 2.4 in Chapter 2. The oscillating electric field vector ($\overrightarrow{E}$) of an incident linearly polarized light can be decomposed into two parts. One component is oscillating in the plane of the incidence called p component ($\overrightarrow{E_p}$) and the other is oscillating perpendicular to that plane called s component ($\overrightarrow{E_s}$). The complex reflection coefficients for both components (r_s & r_p) are defined as [117]

$r_s = [\ |\ E_s^r\ |\ /\ |\ E_s^i\ |\ ]e^{i(\delta^s)}$ and $r_p = [\ |\ E_p^r\ |\ /\ |\ E_p^i\ |\ ]e^{i(\delta^p)}$

Here δ^s & δ^p are the phase difference between incident and reflected beam for s and p component respectively. In Optical Ellipsometry two parameters Δ & Ψ are detected. Δ is the overall phase difference between p & s component (δ^p - δ^s). Amplitude ratio of the two components ($|\ r_p\ |\ /\ |\ r_s\ |$) are defined as $\tan\Psi$. Δ & Ψ are related as the equation $r_s/r_p = \tan\Psi e^{i\Delta}$. This is the most fundamental equation of Optical Ellipsometry. The ellipsometry measurements yield the ratio of the complex reflection coefficients r_p and r_s. Now the calculation of individual Δ & Ψ along with refractive index of the film is not very straightforward and could be done with different models with the help of Fresnel equations. Two primary parameters that are calculated from measurement are complex refractive index and the film thickness.

When a polarized light beam is partially reflected and refracted from a medium j to another medium k, the incident and refracted rays make angles θ_j & θ_k to the normal to the interface, Fresnel equations relate the reflection coefficients to the complex refractive index of the medium as following.

$r_s = (N_j\cos\theta_j - N_k\cos\theta_k)/(N_j\cos\theta_j + N_k\cos\theta_k)$
&
$r_p = (N_k\cos\theta_j - N_j\cos\theta_k)/(N_k\cos\theta_j - N_j\cos\theta_k)$

Here N_j & N_j are complex refractive index of the respective mediums. Now using the Snells law $N_j\sin\theta_j = N_k\sin\theta_k$ and the relation $r_s/r_p = \tan\Psi e^{i\Delta}$ one can calculate the refractive index of medium k taking medium j as air so that $N_j = 1$. For determining film thickness along with taking contribution of the reflection from substrate-film interface, more complex model is used and both the thickness and complex refractive index are calculated more accurately with solving non complex linear equations analytically [118, 119]. The experimental details for the high temperature ellipsometry results presented in this thesis are given in the measurement section of Chapter 4.

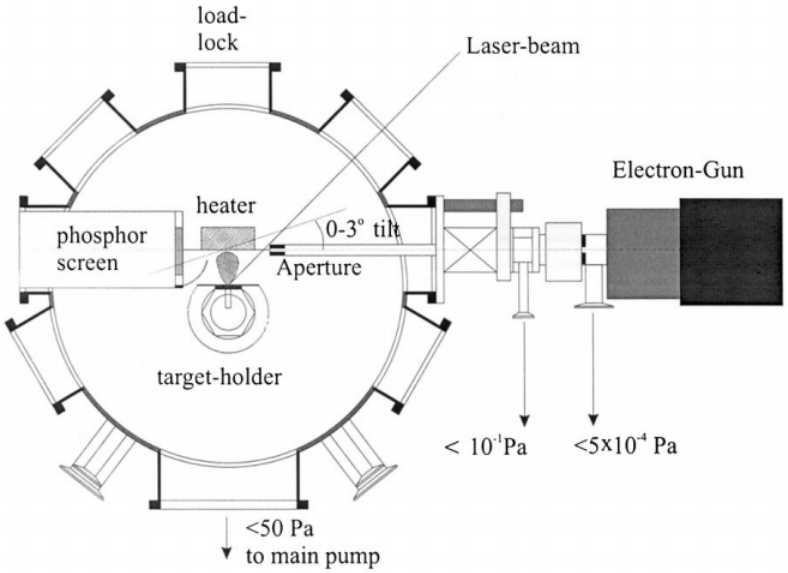

Fig. 3.5 The schematic representation of the RHEED system installed inside a Pulsed Laser Deposition chamber. Adapted from Ref. [122] with the permission of Elsevier

3.2.2 Reflection High Energy Electron Diffraction (RHEED)

Reflection High Energy Electron Diffraction is a well known surface probe diffraction technique to monitor thin film growth as well as the quality of the thin film [120]. A beam of high energy electron preferably in the range of 10 - 100 KeV is reflected from a substrate/film surface at a very small glancing angle (θ_g) around 0.5 - 6°. The reflected beam is detected in a fluorescent phosphor screen. The glancing angle helps the electron beam to interact only with few layers and the surface of the sample. The reflected beam from the surface and upper layers interfere constructively and create diffraction spots in the screen similar to the Laue pattern as observed in SAED in TEM. The observed pattern is analysed with the framework of the construction of Ewald sphere similar to the X-ray diffraction as discussed previously. An experimental RHEED pattern consists of semi circular array of spots correspond to the family of parallel planes. Any deformation in the RHEED spots provides crucial informations about the crystalline quality of the surface [121].

One of the most importance of RHEED technique is the monitoring of thin film growth. Time dependent RHEED intensity is monitored for a particular spot during the growth of thin films. The intensity oscillates periodically with the number of unit cell growth [122]. Hence layer thickness or number of layers could be calculated from the number of full RHEED oscillations. The sharpness in the oscillation also gives an idea of the quality of interface in a heterostructure. The schematics of an experimental set up of RHEED system has been shown in Figure 3.5. The result of RHEED intensity and pattern for the growth of $BaTiO_3/SrIrO_3$ heterostructure has been presented in Chapter 6.

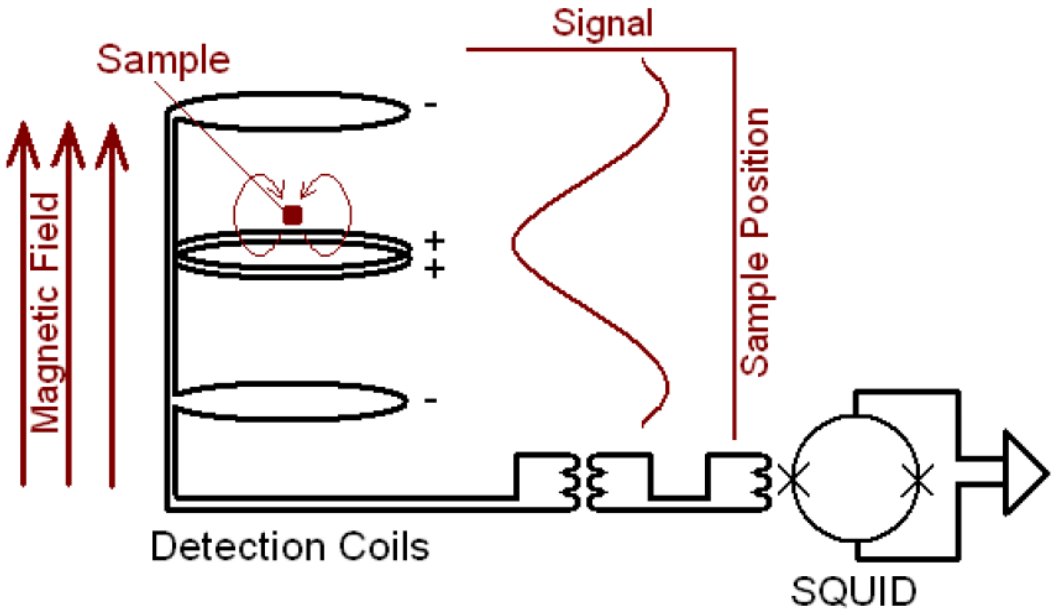

Fig. 3.6 The schematic basic diagram for a SQUID-VSM setup showing the arrangement of superconducting second order gradiometer coil inductively to SQUID. The voltage profile coupled with the SQUID for the detection of magnetic moment has been shown as a function of sample position due to the movement of magnetic specimen through the pickup coil. Adapted from Ref. [125]

3.3 Physical property measurements

3.3.1 DC Magnetization

A commercial Quantum Design's MPMS SQUID-VSM magnetometer has been used for for all the macroscopic bulk magnetization measurements as presented in this thesis. SQUID-VSM can be considered as the hybrid of the two individual magnetometers. One is a Vibrating Sample Magnetometer (VSM) and another is superconducting quantum interference device (SQUID).

Vibrating Sample Magnetometer (VSM) works on the basic principle of Faraday's law of induction. When a magnet moves through a conducting coil, an electric voltage is produced in the circuit. According to the law the induced emf (ϵ) generated in a conducting coil with 'n' turn and area 'A' due to change in magnetic flux ϕ is proportional to the rate of change of flux associated with coil as given by the relation [123] $\epsilon = -n\frac{d\Phi}{dt} = -nA\frac{dB}{dt}$, where B is the induced magnetic field. Now to detect the magnetic field the sample is vibrated through a coil or a combinations in a particular frequency. The accuracy of the detection depends on the coil geometry and the sample positioning. Though the sensitivity of VSM is not much good but the measurement is quite fast.

superconducting quantum interference device (SQUID) is a closed superconducting loop with two parallel tunnel junctions where a thin insulating layer is sandwiched between the two ends of the superconducting wire called as Josephson junctions. According to the formulation of Landau-Ginzburg theory, the magnetic flux (Φ) associated with a superconducting loop is quantized with a value $\phi = -\frac{nhc}{2e}$ [124]. The minimum flux quantum that could be detected is $|\phi_0| = \frac{hc}{2e} = 2.07 \times 10^{-15} Wb$. In a SQUID loop the total superconducting current is a periodic function of the associated magnetic flux in presence of weak magnetic field and they are related as $I_{tot} \propto cos\left(\frac{e\Phi}{\hbar c}\right)$.

In a commercial SQUID-VSM the sample is vibrated with a fixed frequency through a superconducting gradiometer coil which is inductively coupled to a magnetically-shielded, DC SQUID as shown in Figure 3.6. A second order gradiometer coil is used to eliminate any linear or distant field such as earth's magnetic field. A transport rod is used to put the thin film sample and holder through the coils and gradually moves to determining the maximum signal for the thin film position [125]. Then the sample is vibrated about this mean position by a frequency of 14 Hz. SQUID VSM thus combines the high sensitivity of the SQUID with high speed of measurement of a conventional VSM. The conventional protocols used for the temperature dependent and field dependent magnetization measurements have been stated in the measurement sections of respective chapters.

3.3.2 Dielectric Measurements

Measurement of dielectric constant of a material yields very important information regarding the electrical conductivity, dynamics of electric dipoles and polar ordering. Temperature and frequency dependence of dielectric constant has been proved to be an useful tool for investigating different kind of long-range polar ordering including ferroelectric transition. Though there are many standard measurements for dielectric constant, we have used a parallel plate capacitor geometry to measure the frequency and temperature dependent capacitance and hence calculate the dielectric constant.

A standard home built set up has been used for this measurement. The components have been shown in Figure 3.7. They are (i) a 9 T superconducting magnet and liquid He cryostat from Oxford Instruments for magnetic field dependent measurement, (ii) a home made insert with temperature sensor and sample mounting stage, (iii) a temperature controller and (iv) a standard Keysight E4980A LCR meter operating in a frequency range 20 Hz to 2 MHz. A lab view programme is used for automatic data acquisition with temperature and frequency variation. Capacitor geometry has been made with a conducting substrate (Nb:$SrTiO_3$) as bottom electrode and circular gold pad on top of the thin film as top electrode. The sample has been mounted on the temperature stage of the insert and electrodes are connected with copper wires.

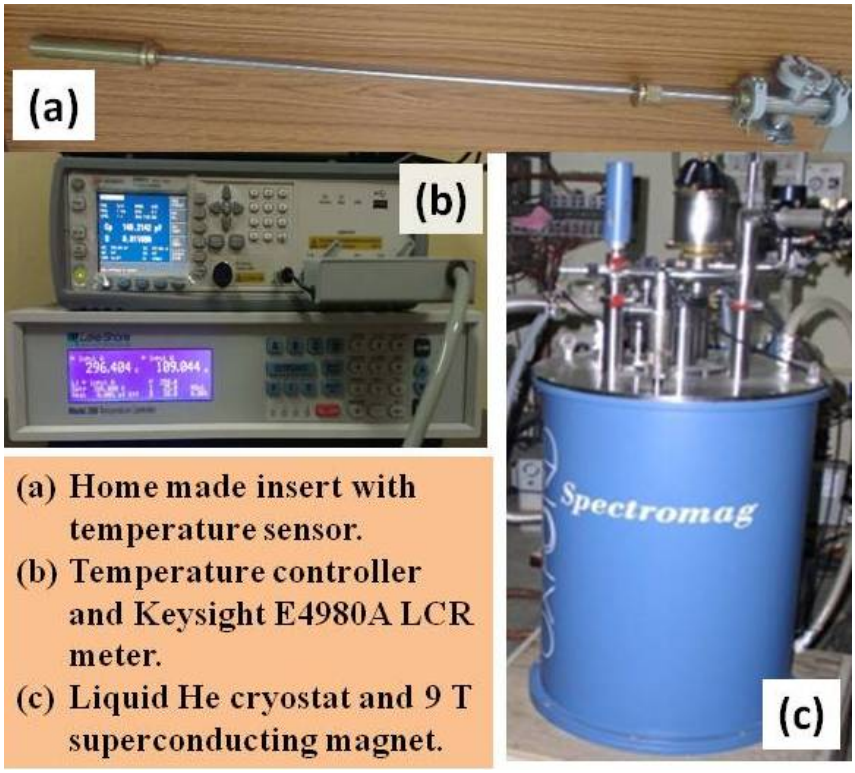

Fig. 3.7 The real Dielectric measurement set up used in this thesis at UGC-DAE-CSR Indore

The complex dielectric permittivity $\epsilon(\omega)$ can be expressed as $\epsilon^{'}(\omega) - i\epsilon^{''}(\omega)$ where the real part $\epsilon^{'}(\omega)$ gives the dielectric constant and $\epsilon^{''}(\omega)$ provides information about the dielectric loss. The dielectric loss or the dissipation factor is quantified as $\epsilon^{''}(\omega)/\epsilon^{'}(\omega) = tan\delta$, where δ is the phase angle in the complex plane. In a dielectric measurement $\epsilon^{'}(\omega)$ and $tan\delta$ are measured as a function of both temperature and frequency. The measurement is done through measuring the complex capacitance of the required material in parallel plate geometry. The LCR meter basically operates in a Wheatstone bridge circuit. With the other known impedances in three arms the complex impedance $Z^*(\omega)$ of the desired material can be evaluated at the null deflection condition of the bridge. The complex capacitance $C^*(\omega)$ is calculated as $C^*(\omega) = -i/\omega Z^*(\omega)$, where ω is the angular frequency of the applied AC voltage. Hence the complex permittivity $\epsilon(\omega)$ is expressed as $\epsilon(\omega) = C^*(\omega)d/\epsilon(0)A$. Here d is the thickness of the film, A is the area of the parallel electrodes and $\epsilon(0)$ is the permittivity of free space. A frequency range of 1 kHz to 100 kHz and a constant DC voltage of 0.2 V has been used for all the dielectric investigations presented in Chapter 5.

3.3.3 Resistivity

Resistivity measurement on thin films has been done in standard four probe measurement. Four gold pads have been deposited with specific gaps in a line array on the film surface. The two end pads are for the current leads (I^+ & I^-) for applying a constant current in the system and two middle ones are the voltage leads (V^+ & V^-) used to measure the voltage difference. The separation between the voltage leads has been keep maximum for better signal. Copper wires were soldered with indium to make contact on the gold pads. A constant current in μA has been applied in the current leads and the corresponding voltage difference has been recorded across the voltage leads. The resistivity is calculated by Ohms law. The temperature and magnetic field dependent measurement has been done inside a liquid He cryostat and 9 T superconducting magnet from Oxford Instruments. A home built insert has been used to mount the sample. The thin films on the insulating substrates ($SrTiO_3$ or Al_2O_3) have been mounted by sticking with GE Varnish. The DC resistivity measurements are done in the temperature range 5K - 300K and in an applied magnetic field 0T - 8T.

CHAPTER 4

Strain-Driven Structure-Ferroelectricity Relationship in h-$TbMnO_3$ Films

This chapter presents the growth of high quality epitaxial h-TMO/YSZ(111) films and their structural transformations are analyzed by means of various ex- and in-situ characterization techniques. A temperature dependent Raman spectroscopy revealed structural phase transition from $P6_3cm$ to $P6_3/mcm$ structure at $T_C \sim 800$ K. Optical ellipsometry, confirming a phase transition at 800 K, indicates a change of charge transfer from oxygen to Mn, at the structural phase transition. In situ transmission electron microscopy (TEM) of the lamella samples displayed an irreversible $P6_3cm$-$P6_3/mcm$ transformation and vanishing of ferroelectric domains already at 410 K. At the same time, the room temperature TEM of h-TMO films after the temperature cycling (300K-1300K-300K) revealed an inhomogeneous microstructure, containing ferroelectric and paraelectric nanodomains with $P6_3cm$ and $P6_3/mcm$ structure, respectively. We point out a strong influence of stress relaxation, induced by the sample geometry as well as by temperature cycling, onto the structure and ferroelectricity in h-TMO thin films. The contents of this chapter are published in ***Physical Review B 102, 104106 (2020)***.

4.1 Introduction

Rare earth manganites, $ReMnO_3$ with Re = La to Lu, manifest a family of strongly correlated electronic oxides with rich emerging properties, for example, high-temperature ferroelectricity, magnetic ordering and magneto-electric coupling [126, 127]. Two distinct crystal structures, i.e. orthorhombic (Pnma) and hexagonal ($P6_3cm$), were revealed for large (La, Pr, Nd, Sm, Gd, Tb, Dy) and small (Y, Ho, Er, Tm, Yb, Lu) rare earth cations, respectively. Both structural polymorphs demonstrate coupled ferroelectric and magnetic properties, although the origin and the emergence of ferroelectric ordering is drastically different. In the Pnma structure, the improper ferroelectricity with very low Curie temperatures, $T_C \sim 15$ K (o-$HoMnO_3$) [128], has a magnetoelastic origin; the modulation of magnetic structure results in a typically small spontaneous polarization, $P_S = 0.5\ \mu C/cm^2$ ($GdMnO_3$) [129]. In contrast, the ferroelectricity in the hexagonal phase originates from the geometric distortion, yielding a very high $T_C \sim 1000$ K [130, 131] and much larger polarization, $P_S = 5.5\ \mu C/cm^2$ in h-$YMnO_3$ [132, 133]. For most of the hexagonal manganites ferroelectricity arises from the K_3 tilting of the MnO_5 bipyramids. The coupling of this distortion to the polar Γ_2^- mode along with a buckling of Re-layer [134] results in an off-centrosymmetric displacement of oxygen and rare earth atoms. These structural modifications, having the form of buckling of atomic chains [135], can be directly visualized by means of a high resolution electron microscopy.

Epitaxial h-$ReMnO_3$ films and heterostructures could be specially interesting for nanoscale science and applications, the growth of which was already demonstrated by different physical and chemical vapor deposition techniques [135]. There were published several reports [136, 137, 138, 139, 140] on hexagonal films with small Re-cations (Ho, Er, Y), showing relatively high ferroelectric transition temperatures, e.g. T_C = 875-1100 K and large saturation polarization, $P_S \sim$ 10-12 $\mu C/cm^2$. However, the h-$YMnO_3$ thin films possess a lower polarization (1.7 $\mu C/cm^2$) than its bulk form (5.5 $\mu C/cm^2$) [141]. General features of thin films, pointed out by Fontcuberta [141], are the reduced values of remnant polarization and ferroelectric Curie temperatures compared to the bulk values. In addition, nanodomains with orientations different from the main epitaxial phase were observed for films with different thickness and grown by different techniques [142]. Likely, such nanodomains are responsible for the reduction of the remnant polarization. Another important parameter, strongly influencing the properties of thin h-$ReMnO_3$ films, is the partial pressure of oxygen, P_{O2}, during preparation and related to it oxygen deficiency. Jang et al.[138] pointed out the oxygen deficiency to be responsible for the appearance of magnetic disorder and spin-glass state concurring with the dominating antiferromagnetic ordering in h-$ReMnO_3$ films. Moreover, the development of an inhomogeneous stress state and strain gradient in the $HoMnO_3$ films, prepared at $P_{O2} \sim$ 10-300 mbar, is shown to be

influenced by oxygen deficiency, resulting in a giant flexoelectric effect12 for films grown at low p_{O2}.

However very little is known on the h-$ReMnO_3$ films with larger RE-cation, like Tb, which can be obtained as a metastable phase in strain-stabilized thin films. The reports on the preparation of h-$TbMnO_3$ films are scarce and the obtained results are controversial. Namely, Lee et al. [143, 144] demonstrated a stabilization of the hexagonal phase in TMO films grown by means of pulsed laser deposition (PLD) on Pt(111)/Al_2O_3(0001) and yttrium-stabilized zirconia (YSZ(111)) substrates. The films were found to be ferroelectric (FE) with $T_C \sim 60$ K and a transition into an antiferroelectric (AFE) phase for $T > T_C$ was observed. Kim et al. [145] reported ferroelectricity at room temperature in a PLD-grown h-TMO film and demonstrated the switching of the ferroelectric polarization by means of a piezo-force microscopy; no AFE phase was observed in contradiction with the previous report. By first principle calculations Kim et al. [145] predicted the ferroelectricity in h-TMO to have the same mechanism as in other hexagonal manganites. However, the information on the ferroelectric domain structure as well as on the Curie temperature for this strain-stabilized h-TMO phase is still absent and the microscopic origin of this FE phase was not experimentally confirmed. A special interest for the h-TMO films is motivated by its lower thermodynamic stability, compared to other h-manganites (Re=Y-Lu), which allows one to expect a pronounced influence of the lattice strain on the ferroelectric/structural phase transition.

The high-temperature structural/ferroelectric transitions in h-manganites have been studied by X-ray diffraction (XRD) [146]. A one-step transition from the low temperature $P6_3cm$ structure to the high temperature $P6_3/mcm$ structure was shown, primarily caused by the Re-O_P displacement of the K_3 phonon mode. A nonlinear optical second harmonic generation (SHG) as a contact-free technique [130, 147, 148, 149], probing the spontaneous polarization, allows one to determine the ferroelectric T_C. However, as noted by Lilienblum et.al [130] to avoid the inhomogeneity effects due to differently polarized ferroelectric domains, a preparation of single-domain state by poling and, hence, the availability of a bottom electrode is necessary even for SHG study of a thin film. In addition, Raman scattering was also shown to be an effective nondestructive optical probe of the structural phase transition in hexagonal manganites. Applied to $YMnO_3$ bulk samples it reveals the change of the A_1 symmetry of the dominating phonon mode at ~ 680 cm^{-1} in the ferroelectric $P6_3cm$ into the A_{1g} symmetry in the paraelectric $P6_3/mcm$ phase [150]. However, studies of high temperature phase transitions in h-films are very limited and one can mention the observation of ferroelectric $T_C \sim 1020$ K by monitoring the temperature behavior of the A_1 mode in the Raman spectra of the multiferroic 200 nm thick h-$LuFeO_3$ thin film [151].

One can conclude that although the ferroelectric behavior of the h-$ReMnO_3$ films were well documented, their ferroelectric (T_C) and magnetic (T_N) values were found to be smaller than those obtained in the corresponding bulk materials. The deviations of the film properties were assigned to the formation of oxygen vacancies [138] as well as to the epitaxy strain [152] and strain gradient effects [137]. Here, we report h-TMO/YSZ(111) films grown by means of a metalorganic aerosol deposition (MAD) technique [153], which provides a high partial oxygen pressure $p_{O2} \sim 0.2$ bar during deposition, allowing to prevent the formation of oxygen vacancies in the film. In addition, the close to equilibrium MAD growth conditions result in epitaxial coherently grown TMO films on YSZ(111) with perfect crystallinity as well as atomically sharp and flat film/substrate interfaces. The atomically resolved HAADF-STEM evidences the characteristic periodic buckling of Tb ions, indicating the presence of the FE domains, vertically aligned with respect to the film plane. The FE/PE transition at $T_C \sim 800$ K was determined by means of temperature dependent Raman spectroscopy and optical ellipsometry.

4.2 Experimental Section

4.2.1 Growth of h-$TbMnO_3$ films

The h-TMO films with a thickness d=50 nm have been grown by MAD technique on commercial YSZ(111) substrates (Crystal GmbH) by using Tb- and Mn-acetylacetonates as precursors. Precursor solutions in dimethylformamide with concentration 0.02 M (for Mn-precursor) and molar ratios Tb/Mn=1.15 was used.The films were grown with the rate, v=6 nm/min, by spraying the precursor solution by dried compressed air onto the YSZ substrate heated to $T_{sub} \sim$ 900-1000 °C in ambient atmosphere. After preparation the films were quenched down in 1 minute to about 600 °C and then cooled down to room temperature in 5 min. The substrate temperature was controlled by a pyrometer and by in-situ optical ellipsometry.

4.2.2 Measurement details

XRD (Cu-K_α radiation, θ - 2θ Bragg-Brentano geometry), rocking curves (ω -scans), asymmetric ϕ -scan and small-angle X-ray reflectivity (XRR) were used to characterize the structure and thickness of the films. Polarization dependent Raman spectroscopy was carried out at room temperature by using a confocal Raman microscope (LabRAM HR Evolution, Horiba Jobin Yvon) in a back scattering geometry with a continuous wave Nd:YAG laser (λ =532 nm, $P_0 = 1.3$ mW). Temperature dependent Raman measurements were performed in back-scattering geometry with a long range 50x objective on the film samples, glued by Ag paste on a Cu sample holder, which was attached to a TiN resistive heater. A NiCr-Ni thermocouple was used to measure the temperature of the Cu sample

holder. The in-situ optical ellipsometry was measured during the growth, cooling and subsequent heating of the films by using a home-made optical setup of the polarizer-modulator-sample-analyser (PMSA) type. A He-Ne laser beam (λ = 0.6328 μm) was focused on the sample at an incident angle close to Brewster angle of YSZ substrate, θ_B $\sim$ 60.5°. The ellipsometric phase shift angle Δ, and polarization rotation angle Ψ, were measured by using lock-in technique at fundamental and second harmonic frequencies, ω = 50 kHz and 2ω, respectively (ω is the modulation frequency of the light polarization). The real and imaginary part of refraction index at λ = 0.6328 μm was calculated using Fresnel formulas by modelling the sample as a thin film and infinitely thick substrate. Additionally, the measurements of the blank substrates were done for reference. The local structure of TMO films was studied by Scanning Transmission Electron Microscopy (STEM) using an FEI Titan 80-300 G2 environmental transmission electron microscope (ETEM), operated at an acceleration voltage of 300 kV. TEM lamellas were prepared by Focused Ion Beam (FIB) lift-out technique using a ThermoFischer (formely FEI) Helios 4UC instrument.

4.3 Results and Discussion

4.3.1 Structural Characterizations

4.3.1.1 X-ray Diffraction (XRD)

In Figure 4.1 (a) we show the XRD patterns of a stoichiometric TMO/YSZ(111) film, prepared with an optimal precursor molar ratio Tb/Mn=1.15. Along with the YSZ(111) substrate peaks one can see the system of reflexes from the (000l) planes of a h-TMO phase, evidencing an out-of-plane epitaxial growth. The calculated c-axis lattice parameter c = 1.1182 nm, from one side, significantly smaller than the theoretically estimated value c_0 = 1.153 nm for a strain-free h-TMO film [145] and, from another side, is much closer to the theoretical value for a strained h-TMO film, c_{th} = 1.1057 nm, also obtained by first principles calculations [145]. Comparing the measured and the theoretical values of the c-lattice parameter for strain-free h-TMO, a large out-of-plane tensile stress, $\varepsilon_\perp$ = (c - c_0)/c_0 $\approx$ - 3%, can be deduced in the MAD grown h-TMO/YSZ films. Note, that the theoretically estimated value of the in-plane a-lattice constant for a strain-free h-TMO is a_0 = 0.620 nm [145], but one cannot compare it with the bulk strain-free value simply because TMO does not exist in the bulk form. However, considering the in-plane epitaxy relation $[11\text{-}20]_{TMO}//[110]_{YSZ}$ [154, 155] observed for epitaxial growth of h-$YMnO_3$/YSZ(111) films, the corresponding in-plane film/substrate lattice mismatch ($\sqrt{2}a_{TMO}/\sqrt{3}a_{YSZ}$ -1) would be fully compensated for a hypothetical TMO film with in-plane lattice constant, $a_{TMO} = (\sqrt{3}/\sqrt{2})a_{YSZ}$ = 0.6277 nm (a_{YSZ} = 0.5125 nm [156]). We performed the reciprocal space mapping(RSM) of the TMO[11-22] peak (Figure 4.1

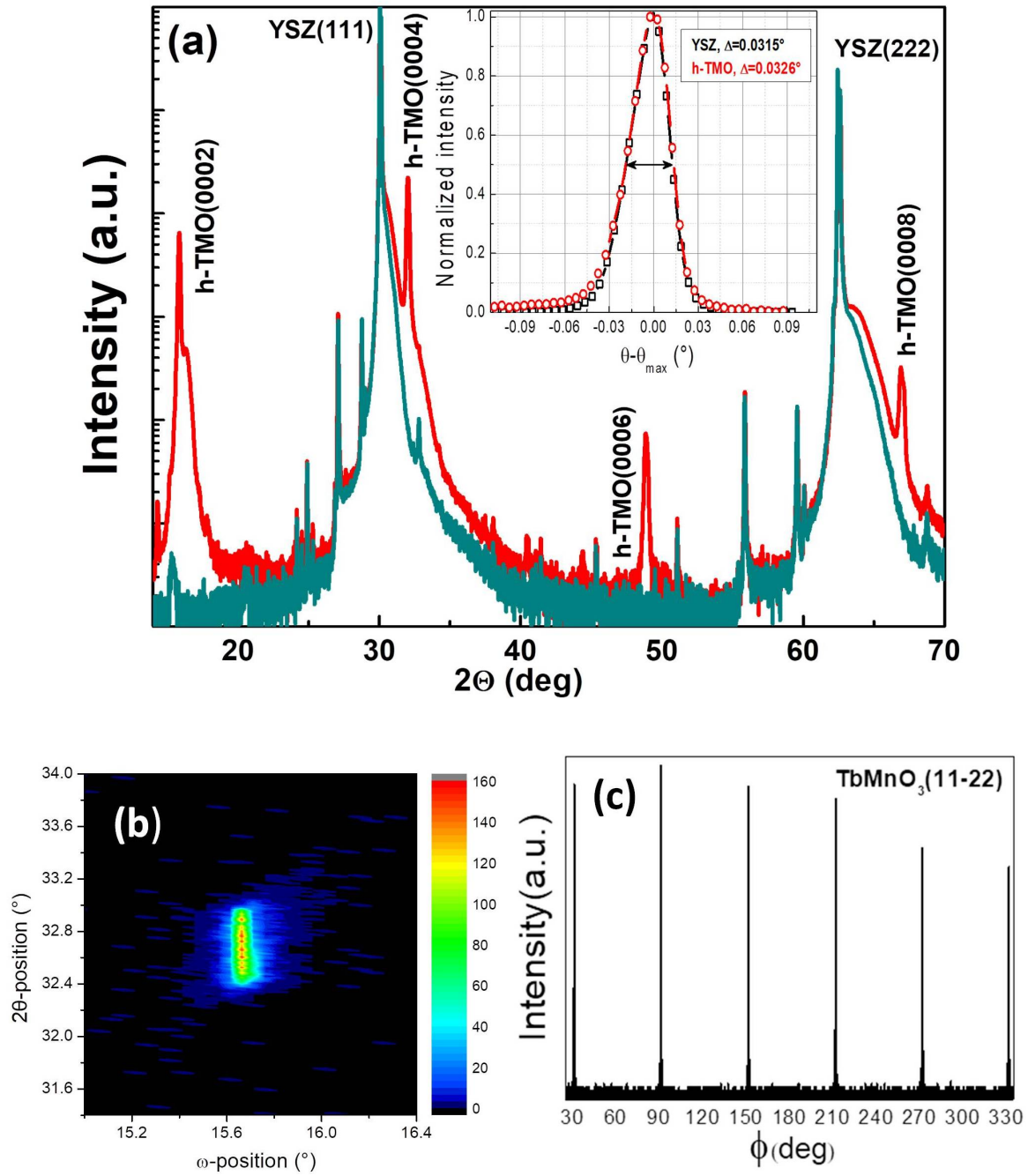

Fig. 4.1 Structural characterization of h-TMO/YSZ(111) films: (a) XRD (θ - 2θ) pattern of a representative film shows the [000l] out-of-plane epitaxy. The inset demonstrates rocking curves of h-TMO[0002] and YSZ[111] peaks with almost the same FWHM $\sim 0.032°$; (b) a reciprocal space mapping (RSM) of a film [11-22] peak and (c) Φ-scan of the [11-22] film peak evidences the in-plane epitaxy with hexagonal symmetry

(b)) and, considering the measured c-axis lattice parameter, c = 1.1182 nm, the in-plane lattice constant a = 0.6277 nm of h-TMO/YSZ(111) film was determined. The measured

value fits perfectly to the above estimated hypothetical a_{TMO}, thus, evidencing a full compensation of the film/substrate in-plane misfit. It exceeds the theoretically estimated lattice constant of a strained-free h-TMO, $a_0 = 0.620$ nm [148] and implies the presence of an in-plane stress $\varepsilon_{\parallel}$ =(a_0 - a_{TMO})/a_0 = -1.2% in the h-TMO/YSZ(111) film. Importantly, no signs of the orthorhombic phase or other impurity phases were seen in XRD for the MAD-grown h-TMO films. The rocking curve of the (0002) peak, shown in the inset of Figure 4.1 (a), displays a full-width-on-half-maximum, $FWHM_{TMO} = 0.033°$, which is very close to that for the substrate, $FWHM_{YSZ} = 0.032°$, measured with our XRD setup. Thus, the crystalline quality of our h-TMO/YSZ(111) films is solely determined by the substrate quality as should be in the case of a true epitaxial growth. In-plane epitaxy of a h-TMO film was verified by the full Φ-scan around the [11-22] peak shown in Figure 4.1 (c). It obeys a six-fold hexagonal symmetry and contains very narrow (FWHM ∼ 0.2°) and intense peaks.

4.3.1.2 Scanning Transmission Electron Microscopy (STEM)

In Figure 4.2 (a), we present a high resolution cross-section STEM image of a h-TMO film on YSZ(111), showing a coherent growth with in-plane epitaxial relationships between the planes $[\text{-}1100]_{TMO}//[\text{1-}10]_{YSZ}$. The atomically sharp and flat film/substrate interface contains no signs of chemical intermixing and misfit dislocations, pointing out the existence of coherent epitaxy of h-TMO/YSZ(111) films in full agreement with X-ray data (Figure 4.1). One can clearly see shifts of Tb ions from the atomic planes, which were also observed for other bulk hexagonal manganites [157, 158, 159, 160] and ferrites [161] and argued to be characteristic feature of the "geometric ferroelectricity". Moreover, following the "Tb shifts" along the same atomic layer one can find regions where the characteristic "up"-"up" shift sequence (left part of Figure 4.2 (b), changes to the "down"-"down" sequence (right part of Figure 4.2 (b)). This signals the crossing of FE domain boundary and allows one to superimpose the TEM image onto the FE domain structure. The latter contains domains with electrical polarization aligned perpendicular to the film plane and with a lateral size varying in the range ∼ 5-20 nm. The observed FE domain boundary/wall is very sharp (typically 1 u.c.), directly linking the "up"- and "down"-shifted Tb ions. The domains are elongated along the z-axis and can originate from the substrate surface as some of large domains were seen to form at the atomic steps, originated from the screw dislocations ending at the substrate surface (Figure 4.2 (c)). However, the domain size seems to be not necessarily correlated with the film thickness as shown in Figure 4.2 (d). It is worth to mention that according to our TEM study the very first 3-4 u.c. of h-TMO do not reveal pronounced and long-range ordered "Tb-shifts", possibly indicating the absence of ferroelectricity in very few layers close to the substrate. Nordlander et. al [140] have related the absence of improper ferroelectricity in ultrathin (3 u.c.) $YMnO_3$ films to the mechanical clamping to the substrate, which leads to the

vanishing of the long-range order in displacements of Y atoms. Apparently, also in case of our strain-stabilized h-TMO/YSZ films the short-range order Tb displacements can be seen in a selected region close to the substrate in Figure 4.2 (c) in full agreement with the results presented in ref [140].

4.3.2 Determination of ferroelectric T_C

4.3.2.1 High temperature STEM & SAED

In Figure 4.3, we present the in-situ TEM heating experiments, performed to monitor the changes of atomic structure and morphology of ferroelectric domains in the stoichiometric h-TMO lamella sample with increasing temperature. Electron diffraction patterns, collected at every 5 K by heating, do not show any changes for T = 300-400 K. However, at T = 405 K new superstructure spots, marked with the white arrow in the inset in Figure 4.3 (c), show up, signalling the beginning of a phase transformation. Finally, at T = 410 K all spots originating from the ferroelectric hexagonal $P6_3cm$ structure along with Tb shifts disappear and another hexagonal $P6_3/mcm$ structure is formed similar to the structural transformation described for the bulk h-$YMnO_3$ [**?**]. One has to note that such structural transformation was found to be irreversible in the h-TMO film lamella. Most probably, it is related to the temperature-induced full stress relaxation because of a plastic deformation of very thin ($\sim$ 20 nm) TEM lamella with very large aspect ratio 1 $\times$ 10. A direct evidence of stress relaxation by formation of misfit dislocations in the TEM lamella sample can be seen in Figure 4.3 , which shows the HRTEM images collected before 4.3 (e) and after 4.3 (f) the in situ TEM annealing. One can see that the sample, being initially coherently strained and displaying FE-domains, was fully relaxed and domain-free after the thermal cycling (300-410-300 K), which results in the formation of a system of misfit dislocations placed at a distance 2 nm. Considering the above estimated in-plane tensile stress as a lattice misfit f = 1.2%, the calculated equilibrium distance between dislocations d = $a_{YSZ}/(2f)$ = 2.1 nm is in excellent agreement with observations in Figure 4.3 (f). This extrinsic transition is very unusual at such low temperature in comparison to the fellow family members of hexagonal manganites. The relaxation of stress presumably by means of plastic deformation in the TEM lamella drives the formation of a hexagonal paraelectric phase already at 410 K << $T_C \sim$ 800 K as will be discussed in next sections. Considering a specially prepared TEM sample the observed reduction of T_C as well as the irreversible character of phase transition both point out its extrinsic origin.

4.3.2.2 High temperature Raman Spectroscopy

Hexagonal structure of TMO films was additionally confirmed by the room temperature polarization dependent Raman spectroscopy shown in the inset in Figure 4.4 (a). Being only visible in the cross-polarization (yx) configuration, the strong Raman line at $\sim$ 683

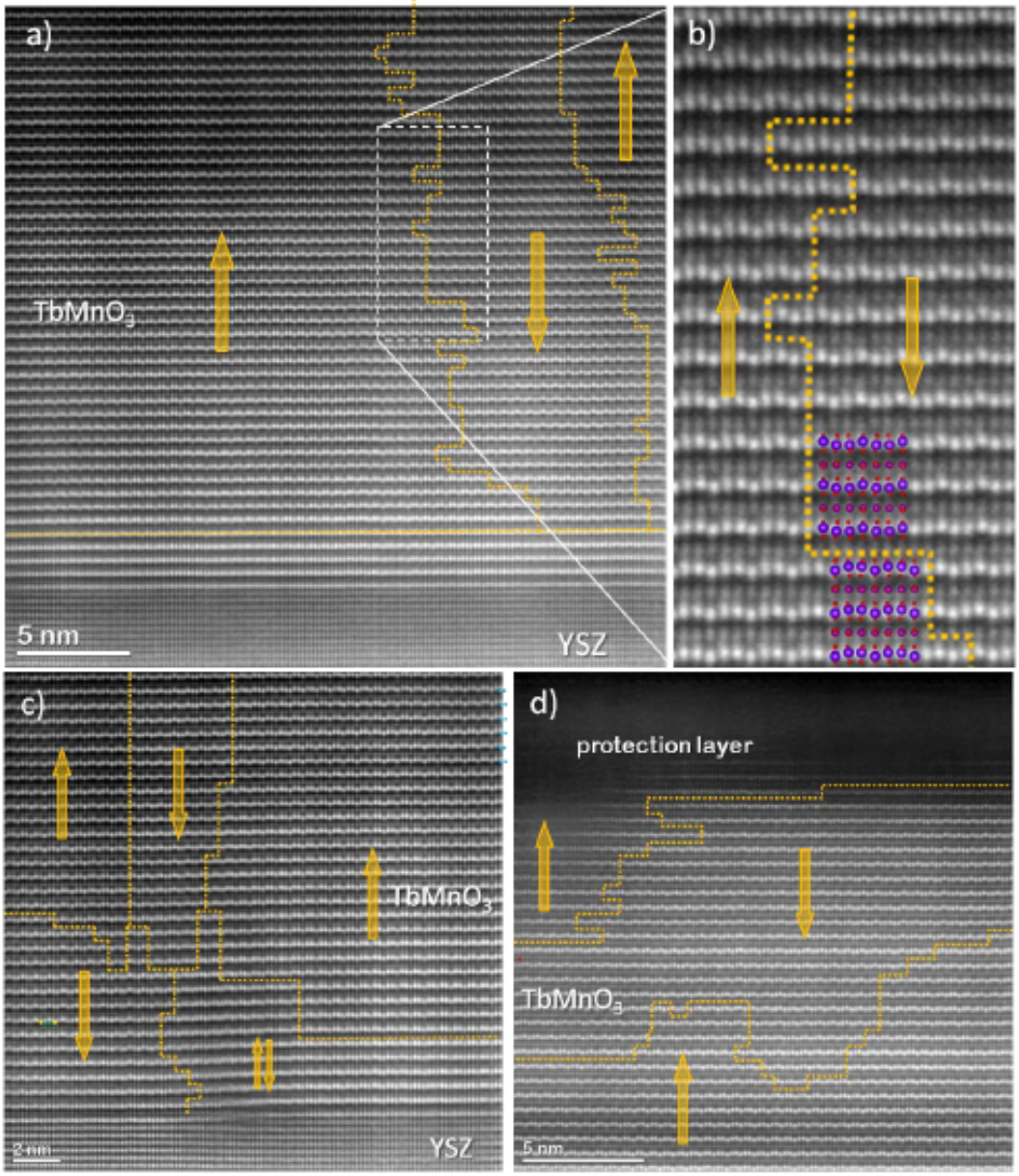

Fig. 4.2 (a) High resolution cross-section TEM image of a h-TMO/YSZ(111) film measured along the [11-20] crystallographic direction of the film with characteristic buckling (rumpling) of Tb atoms. The arrows show the direction of the ferroelectric polarization within one domain. Atomically smooth and flat film/substrate interface as well as the absence of Tb-rumpling can be seen in the very first 4 u.c. of the film. (b) the zoomed part of Figure 4.2 (a) demonstrates the characteristic regions with the "up" (left part) and "down" -rumpling (right part) of Tb ions, separating FE domains with a typical size varying in the range 5-20 nm; (c) HRSTEM image of $TbMnO_3$/YSZ interface showing the origin of FE domain at the atomic height step; (d) HRSTEM image of the top part of the $TbMnO_3$ film. A complicated domain structure is shown by dotted lines marking FE domain walls and pointing "up" and "down" polarization vectors.

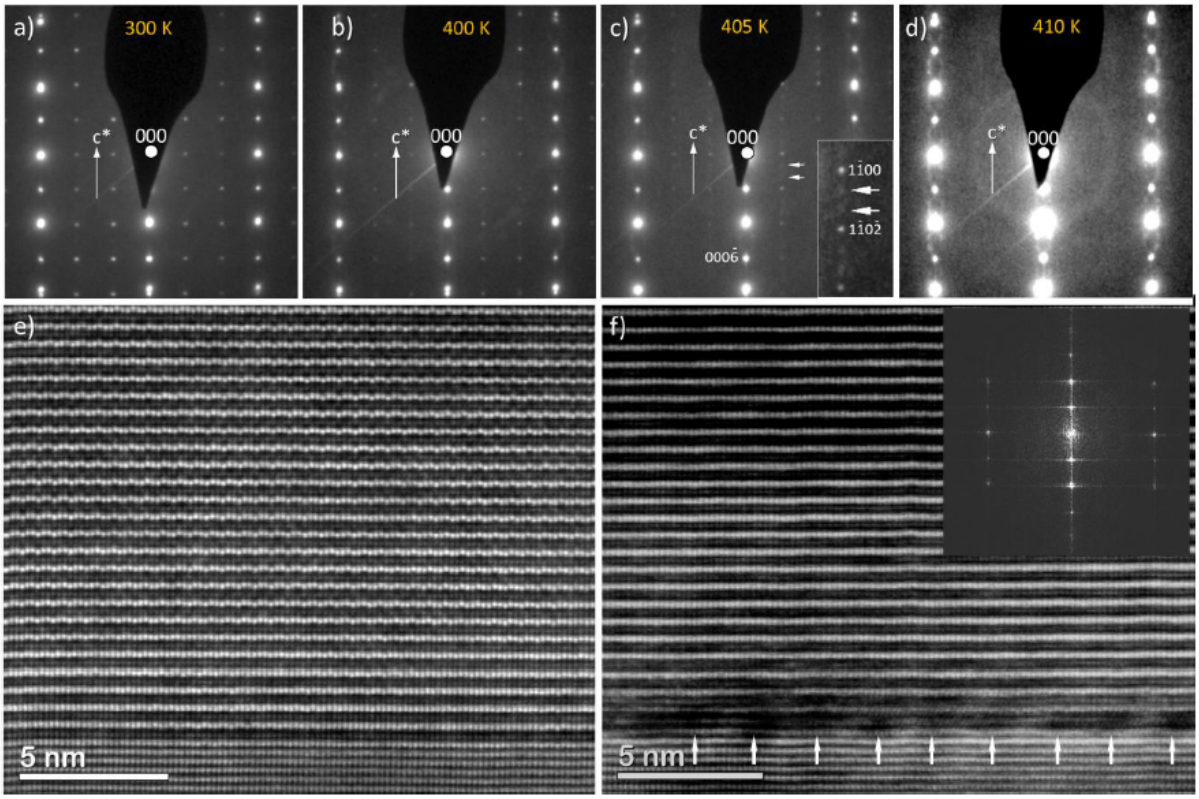

Fig. 4.3 (a)-(d) Electron diffraction, collected at different temperatures upon heating of the TEM lamella up to 410 K, and (e), (f) high resolution STEM images. The initial hexagonal ($P6_3cm$) structure with Tb-shift (e) was irreversibly transformed into a hexagonal ($P6_3/mcm$) structure with planar Tb-planes (f).This irreversible phase transformation is caused by strain relaxation actuated by formation of a system of misfit dislocations as evidenced in (f).

cm^{-1} corresponds to the A_1 mode of the hexagonal structure as shown for hexagonal manganite films [162]. In Figure 4.4 (a) we present the Raman spectra of the h-TMO film measured at fixed temperatures (the spectra are shifted for clarity) taken by heating and cooling (not shown) the sample in the temperature range, T = 293-973 K. The Raman spectra in Figure 4.4 (a) of the film sample were first corrected by the Bose factor, n+1 = $1/(1\text{-}e^{\hbar\omega/KT})$, and then normalized to the strongest substrate peak at $\sim$ 613 cm^{-1} as can be also seen in the inset in Figure 4.4 (a). Qualitatively, it demonstrates a strong temperature dependent Raman behavior with suppression of the film A_1 peak, started already from room temperature, and a complete vanishing of the film peak at T > 873 K. The subtracted (sample-substrate) Raman spectra presented in Figure 4.4 (b) allowed us to analyse quantitatively the temperature behaviour of a single A_1 film peak by fitting the difference spectra at all measured temperatures by Lorentz lines. One can see in Figure 4.4 (c) that the intensity, quantified by the area under the A_1 peak and its height, decrease steeply for T = 300-450 K and then continuously goes down to zero for T =

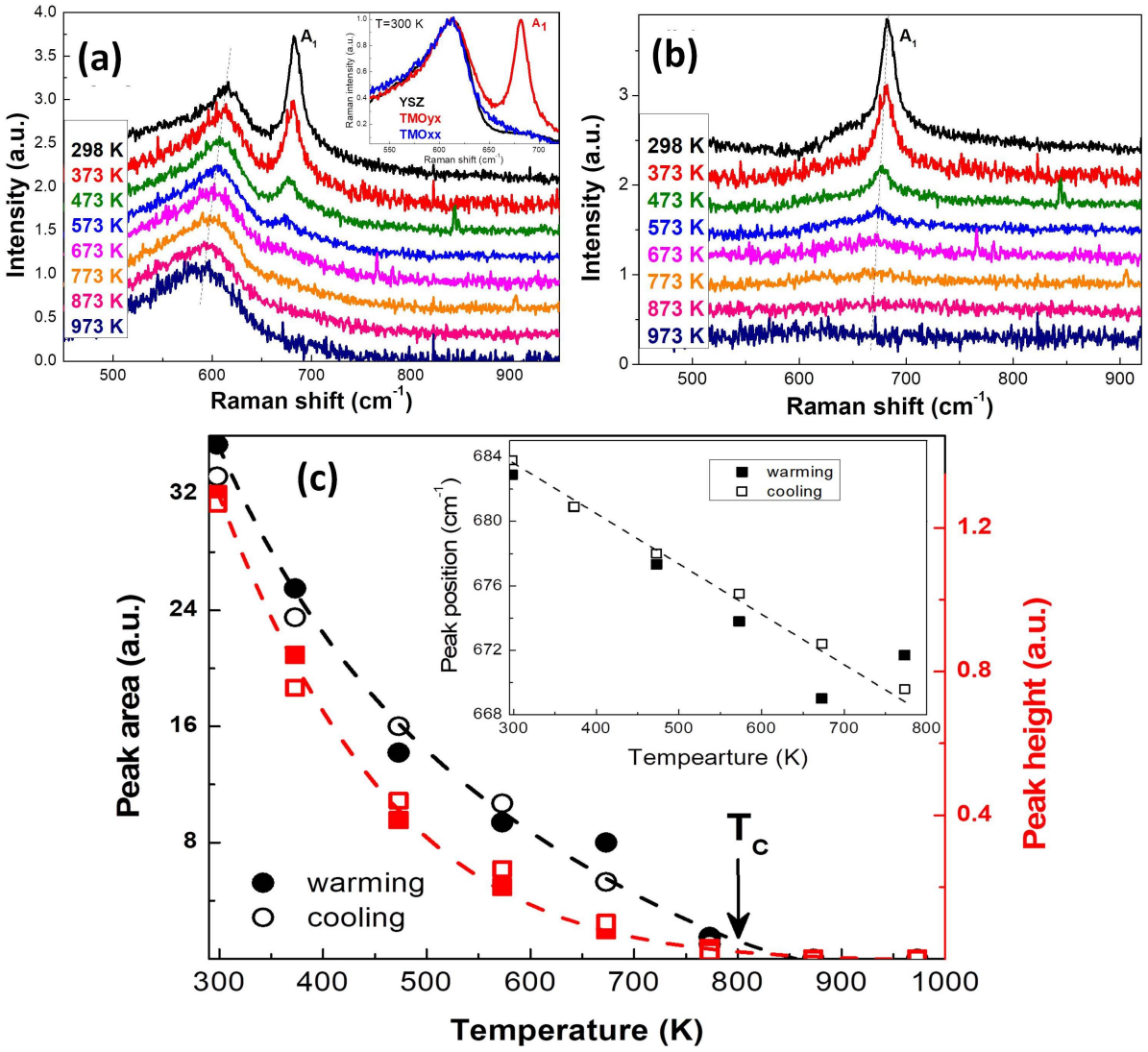

Fig. 4.4 (a) Unpolarised Raman spectra of a h-TMO/YSZ(111) sample, normalized to the spectrum of the substrate. The inset: room temperature polarized Raman spectra of a TMO/YSZ(111) film in XX (red) and XY (blue) polarization geometries confirm the hexagonal structure; (b) Evaluated Raman spectra of the h-TMO film; (c) The area (left scale) and the height of the A_1 peak (right scale) by warming (closed symbols) and cooling (open symbols). Phase transition is indicated by peak vanishing at $T_C \sim 800$ K. The inset in (c) shows the peak position as a function of temperature.

500-773 K, indicating the existence of a structural phase transition at about 800 K. A similar temperature behaviour with vanishing of the A_1 peak for $T > T_C = 1020$ K was reported in h-$LuFeO_3$ film [151]. The position of the A_1 peak in our strain-stabilized h-TMO film shifts almost linearly from ~ 683 cm^{-1} at room temperature down to ~ 668 cm^{-1} at 773 K (see the inset in Figure 4.4 (c)).This linear temperature behaviour agrees with that measured in h-$YMnO_3$ bulk samples [150]. Note, that the A_1 peak in bulk samples of h-$YMnO_3$ [150] did not vanish for $T > T_C \sim 1000$ K, but rather the

symmetry changes to A_{1g}. However, for T > 800 K we cannot further resolve the Raman peak from our 50 nm thick h-TMO film because of very small peak intensity, which in addition superimposes with the Raman contribution of the substrate. After cooling down the film to room temperature the intensity and position of the A_1 Raman peak retain to the same level as before heating, indicating no sizable strain relaxation effects in this film. Thus, the temperature dependent Raman study indicates that a reversible structural phase transition into a paraelectric $P6_3/mcm$ structure occurs around $T_C \sim 800$ K in the optimally grown h-TMO/YSZ(111) film.

4.3.2.3 Temperature dependent Optical Ellipsometry

To support our Raman data and to get an additional insight into the structural phase transition in hexagonal h-TMO films, we studied the temperature dependent optical ellipsometry for T = 300-1200 K. In Figure 4.5 (a) the time dependences of the ellipsometric phase shift, Δ(t), and polarization rotation, Ψ(t), angles are shown during the cooling down of the film. Using double-side polished YSZ substrate we were able to monitor the oscillations in Δ(t) and Ψ(t) due to the interference of the laser beam, reflected from the top and bottom surface of the plane parallel substrate, the thickness of which was changing due to thermal expansion. This allows us to measure the temperature of the sample by calculating the number of oscillations and calibrating the temperature by using a pyrometer: namely, T = 1200 K was achieved at the highest current I = 28 A. One can see in Figure 4.5 (a) that both Δ(t) and Ψ(t) show the following characteristic features: a) continuous changes by about 3-5° at the beginning and at the end of the time scan; and 2) a step-like change of the signal, especially pronounced in Δ(t), changing by 10°, in the middle part of the scan. In Figure 4.5 (b) the time scale was recalculated into the temperature scale by using the relation T(t)=293 K+18 K*t, where the initial point of the x-scale at t=0 corresponds to the finally achieved room temperature T=293 K (20°C). Apparently, both ellipsometric angles Δ(t) and Ψ(t), changes drastically within T = 600-800 K, indicating the phase transition takes place within the same temperature interval as was observed in Raman spectroscopy (Figure 4.4). In addition, the temperature dependence of the real part of the refractive index, n(T),(right scale in Figure 4.5 (b)), was evaluated by assuming a simple optical model of a homogeneous film grown on YSZ substrate with $n_{YSZ} = 2.15$ at $\lambda = 632.8$ nm [163]. At room temperature the evaluated refractive index for a h-TMO film, n ~ 2.12, fits nicely to the values measured for $YMnO_3$ [164]. It decreases drastically from n = 2.12 to n = 2.0, i.e. by 6 %, when the film undergoes the FE/PE phase transition. The endpoint of this transition in n(T) curve can be assigned to the Curie temperature, $T_C = 800$ K, in good agreement with the vanishing of the A_1 Raman peak in Figure 4.4 (c). With thermal expansion coefficient ~ 10^{-5}/K and within the temperature change ~ 103 K, the estimated change of the film thickness d = 50 nm at room temperature by heating/cooling is 0.5 nm, i.e. ~ 1 u.c.

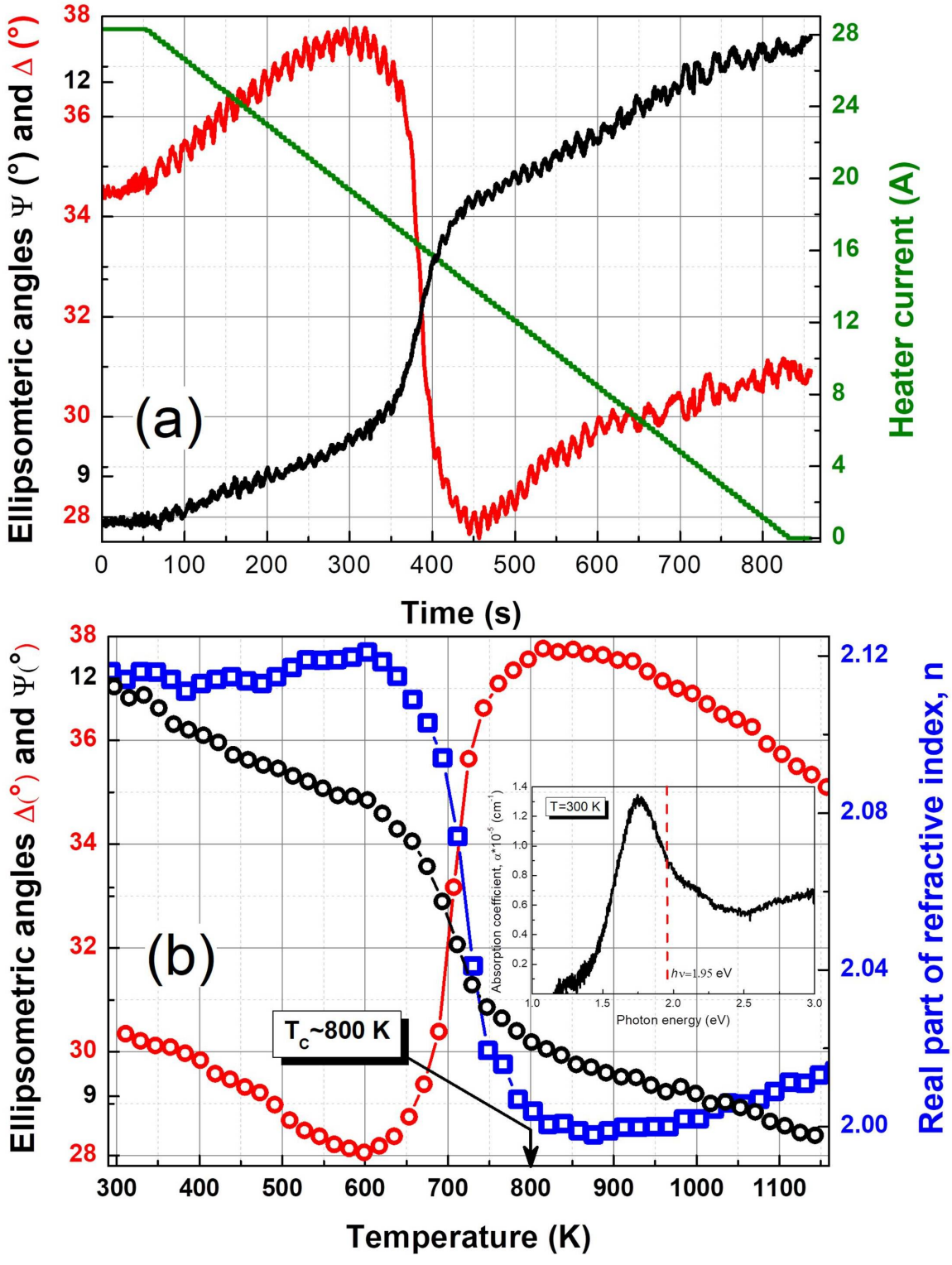

Fig. 4.5 Time (a) and temperature (b) dependences of ellipsometric phase shift Δ(t), and polarization rotation Ψ, angles as well as of the calculated refractive index n. A distinct step-like decrease of n by 6 % indicates the phase transition, the end point of which marks $T_C \sim 800$ K. The inset in (b) shows the absorption spectrum of h-TMO/YSZ(111) film measured at room temperature.

Such small thickness changes cannot result in the observed thermal ellipsometry behavior (Figure 4.5). The origin of the observed ellipsometric behaviour should be related to the change of optical properties and electronic structure of h-TMO at the structural phase transition. The photon energy E $\sim$ 1.96 eV of the He-Ne laser radiation falls within a strong and narrow absorption band with the centre at E = 1.75 eV, as demonstrated by the measured absorption spectrum for a h-$TbMnO_3$/YSZ(111) film shown in the inset of Figure 4.5 (b) [165]). According to the theory [166], the origin of this absorption band in h-manganites is the inter-band charge transfer transition from the occupied oxygen O 2p states into the empty Mn 3d states. Hence, we can conclude that at the structural phase transition the p-d charge transfer changes significantly in the h-TMO film. Here we can speculate that, a modification of the electronic band structure during the $P6_3/mcm$ (PE) to $P6_3cm$ (FE) structural phase transition influences a charge transfer from the O 2p to Mn 3d states. Note, that charge transfer from the Y-O_T (apical oxygen) bonds to the O_T-Mn bonds of Mn 3d - O 2p hybridized states, was found to be responsible for the enhanced ferroelectricity during the annealing-induced orthorhombic-hexagonal phase transition in bulk $YMnO_3$ [167]. However, by using monochromatic ellipsometry we cannot measure the changes of spectral weight transfer at the phase transition. In addition, the absorption peak is known to show a blue shift by decreasing temperature, T=300-15 K [165].

4.4 Conclusions

In conclusion h-TMO films were epitaxially grown by MAD in a strain-stabilized state on YSZ(111) substrate. The estimated in- and out-of-plane tensile stress at room temperature are -1.2 % and -3 %, respectively. Importantly, according to measurements of Raman spectroscopy and optical ellipsometry, the films were prepared in such a way that h-TMO films demonstrate a reversible structural phase transformation with $T_C \sim 800$ K. We call this intrinsic behaviour as it is related to the h-TMO material, prepared in the form of strain-stabilized film. In addition, we would like to shed light on the an extrinsic effect manifesting itself as irreversible phase transformations observed in the same film sample with constrained geometry as observed on TEM lamella during in-situ heating.

CHAPTER 5

Magneto-dielectric Effect in Relaxor Superparaelectric Tb_2CoMnO_6 Film

The following chapter presents investigation of magneto-dielectric properties in partially B-site ordered monoclinic Tb_2CoMnO_6 double perovskite thin film epitaxially grown on Nb:$SrTiO_3$ (001) substrates by metalorganic aerosol deposition (MAD) technique. Transmission electron microscopy and electron energy loss spectroscopy mapping shows the presence and distribution of both Co^{2+} and Co^{3+} ions in the film, evidencing a partial B-site disorder, which was further confirmed by the observation of reduced saturation magnetization at low temperatures. The ferromagnetic Curie temperature, $T_C = 110$ K, is slightly higher as compared to the bulk value (100 K) probably due to an in plane epitaxy tensile strain. Temperature dependent dielectric study reveals an unexpected high temperature dipolar relaxor-glass-like transition at a temperature $T^* \sim 190$ K $> T_C$, which depends on the applied frequency and indicates a superparaelectric behavior. Two different dielectric relaxation peaks have been observed; they merge at T^* where likely a coupling to the disorder-induced short range charge-spin correlations results in a 4% magneto-dielectric coupling. The full content of this chapter has been published in ***Physical Review B 101, 094426 (2020)***.

5.1 Introduction

Magneto-dielectrics and magneto-electric materials with the coupled magnetic and electric dipolar order parameters are of fundamental as well as of technological importance. Rare-earth-based perovskite oxides have been proved to be potential candidates for the next generation memory and spintronic device applications [168, 169, 170, 171, 172, 173, 174]. $A_2BB'O_6$ (A is a rare earth cation, B B′ are transition metal ions) double perovskites with the layered $ABO_3/AB'O_3$ cation-ordered structure along the [111] axis represent themselves an emerging and promising platform to study strong electronic correlations, complex magnetic structure, spin-lattice interaction and magneto-dielectric coupling [175, 176]. $R_2(Co/Ni)MnO_6$ (where R= La to Lu) system having a monoclinic structure with $P2_1/n$ space group is especially attractive as they possess an insulating ferromagnetic (FMI) behavior with relatively high Curie temperatures, $T_C \sim$ 200-300 K, allowing a high temperature magneto-dielectric coupling. FMI originates from a 180°- superexchange interaction between high spin Co^{2+}/ Ni^{2+} and Mn^{4+} ions, described by the second Goodenough-Kanamori-Anderson rule [177, 178, 179]. The FM ordering as well as dielectric behaviour depend strongly on the B-site ordering which controls the superexchange interaction along with hoping of charge. The fully and partially B-site ordered La_2CoMnO_6 has been well explored due to a reasonably high ferromagnetic Curie temperature, T_C=230 K [180], spin-phonon coupling [178]; they reveal a weak magneto-dielectric effect (3%)[181]. Partially disordered La_2NiMnO_6 has been reviewed as a promising multi-glass material where two different glassy states (spin and dipolar) were observed simultaneously, resulting in a stronger magneto-dielectric coupling constant ϵ_{MD} = [ϵ'(8T) - ϵ'(0T)]/ϵ'(0T)×100∼ 16% at room temperature [182]. Considering the smaller radii rare earth ions in the A-site (R=Pr to Lu) the ferromagnetic T_C decreases considerably (down to T_C=48 K for Lu)[175] along with spin-phonon interaction [183]. The trend in the dielectric behavior also remains unchanged from bigger to smaller A-site cations as found in bulk $(La/Tb/Y)_2CoMnO_6$ where dielectric constant decreases monotonically with lowering temperature [184]. La_2CoMnO_6 (LCMO) from the concerned rare earth double perovskite family has been reported to possess a large dielectric constant at room temperature, which gradually decreases with lowering the temperature [184]. Taking ions with smaller ionic radii, like Y^{3+} and Tb^{3+} in the A-site, the trend of decreasing dielectric constant monotonically towards lowering temperature remains similar with no significant deviation [185]. The overall behaviour is the same in case of epitaxial LCMO thin films though the dielectric constant becomes very low [181]. A controllable disorder in a perovskite or double perovskite system can create a dipolar glass that can couple with its magnetic subsystem, inducing a novel magneto-dielectric or rare multi-glass behaviour [186]. Tb^{3+} with a small cation radius in the A-site has a special significance as it can tune and stabilize a novel hexagonal structure in a strained thin film, which cannot sustain in the bulk form as

observed in $TbMnO_3$ [187]. With all these experimental observations and intuitions, the Tb-based double perovskite thin films with controllable B-site (partial) ordering could be suggested as an important and exclusive playground for studying novel magnetic and dielectric transitions along with possible coupling between them. Here we report the epitaxial growth of monoclinic Tb_2CoMnO_6/Nb:$SrTiO_3$(100) thin film by using a metalorganic aerosol deposition (MAD) technique [188]. The established partial B-site disorder in the film is accompanied by an unexpected high temperature relaxor glassy transition along with a superparaelectric behavior. Asymmetrical nature of the temperature dependent dielectric constant is manifested with the three different polarized nanoregions (PNR) present in the system. Moreover, two different dielectric relaxation peaks in frequency domain along with a 4% magneto-dielectric coupling was observed probably due to the interaction of the B-site-disorder-induced local spin moments with the PNRs.

5.2 Experimental Section

5.2.1 Growth of Tb_2CoMnO_6 films

Tb_2CoMnO_6 (TCMO) films have been grown by a metalorganic aerosol deposition technique on commercial electrically conducting 0.5% Nb-doped $SrTiO_3$(100) (NSTO) substrates (Crystal GmbH). Acetylacetonates of Tb, Mn and Co were used as precursors. Precursor solutions in dimethylformamide (DMF) with concentration 0.02 M (for both Co and Mn-precursor) and empirically found molar ratio Tb/(Co+Mn)=1.1 were prepared. The films with thickness, d=80 nm, were grown by spraying the precursor solution by using dry compressed air onto a substrate heated to $T_{sub} \sim 900°C$. The films were grown with an average growth rate of v=15 nm/min and were cooled down to room temperature in 20 min after deposition.

5.2.2 Measurement details

X-ray diffraction (XRD) characterization was performed by using the Bruker D8 spectrometer with Cu-K_α radiation in a θ-2θ Bragg-Brentano geometry. Magnetization as a function of temperature and magnetic field, applied parallel to the film surface (IP), was measured using commercial 7T-SQUID-VSM (Quantum Design Inc., USA) system. Magnetization vs. temperature was measured following the conventional protocols of zero field cooled warming (ZFC) and field cooled warming (FCW) cycles in an applied magnetic field H=100 Oe. The local structure of TCMO films was studied by Scanning Transmission Electron Microscopy (STEM) and electron energy loss spectroscopy (EELS) using a FEI Titan 80-300 G2 environmental transmission electron microscope (ETEM), operated at an acceleration voltage of 300 kV. The TEM is equipped with a Gatan Imaging Filter (GIF) Quantum 965 ER. EELS spectra were taken with a dispersion of 0.05

eV/channel. The convergence and collection semi-angles were about 10 and 22 mrad, respectively. TEM lamellas were prepared by a Focused Ion Beam (FIB) lift-out technique using a Thermo-Fischer (former FEI) Helios 4UC instrument. The temperature- and magnetic-field-dependent complex dielectric measurements were performed by using a home-made insert coupled with 9 T superconducting magnet and a Keysight E4980A LCR-meter operating at frequency range f=20 Hz-2MHz.

5.3 Results and Discussion

5.3.1 Magnetic properties

Temperature dependence of the ZFC & FC magnetic susceptibility, $\chi(T)$, of the TCMO film, measured for μ_0H=100 Oe, is shown in Figure. 5.1(a). One can see a phase transition at T_C=110 K, below which the long-range ferromagnetic ordering develops due the superexchange interaction between Co^{2+} and Mn^{4+} ions [179]. The transition seems to be of a second order as it is not apparently sharp and no warming/cooling hysteresis was observed. The transition temperature in our TCMO film is a bit higher than that observed in a Tb_2CoMnO_6 single crystal (T_C = 100 K) [189], likely, due to an in-plane epitaxial tensile strain in the TCMO thin film, $\varepsilon = -0.6\%$, evaluated from the XRD pattern (Figure 5.7 in Appendix), which shows an out-of-plane epitaxy. The bifurcation between ZFC and FC curves denotes the magnetic irreversibility in the system due to the presence of AFM/FM competing interactions among magnetic domains which are characteristic for ferro- and ferrimagnetic systems with large coercivity in the ordered phase, irrespective of what origin. It means that along with the dominating Co^{2+}/Mn^{4+} FM superexchange the AFM interactions of Mn^{4+}/Mn^{4+} and/or Co^{2+}/Co^{2+} type could be present, although no additional features were observed at low temperatures due to the domain-wall de-pinning process similar to that observed in a single crystal [189]. The anomalous increase in FC curve at 18 K is due to the ordering of spins of Tb^{3+} ions, which are likely FM-coupled to the Co^{2+}/Mn^{4+} sites. In Figure 5.1 (b) the field dependence of the isothermal magnetization, M(H), measured at 5 K is shown. The evaluated magnetization close to saturation, $M_S \sim 5.5\ \mu_B$/f.u., is significantly smaller than the theoretical value (6 μ_B/f.u.) for a fully B-site ordered Co^{2+}/Mn^{4+} system. Moreover, the Tb^{3+} ions possess an even higher moment of 9.72 μ_B/Tb^{3+} due to the spin-orbit coupling and, considering their additive contribution, the total magnetic moment of the TCMO system should be even much larger. Recently, the TCMO single crystal has been shown to have a strong magnetic anisotropy of Tb^{3+} ions, which prefer to order along the c-axis yielding a large value of $M_S \sim 9.73\mu_B$/f.u. [189]. As for our TCMO/Nb:STO(001) film, the c-axis according to XRD (Figure 5.7) stays perpendicular to the film plane, the observed value of $M_S \sim 5.5\ \mu_B$/f.u. seems to be quite small though we dont know the

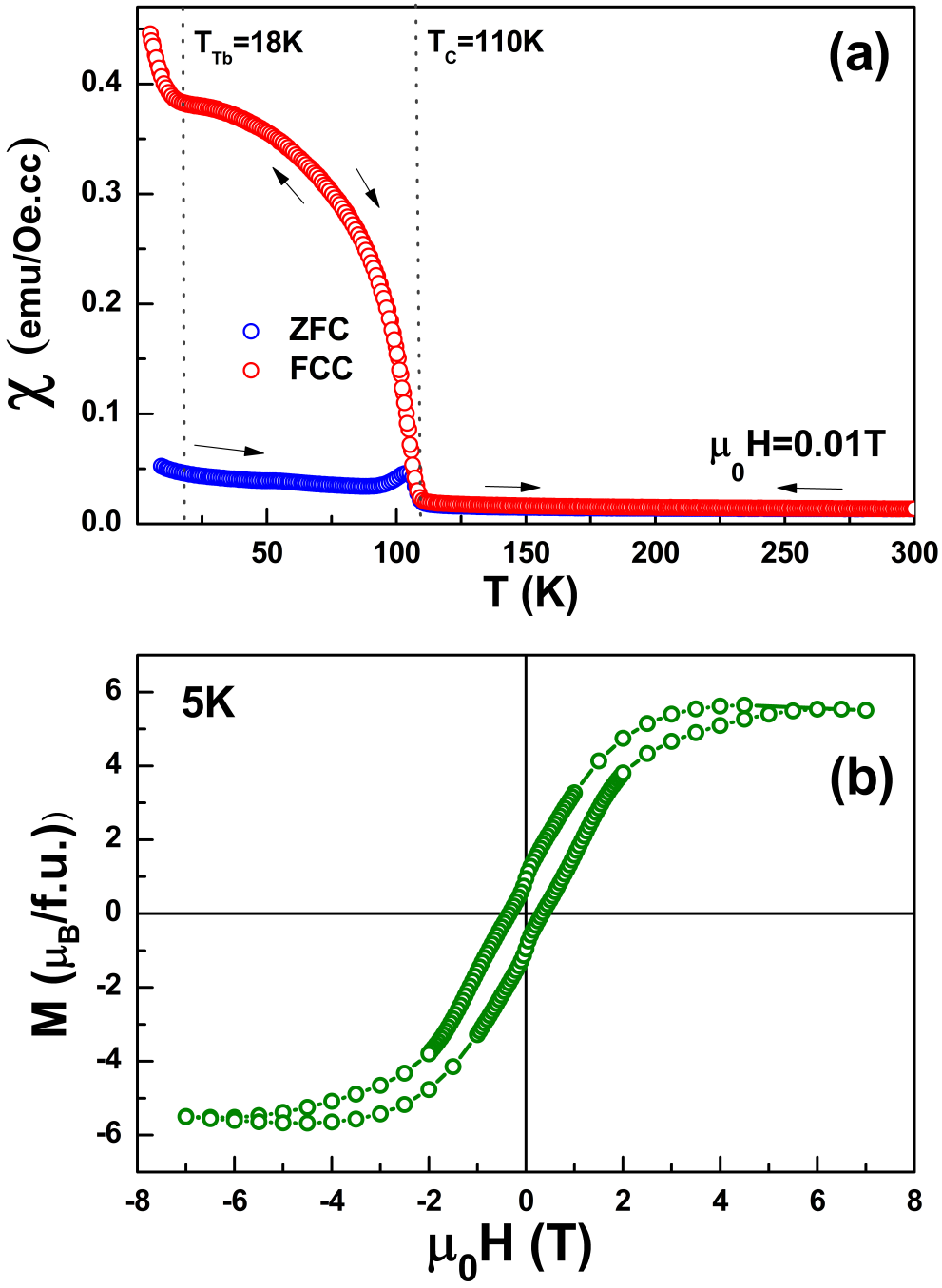

Fig. 5.1 (a) zero-field-cooled (blue, ZFC) and field-cooled (red, FC) magnetic susceptibility ($\chi(T)$) as a function of temperature (T) in the TCMO film. (b) Isothermal magnetization with applied external magnetic field at 5K.

exact orientation of the magnetic easy axis for our film. From the trend and comparison to the single crystal data it could be concluded that the direction of applied magnetic field is somewhere in between the magnetic easy and hard axis of the film. A very small value of remnant $M_r = 1.1\ \mu_B$/f.u. and a large coercive field of H_C=0.35 T as compared to that of the TCMO single crystal is in line with significant amount of Mn^{3+} disorder along with Co^{2+}-O- Co^{2+} and Mn^{4+} -O- Mn^{4+} interactions, contributing to the AFM phase boundaries and developing FM/AFM competitive interactions [179]. The presence of Mn^{3+}/ Co^{3+} ions, making a finely distributed partial disorder within the film, as well as a dominance of Co^{2+}/Mn^{4+} oxidation states responsible for the main FM phase has been further confirmed by EELS mapping in HRTEM, shown in Figure 5.8 in Appendix. Determination of the percentage of B site ordering is not straight forward as in the case of La_2CoMnO_6 where only Co and Mn ordering are present. Ordering percentage can be calculated from the M_S value in low temperature M-H loop and comparing it with fully ordered Co^{2+}/Mn^{4+} system. Here in case of Tb_2CoMnO_6 we have an additional contribution of Tb^{3+} ions as discussed. In the FC magnetic susceptibility data we see around 15 % increase of the magnetic susceptibility bellow 18K due to Tb^{3+} ordering. So we calculate the M_S value for only Co and Mn in TCMO by a 15 % reduction to the measured value of M_S i.e 5.5 μ_B/f.u. Comparing the new M_S value of 4.7 μ_B/f.u. with fully B site ordered system of 6 μ_B/f.u. we can conclude that our system is approximately 78 % ordered.

5.3.2 Dielectric measurements

5.3.2.1 Temperature dependence

In Figure 5.2 (a) we present the temperature dependence of the real part of dielectric constant, $\epsilon^{'}$(T), measured for different frequencies, showing a broad maxima of $\epsilon^{'}$(T) which is of same order as that observed in the LCMO film [181]. The temperature of the maximum, T_m, depends on the frequency and shifts to higher temperatures with increasing frequency. This kind of glassy behaviour is very new for the A_2CoMnO_6 double perovskites and probably indicates a ferroelectric relaxor behaviour, which is not associated with any structural transition in the system. With further lowering the temperature ($T \leq 100 - 120K$), $\epsilon^{'}$(T) starts to increase again possibly due to the electronic contribution from the conducting Nb:STO substrate and the substrate/film interface. The observed ferroelectric relaxor behaviour can be fitted with the Curie-Weiss law, $\epsilon^{'}$(T)=C/(T-Θ) in the paraelectric region [190] above the frequency dependent relaxor transition temperature, $T_m \sim$ 150-200 K, as shown in Figure 5.2 (b). The fitting parameters are presented in Appendix (Table 5.1). At low frequencies the data were fitted well with the Curie constant, C = 8 $\times 10^3$, and the Curie temperature, $\Theta\sim$ 150 K, respectively. With increasing frequency, the data start to deviate from the Curie-Weiss law. As for high frequencies the

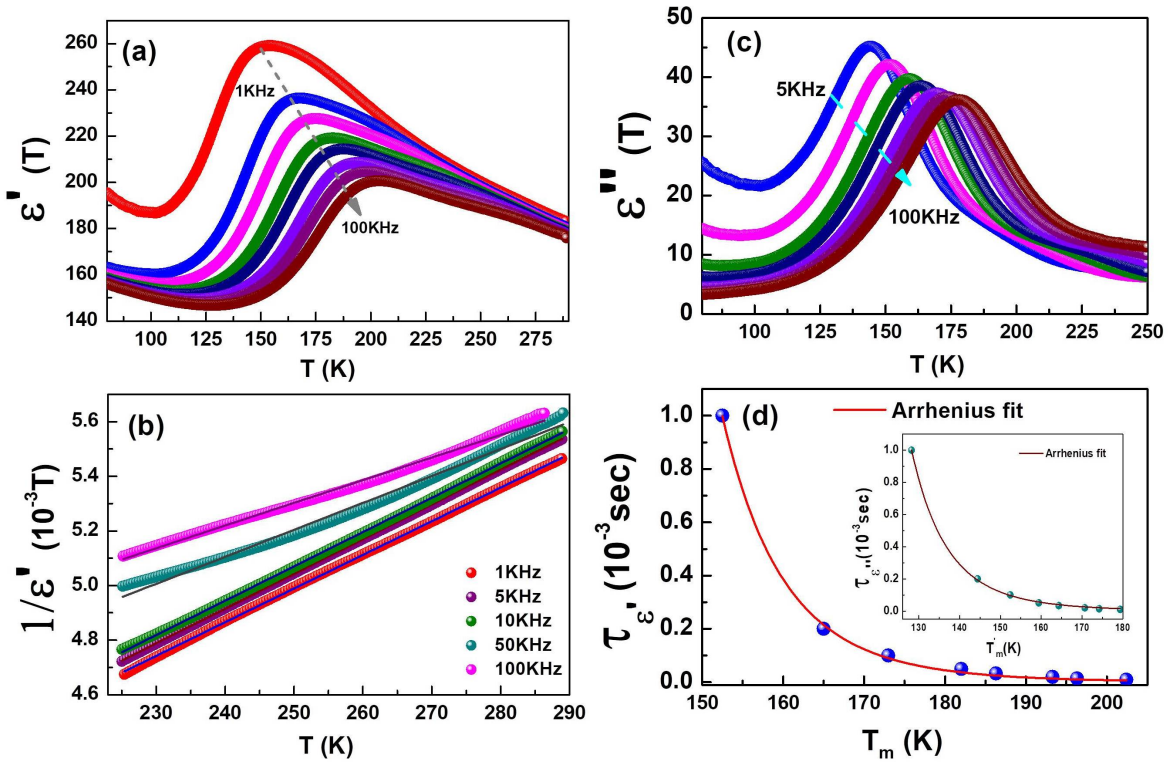

Fig. 5.2 (a) Dielectric constant ($\epsilon^{'}$(T)) vs temperature at different applied frequencies (1-100 KHz). (b) Curie-Weiss fit for the $\epsilon^{'}$(T) above the relaxor glass transition for different frequencies. (c) Temperature dependence of the dielectric loss part $\epsilon^{''}$(T) with different applied frequencies showing relaxation peaks. (d) Arrhenius fit for the relaxation time vs peak temperature for the dielectric constant $\epsilon^{'}$(T) and dielectric loss $\epsilon^{''}$(T) (inset).

transition temperatures T_m increase, the fitting range becomes to be not far away from the transition temperature. The short range correlations among electric dipoles emerge, being frequency dependent and causing deviation from an ideal ferroelectric behaviour. The plausible interpretation is the formation of small Polar Nano Regions (PNR), having different responses for sufficiently high frequency. For an ideal ferroelectric case the Curie-Weiss fit should not depend on the applied frequency. In Figure 5.2 (c) one can see a broad relaxation peak (T_m) in the temperature dependence of the dielectric loss, $\epsilon^{''}$(T), which also shows a frequency dispersion. The observed relaxation in both real, $\epsilon^{'}$(T), and imaginary part, $\epsilon^{''}$(T), of dielectric constant could be interpreted in the framework of a dipolar glass model [191]. It considers small dipolar regions, induced in the system by the B-site disorder, the dipole moment of which fluctuates/vibrates thermally at high temperatures $T > T_m$. Analogously to the spin glass, the dipoles are expected to be frozen at low temperatures. The freezing temperature (T_f) is finite if the interaction be-

tween dipoles is strong enough. The dynamics of a PNR can be described by the so called Vogel-Fulcher (VF) formalism $f^{-1} = \tau_0 \exp[U_a(K_B(T_m\text{-}T_f))]$, where f is the frequency of an applied electric field, the T_m is the relaxation peak maxima [192, 193, 194, 195]. If the electrostatic interaction among the dipoles is not strong enough to freeze them cooperatively, then dipoles can vibrate with external ac electric field at any finite temperature and can show a thermally activated Arrhenius behaviour down to $T_f \rightarrow 0K$. Both VF and the Arrhenius law $f^{-1} = \tau_0 \exp[U_a(K_B(T_m))]$ as well as a power law were tried to fit the data. The best fit was obtained with Arrhenius behaviour, shown in Figure 5.2 (d) for both $\epsilon^{'}$ and $\epsilon^{''}$. The activation energies, calculated from the fits are Ua=0.25 eV and 0.16 eV for $\epsilon^{'}$ and $\epsilon^{''}$, respectively; they look physically reasonable and are of the same order of magnitude as activation energies $\sim$ 0.1 eV for a typical relaxor ferroelectric [191]. The evaluated relaxation time, $\tau_0 = 1.59 \times 10^{-12}$ s, corresponds roughly to characteristic phonon frequencies of few THz, obtained from Raman spectra of similar double perovskite films [178].

The observed asymmetry in the relaxor peak in $\epsilon^{'}(T)$ has been analysed in terms of diffuse phase transition model, which describes the temperature dependent dielectric permittivity as well as the size distribution of PNRs by means of a Gaussian function: $1/(\sqrt{2\pi\sigma^2})\exp[-(T - T_m)^2/(2\sigma^2)]$ [191]. Our experimental data can be fitted well by this distribution function and the $\epsilon^{'}(T)$ relaxor behaviour was found to be a superposition of three different maxima, denoted as T_m^1 , T_m^2 and T_m^3, exemplary shown in Figure 5.3 (a) for f=10 kHz. The experimental data were fitted for all frequencies and three frequency dependent temperatures are presented in Appendix (Table 5.2). Again VF, activation law and power law were tried to fit these three temperatures and we found the Arrhenius behaviour provides the best fits as shown in Figure 5.3 (b), (c) and (d). The calculated activation energies, 0.22, 0.30 and 0.32 eV, look also physically reasonable. From the deconvolution of the $\epsilon^{'}$ peaks we obtained three types of PNRs, which may differ in their microscopic origin and have distinguishable size distributions. These three distinct classes of dipoles can be related to their microscopic origin, taking into account that electric dipoles in TCMO may originate from the oxygen bonds with Co^{2+} and Mn^{4+} ions in the CoO_6 and MnO_6 octahedrons, which are getting distorted/polarized in an applied electric field. The third contribution could be caused by the disorder-induced presence of the Mn^{3+} as well as of Co^{3+} ions. All these PNRs started to interact with lowering temperature. Due to the difference in their distributions as well as in the activation energies, they respond differently with external frequency and with temperature. The overall macroscopic response, hence, shows a ferroelectric relaxation. Instead of the ferroelectric relaxor-glass-like behaviour, described by the Vogel-Fulcher (VF) formalism as a mostly suitable for a dipolar glass model, our system could be more accurately interpreted by the Arrhenius law. This scenario is an indication that partially disordered TMCO film could be considered as a

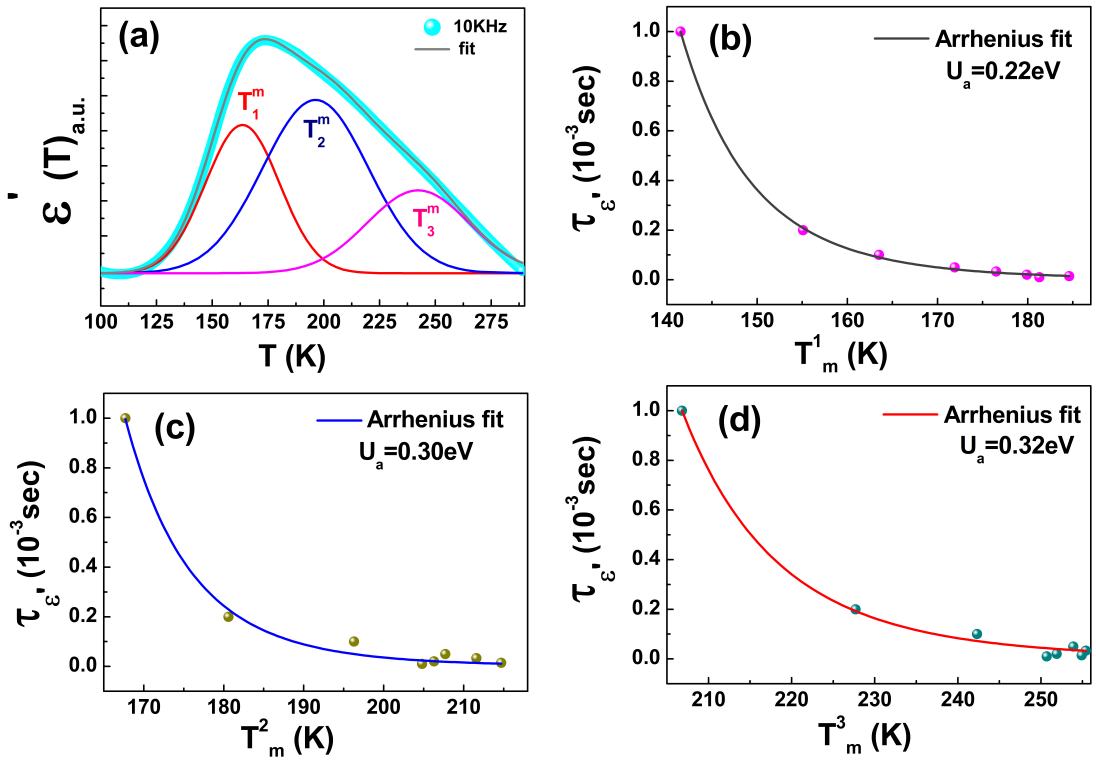

Fig. 5.3 (a) Gaussian fit for the temperature dependent dielectric constant $\epsilon^{'}$(T) and deconvolution of three peaks signifying the presence of three different types of PNRs. (b),(c) and (d) are Arrhenius fits for three relaxation times related to these three different peak temperatures: T^1_m, T^2_m and T^3_m.

superparaelectric, i.e. a blocked relaxor at low temperatures and non-zero frequencies, rather than as a dipolar glass.

5.3.2.2 Frequency dependence

In order to inspect the mechanisms of interactions among these dipoles, the dielectric loss ($\epsilon^{''}$) has been analysed in the frequency domain for different temperatures. For the used frequency range, f=20 Hz - 2 MHz, two main mechanisms are known to be responsible for the dipolar relaxation: (1) the Maxwell-Wagner (MW) mechanism originated from the local charge accumulation at grain boundaries [196] and (2) the Debye relaxation, which is the dipolar contribution from the hopping of charge carriers among asymmetric sites (Mn^{4+}, Co^{2+} and Mn^{3+}) [197]. Figure 5.4 (a) shows the dielectric relaxation over the frequency range for the temperatures in the relaxor transition regime. At very low frequencies, f < 200 Hz, one can see a MW behaviour, which is manifested by a linear decrease of $\epsilon^{''}$ with increasing frequency in the logarithmic ω - scale. With further increasing frequency the data start to deviate from the MW behaviour and display two distinct

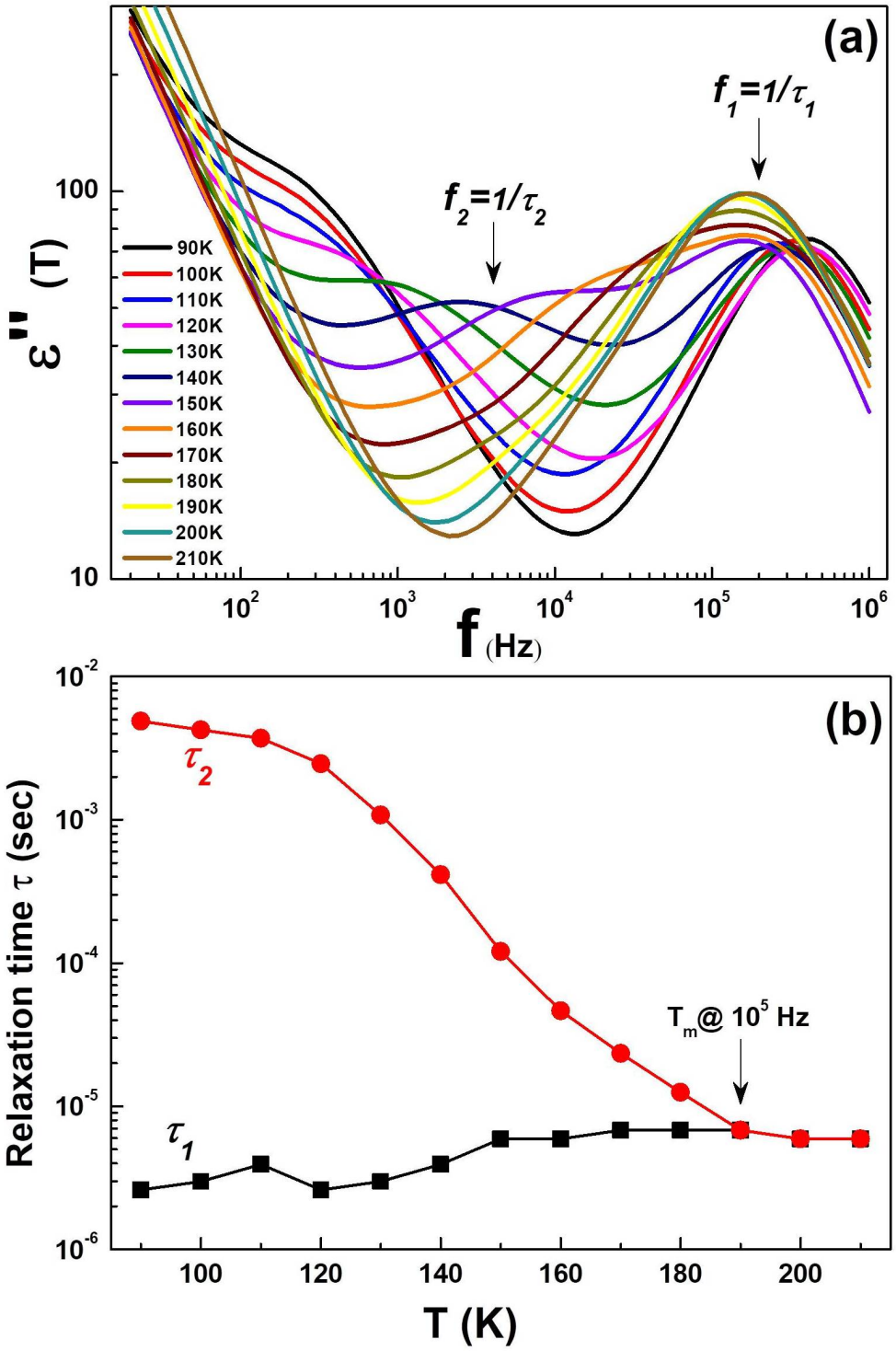

Fig. 5.4 (a) Frequency dependence of the dielectric loss part ϵ''(T) measured for different temperatures in the frequency range of f=20 Hz - 2 MHz; (b) Temperature dependence of the two different Debye relaxation times $\tau_1 = 1/f_1$ and $\tau_2 = 1/f_2$, evaluated from the positions of peaks in Figure 4(a)

Debye relaxation peaks at frequencies, denoted as $f_1 = 1/\tau_1$ and $f_2 = 1/\tau_2$. These two relaxation behaviours could be recognized as $\beta(\tau_1)$ and $\alpha(\tau_2)$-like processes in a glassy system [198]. Indeed, the frequency f_2 increases with increasing temperature and merges with the f_1 at a temperature T_C, which is comparable with the glass transition temperature in an amorphous material [199]. The slower $\alpha(\tau_2)$ relaxation is, analogously to glasses, a primary relaxation process in this dipolar glassy system and can be assigned to the major charge transfer between the Co^{2+} - Mn^{4+} sites. A secondary, or faster β process, develops from the localized disorder or minor sites, occupied likely by Mn^{3+} and/or Co^{3+} ions. Interestingly, one can see that these two processes merge at a temperature around 190 K giving a single relaxation peak at around 100 kHz as shown in Figure 5.4.

5.3.3 Magneto-Dielectric investigation

Magneto-dielectric (MD) analysis has been done by dielectric measurements in an applied magnetic field, B= 8T, at f=100 kHz. Here we can observe a characteristic change in the dielectric constant in the vicinity of the relaxor transition at $T_m \sim 195$ K at this frequency as shown in Figure 5.5 (a). The temperature dependence of the MD coupling constant ϵ_{MD} =($\epsilon^{'}$ (8T) - $\epsilon^{'}$ (0T))/$\epsilon^{'}$ (0T))×100 along with the derivative of dielectric constant ($\delta\epsilon^{'}/\delta T$) in Figure 5.5 (b) shows that | ϵ_{MD} | increases by cooling down the system and takes the highest value of 4% close to the relaxor transition. Moreover, the MD effect is negative, i.e. $\epsilon^{'}$ decreases in applied magnetic field. By further lowering the temperature MD coupling decreases again as dipoles are started freezing. The absence of the magnetoresistance (Figure 5.6) confirms that the MD coupling is intrinsic to the dipoles present in the material. Moreover, the temperature dependence of electrical resistance, R(T), can be fitted by a variable-range-hopping (VRH) Motts behaviour [200], $\rho(T) = \rho_0 \exp(T_0/T)^{1/4}$, with $T_0 = 211$ K and $\rho_0 = 7{\times}10^{-4}\Omega cm$, which illustrates a disorder-dominated charge transport. The so called Mott temperature T_0 =211 K is given [200] by the formula, $k_B T_0 = \beta/(g(E_F)R^3_{loc})$, where $\beta = 21$ and $g(E_F)$ and R_{loc} are the density of states at the Fermi level and localization radius of charge carriers, respectively. Considering characteristic values of $g(E_F) \sim 10^{27}$-10^{28} (eV m^3)$^{-1}$ we get $R_{loc} \sim 5$ - 10 nm, which is in good agreement with the observed nm-scale disorder in EELS spectra in Figure 5.8. As indicated previously, mostly the Debye processes [197], originating from a charge transfer between dipoles, contribute to the dielectric constant at high frequencies. Dielectric constant increases up to the relaxor transition mainly from the contribution of activated dipoles due to the charge transfer from Mn^{3+} to other sites. Bellow the relaxor transition Mn^{4+} and Co^{2+} start interacting magnetically with the other disorder sites and dielectric relaxation peak splits at the same temperature indicating a charge transfer between them (see Figure 5.4 (b)). As the charge transfer is coupled to the spin arrangement, the short-range spin-spin interaction tries to restrict the charge hopping and we can see the 2nd relaxation peak in Figure 5.5 is not that much pronounced as the first

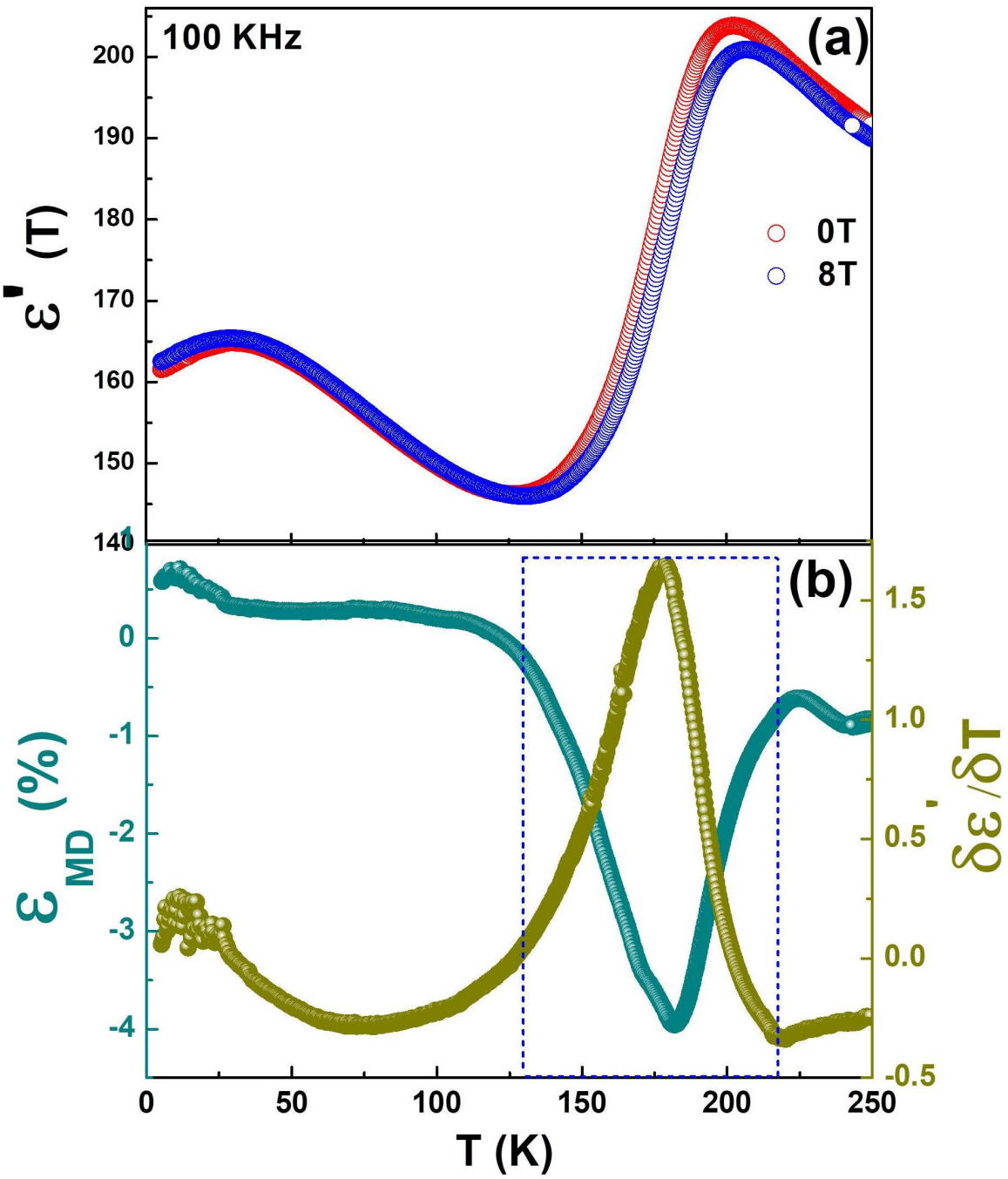

Fig. 5.5 (a) Temperature dependence of the dielectric constant $\epsilon^{'}$(T) at 100 KHz without and with applied external magnetic field of 8T. (b) Temperature dependence of derivative of dielectric constant ($\delta\epsilon^{'}/\delta T$) along with the magneto-dielectric coupling constant ϵ_{MD} (%) showing a maximum 4% magneto-dielectric coupling.

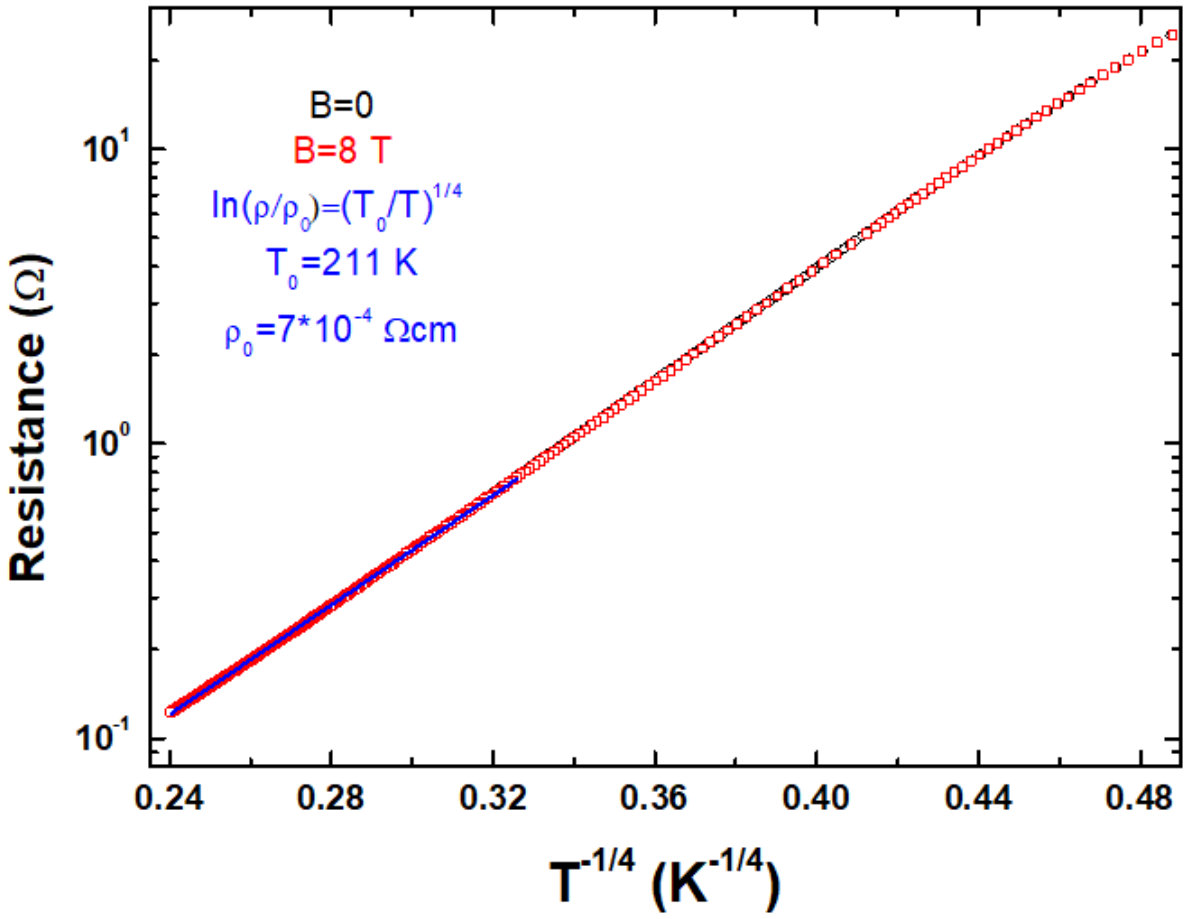

Fig. 5.6 Temperature dependence of DC resistance without and with applied magnetic field (B=8T) showing the absence of the magnetoresistance for the whole temperature range, T= 300-18 K. The measured $\rho(T)$ curve for T=300-50 K can be nicely fitted by the Mott variable-range-hopping behavior

one. With applied strong magnetic field this process is further interrupted and dielectric constant further reduce, causing a 4% negative MD coupling at the same temperature. We have to say that the exact physical mechanism of the observed MD coupling is not known. However, by comparing it with a quite similar high temperature MD effect in the La_2NiMnO_6 [182], a hint onto a probable coupling between the disorder-induced local spins in the paramagnetic region and electric dipoles can be given. One can speculate on the coexistence of very similar temperature scales, i.e. for α - β merging around 190 K, for relaxor transition, $T_m \sim 195$ K, and for the resistivity disorder scale $T_0 \sim 211$ K (Figure 5.6). Surprisingly, the latter is very close to the charge ordering (CO) temperature in manganites [201, 202] i.e. $T_0 \sim T_{CO}$. Note that a peak in a permittivity in THz region was also observed at $T \sim T_{CO}$ in $Pr_{0.65}Ca_{0.28}Sr_{0.07}MnO_3$ [202]. Likely, the closeness of these temperature scales, where a disorder-induced short range Mn^{3+}/Co^{3+} charge correlations, stabilized at $T < T_0 \sim T_{CO}$, coexist and interplay with superparaelectric dipole

regions could result in an unusual MD coupling. It is also highly unexpected to have a spin glass transition at such high temperature that can explain this MD coupling in terms of multi-glass behaviour. Due to huge background signal from the substrate and the interface, we were unable to resolve any short range spin correlations for T >> T_C from the Curie-Weis fit of the $1/\chi(T)$ curve. Further detail studies of the relationship between the B-site disorder and MD coupling are necessary to elucidate its mechanism.

5.4 Conclusions

In summary, we have grown monoclinic phase of Tb_2CoMnO_6 double perovskite thin film on Nb:$SrTiO_3$ (100) by using MAD technique. TEM and EELS mapping shows the presence and distribution of both Co^{2+} as well as Co^{3+} ions in the film, evidencing a partial B-site disorder, further confirmed by the observed reduction of the saturation magnetization at low temperatures. The ferromagnetic T_C = 110 K was slightly higher as compared to the bulk value due to an in plane tensile strain. Two different dielectric relaxation peaks (β and α) have been observed that merge at a temperature close to the relaxor glass transition. Moreover, we observed an unexpected high temperature relaxor-glass-like transition and a superparaelectric behavior, at which a probable coupling to short range correlated local spin moment results in a 4% magneto-dielectric coupling.

5.5 Appendix

Table 5.1 Curie-Weiss Fit parameters

Frequency(KHz)	Curie constant	$\Theta(K)$	T_m(K)
1	8.1 $\times 10^3$	154.8	152.6
5	7.9 $\times 10^3$	146.4	166.6
10	8.0 $\times 10^3$	153.4	172.5
50	10 $\times 10^3$	277.2	192.6
100	12 $\times 10^3$	388.7	202.5

Table 5.2 Peak temperatures from fitting of temperature dependent dielectric maxima ($\epsilon^{'}$)

Frequency(KHz)	T_m^1(K)	T_m^2(K)	T_m^3(K)
1	141.5	167.7	206.8
5	155.1	180.6	227.7
10	163.5	196.3	242.3
20	171.9	207.7	253.9
30	176.5	211.6	255.4
50	179.9	206.3	251.9
70	184.6	214.7	254.9
100	181.3	204.8	250.7

Table 5.3 Value of τ_0 of the various Arrhenius laws for the temperature of the maximum in dielectric constant ($\epsilon^{'}$(T))

	T_m(K)	T_m^1(K)	T_m^2(K)	T_m^3(K)
τ_0(sec)	1.59×10^{-12}	1.60×10^{-8}	1.15×10^{-9}	1.70×10^{-8}

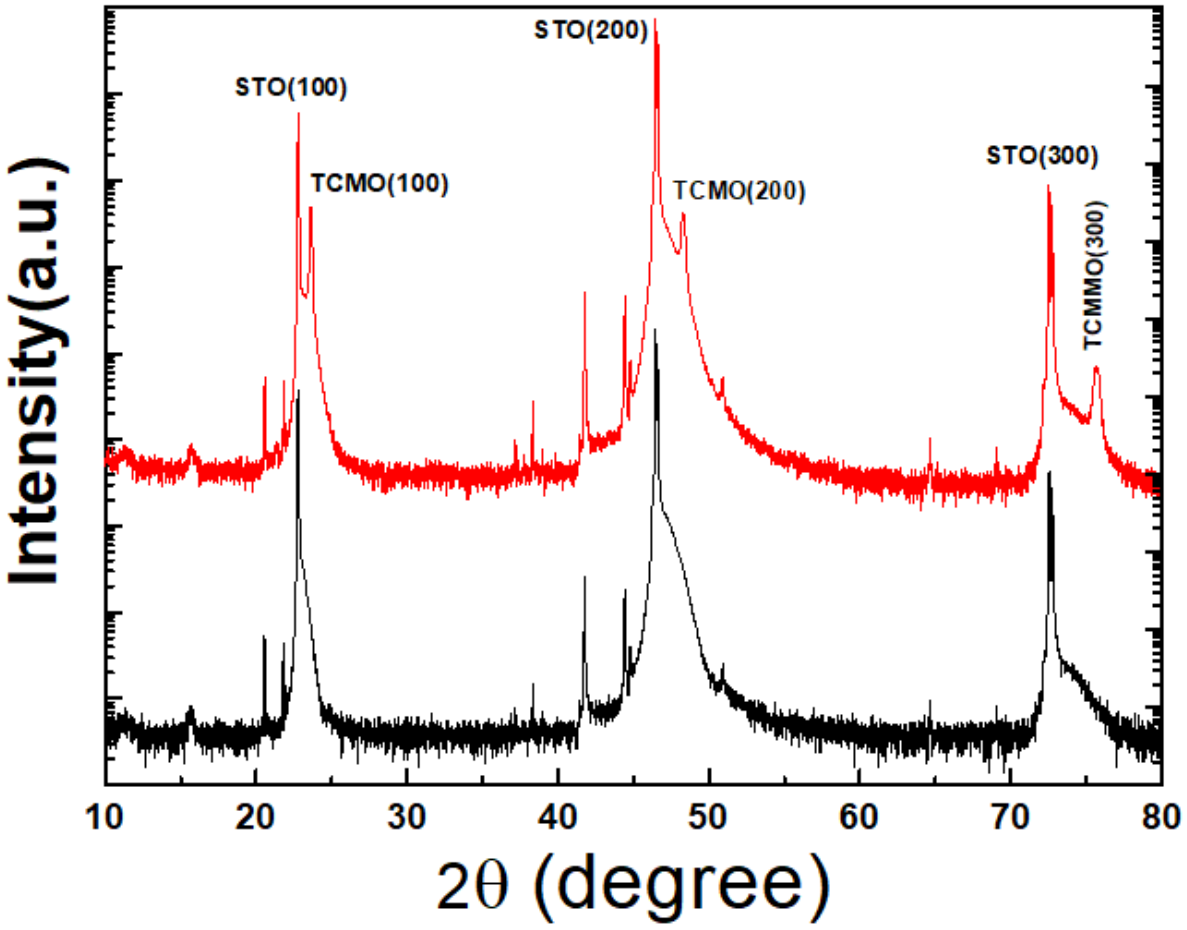

Fig. 5.7 XRD $\Theta - 2\Theta$ scan for Tb_2CoMnO_6/Nb:$SrTiO_3$ (100) (red) and Nb:$SrTiO_3$ (100) substrate (black) show the (h00) peaks from the substrate and the (00l) peaks of the TCMO, evidencing an out-of-plane epitaxy of the film. The artefact peaks, also seen in the XRD pattern from the substrate, originate from the K_β lines, sample holder and impurities in the X-ray tube. The calculated out-of-plane lattice parameter of TCMO is 0.75 nm while the bulk single crystal lattice parameter is 0.7547 nm (ref. 22). The calculated tensile biaxial strain in the film is -0.6 %.

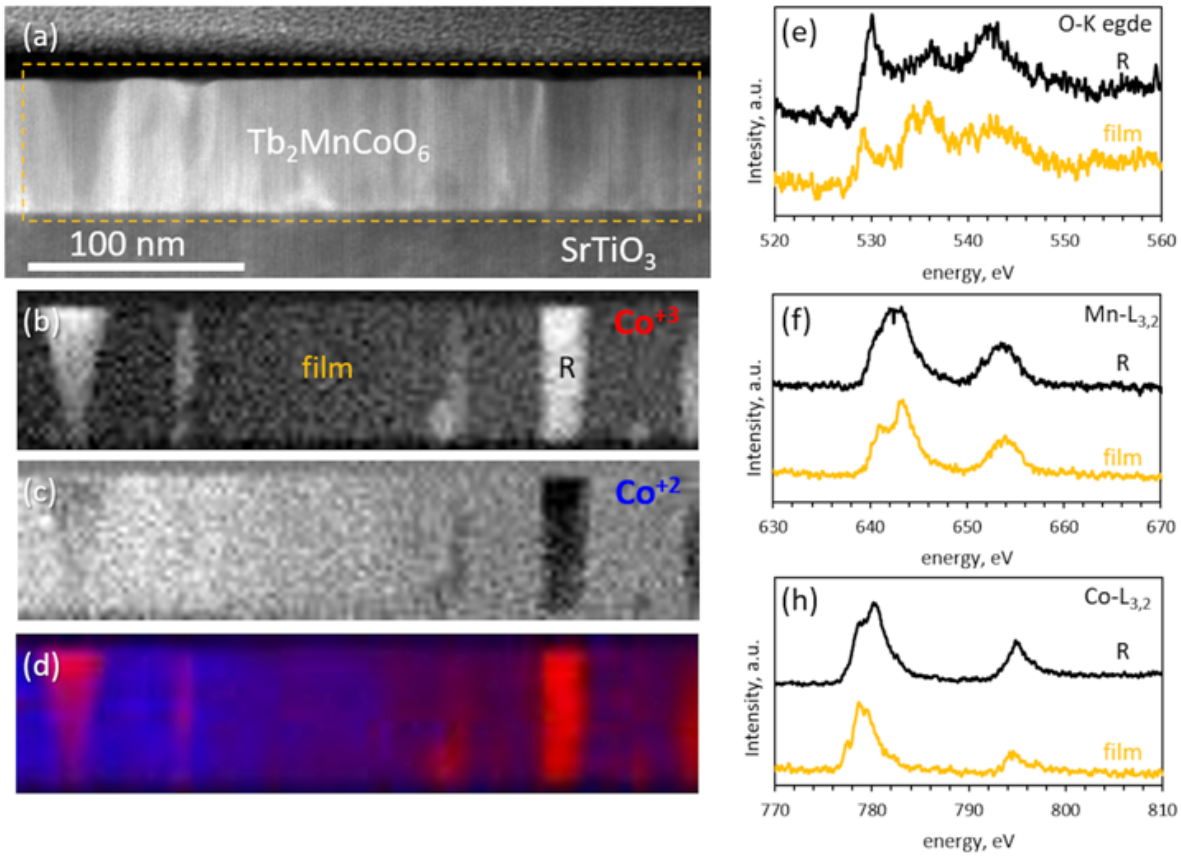

Fig. 5.8 a) HAADF image of TCMO film. The distribution of Co^{3+} (b) and Co^{2+} (c) within a selected region in the film. One can see that some regions, marked as R in (b), have excess of Co^{3+} ions, whereas the rest of the film is mostly containing Co^{2+} (c) i.e. corresponds to the ordered TMCO. (d) Superposition of Co^{3+} (b) and Co^{2+} (c) within a region in the film. The EELS spectra of Co-$L_{3,2}$ (e) and Mn-$L_{3,2}$ (f) within the film have the form typical to that for the B-site ordered double La_2CoMnO_6), thus confirming the predominance of Co^{2+}/Mn^{4+} oxidation state within the film. The spectra from the selected region R in (b) indicate the presence of Co^{3+} and Mn^{3+} ions. One has to say that even the defect-free region, marked as film in (b) contains a background with both Co^{2+} and Co^{3+} oxidation states, indicating the presence of disorder at a nm-scale.

CHAPTER 6

Interfacial Coupling Induced Enhanced Magnetic Ordering in $BaTiO_3$-$SrIrO_3$ Heterostructures

This chapter presents the growth of 3d-5d based relaxed $BaTiO_3/SrIrO_3$ heterostructures, to obtain emergent phenomena arising from the interfacial coupling between B-site (Ti^{4+}; $3d^0$ and Ir^{4+}; $5d^5$) cations. Parent $BaTiO_3$ film shows weak ferromagnetic ordering at $T_C \sim 136$ K, due to the oxygen vacancies, in contrast of paramagnetic nature in strong spin-orbit coupled $SrIrO_3$ film. Interestingly, in $BaTiO_3/SrIrO_3$ heterostructure we observed magnetic ordering at $T_C \sim 160$ K. X-ray photoelectron spectroscopy of O 1s and Ti 2p reveals the presence of oxygen vacancies and Ti^{3+} states in $BaTiO_3/SrIrO_3$, similar to the parent $BaTiO_3$. However, significant changes in Ir 4f spectrum line shape with coverage has been observed in $BaTiO_3/SrIrO_3$, in contrast of parent $SrIrO_3$. Therefore, this remarkable enhancement in T_C is attributed with the interfacial charge transfer process and the presence of strong spin-orbit coupling. The contents of this chapter are ***Under Preparation*** for submission.

6.1 Introduction

Interfacial charge transfer between 3d, 4d and 5d transitional metal-based oxide thin film heterostructures and superlattices generates novel electronic and magnetic properties. Transition metal oxide (TMOs) thin films show ample phenomena due to the interplay between its spin, lattice, charge and orbital degrees of freedom [203]. Recently, research activities on the interfacial coupling between 3d and 4d based TMO thin films with its 5d counterpart has increased immensely with the observation of novel magnetism with its tunability ($SrMnO_3$/$SrIrO_3$, $LaNiO_3$/$SrIrO_3$, and $LaMnO_3$/$SrIrO_3$), magnetic anisotropy ($La_{0.7}Sr_{0.3}MnO_3$/$SrIrO_3$), nanoscale skyrmions and topological Hall effect ($SrRuO_3$/$SrIrO_3$) among these various hetero-structures and superlattices [204, 205, 206, 207, 208, 209, 210, 211, 212]. All these phenomena are consequences of the charge transfer at the heterointerface, interfacial strain due to lattice mismatch and most importantly due to the presence of high spin-orbit coupling, giving rise to the Dzyaloshinskii-Moriya (DM) interaction [213, 214]. Creation, control and tuning of magnetic phenomena originating from the interfacial coupling is not only important fundamentally, but also useful for various spintronic applications [215]. Furthermore, this interfacial charge transfer and consequent polar catastrophe induced magnetic phenomena would also be more appealing fundamentally where to induce magnetism as well as tuning of magnetic ordering temperature in non-magnetic heterostructures.

In this regard, 3d based $BaTiO_3$ serves as an ideal platform, since it is a well-known ferroelectric material having empty d orbitals (Ti^{4+}; $3d^0$), hence absence of magnetic ordering [216]. However, several studies have shown that it could become ferromagnetic in presence of oxygen vacancies, generating Ti^{3+} states with fractional occupancy of an additional electron (Ti^{3+}; $3d^1$) in the t_{2g} orbital [217, 218, 219, 220, 221]. Thus, it is of critical importance to obtain magnetism in $BaTiO_3$, especially in its thin film form, which may play a significant role in the ferroelectric proximity effect [222]. Moreover, interestingly, by growing the heterostructure consisting of 3d based $BaTiO_3$ with strong spin-orbit coupled 5d based $SrIrO_3$ (Ir^{4+}; $5d^5$), perhaps magnetic ordering temperature could be tuned (enhanced) with the interfacial charge transfer (between Ti^{3+}, Ti^{4+} and Ir^{4+}) and presence of strong spin-orbit coupling at the 3d/5d heteointerface. $BaTiO_3$ is a 3d based TMO with strong correlation (U $\sim$ 5-7 eV) and weak spin-orbit coupling (Δ_{soc} $\sim$ 0.01-0.1eV), whereas the paramagnetic semi-metallic $SrIrO_3$ is a 5d based TMO with modest correlation effect (U $\sim$ 1-3 eV), but having strong spin-orbit coupling (Δ_{soc} $\sim$ 0.2-1eV), which hosts the DM interaction [223, 224, 225, 226, 227, 228]. Recently, it has been shown that ultra-thin 3d-4d based $BaTiO_3$/$SrRuO_3$ interface forms tunable DM interaction due to the ferroelectric proximity effect, thus stabilizing skyrmion features [229]. Therefore, it would be indeed interesting to investigate the 3d-5d based $BaTiO_3$/$SrIrO_3$

heterostructure (with no long-range magnetic order in either of the parent compound) where all these above energy scales may increase collectively to yield the unexpected magnetic phenomena.

Therefore, in this study first we have individually grown $BaTiO_3$ and $SrIrO_3$ thin films. $BaTiO_3$ shows weak ferromagnetic ordering at $T_C \sim 136$ K, due to oxygen vacancies. In contrast, magnetic ordering is found to be absent in $SrIrO_3$. Thereafter, we have grown 3d-5d based $BaTiO_3/SrIrO_3$ heterostructure, showing enhanced magnetic ordering temperature with $T_C \sim 160$ K. Structural, magnetic and chemical characterizations suggest that rather than strain-induced structural distortion in $SrIrO_3$, interfacial charge transfer and strong spin-orbit coupling plays a crucial role in enhancing T_C in relaxed $BaTiO_3/SrIrO_3$ heterostructures.

6.2 Experimental Details

6.2.1 Growth of $BaTiO_3/SrIrO_3$ heterostructures

20 nm $BaTiO_3$ (BTO), 20 nm $SrIrO_3$ (SIO) and their $BaTiO_3/SrIrO_3$ (BTO/SIO) heterostructures are grown on (001) $SrTiO_3$ (STO) substrates by pulsed laser deposition (PLD). Films are grown at ~ 650 °C with a KrF excimer laser ($\lambda = 248$ nm, 20 ns pulse-width) of fluence ~ 2.5 J/cm^2 and repetition rate of 4 Hz. Growth pressure for SIO films have always been kept constant at 100 mTorr. However, for BTO, different oxygen partial pressure are used, with $30 \leq P_{o2} \leq 100$ mTorr with a focus on 50 mTorr. Literature report shows that stoichiometric BTO films could be grown at $P_{o2} \geq 150$ mTorr [230]. Since our primary goal of this work is to induce magnetism via oxygen vacancy in BTO films, therefore we have chosen the above-mentioned P_{o2} during growth of BTO.Film growth has been visualized using in-situ high pressure RHEED as presented in Figure 6.1.

6.2.2 Measurement details

The structural characterization of the films are done by θ - 2θ scans using Cu-K_α ($\lambda = 1.54$ Å) x-ray diffraction (Bruker D2 Phaser Desktop Diffractometer). Reciprocal space mapping (RSM) is carried out using high resolution x-ray diffractometer (Bruker D8 Discover HRXRD). Magnetization with respect to temperature and applied magnetic field is measured using commercial 7T-SQUID-VSM (Quantum Design Inc., USA) system. These measurements were performed with applied magnetic field parallel or in-plane to the film surface (IP). Magnetization vs. temperature was measured following the conventional protocols of zero field cooled warming (ZFC) and field cooled warming (FCW) cycles in the presence of applied magnetic field $\mu_0 H = 100$ Oe. X-ray photoelectron spectroscopy (XPS) was done with a K_α X-ray Photoelectron Spectrometer (Thermo-fisher Scientific Instrument, UK). It was carried out in an ultra-high vacuum chamber (2×10^{-9} mBar)

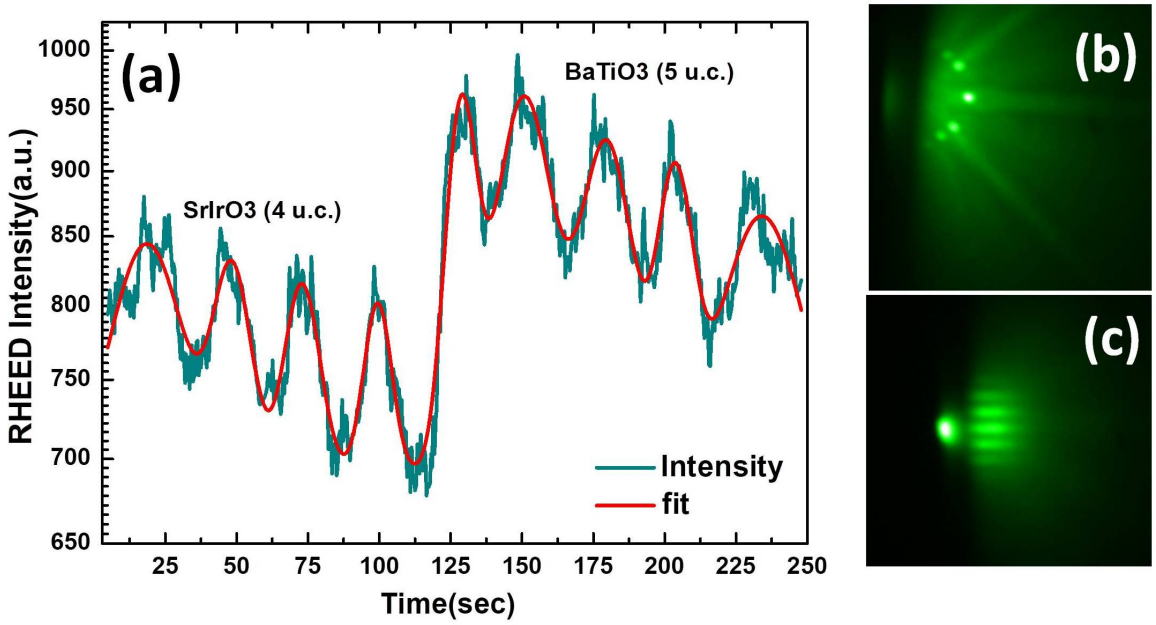

Fig. 6.1 Visualization of BTO/SIO growth.(a) RHEED intensity of BTO(5 u.c.)/SIO(4 u.c.) (b)& (c) RHEED pattern before & after deposition

by using an Al K_α x-ray source with 6 mA beam current (beam spot size on the sample was $\sim$ 400 μm). Before recording XPS, in-situ ion beam etching (energy 1000 eV) was used for 30s to clean off surface contaminations.

6.3 Results and Discussion

6.3.1 Structural details

Figure 6.2 depicts the growth and structure of the $BaTiO_3/SrIrO_3$ hetero-structure on $SrTiO_3$ (001) (STO) single crystalline substrate. The x-ray diffraction θ - 2θ scan of the film along with the substrate has been presented in Figure 6.2 (a). Here we can see that our film is of single phase and oriented along pseudo cubic (001) direction with the both oriented peaks of $SrIrO_3$ (SIO) and $BaTiO_3$ (BTO) as observed before for independent growth of the respective materials [231, 232]. This oriented growth could be explained with the hierarchical small lattice mismatch among STO, SIO and BTO. The pseudo-cubic lattice parameters of the bulk single crystal of the above materials are 3.90 Å, 3.96 Å and 3.99 Å, respectively [231, 232]. The calculated pseudo-cubic lattice parameters of SIO and BTO in our case from the XRD are 3.96 Å and 4.137 Å, respectively, which are in well agreement with the orthorhombic SIO, and the tetragonal BTO film on STO (001) reported in earlier studies [231]. The calculated hierarchical lattice mismatches are (a_{SIO}-

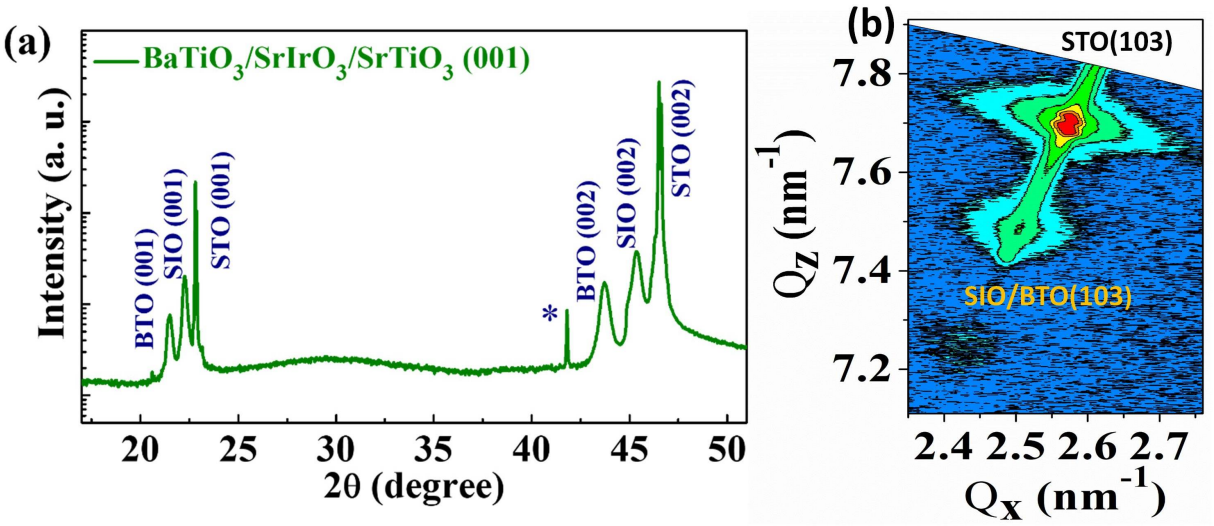

Fig. 6.2 (a) X-ray diffraction θ - 2θ scan of $BaTiO_3$ (20 nm)/$SrIrO_3$ (20 nm) heterostructure grown on $SrTiO_3$ (001) substrate showing the oriented growth of the film. Asterisks are from the substrate. (b) Reciprocal Space Mapping (RSM) showing the relaxed nature of the heterostructure.

$a_{STO})/a_{STO} \sim 2.32$ % and (a_{BTO}-a_{SIO})/$a_{SIO} \sim 3.56$ %. To get a detail insight about the strain and substrate-film epitaxial relationship a reciprocal space mapping (RSM) around asymmetric (103) reflection has been performed as presented in Figure 6.2 (b). Here q_x and q_z correspond to in plane and out of plane direction. From the figure, we can see that our hetero-structure is fully epitaxial and strain relaxed as the film spot has a different q_x than the substrate. Here we cannot distinguish SIO and BTO spots from the overall film reflection (elongated continuous reflection of the film), mostly due to very low in plane lattice mismatch between them.

6.3.2 Magnetic measurements

The temperature dependent magnetization (M-T) measurements for BTO, SIO and BTO/SIO heterostructures have been presented in Figure 6.3 (a). A ferromagnetic-like transition has been observed in BTO film grown at $P_{o2} = 50$ mTorr with magnetic ordering at $T_C \sim$ 136 K. Although it is not so prominent, however we also observed a hump at T $\sim$ 160 K, which may be due some local ordering in BTO. Films grown at other P_{o2} shows absence of any kind of magnetic ordering (Figure 6.9 (a), Appendix). Such a narrow growth window for occurrence of magnetic ordering in BTO is very surprising. Calculation shows that vacancies in BTO is indeed a crucial factor in obtaining high ferromagnetic T_C, as it varies substantially for different vacancy species (O, Ti and Ba) [220]. Intuitively, the origin of ferromagnetism in non-magnetic BTO film is thought to be a consequence of the presence of oxygen vacancies (O_V) inducing double exchange mechanism scenario with hopping

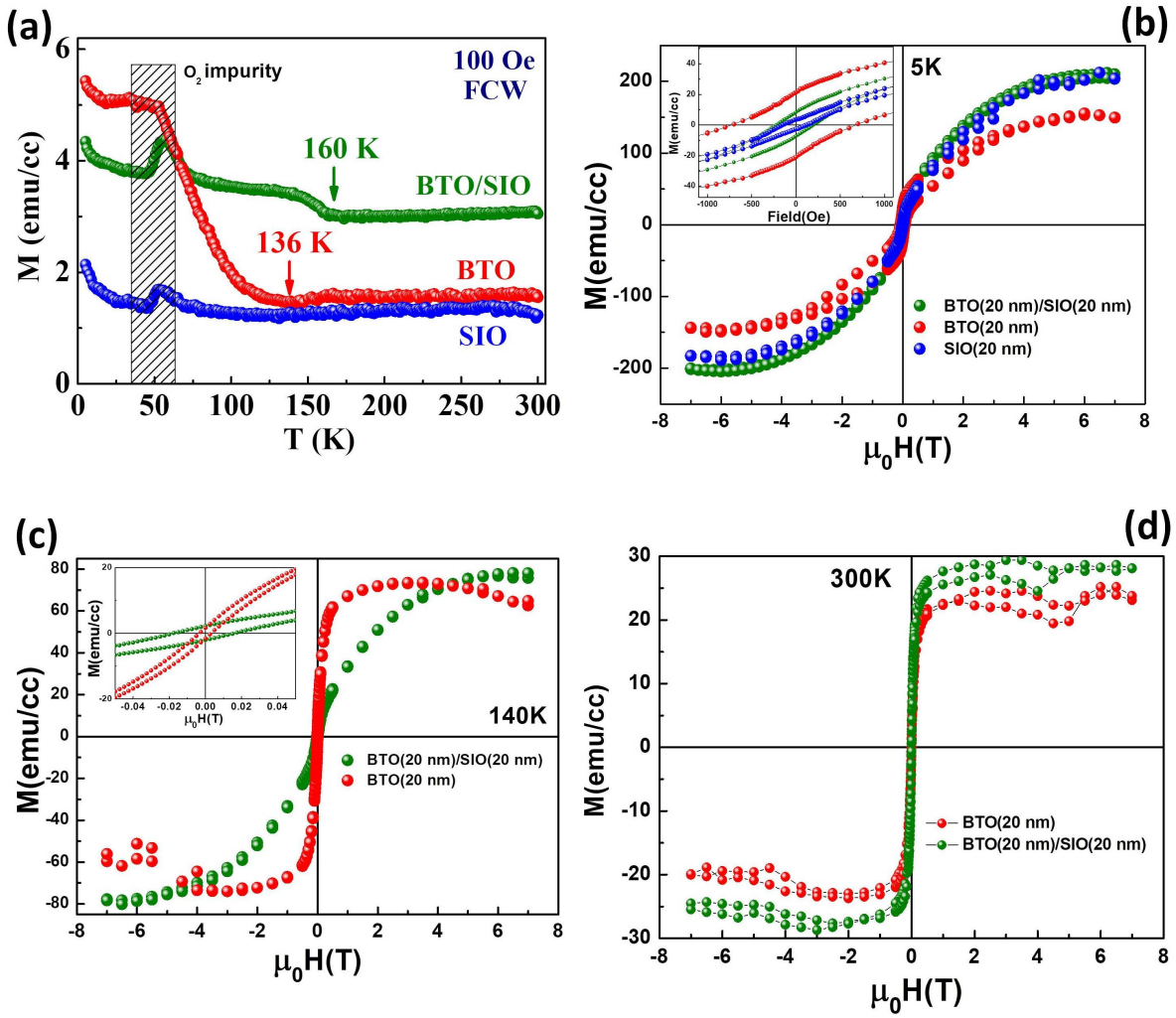

Fig. 6.3 (a) Temperature dependent magnetization (M-T) of BTO/SIO heterostructure along with individual BTO and SIO. The peak at $\sim$ 50 K is the instrumental oxygen artefacts. Asterisk corresponds to the possible local moment ordering. (b)-(d) Field dependent magnetization (M-H) of BTO and BTO/SIO films at various temperatures.

of charge carriers as $Ti^{4-\epsilon}$ -O- $Ti^{3+\epsilon}$, investigated both theoretically and experimentally [217, 218, 219, 220]. Raeliarijaona et al., predicted that T_C due to oxygen vacancy should be $\sim$ 120 K, which is close to our observed value [220]. Considering the T_C, Majumder et al., has reported magnetic ordering in BTO film with $T_C \sim 42$ K [182]. However they grew films on LAO (001) substrate, hence different lattice energy which affected the magnetic T_C. This higher T_C value could be explained with the theoretical framework that predicts O_V induced magnetization in BTO originates from the spin polarization of itinerant electrons at Ti t_{2g} orbitals [220]. Interestingly, below T_C (at T = 77 K), the resistivity is found to be lower ($\sim$ 0.12 MΩ-cm) (Figure 6.4) than the non-magnetic insulating BTO ($\sim$ 10 MΩ-cm) film [233], indicating the presence of itinerant electrons. Additionally, M-T data of 5d based SIO shows paramagnetic behavior without any long-range mag-

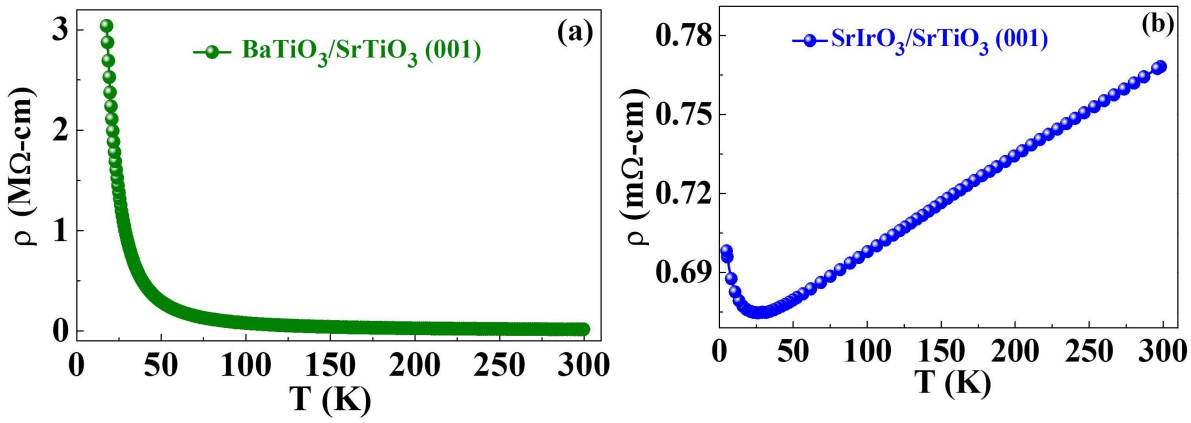

Fig. 6.4 Temperature dependent resistivity of (a) $BaTiO_3$ and (b) $SrIrO_3$ films.

netic ordering (Figure 6.3 (a)) over the whole temperature range, as expected, due to the weak correlation effect in 5d [224, 226]. The resistivity feature is also found to be similar with the reported ones (Figure 6.4). Surprisingly, in case of BTO/SIO heterostructure, in M-T data we also observed weak ferromagnetic ordering but with enhanced ordering temperature ($T_C \sim 160$ K). For clarity, we present the derivative of the magnetization ($\delta M/\delta T$) data (Figure 6.8, Appendix) which clearly shows the presence of magnetic ordering at $T_C \sim 136$ K (for BTO) and $T_C \sim 160$ K (for BTO/SIO). Since, for both BTO and BTO/SIO, the growth conditions were kept similar, therefore this remarkable 40 K enhancement in T_C is not only due to the changes in electronic configuration ($Ti^{4-\epsilon}$ -O-$Ti^{3+\epsilon}$) in BTO, but also due to the presence of additional interaction(s) at the BTO/SIO interface. Interestingly, from M-T data it is clearly seen that low temperature moment in BTO/SIO heterostructure is lower than the parent BTO. This is consistent with the fact that, wider 5d-orbitals and weak correlation effect affect the spin-alignment, thus reducing the net magnetic moment. For further confirming the appearance of magnetic ordering, the isothermal magnetization measurements (M-H) at T = 5K, 140 K and 300 K (Figure 6.3 (b)-(d)) have been performed. M-H data shows that for BTO film, saturation moment (M_S) increases with lowering the temperature and at T = 5K it becomes maximum ($M_S \sim 150$ emu/cc) (Figure (b)). At T = 5K, coercive field (H_C) of the BTO heterostructure is ~ 675 Oe (Figure 6.3 (b)). For BTO/SIO heterostructure, however the M_S is higher at T= 5K, but interestingly, M_S at T= 300 K was found to be slightly higher than at T = 140 K (Figure 6.3 (c)). At T=5 K, coercive field (H_C) of the BTO/SIO heterostructure ($H_C \sim 200$ Oe) is lower than the only BTO film ($H_C \sim 675$ Oe). This confirms the presence of weak ferromagnetic or canted anti-ferromagnetic ordering in BTO/SIO with $T_C \sim 160$ K. Interestingly, even for BTO/SIO heterostructure, the magnetic ordering is found only in films grown at $P_{o2} = 50$ mTorr (Figure 6.9 (b),Appendix), as similar observed in case of parent BTO (Figure 6.9 (a),Appendix). This indicates that indeed growth pressure is a crucial factor and importantly the BTO and SIO film quality in BTO/SIO remains as

similar as parent BTO or SIO, thus ruling out the possibility of extrinsic effects for the enhanced T_C.

The possible interaction scenarios affecting the magnetic T_C could be as followings. (1) In BTO, there already exists a double exchange $Ti^{4-\epsilon}$ -O- $Ti^{3+\epsilon}$ interaction as discussed earlier. (2) Additionally, due to the presence of Ir^{4+}, there could exists another possible interaction pathway i.e. Ti^{4+} -O- Ir^{4+}, which is attributed with the hopping of Ir^{4+} $5d^5$ charge carriers from t_{2g} orbital to the vacant t_{2g} of Ti^{4+} $3d^0$ orbital as a super exchange interaction. (3) Moreover, an interfacial transfer from Ir^{4+} to Ti^{3+} could also be possible, as similar to observed case of interfacial charge transfer from Ir^{4+} to Mn^{3+} in iridatemanganite heterostructure [234]. All these couplings possibly yields in enhancement of T_C in the BTO/SIO heterostructure. Importantly, strong spin-orbit coupling (5d) also host the DM interaction (forming chiral interaction between two atomic spins) [213, 214], which may also affect the exchange interaction energy and enhancement in T_C [215]. Recently, in SIO based superlattices, canted anti-ferromagnetic ordering has been observed due to the structural distortion in SIO, resembling to the canted anti-ferromagnetism in Sr_2IrO_4 [235]. However, in our case RSM data shows that BTO/SIO film is fully relaxed (Figure 6.2 (b)) and SIO is non-magnetic as shown earlier (Figure 6.3 (a)). This clearly indicates that indeed the major factors playing role for occurrence of magnetism and its enhancement is the charge transfer process, rather than strain effect.

6.3.3 Electronic structure and interface

To investigate the presence of all these above-mentioned electronic structure (Figure 6.5) and chemical states (i. e. O_V, Ti^{4+}, Ti^{3+}, and Ir^{4+}) responsible for various form of interfacial couplings, we performed the X-ray photoelectron spectroscopy (XPS). For parent BTO film, in O 1s XPS, along with the lattice oxygen peak (at $\sim$ 530.1 eV) we also observed an additional peak (at $\sim$ 532.3 eV), which corresponds to O_V (Figure 6.6 (a)) [217]. Now, in BTO, if oxygen vacancies exist then it will lead to the occurrence of Ti^{3+}, to compensate the charge imbalance. Consistently, in Ti 2p XPS, along with the characteristic Ti^{4+} (with universal spin-orbit peak splitting of $\sim$ 5.7 eV), we also observed the Ti^{3+} states (Figure 6.6 (b)).These features confirms the oxygen vacancy induced ferromagnetism in BTO with the double exchange hopping mechanism of charge carriers i.e. $Ti^{4-\epsilon}$ -O- $Ti^{3+\epsilon}$ [217, 220].

For the BTO/SIO heterostructure, O 1s and Ti 2p XPS are almost similar to the parent BTO film, again confirms that BTO film quality in BTO/SIO heterostructure is as similar as parent BTO (Figure 6.6 (c) and (d)). In order to probe the interfacial charge transfer process (between 3d Ti and 5d Ir) in BTO/SIO heterostructure, we performed the depth-dependent XPS of Ti 2p and Ir 4f, with varying thickness of top BTO film while keeping

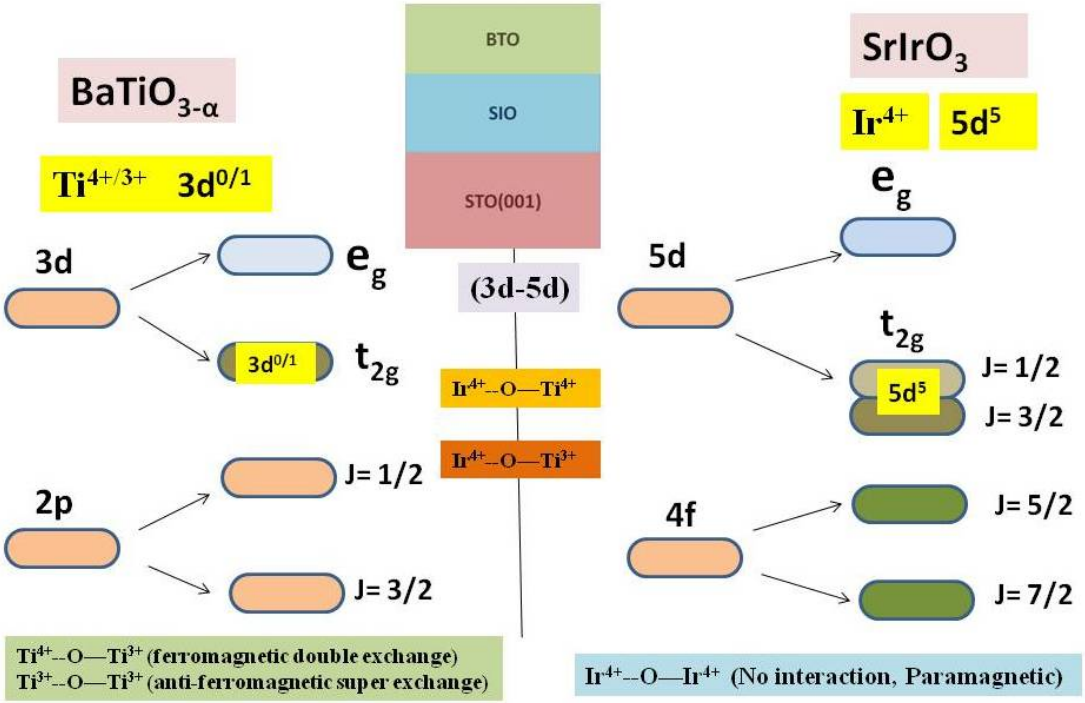

Fig. 6.5 Schematics of electronic structure for $BaTiO_3$ and $SrIrO_3$, along with the magnetic interactions present in the system

the thickness of bottom SIO film constant (Figure 6.6 (e) and (f)). From the electronic band structure, for 5d-Ir, t_{2g} band is close to the 4f $J_{5/2}$ band [214], whereas for 3d-Ti, the 3d t_{2g} is close to 2p $J_{1/2}$ band [236]. Thus while probing Ti 2p and Ir 4f, these two sub-bands should be affected if electronic reconstructions to occur at the interface. Moreover, due to the wider d-orbitals of 5d than 3d, the effect should be more prominent in 5d Ir-site. As shown in Figure 6.6 (e), the relative intensity of $4f_{5/2}$ (which is proportional to the electronic population) decreases while probing interfacial Ir, with line shapes showing significant changes along with coverage, reflecting the electronic charge redistribution at Ir-site. In addition, binding energy of $4f_{5/2}$ shifts towards higher value ($\sim$ 1.3 eV) for BTO/SIO with respect to the parent SIO. In contrast, Ti $2p_{1/2}$ binding energy shifts negligibly towards higher value ($\sim$ 0.1 eV) while probing interfacial Ti (Figure 6.6 (f)). In addition, the change in the relative intensity is not so prominent for Ti $2p_{1/2}$ [237], possibly due to low overlapping of 3d orbitals in presence of strong crystal field. These observations suggests the charge transfer process at the interface with the effect of all relevant energy parameters causing the magnetic coupling between 3d and 5d ions and hence changing the T_C.

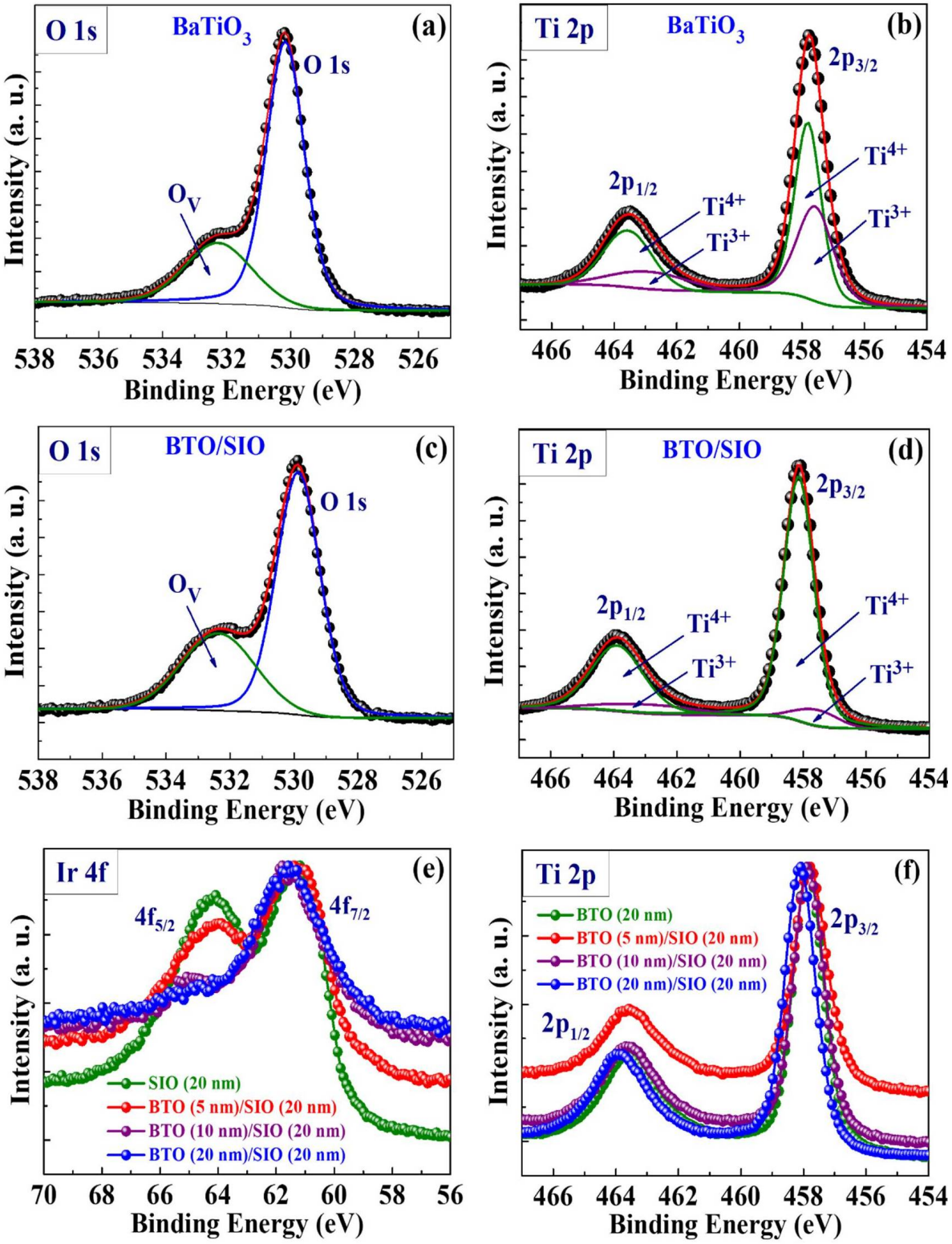

Fig. 6.6 (a), (b) XPS of O 1s and Ti 2p of BTO film.(c), (d) O 1s and Ti 2p edge XPS spectra of the BTO/SIO heterostructure. (e) Ir 4f and (f) Ti 2p XPS spetra for various thiknesses of BTO/SIO heterostcrutrues, with constant SIO thickness (20 nm), to probe the interface.

6.4 Appendix

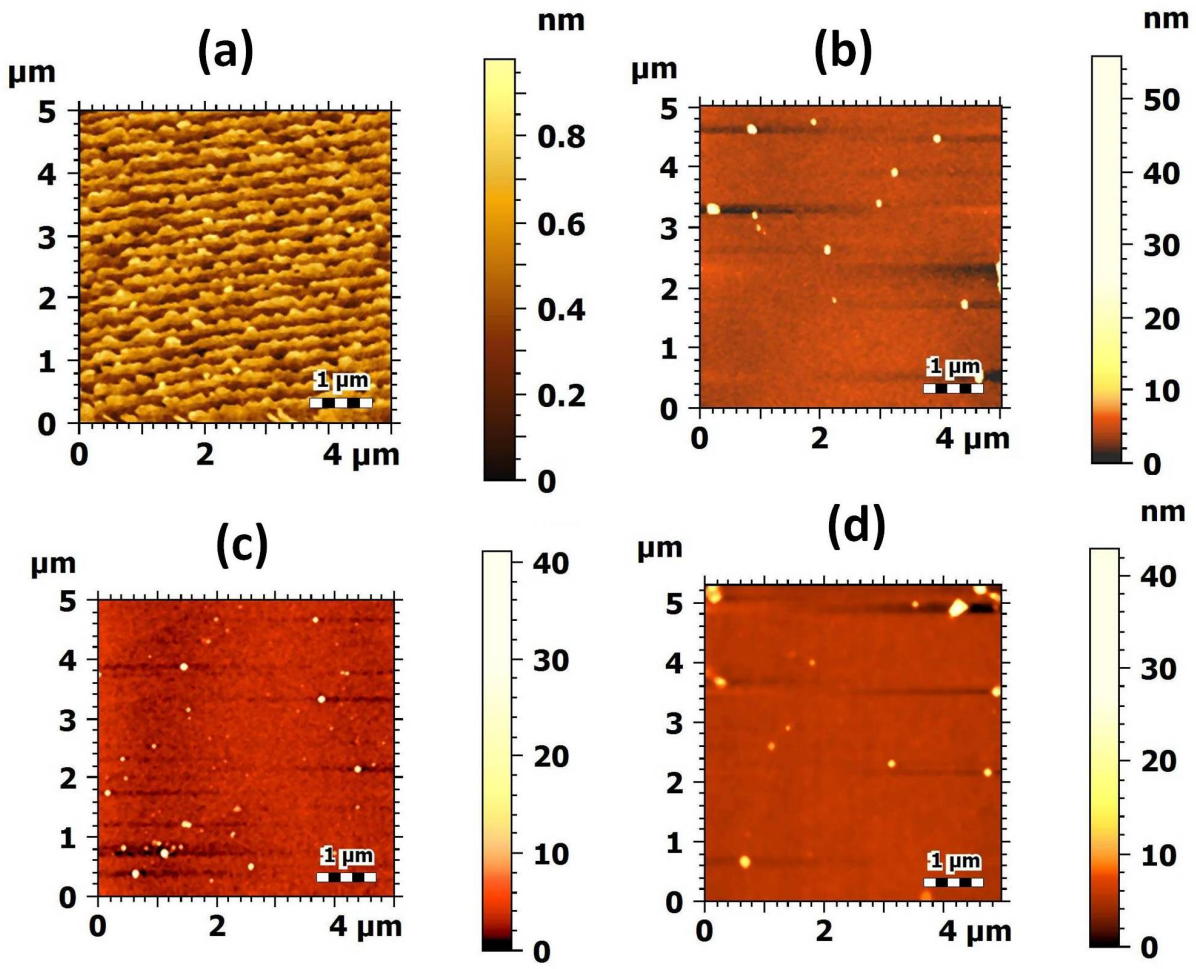

Fig. 6.7 Atomic Force Microscopy image of (a)STO(001) substrate with atomic steps and RMS surface roughness of 0.4 nm (b) SIO film with RMS surface roughness of 1.1 nm (c) BTO film with RMS surface roughness of 1 nm (d)SIO/BTO heterostructure with RMS surface roughness of 1 nm.

6.5 Conclusions

In summary, we have grown 3d-based $BaTiO_3$, 5d-based $SrIrO_3$ and 3d/5d based heterostructures $BaTiO_3/SrIrO_3$ by PLD. Parent $BaTiO_3$ shows weak ferromagnetic ordering at $\sim$ 136 K, consequence of oxygen vacancies, whereas $SrIrO_3$ is paramagnetic. Remarkably, BTO/SIO shows enhanced magnetic ordering temperature with $T_C \sim 160$ K. This remarkable enhancement is attributed with the interfacial charge transfer and the presence of strong spin-orbit coupling. We establish the presence of two new plausible interactions in the system namely Ti^{4+} -O- Ir^{4+} and Ti^{3+} -O- Ir^{4+}. Most likely one is ferromagnetic and other is antiferromagnetic. Although, in-depth microscopic measurements are neces-

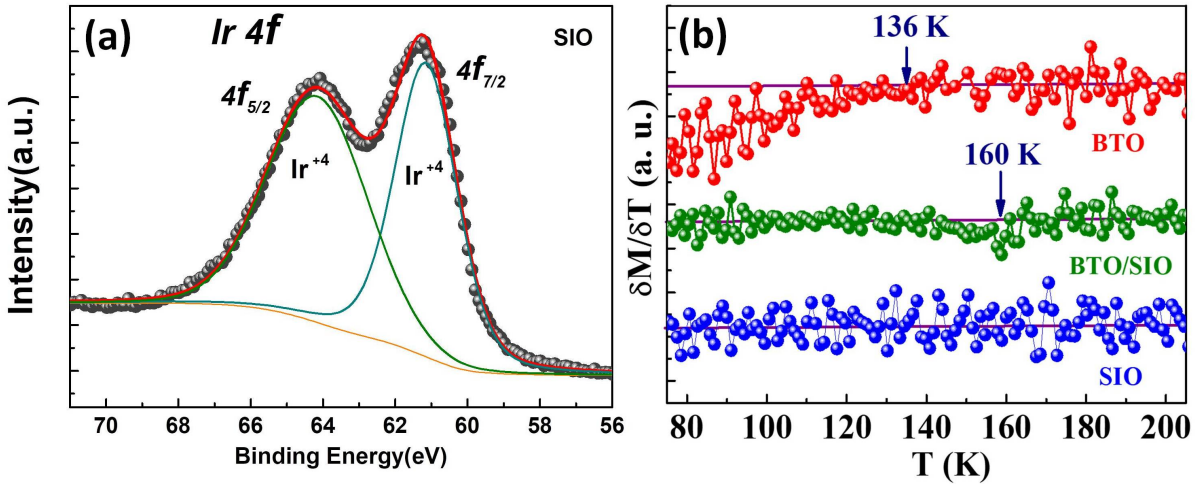

Fig. 6.8 (a) XPS spectra of Ir 4f in parent $SrIrO_3$ showing the presence of Ir^{4+} (b) Derivative of magnetization with temperature ($\delta M/\delta T$) shows the magnetic transitions of the discussed samples.

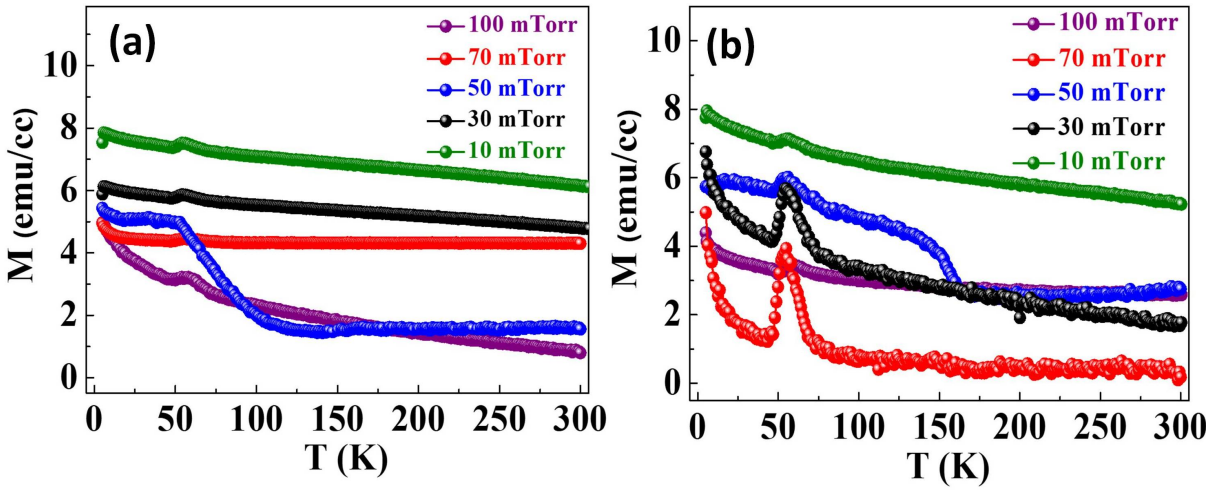

Fig. 6.9 Temperature dependent magnetization (M-T) of (a) BTO and (b) BTO/SIO heterostructures grown at various oxygen pressure (P_{o2}). Magnetic ordering is observed only for film grown at P_{o2} = 50 mTorr. The peak at $\sim$ 50 K is the instrumental oxygen artefacts.

sary to quantify the dominant interaction mechanism(s); nevertheless, our study provides an avenue to tune magnetic T_C in oxide thin film heterostructures.

CHAPTER 7

Summary and Future Outlook

The field of Oxide Thin films has come a long way from its childhood days and has become one of the most active areas of research within condensed matter physics. Our work presents a few interesting findings on polar and magnetic ordering in such systems: *How epitaxial strain and partial disordering lead to novel structural phase along with magnetic and ferroelectric ordering that are inaccessible or absent in bulk materials.* We have focused on three distinct perovskite material systems namely h-$TbMnO_3$, Tb_2CoMnO_6 and $BaTiO_3/SrIrO_3$.

To summarize the brief interesting outcomes and scope of this thesis

- ***A recently discovered hexagonal phase of conventional magneto-electric o-$TbMnO_3$:*** This hexagonal phase is strain stabilized in thin films and does possess geometrical ferroelectricity at room temperature. This thesis presents the growth of high quality epitaxial strain stabilized hexagonal phase of $TbMnO_3$ films on YSZ(111) substrate and their structural transformations analyzed by means of various ex- and in-situ characterization techniques. Our deposition technique and procedure results a way better growth of this artificial metastable phase in terms of single crystalline quality as well as the sharpness of substrate-film interface of h-$TbMnO_3$/YSZ(111) films. Detail combined high temperature measurements such as Transmission Electron Microscopy, Raman Spectroscopy and Optical ellipsometry point out the ferroelectricity $T_C \sim 800$ K and a structural phase transition from

$P6_3cm$ to $P6_3/mcm$ structure for the first time. The results & findings have been published in ***Physical Review B 102, 104106 (2020)***.

- ***Magneto-Dielectric properties of partially B-site ordered monoclinic Tb_2CoMnO_6 double perovskite thin film epitaxially grown on Nb:$SrTiO_3$ (001) substrates for the very first time by metalorganic aerosol deposition (MAD) technique:*** Transmission electron microscopy and electron energy loss spectroscopy mapping shows the presence and distribution of both Co^{2+} and Co^{3+} ions in the film, evidencing a partial B-site disorder, which was further confirmed by the observation of reduced saturation magnetization at low temperatures. The ferromagnetic Curie temperature, $T_C = 110$ K, is slightly higher as compared to the bulk value (100 K) probably due to an in plane epitaxy tensile strain. Temperature dependent dielectric study reveals an unexpected high temperature dipolar relaxor-glass-like transition at a temperature $T^* \sim 190$ K $> T_C$, which depends on the applied frequency and indicates a superparaelectric behavior. Two different dielectric relaxation peaks have been observed; they merge at T^* where likely a coupling to the disorder-induced short range charge-spin correlations results in a 4% magneto-dielectric coupling. The presented whole content and findings have been published in ***Physical Review B 101, 094426 (2020)***.

- ***The growth of 3d-5d based relaxed $BaTiO_3/SrIrO_3$ heterostructures, to obtain emergent phenomena arising from the interfacial coupling between B-site (Ti^{4+}; $3d^0$ and Ir^{4+}; $5d^5$) cations:*** Parent $BaTiO_3$ film shows weak ferromagnetic ordering at $T_C \sim 136$ K, due to the oxygen vacancies, in contrast of paramagnetic nature in strong spin-orbit coupled $SrIrO_3$ film. Interestingly, in $BaTiO_3/SrIrO_3$ heterostructure we observed magnetic ordering at $T_C \sim 160$ K. X-ray photoelectron spectroscopy of O 1s and Ti 2p reveals the presence of oxygen vacancies and Ti^{3+} states in $BaTiO_3/SrIrO_3$, similar to the parent $BaTiO_3$. However, significant changes in Ir 4f spectrum line shape with coverage has been observed in $BaTiO_3/SrIrO_3$, in contrast of parent $SrIrO_3$. Therefore, this remarkable enhancement in T_C is attributed with the interfacial charge transfer process and the presence of strong spin-orbit coupling. We establish the presence of two new plausible interactions in the system namely Ti^{4+} -O- Ir^{4+} and Ti^{3+} -O- Ir^{4+}. The outcomes and results are ***Under Preparation*** for submission.

As a future outlook we would like to continue the following

- With a suitable bottom electrode we would like to the study the room temperature polarization switching with external electric field in hexagonal $TbMnO_3$. A Pt electrode on Al_2O_3 (0001) or YSZ (111) could be useful in this respect. Also a temperature dependent study of second harmonic generation (SHG) is planned to

be carried out for the detail study of the dipole dynamics while interacting with photon.

- We would like to study a detail phase diagram of the ferroelectric relaxor glass transition with respect to the degree of B site ordering in Tb_2CoMnO_6. This study could be carried in a series of films deposited in different oxygen partial pressures or tuning the Co:Mn ratio in MAD technique. We would also like to explore the growth on STO (111) substrate. It will be fantastic to see the (111) growth with super-lattice peak.

- With the recent discovery of the ferroelectrically tunable magnetic skyrmion in $BaTiO_3/SrRuO_3$ heterostructure,we would like to study the same in our $BaTiO_3/SrIrO_3$ system. Ir as a 5d element with more strong spin orbit coupling and $BaTiO_3$ with magnetic ordering it will be interesting to study if we could tune the skyrmion dynamics with both external electric and magnetic field. Currently we are trying to grow the $BaTiO_3/SrIrO_3$ superlattice to understand the interfacial charge transfer in detail.

Appendices

APPENDIX A

Ferromagnetism and Transport in $B_XC_YN_Z/Al_2O_3$ thin films

Boron carbonitride ($B_XC_YN_Z$) represents an interesting family of materials containing all light elements and two dimensional graphene like hybrid layers. In this work, we have grown thin films of this compound using Pulsed Laser Deposition (PLD) method, and investigated their magnetic and transport properties in their entirety along with the detailed electronic structure using various spectroscopic techniques. In depth analysis of the typical role of dopants and defects, especially the prevalent nitrogen defects, is elucidated using Density Functional Theory (DFT) calculations to understand the experimental observations. A dramatic crossover in the transport mechanism of charge carriers is observed in this system with the change in doping level of specific nitrogen defects. A robust and high saturation magnetization is achieved in BCN films which is higher by almost hundred times as compared to that in similarly grown undoped carbon film. The content of this chapter has been published in ***Journal of Magnetism and Magnetic Materials 479 (2019), 67-73***.

A.1 Introduction

Possible tuning of magnetism & electronic structure among the different forms of carbon has attracted significant attention of experimentalists and theorists for several decades [238, 239]. One of the most significant efforts in this context is directed towards inducing a magnetic moment by chemical incorporation of one or more of dopants or defects in the carbon system [240, 241, 242, 243, 244, 245]. Surface functionalization by adatoms or development of interfacial systems with other functional non-magnetic materials provide alternate options for inducing magnetism [246]. Further, finite carbon nanostructures provide interesting opportunities to generate tunable magnetism in carbon forms via incorporation of vacancies [247, 248], voids, line defects [249] particularly zigzag edges which are responsible for the ferromagnetic ordering via edge states[250, 251, 252, 253]. Magnetism derived from doped carbon sheets have attracted attention as a robust, scalable and practical solution to this phenomenon. Hybridizing graphene with h-BN layers, nitrogen or h-BN doped graphene, and the novel 2D material $B_XC_YN_Z$ have drawn significant attention lately in terms of the manipulation of their electronic as well as magnetic properties. Several insightful and interesting experimental and theoretical studies have also been performed on the hybridization and doping scenario of h-BN and N in graphene or graphite system predicting the possible ferromagnetism and tunability of band gap [254, 255, 256, 257, 258, 259, 260, 261, 262]. The fundamental role of nitrogen defects in powdered graphene resulting the magnetic ordering has also well attended experimentally [263, 264, 265, 266]. In many of the experimental studies chemical synthesis routes [267, 268, 269, 270] have been used which are suitable for some specific domains as application such as supercapacitor, CO_2 reduction and hydrogen evolution reaction etc [271, 272]. The possibility of hybridization of graphene with hexagonal BN layers in thin film format through vapour phase deposition [273, 274, 275, 276], tunable electrical and electronic behaviours are also well studied [277, 278]. Here in this study, we have explored the possibility of realizing ferromagnetic ordering and realizing its connection with the chemistry of dopant and electronic states in nitrogenated turbostratic carbon films deposited with pulsed laser deposition (PLD) technique. This approach and the thin film form of the material is suitable for many key analyses of transport, magnetism along with structural properties; also being ready at the same time for device fabrication. The immense strength of stoichiometry-tunability of the PLD technique is already well established in numerous studies on many materials and already used to grow BCN films [279, 280]. Our ammonia assisted reactive PLD growth approach for better nitrogen incorporation in the $B_XC_YN_Z$ system, a comprehensive multi-technique (XPS, XANES and Raman spectroscopy) analytical experimental study combined

with detailed Density Functional Theory based theoretical support for the specific experimentally targeted regime of materials stoichiometry are the new aspects of this study vs the reported works. Specifically, we have restricted to high nitrogen, low boron doping regime. An in depth analysis brings out the key role of pyridinic and triazinic defects in magnetic ordering observed up to room temperature. Carrier transport is also significantly influenced by the defects and doping concentrations resulting in an interesting crossover in the transport mechanism for a critical doping concentration. Importantly, we further demonstrate that a substantial presence of B and N dopants can lead to an order of magnitude enhancement of saturation magnetization in carbon films.

A.2 Experimental and Computational details

Resistivity measurements are performed by conventional four-probe method within the temperature range of 5 K- 300 K. Magnetization with respect to temperature and applied magnetic field is measured using commercial 7T-SQUID-VSM (Quantum Design Inc., USA) system. These measurements were performed with applied magnetic field parallel or in-plane to the film surface (IP). Magnetization vs. temperature was measured following the conventional protocols of zero field cooled warming (ZFC) and field cooled warming (FCW) cycles in the presence of applied magnetic field μ_0H = 100 Oe. The spin-polarized density functional theory (DFT) calculations [281, 282] were performed within the projector augmented wave formalism, [283] for a plane-wave basis with a kinetic energy cut-off of 600 eV using Vienna ab-initio simulation package. The exchange-correlation energy was computed using the Perdew-Burke- Ernzerhof (PBE) form of generalized gradient approximation (GGA) [284]. The lattice and ions were relaxed until the Hellman-Feynmann forces met the relaxation criteria of 0.015 eV/. The Brillouin zone was sampled using a Γ-centered 8×6×1 k-grid, and a dense mesh of Γ-centered 24×18×1 k-grid was used for the evaluation of density of states (DOS). Nitrogen and boron atoms were doped in a rectangular supercell of graphene containing 48 carbon atoms. The periodic images of the supercell along the direction of vacuum were separated by 12 Å. The self-interaction error inherent to GGA functional results in spurious electron delocalization and incorrect magnetic solutions for both defects and dopants in graphene.To remedy this, we calculated the electronic and magnetic properties using the strongly constrained and appropriately normed (SCAN) meta-GGA functional [285]. Room temperature Raman Spectra are recorded on films using an upright confocal LabRAM HR 800 Raman Microscope (HORIBA Jobin Yvon SAS, rue de Lille, France) with 488 nm laser excitation. X-ray photoemission spectroscopy (XPS) measurements were performed using Al-K_α (E = 1486.7eV) lab-source. X-

ray absorption near-edge structure (XANES) spectra at C, B and N K-edges were collected in total electron yield (TEY) mode. Room temperature valence band spectrum (VBS) was recorded with photon energy hν = 40 eV. Both XANES and VBS are performed using synchrotron radiation source at RRCAT, Indore at integrated photoemission spectroscopy beamline (BL-02) in INDUS-1 and polarized light soft X-ray absorption spectroscopy beamline (BL-01) in INDUS-2, respectively. Before recording the XPS, VBS and XANES spectra, the sample surface is sputtered using high energy Argon ions inside the chamber where base pressure is maintained at 1 $\times 10^{-10}$ mbar in order to expose the uncontaminated surface

A.3 Growth and structure of $B_X C_Y N_Z$ thin films

BCN films of thickness about 500 nm are deposited on r-cut Al_2O_3 single crystal substrates using pulsed laser deposition (PLD) method employing a KrF excimer laser (λ = 248 nm) at a frequency 10 Hz and an energy density 2.5 J/cm^2. PLD target pellets were made by manual mixing of h-BN and graphite powders (Sigma-Aldrich USA) in different atomic ratios and pressing them at high pressure. For example, BCN-90 indicates the target is composed of 90 at.% carbon and 10 at.% h-BN. We have made three sets of BCN films namely BCN-90, BCN-98 and BCN-100. All depositions were performed at the substrate temperature of 750°C and in the presence of ammonia-argon gas mixture (30% ammonia) with chamber pressure of 10^{-1} mbar. Pure carbon film was also deposited in vacuum with base pressure 10^{-6} mbar. All films were annealed for 15 minutes at the growth temperature after deposition and cooled naturally. The detailed electronic structure has been explored using various spectroscopic techniques like X-ray photoelectron spectroscopy (XPS), X-ray absorption near edge spectroscopy (XANES) and Raman Spectroscopy.

A.3.1 X-ray photoelectron spectroscopy (XPS)

Here we present and discuss the results of x-ray photoelectron spectroscopy (XPS) performed on two BCN thin films of different stoichiometries along with a carbon film, all grown by the pulsed laser deposition (PLD) technique, in ammonia atmosphere. The deposition of pure carbon film in ammonia was performed to serve as a reference for the degree of incorporation of nitrogen from the ambient during deposition as well as the specific role of boron on the film growth and stoichiometry. First we discuss the stoichiometry analysis based on the total areas of the fitted components, presented in Table-A.1.

From the elemental analysis, the N:C ratio in BCN-100 (No BN in the PLD target) is 0.12 which implies that 12 at.% nitrogen gets got incorporated or fixed into the

Table A.1 Stoichiometry analysis from XPS fitting

Sample	PLD Target content	B 1s area	C 1s area	N 1s area	N:C	B:C
BCN-90	90 at.% graphite + 10 at.% BN	747	9069	3114	0.34	0.08
BCN-98	98 at.% graphite + 2 at.% BN	283	11760	1807	0.15	0.02
BCN-100	100 at.% graphite + 0 at.% BN	–	12557	1037	0.08	–

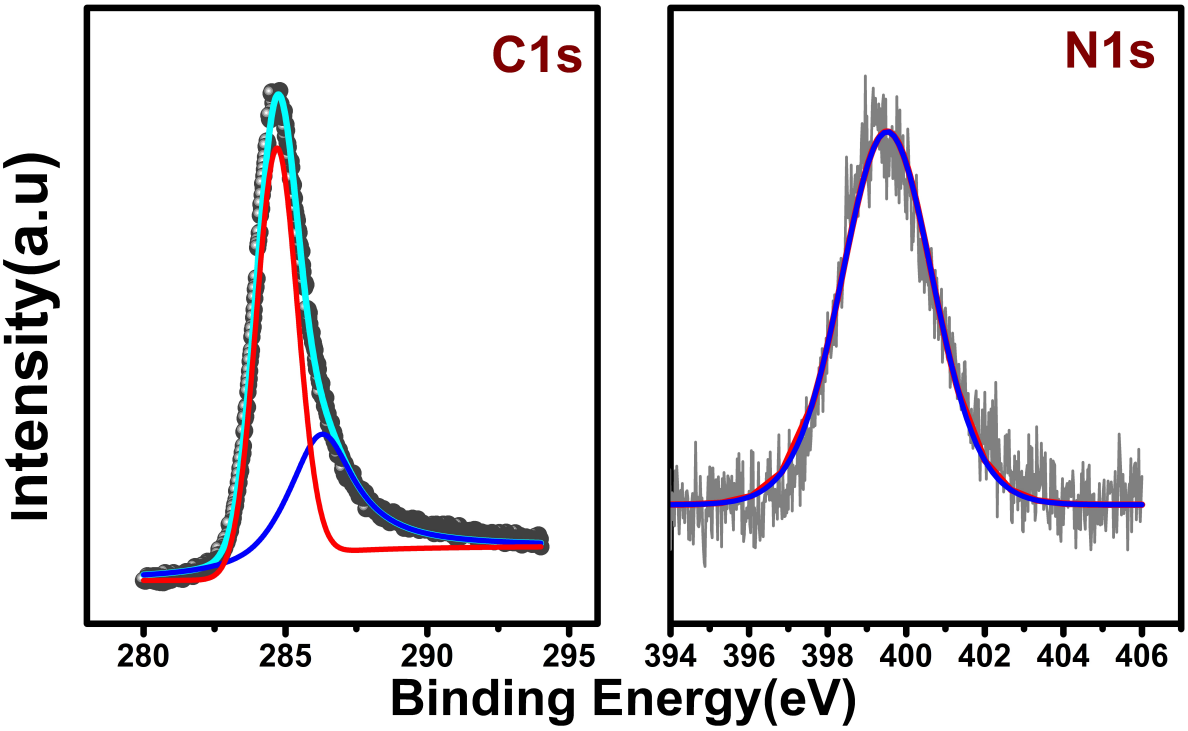

Fig. A.1 C1s and N1s core x-ray photoelectron spectra of BCN-100

film from the gas phase ammonia during deposition. For BCN-98 (which has 2 at.% BN in the target) the ratio is a bit higher, as expected, due to the nitrogen contributed by the target in addition to that entering from the gas phase. In the BCN-90 case we can see significant incorporation of nitrogen (34 at.%). This is more than the algebraic addition of 12 at.% entering from the gas phase and 10 at.% contributed by the target. This implies that boron helps in fixing nitrogen into the growing film. Now we turn to the analysis of chemical states/bonding. In Figure-A.1 for the BCN-100 case the C1s spectrum can be deconvoluted into two peaks. The peaks at 284.7 eV and 286.3 eV correspond to sp^2 C-C and C-N bonds, respectively. These peaks are very similar to those reported in Carbon Nitride films [286]. The N1s spectrum was fitted to a symmetric Gaussian form with the centre at 399.5eV implying significant contribution of C-N bonds in the sample, as expected. Figure-A.2 (a) and (b) show XPS core level spectra of C 1s, B 1s and N 1s for

the BCN-90 and BCN-98 films, respectively. In both the B1s spectra the feature is composed of two deconvoluted peaks. For the BCN-90 case the peaks are at 190.4 eV and 191.9 eV. The peak at lower energy corresponds to B-C bonds, while the peak at higher energy corresponds B-N bonds; as the electronegativity difference between B and C is lower than B and N [287]. For the BCN-98 case the peak for the B-C bond is shifted to 189.6 eV and the peak for the B-N bond is shifted to 192.4 eV. As the carbon concentration is more in this case, boron is likely to be bonded with carbon rather than nitrogen. The electronegativity of carbon is lower than nitrogen and hence the B-C bond energy gets shifted to lower side. For the same reason the bond energy for B-N is shifted to higher value as carbon is more electronegative than boron and it perturbs the B-N bond formation. Also, from the peak area it is clear that for the BCN-90 case the B-N bond formation is more favoured than the B-C bond formation, while in the BCN-98 case they are equally favourable. The whole feature is entirely different from the reported B1s spectra of h-BN [288] and hence one can conclude that there is no h-BN domain formation in both the cases. The C1s spectra can also be deconvoluted into 3 peaks. For the BCN-90 case these peaks are located at 284.6 eV, 285.6 eV and 288.5 eV, which correspond to C-C, C-N, and C-B bonds, respectively [289]. The peak for the C-C bond is close to the peak observed for sp2 C-C bond in graphite at 284.9 eV. For the BCN-98 sample the peaks are slightly shifted towards lower energy due to the presence of less nitrogen which is highly electronegative. From the peak area analysis it is clear that the main contribution is from the C-C bond due to the presence of large amount of carbon. Next is the contribution from C-N bond and for both the cases small amount of Boron contributes to the C-B bond density, which is less in BCN-90 sample than in BCN-98. The N1s spectra are also composed of two deconvoluted peaks. For BCN-90 the peaks are at 399.3 eV and 401.1 eV. The peak at lower energy corresponds to the C-N bond and the peak at higher energy corresponds to the B-N bond. In the BCN-98 case the peak positions are almost the same as the chemical shift of 0.1 eV. Due to the presence of significant amounts of carbon and nitrogen in the system the C-N peak is prominent in both the cases and very close to the C-N peak observed in carbon nitride films at 399.8 eV in the form of sp^2 coordinated pyridine like nitrogen [286]. As the presence of Boron is more in BCN-90, the B-N peak is also prominent in comparison with the BCN-98 case. From the peak area analysis of the XPS data, it can be concluded that in both the BCN-90 and BCN-98 samples the amount of the bond formation is in order of C-C > C-N > B-N > B-C and that is reasonable as predicted from the theoretical model of BCN [290]. For the BCN-98 case B-C is more favoured than B-N. Since the bonding nature of nitrogen is not fully and clearly understood from the XPS results, we resorted to the x-ray absorption near edge spectroscopy (XANES) measurements which give more detailed information

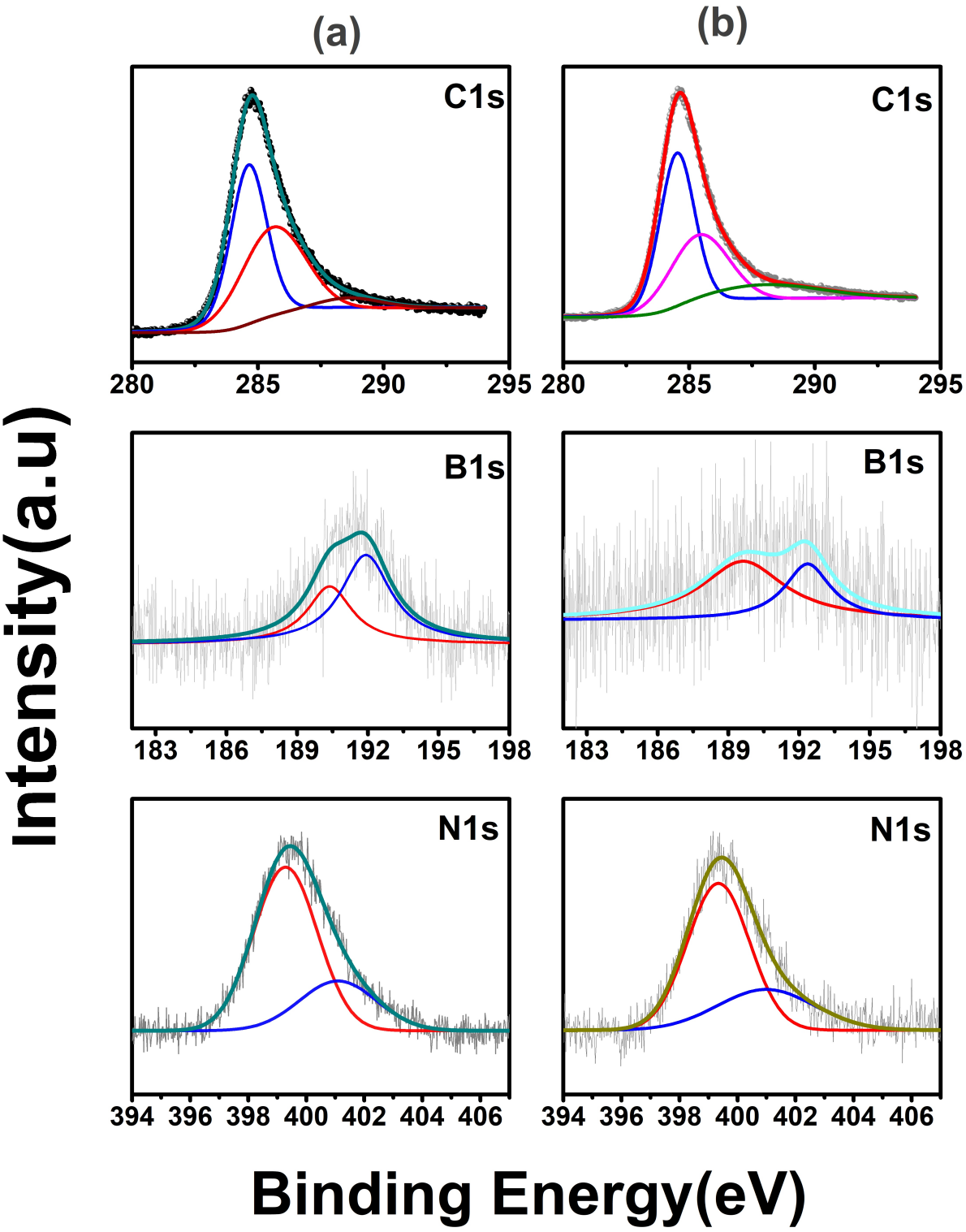

Fig. A.2 C1s, B1s and N1s core x-ray photo electron spectra of (a) BCN-90 and (b) BCN-98

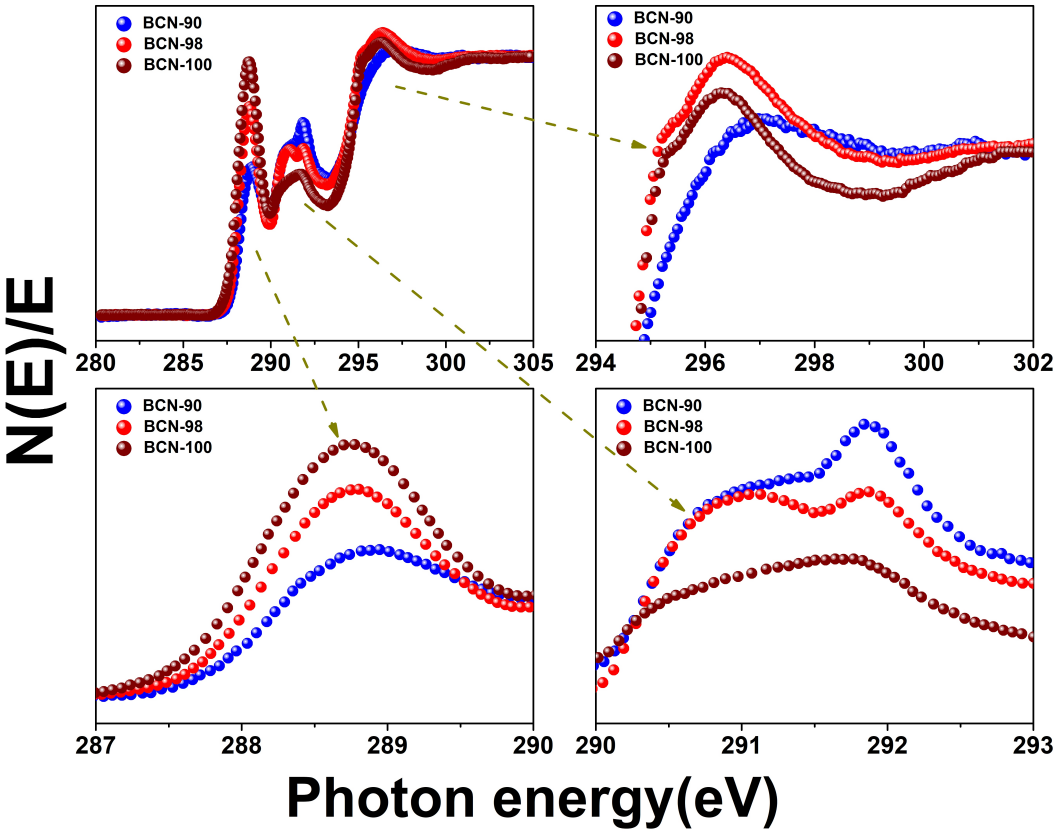

Fig. A.3 X-ray near edge spectra for Carbon K edge of BCN-90, 98 and 100

Table A.2 XANES peak analysis

Carbon K edge	I($\sigma(1)^*$)	I($\sigma(1)^*$)	I($\sigma(1)^*$)/I(π^*)	I($\sigma(2)^*$)/I(π^*)
BCN-90	0.75	1.03	1.25	1.77
BCN-98	0.65	1.10	0.79	1.34
BCN-100	0.55	1.06	0.56	1.11

about the local environment, as discussed in the next sub-section.

A.3.2 X-ray absorption near edge spectroscopy (XANES)

Now we present and discuss the x-ray absorption near edge spectra (XANES) for the carbon K edges for the three samples of interest. Many theoretical and computational approaches using Dipole Approximation, Quasi Particle Model and Multiple Scattering Theory are able to explain the experimental features successfully to certain extent [291]. Due to physical complexity in the real experimental scenario comparative study or analysis of dissimilarity between the shape, area and intensities of different K edges are strongly employed to study the local bonding environment [292]. So far as the carbon K edge (Figure-A.3) for the three samples of interest is

concerned, the peak at 288.8 eV corresponds to the 1s to π^* transition. This peak is well shifted to the higher energy from the position observed in graphite, boron carbide [293] and in graphitic carbon nitride, which is around 285 eV [294, 295]. This asymmetric peak is more close to the π^* peak due to pyridinic[55] and triazinic nitrogen contributions, as observed in the CN_x compounds [296]. The σ^* feature can be distinguished into two different regions $\sigma(1)^*$ and $\sigma(2)^*$ in the ranges 290 eV to 293 eV and 295 eV to 301 eV, respectively. The $\sigma(1)^*$ feature is composed of C-B or C-C and pyridinic C-N bond with maxima at 291 eV and 291.8 eV, respectively. As the C-C and C-B bond energies are very close, we cannot distinguish it between BCN-90 and BCN-98. In BCN-100 we can observe the background of C-C signature due to the absence of boron. The pyridinic C-N contribution is seen to be increasing with increasing nitrogen concentration from BCN-100 to BCN-90, as observed from the XPS data. The crucial role of boron in BCN compounds can be observed from the $\sigma(2)^*$ feature. Here we can see the significant enhancement of triazinic C-N bond in BCN-98. Thus an optimum doping of 2 at.% boron in the framework triggers or favours the triazinic nitrogen which is lowest in the case of 10 at.% doping in BCN-90. Calculating the σ^* to π^* intensity ratio as in TABLE-A.2 we can conclude that sp2 hybridization decreases with lowering the boron concentration in the material. For the special case of BCN-98 there is an optimum proportion ratio of the triazinic and pyridinic sp2 C-N bond which leads to the distinguishable magnetic and transport properties, as will be discussed later.

A.3.3 Raman Spectroscopy

In Figure-A.4 (a), (b) and (c) we show the room temperature Raman spectra of the three samples, BCN-100, BCN-98 and BCN-90, respectively, which are somewhat different as compared to previous report on bulk forms [297]. The sharp peak around 1602 cm^{-1} is denoted as G band which occurs due to the in plane optical phonon vibration E_{2g} mode near the center of the Brillouin zone [298]. The strong signature of this mode implies the presence of sp^2 hybridized 2 dimensional layers in the system [299]. The peak is significantly shifted to higher energy from the G band observed in graphite around 1580 cm^{-1}. Incorporation of strongly bonded nitrogen in the lattice plane results in a significant amount of bond stretching which affects the in-plane phonon vibration with the resultant Raman mode shifting to higher energy. This effect is very similar to the reported case of nitrogen doped grapheme sheets [300]. The asymmetric nature of the G band is predicted to emanates from the $D^{'}$ mode arising due to the distortion that causes double resonance process in phonon scattering. The intense peak around 1360 cm^{-1} is denoted as D band which occurs due to the A_1g mode also resulting from the double resonance phonon scattering [299]. This mode is triggered by the induced disorder, defects and sp_2 bond breakage

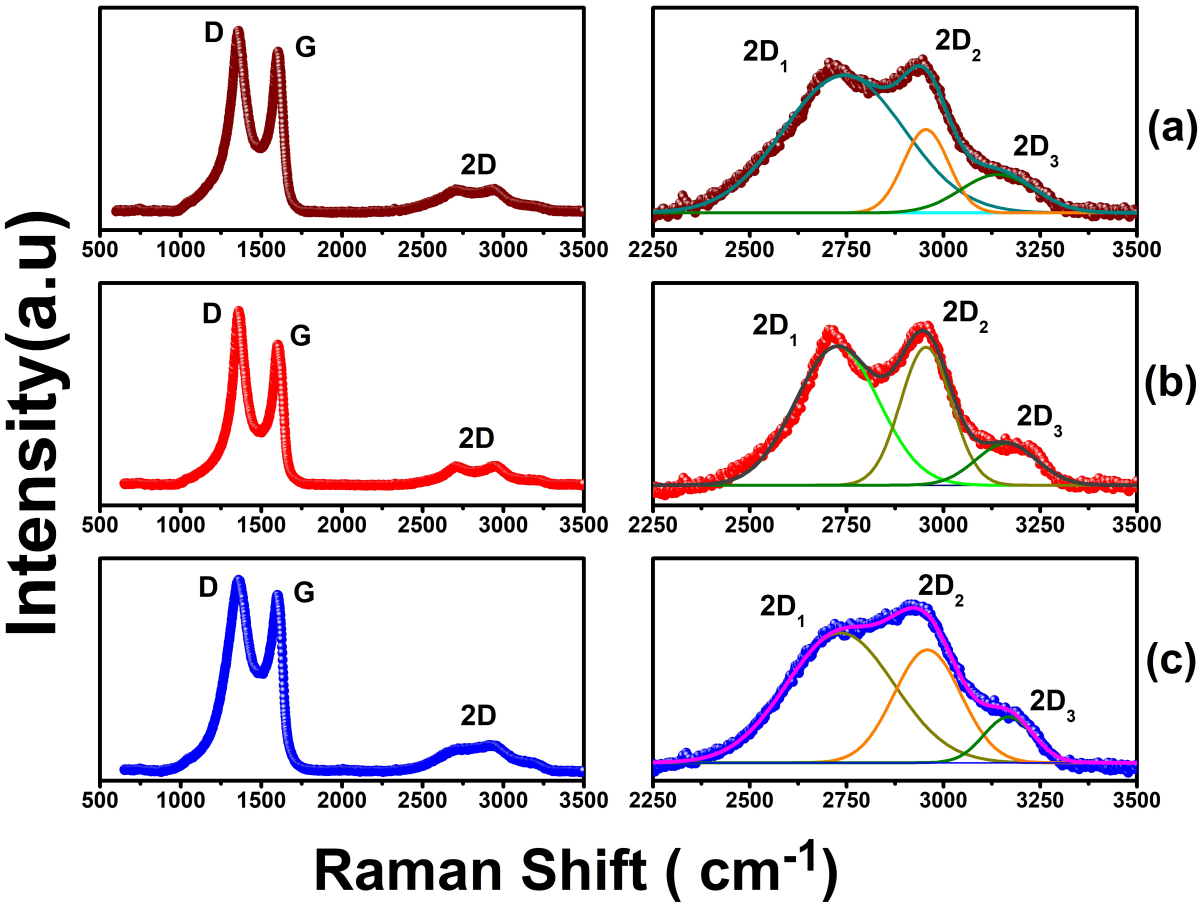

Fig. A.4 Raman Spectra and peak fitting for 2D band splitting of (a) BCN-100, (b) BCN-98 and (c) BCN-90

Table A.3 Raman band analysis

Sample	I_D/I_G	I_{2D1}/I_G	I_{2D2}/I_G	I_{2D3}/I_G
BCN-90	1.09	0.12	0.10	0.04
BCN-98	1.24	0.11	0.11	0.03
BCN-100	1.13	0.12	0.07	0.03

due to finite crystallinity and lattice distortion. Presence of this D band indicates the turbostraticity in the layered material. The band in the range 2500 cm^{-1} to 3500 cm^{-1} is referred to as 2D band which is basically an overtone of D band. As the Raman mode corresponding to the 2D band is extremely sensitive to in-plane stretching, strain and applied stress [301] we can observe the crucial role played by boron in the nitrogenation of the lattice from this mode. For all the three samples of interest the 2D band can be deconvoluted into three Gaussian contributions denoted as $2D_1$, $2D_2$ and $2D_3$. In TABLE-A.3 the intensity ratios of D and 2D bands with respect to the G band are listed. The disorder in turbostratic graphite like system

can be mathematically related with D to G band intensity ratio through following equation $I_D/I_G = C(\gamma)/L_a$ [299]. $C(\gamma)$ is a constant for particular excitation energy and L_a is the average distance among defect sites or the crystalline patches separated by grain boundaries. Taking $C(\gamma) = 4.4$ nm for excitation wavelength 488 nm we can calculate from the table that the average inter-defect distances are 4.04 nm, 3.55 nm and 3.89 nm for BCN-90 , BCN-98 and BCN-100 respectively. Thus, for the BCN-98 case the defect sites are denser than the other two cases resulting in the interesting electrical and magnetic features which are discussed in the next sub-sections. The splitting and broadening of the 2D band depends on several parameters like number of layers, inter layer interaction, layer orientation, excitation energy and induced strain in the plane. In our case, as the excitation energy and thickness are the same for all the samples, the disorder and induced strain are the main responsible mechanisms here. From Figure A.4 we can observe a sharp and intense splitting in the 2D band for BCN-98, suggesting that optimal 2 at.% doping of boron is inducing more strain in the nitrogeneted framework. The equality of $2D_1$ and $2D_2$ intensity ratio to G band could be due to the strain uniformity induced by pyridinic and triazinic nitrogens in the sp^2 bonded layer. The overall abundance of pyridine and triazine-like configurations in addition to vacancy defects is clear from the present experimental results that are discussed already. Using the first-principles DFT approach, we therefore investigated the structural, electronic, and magnetic features of these individual defect configurations and their concurrent interactions.

A.4 Density Functional Theory Calculations

The electronic structure of BCN compounds were theoretically modelled with the information from the spectroscopic analysis using the spin-polarized DFT calculations.In order to gain some insights into the microscopic mechanism of the induced spin due to the presence of different type of C-N bonds and possible role for boron, we resorted to the density functional theory (DFT) calculations, as addressed below. Specifically, we attempt to elucidate the microscopic mechanism of long-range magnetism by considering interactions among the different defect complexes. Previous reports on magnetically ordered N-doped graphene have attributed the behaviour to an abundance of pyridinic and substitutional N complexes separately [263, 302]. However, the synergistic effects of interacting defects on the overall magnetism have not been explicitly addressed, which are essential to understand the long-range magnetic ordering. We consider the interaction of trimerized pyridine with other defects since trimerized pyridine is present in significant quantities. A maximum N concentration of 15 at.% is considered in the following discussion. For two trimerized pyridines in close proximity, the spin polarization is mainly due top_z

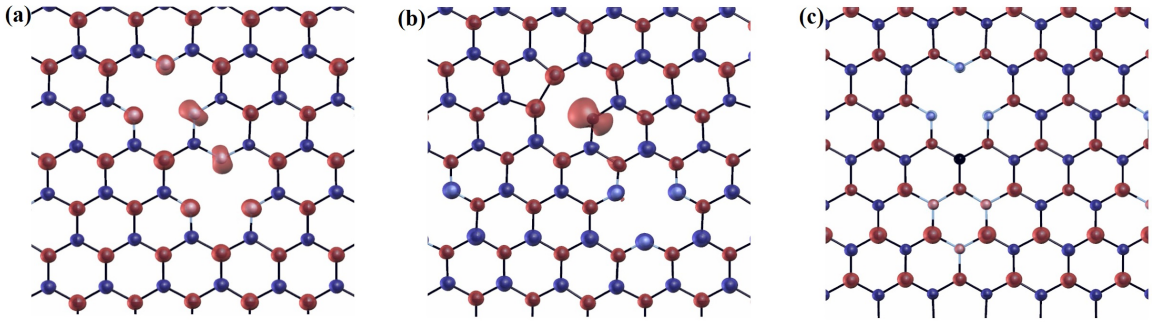

Fig. A.5 Spin charge densities for the interacting pairs of (a) trimerized pyridine - trimerized pyridine, (b) trimerized pyridine - monovacancy and (c) trimerized pyridine - triazine configuration.

states and an additional fractional moment is induced on sp^2 states of N atoms, which contributes as a paramagnetic centre [Figure-A.5 (a)]. Investigating the density of states we find that the nitrogen sp^2 states appear as mid-gap states. With increasing distance between the two pyridinic defect complexes, the sp^2 contribution to the magnetism vanishes and only p_z states generate a semi-local moment mediated via direct exchange. For a pyridinic defect interacting with neighboring monovacancy, the magnetic exchange between the two defects shows a sublattice site dependence.The defect-induced p_z spins for the defects on the same sublattice sites align parallel and result in a ferromagnetic exchange in accordance with Lieb's theorem whereas an antiparallel alignment of spins is observed for two defects placed on opposite sublattice [303]. The unpaired sp^2 state of the vacancy retains its local moment and is robust to carrier doping and/or structural changes in the presence of neighboring defect [Figure-A.5 (b)]. In addition, we also report magnetic solutions for interacting monovacancy with mono and dimerized pyridine. Lastly, the magnetic interaction between the triazine and pyridine defect complexes generates both ferromagnetic and antiferromagnetic order depending on the sub-lattice site [Figure-A.5 (c)]. Interestingly, the p-doped pyridine alters the half-metallic behaviour of triazine, however an indirect exchange is still possible due to the presence of p_z conduction electrons at the Fermi level. Thus, we propose the primary mechanism driving the ferromagnetic order is a direct exchange among the nitrogen defect configurations due to the high concentration of N atoms in the turbostratic BCN thin films. The spatial extent of ~ 2 nm for the unpaired p_z states of monovacancy exceeds the experimentally estimated inter-defect distances [246]. However, the sensitivity of p_z states towards disorder can limit the role of direct exchange. Further, it is predicted that disorder in pure graphene leads to Anderson insulating behaviour for vacancy defect with higher concentration, and a substantial gap opening could

originate in case of N substitution [304, 305] In such a scenario, the scattering of conduction electrons will result in loss of carrier-mediated indirect exchange pathways. However, the formation of bound magnetic polarons in monovacancy and pyridinic defects is another possibility of inducing ferromagnetic order through an indirect exchange that does not depend on conduction electrons [306, 307].

A.5 Magnetic measurements

Isothermal field dependent magnetization curves for all three BCN samples of interest are presented in Figure-A.6 (a) and (b) at 300K and 5K, respectively. Diamagnetic contribution from the substrate has been subtracted from the raw data by following the standard procedure of fitting to the large field linear contribution. We can observe from these data that at room temperature (300 K) ferromagnetic ordering is present in all the cases with small coercive field values (H_C) and saturation magnetizations (M_S), and the two are anti-correlated. At 5K, the M_S increases in each case but magnetizing the sample is seen to get harder, as expected for the case of the magnetic system with disorder. Disorder can favour spin canting in the system, which resists the saturation of the net magnetization, very similar to a spin glass system [308]. The disorder in the present case is related to the nitrogen incorporation as dopant and the specific nature of disorder highly depends on the defect type and its consequence for the creation of vacancy defect due to issues of charge balance. Therefore, it is of crucial interest to discuss the nitrogen concentration dependence of the bulk magnetization parameters. In Figure-A.6 (c) and (d) we present the H_C and M_S values with respect to the nitrogen concentration present in the system for all the three samples at 300K and 5K, respectively. At room temperature, the saturation magnetization increases while the coercive field decreases monotonically with the increase in the nitrogen concentration from BCN-100 to BCN-90. From the previous spectroscopic analysis (X-ray photoelectron spectroscopy and X ray absorption near edge spectroscopy) both the triazinic and pyridinic sp^2 C-N bonds lead to induced spins at the defect sites, thereby rendering higher M_S with increased nitrogen concentration. If we consider this as an inhomogeneous ferromagnet with the presence of disorder, more in the form of correlated ferromagnetic clusters, increase in the spin density with increasing nitrogen concentration can induce enhanced correlations and larger cluster size thereby decreasing the coercive field. At 5K the behaviour of M_S is the same as at 300K, although with increased saturation magnetization in each case; but interestingly we observe a drastic increase in H_C for BCN-98. This anomalous increment appears to be directly connected to the increase of triazinic sp^2 C-N bond concentration as reflected in the X-ray absorption near edge (XANES) spectra for this specific case.

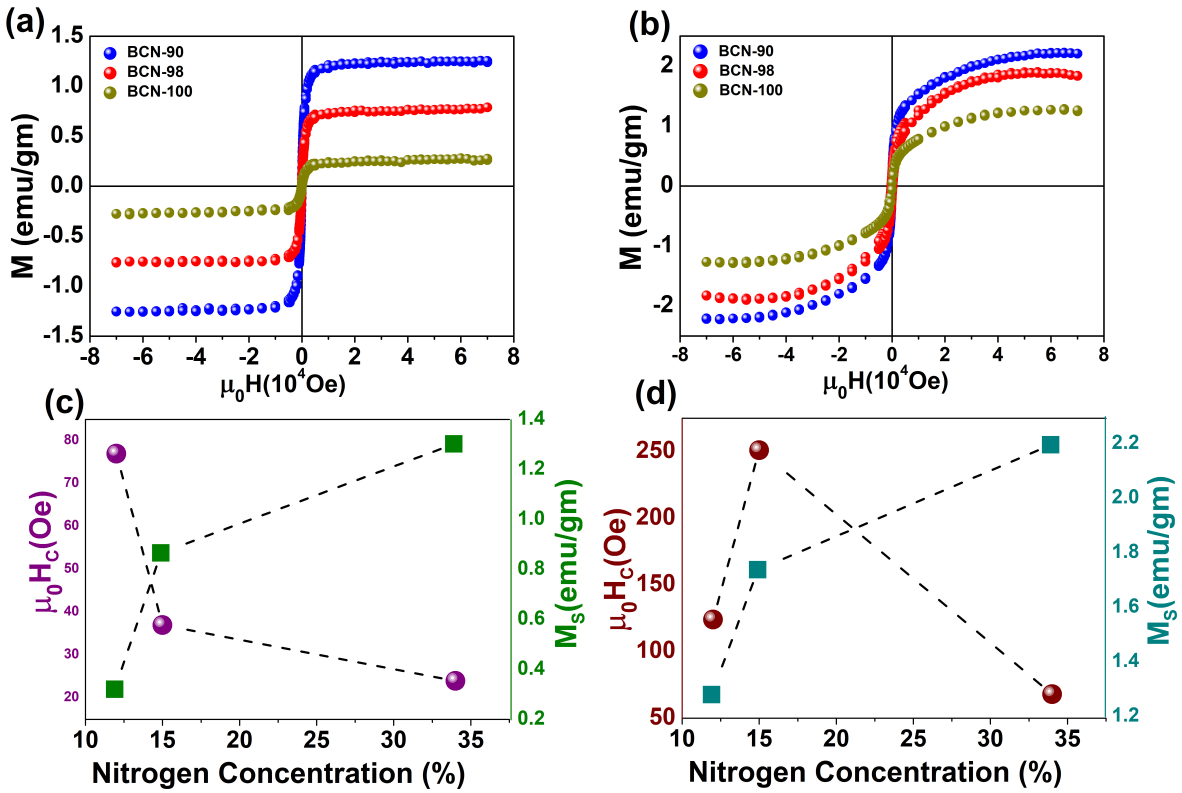

Fig. A.6 (a) and (b) represent the isothermal M-H loop for three BCN Samples at 300 K and 5 K respectively. (c) and (d) represent the dependence of coercivity H_C and saturation magnetization M_S on nitrogen concentration in films at 300 K and 5 K respectively

This ferromagnetic condition of the sample is reminiscent of single domain magnetic clusters, which give very high coercive field value. The low coercive field for the BCN-90 case, where the nitrogen defect concentration is substantially higher, reflects the case of a more homogeneous ferromagnetic system. In Figure-A.7, we present the data for temperature dependent magnetization. Figure-A.7 (a), (b) and (c) represent the zero field cooling (ZFC) and field cool warming (FCW) data of M vs T for BCN-90, 98 and 100 samples, respectively, with an applied field 100 Oe. We can see that the bifurcation between the ZFC and FCW curves increases with the increasing nitrogen (and boron) contents. This reveals the nature of evolution of the magnetic state with increased spin density in the presence of disorder. The bifurcation temperature is almost near room temperature in all cases including the case of BCN-100 wherein there is no boron. The BCN-98 and BCN-100 samples both show ferromagnetic ordering developing near 130 K, which is distinctly defined in the BCN-98 case. In the BCN-90 case, this transition is not clearly seen possibly because of its significant broadening due to enhanced doping concentration

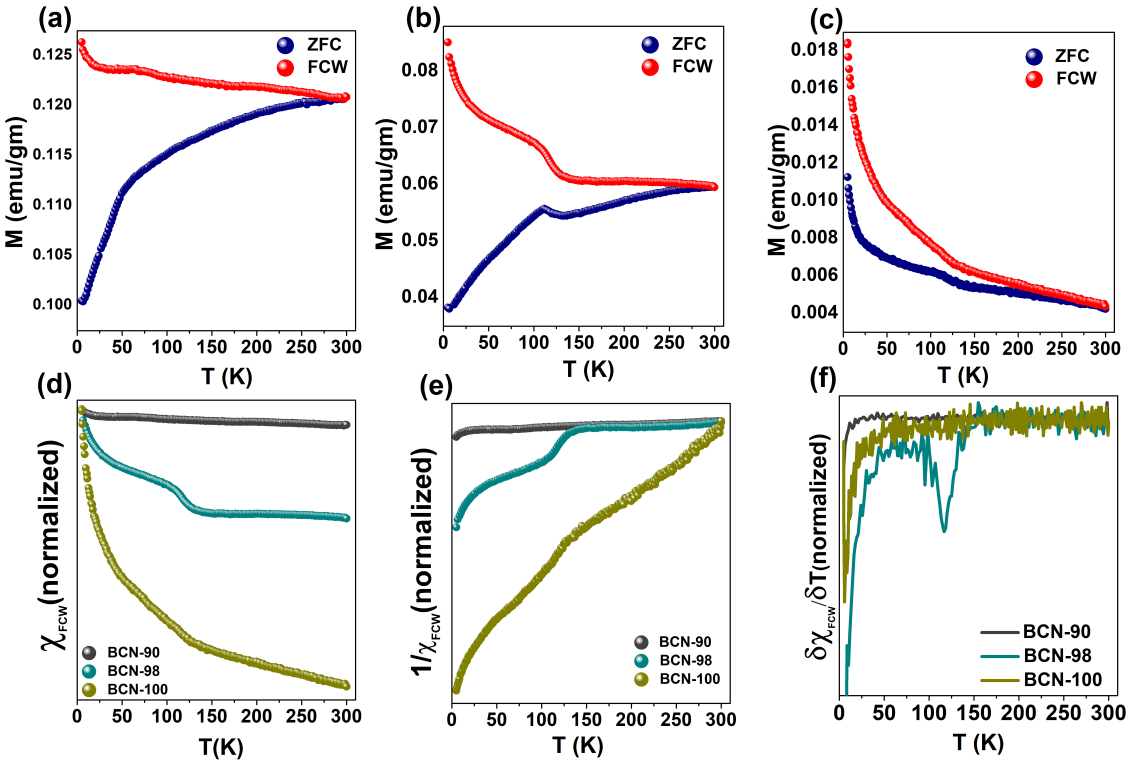

Fig. A.7 (a), (b) and (c) represent the ZFC and FCW curves for BCN-90, 98 and 100 respectively. (d) normalised susceptibility vs temperature. (e) inverse susceptibility vs temperature (f) derivative of susceptibility vs temperature.

and related spin disorder. In this case of BCN-90 a sharper downturn in ZFC and inflection in FCW is noted around 65K. At about the same temperature even in the BCN-98 sample an upturn is seen in FCW. Behaviour of FCW susceptibility (χ_{FCW}) and inverse of χ_{FCW} of the samples are shown in Figure-A.7 (d) and (e). As our materials are weakly ferromagnetic at room temperature and are not homogeneous ferromagnets, they do not follow the Curie-Weiss law in our temperature range. To understand the magnetic transition more clearly the derivative of χ_{FCW} with respect to temperature is plotted in Figure-A.7 (f). For the rather special case BCN-98, as mentioned earlier we can see the drastic change of the derivative around 130 K resulting in a strong dip in the plot. This is indicative of the clear magnetic transition for a critical doping concentration.

A.6 Transport properties

Now we will begin the discussion of the temperature dependent transport properties of the charge carriers in the BCN samples mentioned above.

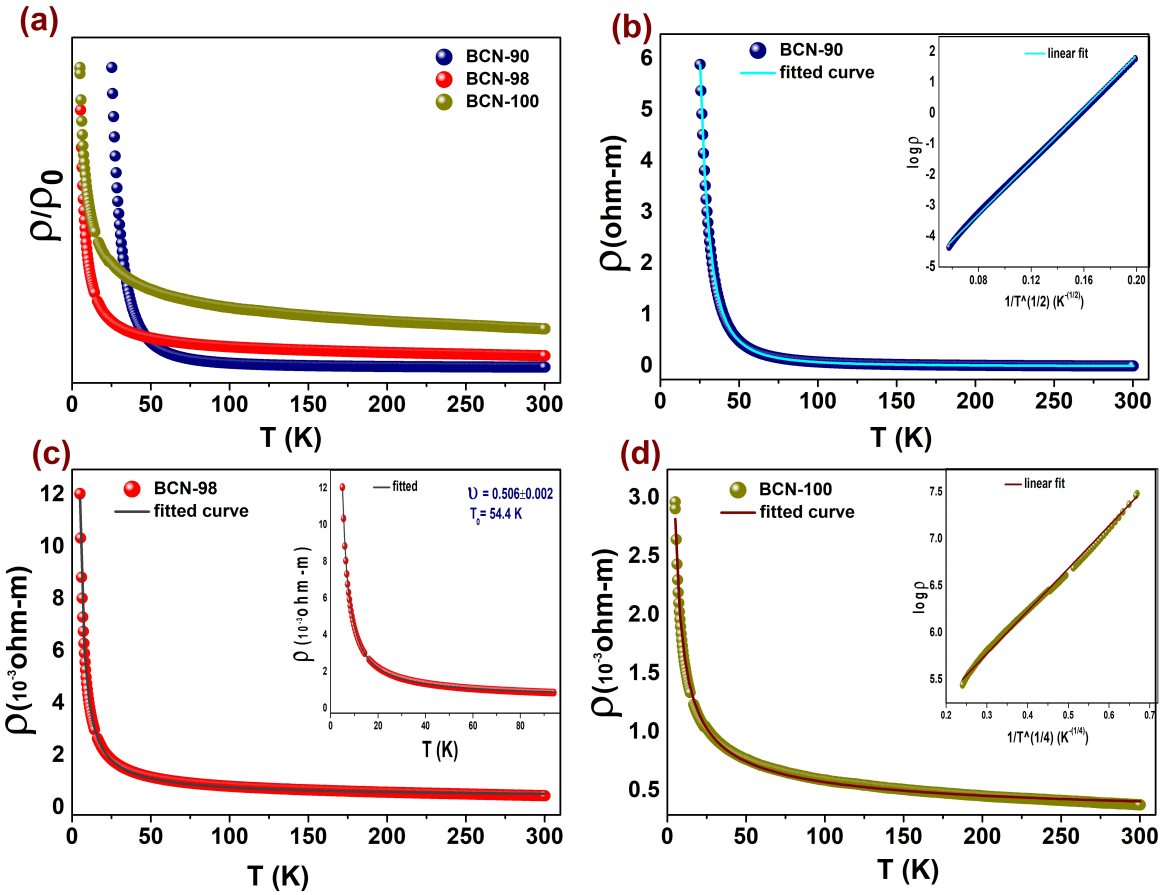

Fig. A.8 (a) Normalized resistivity vs temperature. (b), (c) and (d) represent the temperature dependent resistivity curve with non linear fitting. Linear fits are shown for (b) and (d) (inset). Non linear fit is shown for small range bellow the crossover for BCN-98 in (c) (inset).

Table A.4 Nonlinear fitting parameters

	BCN-90	BCN-98	BCN-100
T_0 (K)	1226.1	94.1	311.2
ν	0.536 ±0.001	0.442 ±0.002	0.260 ±0.004

In case of a regular and perfect crystalline defect free semiconductor, more electrons are pumped to the conduction band from the valence band with increased temperature, and the dc-resistivity is decreased as $\exp(E_g/k_BT)$, where E_g is the activation energy and k_B is Boltzmann constant. The scenario is much different in semi-crystalline, or disordered systems with the presence of defects. In such cases, the density of states is extended or defused through the band gap due to the localised or trapped states because of the presence of local deformations, disorder in crystal lattice, and defects. Over the full temperature range the transport mechanism is primarily governed by two different mechanisms. Below a certain characteristic temperature and under low electrical bias,the transport mechanism is fully dominated by the hopping of charge carriers among these localised states. Above this temperature transport will be the usual band conduction. The specific characteristic temperature can vary with the induced disorder in the system or more specifically with the density of localised states near Fermi level E_F. Incorporating the possibility of hopping of carriers to sites with minimum hoping energy, irrespective of nearest neighbour or not, two most successful theoretical models of variable range hopping (VRH) have been proposed and widely used to explain the experimental transport data. The main assumption behind the model proposed by Mott [309] is the approximation of a constant density of states around the Fermi level, $N(E_F)$ irrespective of energy of the system. Efros and Shklovskii on the other hand explained that below a certain critical temperature the density of states may not be constant and it becomes non uniform near E_F due to the coulomb interactions among carriers [310]. Incorporation of this interaction causes a dip in the density of states around E_F known as the Coulomb gap. Both model can be described mathematically by the following equation [311] $\rho = \rho_0 \exp(T_0/T)^{\nu}$.$\rho$ is the dc-resistivity, ρ_0 is a constant, and T_0 is the characteristic temperature. In the Mott model the value of ν is 1/3 and 1/4 for 2D and 3D systems, respectively; while $\nu = 1/2$ for all the systems in the ES model which possesses the Coulomb gap. In Figure-A.8 we show the transport data for our BCN-90, BCN-98 and BCN-100 samples.Temperature dependent normalised dc resistivity data for the samples are shown in Figure-A.8 (a) for comparison. For the determination of the hopping mechanism in each case, the curves are non linear fitting has been done directly to equation (2) with varying the parameters ρ_0 , T_0 and ν as presented in Figure-A.8 (b), (c) and (d). The important parameters are tabulated in Table A.4. Here we can observe that the value of ν is very close to 1/2 for BCN-90 and it is close to 1/4 for BCN-100. It is clear that for BCN-90 the hopping of charge carriers is governed by the Mott model over the entire temperature range and the same can be understood from the fact that the characteristic temperature T_0 is 1226 K which is far above our measurement range. For the BCN-100 case the ES model fits the data very well over the whole

range, as T_0 is above room temperature. The most interesting case is the BCN-98 sample (as was also noted in the analysis of the magnetic data for its unique defect-related properties, and its electronic structure reflected in the spectroscopy data) where ν does not match either with 1/2 or 1/4 and it lies between these values. This crossover between Mott and ES Scenarios is very clear from the value of the critical temperature T_0 of 94 K that lies within the concerned temperature range of our measurement. For further clarification, the low temperature data up to the crossover temperature was fitted (Figure-A.8 (c) inset) to equation (2) and the fitted value of ν was found to be 0.506 ± 0.002 which is closer to 1/2 consistent with the ES model. Below the critical temperature Coulomb interaction becomes dominant resulting into the applicability of the ES process [312]. From the whole picture the crucial as well as interesting role played by boron in the electronic structure is thus very important. With increasing the doping concentration of boron in nitrogenated turbostratic carbon framework, the hopping mechanism of charge carriers among the localized states is seen to be changing dramatically with a clean crossover for an optimum 2 at.% doping as in BCN-98. From a continuous and constant density of states $N(E_F)$ near Fermi level with no boron doping, we can get a transition to a clear Coulomb gap state with increasing boron concentration in the material. The carrier localisation length (ξ) and the $N(E_F)$ can be related to the calculated average inter-defect sites distance (L_a) from Raman spectroscopy and the proposition from DFT first principle calculations.

A.7 Conclusions

$B_XC_YN_Z$ thin films are grown using the ammonia assisted Pulsed Laser Deposition (PLD) method, and their detail electronic structure, magnetic and transport properties are analysed using various spectroscopic techniques like X-ray photoelectron spectroscopy (XPS) and X-ray absorption near edge spectroscopy (XANES). Theoretical insights are obtained using Density Functional Theory (DFT) calculations predicting the possible interaction among different kind of defects. A dramatic crossover in the transport mechanism of charge carriers is observed with the change in the doping level of specific nitrogen defects. A robust and high saturation magnetization is achieved in the $B_XC_YN_Z$ films, which is seen to be higher by almost hundred times as compared to the similarly grown dopant free turbostratic graphene film. An anomalous transition and increase in the coercive field is also observed at low temperature with critical dopant concentration. The detail comparison of the experimental data with the theoretical results brings out the intriguing role of specific nitrogen defects in defining the physical properties of this hybrid 2D layered material.

Bibliography

[1] L.W. Martin et al. Advances in the growth and characterization of magnetic, ferroelectric, and multiferroic oxide thin films. Materials Science and Engineering R 68 (2010) 89-133

[2] Hwang, H., Iwasa, Y., Kawasaki, M. et al. Emergent phenomena at oxide interfaces. Nature Mater 11, 103-113 (2012)

[3] Masatoshi Imada, Atsushi Fujimori, and Yoshinori Tokura. Metal-insulator transitions. Rev. Mod. Phys. 70, 1039 (1998)

[4] Kyle M. Shen, J.C. Seamus Davis Cuprate high-Tc superconductors.Materials Today 11(2008) 14-21

[5] A P Ramirez. Colossal magnetoresistance J. Phys.: Condens. Matter 9 (1997) 8171-8199

[6] M. Bibes and A. Barthelemy, "Oxide Spintronics," in IEEE Transactions on Electron Devices, vol. 54, no. 5, pp. 1003-1023, May 2007

[7] Ishihara T. (2017) Inorganic Perovskite Oxides. In: Kasap S., Capper P. (eds) Springer Handbook of Electronic and Photonic Materials. Springer Handbooks. Springer, Cham. 978-3-319-48931-5

[8] Stephen Blundell, Magnetism in Condensed Matter, Oxford University Press Inc.,0-19-850592-2,(2001)

[9] Karmakar Koushik, Disorder in the Quantum Spin-Chains Sr_2CuO_3 and

$SrCuO_2$, PhD Thesis, Indian Institute of Science Education and Research, Pune (2016)

[10] J. Hubbard, Electron correlations in narrow energy bands. Proceedings of the Royal Society of London A: Mathematical,Physical and Engineering Sciences 276, 238-257 (1963).

[11] Junjiro Kanamori, Electron Correlation and Ferromagnetism of Transition Metals, Progress of Theoretical Physics, Volume 30, Issue 3, September 1963, Pages 275-289

[12] F. H. L. Essler et al., The one-dimensional hubbard model, Cambridge Books Online (Cambridge University Press, 2005).

[13] A. Fujimori et al.,Multielectron satellites and spin polarization in photoemission from Ni compounds. Physical Review B 29, 5225-5227 (1984).

[14] A. Fujimori and F. Minami,Valence-band photoemission and optical absorption in nickel compounds. Physical Review B 30, 957-971 (1984)

[15] J. C. Bonner and M. E. Fisher,Linear Magnetic Chains with Anisotropic Coupling. Physical Review 135, A640 (1964)

[16] Goodenough, J B (1963). Magnetism and the Chemical Bond. Interscience-Wiley, New York

[17] Gen Matsumoto, Study of $(La_{1-x}Ca_x)MnO_3$. I. Magnetic Structure of $LaMnO_3$. J. Phys. Soc. Jpn. 29, pp. 606-615 (1970)

[18] Goodenough, J B, Theory of the Role of Covalence in the Perovskite-Type Manganites [La, M(II]MnO_3. Phys. Rev. 100: 564 (1955)

[19] Junjiro Kanamori, Theory of the Magnetic Properties of Ferrous and Cobaltous Oxides, I, Progress of Theoretical Physics, Volume 17, Issue 2, 177-196, 197-222 (1957)

[20] Goodenough, J B, An interpretation of the magnetic properties of the perovskite-type mixed crystals $La_{1-x}Sr_xCoO_{3-\lambda}$, J. Phys. Chem. Solids, Volume 6, Issues 2-3, August 1958, Pages 287-297

[21] Kanamori, J, Superexchange interaction and symmetry properties of electron orbitals. J. Phys. Chem. Solids, Volume 10, Issues 2-3, July 1959, Pages 87-98

[22] I. Dzyaloshinskii (1958). "A thermodynamic theory of "weak" ferromag-

netism of antiferromagnetics". Journal of Physics and Chemistry of Solids. 4 (4): 241

[23] T. Moriya (1960). "Anisotropic Superexchange Interaction and Weak Ferromagnetism". Physical Review. 120 (1): 91

[24] Naoto Nagaosa1 and Yoshinori Tokura1,"Topological properties and dynamics of magnetic skyrmions". Nature Nanotechnology , Vol 8 ,December 2013

[25] Wang, J et al. "Epitaxial BiFeO3 Multiferroic Thin Film Heterostructures". Science. 299 (5613): 17191722

[26] S. B. Lang and H. L. W. Chan, Frontiers of Ferroelectricity. Springer, Boston, MA, 2007.

[27] J. Valasek, Piezo-Electric and Allied Phenomena in Rochelle Salt. Phys. Rev., vol. 17, p. 475, 1921

[28] C. H. Ahn, K. M. Rabe, and J.-M. Triscone, Ferroelectricity at the Nanoscale: Local Polarization in Oxide Thin Films and Heterostructures. Science 303, 5657, 488-491 (2004)

[29] P. S. Halasyamani, K. R. Poeppelmeier: Non-centrosymmetric oxides, Chem. Mater. 10, 2753-2769 (1998) 178

[30] U. Opik, M. L. H. Pryce: Studies of the JahnTeller effect I: A survey of the static problem, Proc. Roy. Soc. A 238, 425-447 (1957) 178

[31] M. Lilienblum et al., Ferroelectricity in the multiferroic hexagonal manganites. Nat. Phys. 11, 1070-1073 (2015)

[32] B.B. Van Aken, T.T.M. Palstra, A. Filippetti, and N. Spaldin, The origin of ferroelectricity in magnetoelectric $YMnO_3$. Nat. Mater. 3, 164 (2004)

[33] C.J. Fennie and K.M. Rabe, Ferroelectric transition in $YMnO_3$ from first principles. Phys. Rev. B 72, 1 (2005).

[34] J. van den Brink and D. I. Khomskii, Multiferroicity due to charge ordering. Journal of Physics: Condensed Matter, vol. 20, no. 43, p. 434217, 2008

[35] G. T. Rado and J. M. Ferrari, Electric field dependence of the magnetic anisotropy energy in magnetite (Fe_3O_4). Phys. Rev. B, vol. 12, p. 5166, 1975

[36] N. Ikeda, H. Ohsumi et al., Ferroelectricity from iron valence ordering in the charge-frustrated system $LuFe_2O_4$. Nature, vol. 436, p. 1136, 2005

[37] Fiebig, M., Lottermoser, T., Meier, D. et al. The evolution of multiferroics. Nat Rev Mater 1, 16046 (2016)

[38] L. E. Orgel, The stereochemistry of B subgroup metals. Part II. The inert pair. J. Chem. Soc., p. 3815, 1959

[39] T. Kimura, S. Kawamoto, I. Yamada, M. Azuma, M. Takano, and Y. Tokura, Magnetocapacitance effect in multiferroic $BiMnO_3$. Phys.Rev. B, vol. 67, p. 180401, 2003

[40] Mostovoy M, Ferroelectricity in Spiral Magnets. Phys. Rev. Lett. 96 067601 (2006)

[41] Sergienko I A and Dagotto E, Role of the Dzyaloshinskii-Moriya interaction in multiferroic perovskites. Phys. Rev. B 73 094434 (2006)

[42] Tokura, Y., Seki, S. Nagaosa, N. Multiferroics of spin origin. Rep. Progress Phys. 77, 076501 (2014)

[43] Kimura, T. et al. Magnetic control of ferroelectric polarization. Nature 426, 55-58 (2003

[44] Yamasaki Y, Sagayama H, Goto T, Matsuura M, Hirota K,Arima T and Tokura Y , Electric Control of Spin Helicity in a Magnetic Ferroelectric. 2007 Phys. Rev. Lett. 98 147204

[45] M. Coll, J. Fontcuberta, M. Althammer, M. Bibes et al. Towards Oxide Electronics: A Roadmap. Appl. Surf. Sci. 482, 1 (2019)

[46] Ramesh, R., Schlom, D.G. Creating emergent phenomena in oxide superlattices. Nat Rev Mater 4, 257-268 (2019)

[47] Ohtomo, A., Hwang, H. A high-mobility electron gas at the $LaAlO_3/SrTiO_3$ heterointerface. Nature 427, 423-426 (2004)

[48] Li, D., Lee, K., Wang, B.Y. et al. Superconductivity in an infinite-layer nickelate. Nature 572, 624-627 (2019)

[49] D.G. Schlom, L.-Q. Chen, C.-B. Eom, K.M. Rabe, S.K. Streiffer, J.-M. Triscone, Strain Tuning of Ferroelectric Thin Films. Annual Review of Materials Research 37 (2007) 589-626

[50] Stengel, M., Vanderbilt, D. Spaldin, N. Enhancement of ferroelectricity at metaloxide interfaces. Nature Mater 8, 392-397 (2009)

[51] Haeni, J., Irvin, P., Chang, W. et al. Room-temperature ferroelectricity in strained $SrTiO_3$. Nature 430, 758-761

[52] K.J. Choi, M. Biegalski, Y.L. Li, A. Sharan, J. Schubert, R. Uecker, P. Reiche, Y.B. Chen,X.Q. Pan, V. Gopalan, L.-Q. Chen, D.G. Schlom, C.B. Eom, Enhancement of Ferroelectricity in Strained $BaTiO_3$ Thin Films. Science 306 (2004) 1005

[53] C.S. Ganpule, V. Nagarajan, B.K. Hill, A.L. Roytburd, E.D. Williams, R. Ramesh, S.P.Alpay, A. Roelofs, R. Waser, L.M. Eng, Imaging three-dimensional polarization in epitaxial polydomain ferroelectric thin films. J. Appl. Phys. 91 (2002) 1477

[54] V. Nagarajan, C.S. Ganpule, H. Li, L. Salamanca-Riba, A.L. Roytburd, E.D. Williams,R. Ramesh, Control of domain structure of epitaxial $PbZr_{0.2}Ti_{0.8}O_3$ thin films grown on vicinal (001) $SrTiO_3$ substrates. Appl. Phys. Lett. 79 (2001) 2805

[55] Y.-H. Chu, M.P. Cruz, C.-H. Yang, L.W. Martin, P.-L. Yang, J.-X. Zhang, K. Lee, P. Yu,L.-Q. Chen, R. Ramesh, Domain Control in Multiferroic $BiFeO_3$ through Substrate Vicinality. Adv. Mater. 19 (2007) 2662

[56] Y.-H. Chu, Q. He, C.-H. Yang, P. Yu, L.W. Martin, P. Shafer, R. Ramesh, Nanoscale Control of Domain Architectures in $BiFeO_3$ Thin Films. Nano Lett. 9 (2009) 1726

[57] Y.-H. Chu, Q. Zhan, L.W. Martin, M.P. Cruz, P.-L. Yang, G.W. Pabst, F. Zavaliche, S.-Y. Yang, J.-X. Zhang, L.-Q. Chen, D.G. Schlom, I.-N. Lin, T.-B. Wu, R. Ramesh, Nanoscale Domain Control in Multiferroic $BiFeO_3$ Thin Films. Adv.Mater. 18 (2006) 2307

[58] Bibes, M., Barthlmy, A. Towards a magnetoelectric memory. Nature Mater 7, 425-426 (2008)

[59] Bin Xu, Vincent Garcia, Stphane Fusil, Manuel Bibes, and L. Bellaiche, Intrinsic polarization switching mechanisms in $BiFeO_3$. Phys. Rev. B 95, 104104

[60] Wei, Y., Nukala, P., Salverda, M. et al. A rhombohedral ferroelectric phase in epitaxially strained $Hf_{0.5}Zr_{0.5}O_2$ thin films. Nature Mater 17, 1095-1100 (2018)

[61] Y. Suzuki,Epitaxial Spinel Ferrite Thin Films. Annu. Rev. Mater. Res. 31

(2001) 265

[62] Y. Tokura, Y. Tomioka, Colossal magnetoresistive manganites. J. Magn. Magn. Mater. 200 (1999) 1

[63] C. Kwon, M.C. Robson, K.-C. Kim, J.Y. Gu, S.E. Lofland, S.M. Bhagat, Z. Tranjanovic, M. Rajeswari, T. Venkatesan, A.R. Katz, R.D. Gomez, R. Ramesh, Stress-induced effects in epitaxial $(La_{0.7}Sr_{0.3})MnO_3$ films. J. Magn. Magn. Mater. 172 (1997) 229

[64] Y. Suzuki, H.Y. Hwang, S.-W. Cheong, R.B. Van Dover, The role of strain in magnetic anisotropy of manganite thin films. Appl. Phys. Lett. 71 (1997)140

[65] V. Moshnyaga, L. Sudheendra, O.I. Lebdev, S.A. Ko ster, K. Gehrke, O. Shapoval, A.Belenchuk, B. Damaschke, G. van Tendeloo, K. Samwer, A-Site Ordering versus Electronic Inhomogeneity in Colossally Magnetoresistive Manganite Films. Phys. Rev. Lett. 97 (2006)107205

[66] T. Zhao, A. Scholl, F. Zavaliche, K. Lee, M. Barry, A. Doran, M.P. Cruz, Y.-H. Chu, C.Ederer, N.A. Spaldin, R.R. Das, D.M. Kim, S.H. Baek, C.B. Eom, R. Ramesh, Electrical control of antiferromagnetic domains in multiferroic $BiFeO_3$ films at room temperature. Nature Mater. 5 (2006) 823

[67] T. Atou, H. Chiba, K. Ohoyama, Y. Yamaguichi, Y. Syono, Structure Determination of Ferromagnetic Perovskite $BiMnO_3$. J. Solid State Chem. 145(1999) 639

[68] D. Ito, N. Fujimura, T. Yoshimura, T. Ito, Ferroelectric properties of $YMnO_3$ epitaxial films for ferroelectric-gate field-effect transistors. J. Appl. Phys. 93 (2003) 5563

[69] P. Salvador, T.-D. Doan, B. Mercey, B. Raveau, Stabilization of $YMnO_3$ in a Perovskite Structure as a Thin Film. Chem. Mater. 10 (1998) 2592

[70] Lee, J., Fang, L., Vlahos, E. et al. A strong ferroelectric ferromagnet created by means of spinlattice coupling. Nature 466, 954-958 (2010)

[71] H. Zheng, J. Wang et al. Multiferroic $BaTiO_3$-$CoFe_2O_4$ Nanostructures, Science 303 (2004) 661

[72] P. Yu, J.-S. Lee, S. Okamoto, M. D. Rossell, M. Huijben, C.-H. Yang, Q. He, J. X. Zhang, S. Y. Yang, M. J. Lee, Q. M. Ramasse, R. Erni, Y.-H. Chu, D. A. Arena, C.-C. Kao, L. W. Martin, and R. Ramesh, Interface Ferromagnetism and Orbital Reconstruction in $BiFeO_3$ - $La_{0.7}Sr_{0.3}MnO_3$ Heterostructures.

Phys. Rev.Lett. 105, 027201 (2010)

[73] C. Adamo, X. Ke, P. Schiffer, A. Soukiassian, M. Warusawithana, L. Maritato, D.G. Schlom, Electrical and magnetic properties of $(SrMnO_3)_n/(LaMnO_3)_{2n}$ superlattices. Appl. Phys. Lett. 92 (2008) 112508

[74] A. Bhattacharya, S.J. May, S.G.E. te Velthius, M. Warusawithana, X. Zhai, B. Jiang,J.-M. Zuo, M.R. Fitzsimmons, S.D. Bader, J.N. Eckstein, Metal-Insulator Transition and Its Relation to Magnetic Structure in $(LaMnO_3)_{2n}/(SrMnO_3)_n$ Superlattices. Phys. Rev. Lett. 100 (2008)257203

[75] Yadav, A., Nelson, C., Hsu, S. et al. Observation of polar vortices in oxide superlattices. Nature 530, 198-201 (2016)

[76] Das, S., Tang, Y.L., Hong, Z. et al. Observation of room-temperature polar skyrmions. Nature 568, 368-372 (2019)

[77] Mundy, J., Brooks, C., Holtz, M. et al. Atomically engineered ferroic layers yield a room-temperature magnetoelectric multiferroic. Nature 537, 523-527 (2016)

[78] O. Auciello, J. F. Scott, R. Ramesh: The physics of ferroelectric memories,Physics Today 51, 22-27 (1998) 196

[79] J. F. Scott: Ferroelectric Memories (Springer 2000) 196

[80] S. Parkin, X. Jiang, C. Kaiser, A. Panchula, K. Roche, M. Samant: Magnetically engineered spintronic sensors and memory, Proc. IEEE 91, 661-680(2003) 196

[81] Gajek, M., Bibes, M., Fusil, S. et al. Tunnel junctions with multiferroic barriers. Nature Mater 6, 296-302 (2007)

[82] M. Ohring, Materials Science of Thin Films: Deposition and Structure, Academic Press, San Francisco, 2002

[83] James M. Rondinelli and Nicola A. Spaldin.Substrate coherency driven octahedral rotations in perovskite oxide films.Phys. Rev. B 82, 113402 (2010)

[84] D.L. Smith, Thin-Film Deposition: Principles and Practice, McGraw Hill, San Francisco, 1995

[85] V. Moshnyaga, I. Khoroshun, A. Sidorenko, P. Petrenko, A.Weidinger, M. Zeitler, B. Rauschenbach, R. Tidecks, K. Samwer: Preparation of rare-earth

manganite-oxide thin films by metalorganic aerosol deposition technique, Applied Physics Letters 74, 2842 (1999)

[86] V. Moshnyaga: Metal-Insulator Transition and Magnetoresistance in Manganite Thin Films: Lattice Strain and Disorder Effects, Kapitel 15 aus: A.V. Narlikar: Frontiers in Magnetic Materials, Springer Verlag, 1. Auflage 2005

[87] V. Moshnyaga, A. Belenchuk, S. Hhn, C. Kalkert, M. Jungbauer, O. I. Lebedev, S. Merten, K.- Y. Choi, P. Lemmens, B. Damaschke, K. Samwer: Intrinsic antiferromagnetic coupling underlies colossal magnetoresistance effect: Role of correlated polarons, Physical Review B 89, 024420 (2014)

[88] M. Jungbauer, S. Hhn, R. Egoavil, H. Tan, J. Verbeeck, G. Van Tendeloo, V. Moshnyaga: Atomic layer epitaxy of Ruddlesden-Popper $SrO(SrTiO_3)_n$ films by means of metalorganic aerosol deposition, Applied Physics Letters 105, 251603 (2014)

[89] I. V. Khoroshun, E. V. Karyaev, V. T. Moshnyaga, G. A. Kiosse, M. A. Krachun, V. M. Zakosarenko, V. Yu Davydov: Characteristics of epitaxial Y-Ba-Cu-O thin films grown by aerosol MOCVD technique, Supercond. Sci. Technol. 3, 493-496 (1990)

[90] Christoph Meyer: Strukturelle und optische Eigenschaften dnner mithilfe von metallorganischer Aerosol Deposition hergestellter ZnO-Schichten, Masterarbeit, Georg-August-Universität Göttingen (2013)

[91] R. Egoavil, S. Hhn, M. Jungbauer, N. Gauquelin, A. Bche, G. Van Tendeloo, J. Verbeeck: Phase problem in the B-site ordering of La_2CoMnO_6: impact on structure and magnetism, Nanoscale 7, 9835 (2015)

[92] Sebastian Hhn: Kationen-Ordnung in ferri/ferromagnetischen perowskitischen Dnnfilmen, Dissertation, Georg-August-Universität Göttingen (2015)

[93] C. Meyer, S. Hhn, M. Jungbauer, S. Merten, B. Damaschke, K. Samwer, V. Moshnyaga: Tipenhanced Raman spectroscopy (TERS) on double perovskite La_2CoMnO_6 thin films: field enhancement and depolarization effects, J. Raman Spectrosc. 48, 46-52 (2017)

[94] HiTec Zang GmbH: SyrDos-Präzisions-Spritzendosierer-Familie, Datenblatt (2017)

[95] Markus Jungbauer:Gestaltung der elektronischen Korrelationen in Perowskit-Heterostrukturen auf atomarer Skala, Dissertation, Georg-

August-Universität Göttingen (2015)

[96] Fryderyk Lyzwa: Wachstum und Charakterisierung von Ruddlesden-Popper $SrO(SrTiO_3)_{n=4}$ Schichten mittels Atomlagenepitaxie, Masterarbeit, Georg-August-Universität Göttingen,(2016)

[97] Sven Esser: Untersuchung der Elektronen-Gitter Korrelation in VO2 Dnnfilmen, Masterarbeit, Georg-August-Universität Göttingen (2016)

[98] Victor Pfahl: Sauerstoffarme MAD: Struktur und Magnetotransport von Magnetitschichten, Masterarbeit, Georg-August-Universität Göttingen (2014)

[99] Philipp Ksoll: Wachstum von oxidischen Mikrostrukturen mittels Metallorganischer Aerosol Deposition, Masterarbeit, Georg-August-Universität Göttingen (2017)

[100] D. Dijkkamp, T. Venkatesan, X. D. Wu, S. A. Shaheen, N. Jisrawi, Y. H. Min-Lee, W. L. McLean and M. Croft, Preparation of YBaCu oxide superconductor thin films using pulsed laser evaporation from high T_c bulk material. Appl. Phys. Lett. 51 619 (1987)

[101] Abhijit Biswas: Transport Phenomena in Perovskite Thin film: La doped $SrTiO_3$ and $SrIrO_3$. Dissertation, POSTECH, South Korea (2014)

[102] Venkatesan T., Harshavardhan K.S., Strikovski M., Kim J. (2005) Recent Advances in the Deposition of Multi-Component Oxide Films by Pulsed Energy Deposition. In: Thin Films and Heterostructures for Oxide Electronics. Multifunctional Thin Film Series. Springer, Boston, MA.

[103] Rijnders, G. and Blank, D.H.A. (2006). Growth Kinetics During Pulsed Laser Deposition. In Pulsed Laser Deposition of Thin Films, R. Eason (Ed.)

[104] B. Cullity, Elements of X Ray Diffraction - Scholars Choice Edition. Addison-Wesley series in metallurgy and materials, Scholars Choice, 2015

[105] Widjonarko, N.E. Introduction to Advanced X-ray Diffraction Techniques for Polymeric Thin Films. Coatings 2016, 6, 54

[106] Charles Kittel, Introduction to Solid State Physics,John Wiley Sons, Inc,2005,ISBN: 0-471-41526-X

[107] C. C. Chusuei and D. W. Goodman, Encyclopedia of Physical Science and Technology, vol. 17, pp. 921938(2002)

[108] Frank de Groot and Akio Kotani, Core Level Spectroscopy of Solids (CRC Press, Taylor Francis Group) (2008)

[109] G.Greczynski and L.Hultman. X-ray photoelectron spectroscopy:Towards reliable binding energy referencing.Progress in Materials Science 107 (2020) 100591

[110] C.V. Raman K. S. Krishnan, A New Type of Secondary Radiation, Nature 121, 501- 502 (1928)

[111] Jones, R.R., Hooper, D.C., Zhang, L. et al. Raman Techniques: Fundamentals and Frontiers. Nanoscale Res Lett 14, 231 (2019)

[112] E. Granado, A. Garca, J. A. Sanjurjo, C. Rettori, I. Torriani, F. Prado, R.D. Sanchez, A. Caneiro, and S. B. Oseroff, Magnetic ordering effects in the Raman spectra of $La_{1-x}Mn_{1-x}O_3$. Phys. Rev. B 60, 11879 (1999).

[113] Egerton R F 2011 Electron energy-loss spectroscopy in the electron microscope, 3rd edition.(New York-Dordrecht-Heidelberg-London: Springer)

[114] F Hofer, F P Schmidt, W Grogger and G Kothleitner, Fundamentals of electron energy-loss spectroscopy. IOP Conf. Series: Materials Science and Engineering 109 (2016) 012007

[115] Muller, D.A.; Grazul, J. (2001). "Optimizing the environment for sub-0.2 nm scanning transmission electron microscopy". J. Electron. Microsc. 50 (3): 219-226

[116] Jingyue Liu, Scanning transmission electron microscopy and its application to the study of nanoparticles and nanoparticle systems, Journal of Electron Microscopy, Volume 54, Issue 3, June 2005, Pages 251-278

[117] H. Motschmann, R. Teppner,Ellipsometry in Interface Science,Studies in Interface Science,Elsevier,Volume 11,2001,Pages 1-42,ISSN 1383-7303,ISBN 9780444509482

[118] D. L. Wood and K. Nassau, Refractive index of cubic zirconia stabilized with yttria. Appl. Opt. 21, 2978 (1982)

[119] H. Fujiwara. Spectroscopic Ellipsometry. Principles and Applications. John Wiley Sons, Ltd. (2007)

[120] Ichimiya A & Cohen P I (2004). Reflection High Energy Electron Diffraction. Cambridge University Press: Cambridge, UK. pp. 1, 13, 16, 98, 130, 161.

ISBN 0-521-45373-9

[121] Hasegawa, S. (2012). Reflection HighEnergy Electron Diffraction. In Characterization of Materials, E.N. Kaufmann (Ed.),pp. 1-14

[122] G.J.H.M. Rijnders et al. In-situ growth monitoring during PLD of oxides using RHEED at high oxygen pressure. Materials Science and Engineering B56 (1998) 223-227

[123] Griffiths, David J. (1999). Introduction to Electrodynamics (3rd ed.). Upper Saddle River, NJ: Prentice Hall.ISBN 0-13-805326-X.

[124] Barone, A.; Paterno, G. (1982). Physics and Applications of the Josephson Effect. New York: John Wiley Sons. ISBN 978-0-471-01469-0.

[125] Magnetic Property Measurement System- SQUID VSM Users Manual (Quantum design).Part Number 1500-100, E0

[126] B. Lorenz, Hexagonal Manganites($RMnO_3$): Class (I) Multiferroics with Strong Coupling of Magnetism and Ferroelectricity. ISRN Condens. Matter Phys. 2013, 497073 (2013)

[127] M. Balli, B. Roberge, P. Fournier, and S. Jandl, Review of the Magnetocaloric Effect in $RMnO_3$ and RMn_2O_5 Multiferroic Crystals. Crystals 7, 44 (2017)

[128] N. Lee, Y.J. Choi, M. Ramazanoglu, W. Ratcliff, V. Kiryukhin, and S.W. Cheong, Mechanism of exchange striction of ferroelectricity in multiferroic orthorhombic $HoMnO_3$ single crystals. Phys. Rev. B 84, 020101(R) (2011)

[129] X. Li, C. Lu, J. Dai, S. Dong, Y. Chen, N. Hu, G. Wu, M. Liu, Z. Yan, and J.M. Liu, Novel multiferroicity in $GdMnO_3$ thin films with self-assembled nano-twinned domains. Sci Rep 4, 7019 (2015)

[130] M. Lilienblum, T. Lottermoser, S. Manz, S.M. Selbach, A. Cano, and M. Fiebig, Ferroelectricity in the multiferroic hexagonal manganites. Nat. Phys. 11, 1070 (2015)

[131] D. Lee, A. Yoon, S.Y. Jang, J.G. Yoon, J.S. Chung, M. Kim, J.F. Scott, and T.W. Noh, Giant Flexoelectric Effect in Ferroelectric Epitaxial Thin Films. Phys. Rev. Lett. 107, 057602 (2011)

[132] B.B. Van Aken, T.T.M. Palstra, A. Filippetti, and N. Spaldin, The origin of ferroelectricity in magnetoelectric $YMnO_3$. Nat. Mater. 3, 164-170 (2004)

[133] C.J. Fennie and K.M. Rabe, Ferroelectric transition in $YMnO_3$ from first principles. Phys. Rev. B 72, 1 (2005)

[134] A.N. Pirogov, Polarization in $RMnO_3$ multiferroics. Acta Crystallogr. Sect. B Struct. Sci. Cryst. Eng. Mater. 72, 1 (2016)

[135] J.A. Mundy, et al, Atomically engineered ferroic layers yield a room-temperature magnetoelectric multiferroic. Nature 537, 523 (2016)

[136] L.W. Martn, Y.H. Chu, R. Ramesh, Advances in the growth and characterization of magnetic, ferroelectric, and multiferroic oxide thin films. Mater. Sci. Eng., R Rep. 68 89 (2010)

[137] D. Lee, A. Yoon, S.Y. Jang, J.-G. Yoon, J.-S. Chung, M. Kim, J. F. Scott, and T.W. Noh, Giant Flexoelectric Effect in Ferroelectric Epitaxial Thin Films. Phys. Rev. Lett. 107, 057602 (2011)

[138] S.Y. Jang, D. Lee, J.-H. Lee, T. W. Noh, Y. Jo, M.-H. Jung, and J.-S. Chung, Oxygen vacancy induced re-entrant spin glass behavior in multiferroic $ErMnO_3$ thin films. Appl. Phys. Lett. 93, 162507 (2008)

[139] J.H. Lee, P. Murugavel, D. Lee, and T. W. Noh, Multiferroic properties of epitaxially stabilized hexagonal $DyMnO_3$ thin films. Appl. Phys. Lett. 90, 012903 (2007)

[140] J. Nordlander, M. Campanini, M.D. Rossell, R. Erni, Q.N. Meier, A. Cano, N.A. Spaldin, M. Fiebig, and M. Trassin, The ultrathin limit of improper ferroelectricity. Nat. Comm. 10, 5591 (2019)

[141] J. Fontcuberta, Multiferroic $RMnO_3$ thin films: Films fins de $RMnO_3$ multiferroque. C. R. Physique 16, 204 (2015)

[142] T. Kordel, C. Wehrenfennig, D. Meier, Th. Lottermoser, M. Fiebig, I. Glard, C. Dubourdieu, J.-W. Kim, L. Schultz, K. Drr, Nanodomains in multiferroic hexagonal $RMnO_3$ films (R = Y, Dy, Ho, Er). Phys. Rev. B 80, 045409 (2009)

[143] J.H. Lee, P. Murugavel, H. Ryu, D. Lee, J.Y. Jo, J.W. Kim, H.J. Kim, K.H. Kim, Y. Jo, M.H. Jung, Y.H. Oh, Y.W. Kim, J.G. Yoon, J.S. Chung, and T.W. Noh, Epitaxial Stabilization of a New Multiferroic Hexagonal Phase of $TbMnO_3$ Thin Films. Adv. Mater. 18, 3125 (2006)

[144] J.H. Lee, D. Lee, T.W. Noh, P. Murugavel, J.W. Kim, K.H. Kim, Y. Jo, M.H. Jung, J.G. Yoon, and J.S. Chung, Formation of hexagonal phase of TbMnO3 thin film and its multiferroic properties. Journal of Materials Research, 22(8),

2156-2162 (2007)

[145] D.J. Kim, T.R. Paudel, H. Lu, J.D. Burton, J.G. Connell, E.Y. Tsymbal, S.S.A. Seo, and A. Gruverman, RoomTemperature Ferroelectricity in Hexagonal $TbMnO_3$ Thin Films. Adv. Mater. 26, 7660 (2014)

[146] H. Sim, J. Jeong, H. Kim, S.W. Cheong, and J.G. Park, Studies on the high-temperature ferroelectric transition of multiferroic hexagonal manganite $RMnO_3$. J. Phys. Condens. Matter 30, (2018)

[147] M. Fiebig, V. V. Pavlov, and R. V. Pisarev, Second-harmonic generation as a tool for studying electronic and magnetic structures of crystals: review. J. Opt. Soc. Am. B 22, 96 (2005)

[148] S.A. Denev, T.T.A. Lummen, E. Barnes, A. Kumar, and V. Gopalan, Probing Ferroelectrics Using Optical Second Harmonic Generation. J. Am. Ceram. Soc. 94, 2699 (2011)

[149] T. Iizuka-Sakano, E. Hanamura, and Y. Tanabe, Second-harmonic-generation spectra of the hexagonal manganites $RMnO_3$. J. Phys. Condens. Matter 13, 3031 (2001)

[150] H. Fukumura, S. Matsui, H. Harima, K. Kisoda, T. Takahashi, T. Yoshimura and N. Fujimura, Raman scattering studies on multiferroic $YMnO_3$. J. Phys.: Condens. Matter 19, 365239 (2007)

[151] S. M. Disseler et al, Magnetic Structure and Ordering of Multiferroic Hexagonal $LuFeO_3$. Phys. Rev. Lett. 114, 217602 (2015)

[152] C. Dubourdieu , G. Huot , I. Gelard , H. Roussel , O.I. Lebedev G. Van Tendeloo, Thin films and superlattices of multiferroic hexagonal rare earth manganites. Phil. Magaz. Lett., 87, 203 (2007)

[153] M. Jungbauer, S. Hhn, R. Egoavil, H. Tan, J. Verbeeck, G. Van Tendeloo, and V. Moshnyaga, Atomic layer epitaxy of Ruddlesden-Popper $SrO(SrTiO_3)_n$ films by means of metalorganic aerosol deposition. Appl. Phys. Lett. 105, 251603 (2014)

[154] K.H. Wu, H.-J. Chen, C.C. Hsieh, C.W. Luo, T.M. Uen, J.-Y. Lin, J.Y. Juang, Epitaxial-Strain Effects on Electronic Structure and Magnetic Properties of Hexagonal $YMnO_3$ Thin Films Studied by Femtosecond Spectroscopy. J. Supercond. Nov. Magn. 26, 801 (2013)

[155] N. Jehanathan, O.I. Lebedev, I. Gelard, C. Dubourdieu and G. Van Tende-

loo, Structure and defect characterization of multiferroic $ReMnO_3$ films and multilayers by TEM. Nanotechnology 21, 075705 (2010)

[156] https://crystal-gmbh.com, Crystal Data Sheet Substrates,Yttria-stabilized Zirconium Oxide (YSZ)

[157] M.G. Han, Y. Zhu, L. Wu, T. Aoki, V. Volkov, X. Wang, S.C. Chae, Y.S. Oh, and S.W. Cheong, Ferroelectric Switching Dynamics of Topological Vortex Domains in a Hexagonal Manganite. Adv. Mater. 25, 2415 (2013)

[158] Q.H. Zhang, L.J. Wang, X.K. Wei, R.C. Yu, L. Gu, A. Hirata, M.W. Chen, C.Q. Jin, Y. Yao, Y.G. Wang, and X.F. Duan, Direct observation of interlocked domain walls in hexagonal $RMnO_3$ (R = Tm, Lu). Phys. Rev. B - Condens. Matter Mater. Phys. 85, 2 (2012)

[159] T. Matsumoto, R. Ishikawa, T. Tohei, H. Kimura, Q. Yao, H. Zhao, X. Wang, D. Chen, Z. Cheng, N. Shibata, and Y. Ikuhara, Multivariate Statistical Characterization of Charged and Uncharged Domain Walls in Multiferroic Hexagonal YMnO3 Single Crystal Visualized by a Spherical Aberration-Corrected STEM. Nano Lett. 13, 10, 4594-4601 (2013)

[160] Q. Zhang, G. Tan, L. Gu, Y. Yao, C. Jin, Y. Wang, X. Duan, and R. Yu, Direct Observation of Multiferroic Vortex Domains in $YMnO_3$. Sci Rep 3, 2741 (2013)

[161] V. V Roddatis, A.R. Akbashev, S. Lopatin and A.R. Kaul, Complex structural-ferroelectric domain walls in thin films of hexagonal orthoferrites $RFeO_3$ (R = Lu, Er). Appl. Phys. Lett. 103, 112907 (2013)

[162] N.T.M. Hien, S.Y. Oh, X.B. Chen, D. Lee, S.Y. Jang, T.W. Noh, and I.S. Yang, Raman scattering studies of hexagonal rareearth $RMnO_3$ (R = Tb, Dy, Ho, Er) thin films. J. Raman Spectrosc. 42, 1774 (2011)

[163] D. L. Wood and K. Nassau, Refractive index of cubic zirconia stabilized with yttria. Appl. Opt. 21, 2978 (1982)

[164] L.G. Vieira, J.L. Ribeiro, O. Santo and P.B. Tavares, Infrared anisotropy averaging in polycrystalline samples and resonant scattering: the example of $YMnO_3$. J. Optics 14, 045707 (2012)

[165] W. S. Choi, S. J. Moon, S. S. A. Seo, D. Lee, J. H. Lee, P. Murugavel and T. W. Noh, Optical spectroscopic investigation on the coupling of electronic and magnetic structure in multiferroic hexagonal $RMnO_3$ (R = Gd, Tb, Dy,

Ho, Er) thin films. Phys. Rev. B 78, 054440 (2008)

[166] A. S. Moskvin and R. V. Pisarev, Optical spectroscopy of charge transfer transitions in multiferroic manganites, ferrites, and related insulators. Low temp. Phys. 36, 489 (2010)

[167] S.-H. Liu, J.-C.-A. Huang, X. Qi, W.-J. Lin, Y.-J. Siao, C.-R. Lin, J.-M. Chen, M.-T. Tang, Y.-H. Lee, and J.-C. Lee, Structural transformation and charge transfer induced ferroelectricity and magnetism in annealed $YMnO_3$. AIP Advances 1, 032173 (2011)

[168] Y. Tokura, S. Seki, and N. Nagaosa, Multiferroics of spin origin. Reports Prog. Phys. 77, (2014)

[169] N.A. Spaldin and R. Ramesh, Advances in magnetoelectric multiferroics. Nat. Mater. 18, 203 (2019)

[170] M. Bibes and A. Barthlmy, Towards a magnetoelectric memory. Nat. Mater. 7, 425 (2008)

[171] M. Coll, J. Fontcuberta, M. Althammer, M. Bibes et al. Towards Oxide Electronics: a Roadmap. Appl. Surf. Sci. 482, 1 (2019)

[172] S. Gariglio, A.D. Caviglia, J.M. Triscone, and M. Gabay, A spin-orbit playground: surfaces and interfaces of transition metal oxides. Reports Prog. Phys. 82, (2019)

[173] M. Bibes and A. Barthlmy, Oxide Spintronics. IEEE Trans. Electron Devices 54, 1003 (2007)

[174] L.W. Martin, Y.H. Chu, and R. Ramesh, Advances in the growth and characterization of magnetic, ferroelectric, and multiferroic oxide thin films. Mater. Sci. Eng. R Reports 68, 89 (2010)

[175] M.K. Kim, J.Y. Moon, H.Y. Choi, S.H. Oh, N. Lee, and Y.J. Choi, Investigation of the magnetic properties in double perovskite R_2CoMnO_6 single crystals (R = rare earth: La to Lu). J. Phys. Condens. Matter 27, 426002 (2015)

[176] Y. Shimakawa, M. Azuma, and N. Ichikawa, Multiferroic Compounds with Double-Perovskite Structures. Materials (Basel). 4, 153 (2010)

[177] M. Zhu, Y. Lin, E.W.C. Lo, Q. Wang, Z. Zhao, and W. Xie, Electronic and magnetic properties of La2NiMnO6 and La_2CoMnO_6 with cationic ordering.

Appl. Phys. Lett. 100, 062406 (2012)

[178] C. Meyer, V. Roddatis, P. Ksoll, B. Damaschke, and V. Moshnyaga, Structure, magnetism, and spin-phonon coupling in heteroepitaxial La_2CoMnO_6/Al_2O_3 films. Phys. Rev. B 98, 1 (2018)

[179] R.I. Dass and J.B. Goodenough, Multiple magnetic phases of La_2CoMnO_6. Phys. Rev. B - Condens. Matter Mater. Phys. 67, 014401 (2003)

[180] S. Baidya and T. Saha-Dasgupta, Electronic structure and phonons in La_2CoMnO_6: A ferromagnetic insulator driven by Coulomb-assisted spin-orbit coupling. Phys. Rev. B - Condens. Matter Mater. Phys. 84, 035131 (2011)

[181] M.P. Singh, K.D. Truong, and P. Fournier, Magnetodielectric effect in double perovskite La_2CoMnO_6 thin films. Appl. Phys. Lett. 91, 042504 (2007)

[182] D. Choudhury, P. Mandal, R. Mathieu, A. Hazarika, S. Rajan, A. Sundaresan, U. V. Waghmare, R. Knut, O. Karis, P. Nordblad, and D.D. Sarma, Near-Room-Temperature Colossal Magnetodielectricity and Multiglass Properties in Partially Disordered La_2NiMnO_6. Phys. Rev. Lett. 108, 127201 (2012)

[183] C. Xie, L. Shi, J. Zhao, S. Zhou, Y. Li, and X. Yuan, Spin-phonon coupling in R_2CoMnO_6 (R = Pr, Nd, Sm) thin films under biaxial compressive strain. J. Appl. Phys. 120, 155302 (2016)

[184] J. Blasco, J. Garca, G. Subas, J. Stankiewicz, S. Lafuerza, J.A. Rodrguez-Velamazn, C. Ritter, and J.L. Garca-Muoz, Effects of A-site disorder in the properties of A_2CoMnO_6 (A = La, Tb). J. Phys. Condens. Matter 26, (2014)

[185] J. Blasco, J. Garca, G. Subas, J. Stankiewicz, J.A. Rodrguez-Velamazn, C. Ritter, J.L. Garca-Muoz, and F. Fauth, Magnetoelectric and structural properties of Y_2CoMnO_6: The role of antisite defects. Phys. Rev. B 93, 214401 (2016)

[186] V. V. Shvartsman, S. Bedanta, P. Borisov, W. Kleemann, A. Tkach, and P.M. Vilarinho, (Sr, Mn)TiO_3: A Magnetoelectric Multiglass. Phys. Rev. Lett. 101, 165704 (2008)

[187] J.H. Lee, P. Murugavel, H. Ryu, D. Lee, J.Y. Jo, J.W. Kim, H.J. Kim, K.H. Kim, Y. Jo, M.H. Jung, Y.H. Oh, Y.W. Kim, J.G. Yoon, J.S. Chung, and T.W. Noh, Epitaxial Stabilization of a New Multiferroic Hexagonal Phase of

$TbMnO_3$ Thin Films. Adv. Mater. 18, 3125 (2006)

[188] M. Jungbauer, S. Hhn, R. Egoavil, H. Tan, J. Verbeeck, G. Van Tendeloo, and V. Moshnyaga, Atomic layer epitaxy of Ruddlesden-Popper $SrO(SrTiO_3)_n$ films by means of metalorganic aerosol deposition. Appl. Phys. Lett. 105, 251603 (2014)

[189] J.Y. Moon, M.K. Kim, D.G. Oh, J.H. Kim, H.J. Shin, Y.J. Choi, and N. Lee, Anisotropic magnetic properties and giant rotating magnetocaloric effect in double-perovskite Tb_2CoMnO_6. Phys. Rev. B 98, 174424 (2018)

[190] M. Tyunina and J. Levoska, Coexistence of ferroelectric and relaxor properties in epitaxial films of $Ba_{1-x}Sr_xTiO_3$. Phys. Rev. B 70, 132105 (2004)

[191] C.W. Ahn, C.H. Hong, B.Y. Choi, H.P. Kim, H.S. Han, Y. Hwang, W. Jo, K. Wang, J.F. Li, J.S. Lee, and I.W. Kim, A brief review on relaxor ferroelectrics and selected issues in lead-free relaxors. J. Korean Phys. Soc. 68, pages 1481-1494 (2016)

[192] A.A. Bokov and Z.G. Ye, Front. Ferroelectr. A Spec. Issue J. Mater. Sci. 1, 31 (2007)

[193] D. Viehland, S.J. Jang, L.E. Cross, and M. Wuttig, Freezing of the polarization fluctuations in lead magnesium niobate relaxors. J. Appl. Phys. 68, 2916 (1990)

[194] A.E. Glazounov and A.K. Tagantsev, Direct evidence for VgelFulcher freezing in relaxor ferroelectrics. Appl. Phys. Lett. 73, 856 (1998)

[195] L. Eric Cross, Ferroelectrics 76, 241 (1987)

[196] A. R. von Hippel, Dielectrics and Waves (MIT Press, Cambridge, MA, 1966)

[197] K. C. Kao, Dielectric Phenomena in Solids (Elsevier Academic Press, London, 2004)

[198] F. Kremer and A. Schnhals, Broadband Dielectric Spectroscopy (2003)

[199] P. Lunkenheimer, U. Schneider, R. Brand and A. Loidl, Glassy dynamics. Contemp. Phys. 41, 15 (2000)

[200] Mott, N. F. "Conduction in non-crystalline materials". Philosophical Magazine. Informa UK Limited. 19 (160): 835 (1969)

[201] M. Uehara, S. Mori, C.H. Chen, and S.-W. Cheong, Percolative phase separa-

tion underlies colossal magnetoresistance in mixed-valent manganites. Nature volume 399, pages 560-563 (1999)

[202] A. Pimenov, M. Biberacher, D. Ivannikov, A. Loidl, A. A. Mukhin, Yu. G. Goncharov, and A. M. Balbashov, Scaling of terahertz conductivity at the metal-insulator transition in doped manganites. Phys. Rev. B 73, 220407(R) (2006)

[203] R. Ramesh and D. G. Schlom, Creating emergent phenomena in oxide superlattices, Nat. Rev. Mater. 4, 257 (2019)

[204] J. Nichols et al., Emerging magnetism and anomalous Hall effect in iridate-manganite heterostructures, Nat. Commun. 7, 12721 (2016)

[205] X. Liu et al., Interfacial charge-transfer Mott state in iridatenickelate superlattices, PNAS, 116, 19863-19868 (2019)

[206] K. Huang et al., Tailoring magnetic order via atomically stacking 3d/5d electrons to achieve high-performance spintronic devices, Appl. Phys. Rev. 7, 011401 (2020)

[207] D. Yi et al., Tuning perpendicular magnetic anisotropy by oxygen octahedral rotations in LSMO/SIO superlattices, Phys. Rev. Lett. 119, 077201 (2017)

[208] Di. Yi et al., Atomic-scale control of magnetic anisotropy via novel spinorbit coupling effect in $La_{2/3}Sr_{1/3}MnO_3/SrIrO_3$ superlattices, PNAS, 113, 6397-6402 (2016)

[209] J. Matsuno et al., Interface-driven topological Hall effect in $SrRuO_3$-$SrIrO_3$ bilayer, Sci. Adv., 2, e1600304 (2016)

[210] B. Pang et al. Spin-glass-like behavior and topological Hall Effect in $SrRuO_3/SrIrO_3$ superlattices for oxide spintronics applications, ACS Appl. Mater. Interfaces 9, 3, 3201-3207 (2017)

[211] K. Meng et al., Observation of nanoscale skyrmions in $SrIrO_3/SrRuO_3$ bilayers, Nano Lett. 19, 5, 3169-3175 (2019)

[212] S. Okamoto et al. Charge transfer in iridate-manganite superlattices, Nano Lett. 17, 4, 2126-2130 (2017)

[213] W. Witczak-Krempa et al., Correlated quantum phenomena in the strong spin-orbit regime, Ann. Rev. Condens. Matter. 5, 57-82 (2013)

[214] J. G. Rau, E. K-Hin Lee and H-Y. Kee, Spin-orbit physics giving rise to novel phases in correlated systems: iridates and related materials, Ann. Rev. Condens. Matter. 7, 195-221 (2016)

[215] F. Hellman et al., Interface-induced phenomena in magnetism, Rev. Mod. Phys. 89, 025006 (2017)

[216] M. Acosta et al., $BaTiO_3$-based piezoelectrics: Fundamentals, current status, and perspectives, Appl. Phys. Rev. 4, 041305 (2017)

[217] S. Majumdar et al., Elucidating the origin of magnetic ordering in ferroelectric $BaTiO_{3-\delta}$ thin film via electronic structure modification, J. Phys.: Condens. Matter 31, 205001 (2019)

[218] S. R. Singamaneni et al., Ferroelectric and ferromagnetic properties in $BaTiO_3$ thin films in Si (100), J. Appl. Phys. 116, 094103 (2014)

[219] D. Cao et al. Vacancy-induced magnetism in $BaTiO_3$ (001) thin films based on density functional theory, Phys Chem Chem Phys. 13, 4738 (2011)

[220] A. Raeliarijaona and H. Fu, Ferromagnetism in ferroelectric $BaTiO_3$ induced by vacancies: Sensitive dependence on charge state, origin of magnetism, and temperature range of existence, Phys. Rev. B 96, 144431 (2017)

[221] S. Ramaknath et al, Charge transfer induced magnetism in nanocrystalline $BaTiO_3$, Solid State Commun. 187, 59 (2014)

[222] K. J. Choi et al, Enhancement of ferroelectricity in strained $BaTiO_3$ thin films, Science, 306, 1005 (2004)

[223] S. J. Moon et al., Dimensionality-controlled insulator-metal transition and correlated metallic state in 5d transition metal oxides $Sr_{n+1}Ir_nO_{3n+1}$ (n=1, 2, and ∞), Phys. Rev. Lett. 101, 226402 (2008)

[224] A. Biswas et al., Metal insulator transitions in perovskite $SrIrO_3$ thin films, J. Appl. Phys.116, 213704 (2014)

[225] J. H. Gruenewald et al., Compressive strain-induced metalinsulator transition in orthorhombic $SrIrO_3$ thin films, J. Mater. Research, 29, 2491 (2014)

[226] L. Zhang et al., Tunable semimetallic state in compressive-strained $SrIrO_3$ films revealed by transport behavior, Phys. Rev. B 91, 035110 (2015)

[227] D. J. Groenendijk et al. Epitaxial growth and thermodynamic stability of

$SrIrO_3/SrTiO_3$ heterostructures, Appl. Phys. Lett. 109, 041906 (2016)

[228] K. Nishio et al., Thermodynamic guiding principles in selective synthesis of strontium iridate Ruddlesden-Popper epitaxial films, APL Mater. 4, 036102 (2016)

[229] L. Wang et al. Ferroelectrically tunable magnetic skyrmions in ultrathin oxide heterostructures, Nat. Mater. 17, 1087 (2018)

[230] W. Lei, et al., Quantitative analysis of the oxygen content in $BaTiO_3$ films deposited by PLD using $^{16}O(\alpha,\alpha)^{16}O$ resonant elastic scattering, Thin Solid Films, 340, 66 (1999)

[231] K. R. Kleindienst et al., Structural properties and anisotropic electronic transport in $SrIrO_3$ films, Phys. Rev B 98, 115113 (2018)

[232] O. F. Shoron et al., $BaTiO_3/SrTiO_3$ heterostructures for ferroelectric field effect transistors, Appl. Phys. Lett. 110, 232902 (2017)

[233] S. R. Gilbet et al., Electrical transport properties of epitaxial $BaTiO_3$ thin films, J. Appl. Phys. 80, 969 (1996)

[234] T. Yu et al., Polarity and spinorbit coupling induced strong interfacial exchange coupling: An asymmetric charge transfer in iridatemanganite heterostructure, ACS Appl. Mater. Interfaces 11, 47, 44837 (2019)

[235] J. Matsuno et al., Engineering a spin-orbital magnetic insulator by tailoring superlattices, Phys. Rev. Lett. 114, 247209 (2015)

[236] Y. Song et al., Unconventional crystal-field splitting in noncentrosymmetric $BaTiO_3$ thin films, Phys. Rev. Mater. 4, 024413 (2020)

[237] S. Balaz, Z. Zeng, and L. J. Brillson, Heterojunction band offset and dipole formation at $BaTiO_3/SrTiO_3$ interfaces, J. Appl. Phys. 114, 183701 (2013)

[238] O. V. Yazyev, M.I. Katsnelson, Magnetic correlations at graphene edges: Basis for novel spintronics devices, Phys. Rev. Lett. 100 (2008) 1-4

[239] M. Sepioni, R.R. Nair, S. Rablen, J. Narayanan, F. Tuna, R. Winpenny, A.K. Geim, I. V. Grigorieva, Limits on intrinsic magnetism in graphene, Phys. Rev. Lett. 105 (2010) 1-4

[240] R.R. Nair, M. Sepioni, I.-L. Tsai, O. Lehtinen, J. Keinonen, A. V. Krasheninnikov, T. Thomson, A.K. Geim, I. V. Grigorieva, Spin-half paramagnetism

in graphene induced by point defects, Nat. Phys. 8 (2012) 199-202

[241] H.S.S.R. Matte, K.S. Subrahmanyam, C.N.R. Rao, Novel Magnetic Properties of Graphene: Presence of Both Ferromagnetic and Antiferromagnetic Features and Other Aspects Novel Magnetic Properties of Graphene: Presence of Both Ferromagnetic and Antiferromagnetic Features and Other Aspects, (2009) 9982-9985

[242] J. ervenka, M.I. Katsnelson, C.F.J. Flipse, Room-temperature ferromagnetism in graphite driven by two-dimensional networks of point defects, Nat. Phys. 5 (2009) 840-844

[243] Z. He, H. Xia, X. Zhou, X. Yang, Y. Song, T. Wang, Raman study of correlation between defects and ferromagnetism in graphite, J. Phys. D. Appl. Phys. 44 (2011) 085001

[244] N. Richter, Y.R. Hernandez, S. Schweitzer, J.S. Kim, A.K. Patra, J. Englert, I. Lieberwirth, A. Liscio, V. Palermo, X. Feng, A. Hirsch, K. Mllen, M. Klui, Robust Two-Dimensional Electronic Properties in Three-Dimensional Microstructures of Rotationally Stacked Turbostratic Graphene, Phys. Rev. Appl. 7 (2017) 1-10

[245] R. Mao, Y. Chen, K.W. Kim, Atomistic modeling of phonon transport in turbostratic graphitic structures, J. Appl. Phys. 119 (2016)

[246] R.R. Nair, I.-L. Tsai, M. Sepioni, O. Lehtinen, J. Keinonen, A.V. Krasheninnikov, A.H. Castro Neto, M.I. Katsnelson, A.K. Geim, I.V. Grigorieva, Dual origin of defect magnetism in graphene and its reversible switching by molecular doping, Nat. Commun. 4 (2013) 1-6

[247] R. Faccio, H. Pardo, P.A. Denis, R.Y. Oeiras, F.M. Arajo-Moreira, M. Verssimo-Alves, A.W. Mombr, Magnetism induced by single carbon vacancies in a three-dimensional graphitic network, Phys. Rev. B - Condens. Matter Mater. Phys. 77 (2008) 1-6

[248] J.J. Palacios, J. Fernndez-Rossier, L. Brey, Vacancy-induced magnetism in graphene and graphene ribbons, Phys. Rev. B - Condens. Matter Mater. Phys. 77 (2008) 1-14

[249] J.C. Ren, Z. Ding, R.Q. Zhang, M.A. Van Hove, Self-doping and magnetic ordering induced by extended line defects in graphene, Phys. Rev. B - Condens. Matter Mater. Phys. 91 (2015) 1-7

[250] S. Ganguly, M. Kabir, T. Saha-Dasgupta, Magnetic and electronic crossovers in graphene nanoflakes, Phys. Rev. B. 95 (2017) 1-9

[251] M. Kabir, T. Saha-Dasgupta, Manipulation of edge magnetism in hexagonal graphene nanoflakes, Phys. Rev. B - Condens. Matter Mater. Phys. 90 (2014) 1-9

[252] D. Cho, K.C. Ko, H. Park, J.Y. Lee, Ferromagnetic graphene nanoribbons: Edge termination with organic radicals, J. Phys. Chem. C. 119 (2015) 10109-10115

[253] Y. Nam, D. Cho, J.Y. Lee, Doping Effect on Edge-Terminated Ferromagnetic Graphene Nanoribbons, J. Phys. Chem. C. 120 (2016) 11237-11244

[254] A.M. Ukpong, N. Chetty, Half-metallic ferromagnetism in substitutionally doped boronitrene, Phys. Rev. B - Condens. Matter Mater. Phys. 86 (2012) 1-13

[255] S. Bhowmick, A.K. Singh, B.I. Yakobson, Quantum dots and nanorods of graphene embedded in hexagonal boron nitride, J. Phys. Chem. C. 115 (2011) 9889-9893

[256] R. Martins, Disorder and Segregation in BCN Graphene-Type Layers and Nanotubes:, 5 (2011) 385-393

[257] H. Park, A. Wadehra, J.W. Wilkins, A.H. Castro Neto, Magnetic states and optical properties of single-layer carbon-doped hexagonal boron nitride, Appl. Phys. Lett. 100 (2012)

[258] J. Li, V.B. Shenoy, Graphene quantum dots embedded in hexagonal boron nitride sheets, Appl. Phys. Lett. 98 (2011) 2009-2012

[259] Z. Yu, M.L. Hu, C.X. Zhang, C.Y. He, L.Z. Sun, J. Zhong, Transport Properties of Hybrid Zigzag Graphene and Boron Nitride Nanoribbons, J. Phys. Chem. C. 115 (2011) 10836-10841

[260] M. Kan, Y. Li, Q. Sun, Recent advances in hybrid graphene-BN planar structures, Wiley Interdiscip. Rev. Comput. Mol. Sci. 6 (2016) 65-82

[261] A.Y. Liu, R.M. Wentzcovitch, M.L. Cohen, Atomic arrangement and electronic structure of BC2N, Phys. Rev. B. 39 (1989) 1760-1765

[262] N. kumar, K. Moses, K. Pramoda, S.N. Shirodkar, A.K. Mishra, U. V. Waghmare, A. Sundaresan, C.N.R. Rao, Borocarbonitrides, BxCyNz, J. Mater.

Chem. A. 1 (2013) 5806

[263] P. Boski, J. Tuek, Z. Sofer, V. Maznek, M. Petr, M. Pumera, M. Otyepka, R. Zboil, Doping with Graphitic Nitrogen Triggers Ferromagnetism in Graphene, J. Am. Chem. Soc. 139 (2017) 3171-3180

[264] N. Soin, S.C. Ray, S. Sarma, D. Mazumder, S. Sharma, Y.F. Wang, W.F. Pong, S.S. Roy, A.M. Strydom, Tuning the Electronic and Magnetic Properties of Nitrogen-Functionalized Few-Layered Graphene Nanoflakes, J. Phys. Chem. C. 121 (2017) 14073-14082

[265] Q. Miao, L. Wang, Z. Liu, B. Wei, F. Xu, W. Fei, Magnetic properties of N-doped graphene with high Curie temperature, Sci. Rep. 6 (2016) 21832

[266] C. Zhao, Z. Xu, H. Wang, J. Wei, W. Wang, X. Bai, E. Wang, Carbon-Doped Boron Nitride Nanosheets with Ferromagnetism above Room Temperature, Adv. Funct. Mater. 24 (2014) 5985-5992

[267] N. Kumar, K. Raidongia, A.K. Mishra, U. V. Waghmare, A. Sundaresan, C.N.R. Rao, Synthetic approaches to borocarbonitrides, BCxN (x=1-2), J. Solid State Chem. 184 (2011) 2902-2908

[268] R. Kumar, K. Gopalakrishnan, I. Ahmad, C.N.R. Rao, BN-graphene composites generated by covalent cross-linking with organic linkers, Adv. Funct. Mater. 25 (2015) 5910-5917

[269] L.S. Panchakarla, K.S. Subrahmanyam, S.K. Saha, A. Govindaraj, H.R. Krishnamurthy, U. V. Waghmare, C.N.R. Rao, Synthesis, structure, and properties of boron- and nitrogen-doped graphene, Adv. Mater. 21 (2009) 4726-4730

[270] R. Sen, B.C. Satishkumar, A. Govindaraj, K.R. Harikumar, G. Raina, J.-P. Zhang, A.K. Cheetham, C.N.R. Rao, BCN, CN and BN nanotubes produced by the pyrolysis of precursor molecules over Co catalysts, Chem. Phys. Lett. 287 (1998) 671-676

[271] M. Chhetri, S. Maitra, H. Chakraborty, U. V. Waghmare, C.N.R. Rao, Superior performance of borocarbonitrides, B x C y N z , as stable, low-cost metal-free electrocatalysts for the hydrogen evolution reaction, Energy Environ. Sci. 9 (2016) 95-101

[272] N. Kumar, K.S. Subrahmanyam, P. Chaturbedy, K. Raidongia, A. Govindaraj, K.P.S.S. Hembram, A.K. Mishra, U. V. Waghmare, C.N.R. Rao, Re-

markable uptake of CO_2 and CH4 by graphene-like borocarbonitrides, BxCyNz, ChemSusChem. 4 (2011) 1662-1670

[273] L. Ci, L. Song, C. Jin, D. Jariwala, D. Wu, Y. Li, A. Srivastava, Z.F. Wang, K. Storr, L. Balicas, F. Liu, P.M. Ajayan, Atomic layers of hybridized boron nitride and graphene domains., Nat. Mater. 9 (2010) 430-435

[274] D. Wei, Y. Liu, Y. Wang, H. Zhang, L. Huang, G. Yu, Synthesis of n-doped graphene by chemical vapor deposition and its electrical properties, Nano Lett. 9 (2009) 1752-1758

[275] R.Y. Tay, H. Li, S.H. Tsang, M. Zhu, M. Loeblein, L. Jing, F.N. Leong, E.H.T. Teo, Trimethylamine Borane: A New Single-Source Precursor for Monolayer h-BN Single Crystals and h-BCN Thin Films, Chem. Mater. 28 (2016) 2180-2190

[276] Z. Liu, L. Song, S. Zhao, J. Huang, L. Ma, J. Zhang, J. Lou, P.M. Ajayan, Direct Growth of Graphene / Hexagonal Boron Nitride Stacked Layers, Nano Lett. 11 (2011) 2032-2037

[277] L. Song, L. Balicas, D.J. Mowbray, R.B. Capaz, K. Storr, L. Ci, D. Jariwala, S. Kurth, S.G. Louie, A. Rubio, P.M. Ajayan, Anomalous insulator-metal transition in boron nitride-graphene hybrid atomic layers, Phys. Rev. B - Condens. Matter Mater. Phys. 86 (2012) 1-12

[278] B. Muchharla, A. Pathak, Z. Liu, L. Song, T. Jayasekera, S. Kar, R. Vajtai, L. Balicas, P.M. Ajayan, S. Talapatra, N. Ali, Tunable electronics in large-area atomic layers of boron-nitrogen-carbon, Nano Lett. 13 (2013) 3476-3481

[279] A. Perrone, A.. Caricato, A. Luches, M. Dinescu, C. Ghica, V. Sandu, A. Andrei, Boron carbonitride films deposited by pulsed laser ablation, Appl. Surf. Sci. 133 (1998) 239-242

[280] Z.F. Ying, D. Yu, H. Ling, N. Xu, Y.F. Lu, J. Sun, J.D. Wu, Synthesis of BCN thin films by nitrogen ion beam assisted pulsed laser deposition from a B4C target, Diam. Relat. Mater. 16 (2007) 1579-1585

[281] G. Kresse, J. Hafner, Ab initio molecular dynamics for liquid metals, Phys. Rev. B. 47 (1993) 558-561

[282] G. Kresse, J. Furthmller, Efficient iterative schemes for ab initio total-energy calculations using a plane-wave basis set, Phys. Rev. B - Condens. Matter Mater. Phys. 54 (1996) 11169-11186

[283] P.E. Blchl, Projector augmented-wave method, Phys. Rev. B. 50 (1994) 17953-17979

[284] J.P. Perdew, K. Burke, M. Ernzerhof, Generalized gradient approximation made simple, Phys. Rev. Lett. 77 (1996) 3865-3868

[285] J. Sun, A. Ruzsinszky, J. Perdew, Strongly Constrained and Appropriately Normed Semilocal Density Functional, Phys. Rev. Lett. 115 (2015) 1-6

[286] M. Matsuoka, S. Isotani, R.D. Mansano, W. Sucasaire, R. a C. Pinto, J.C.R. Mittani, K. Ogata, N. Kuratani, X-Ray Photoelectron Spectroscopy and Raman Spectroscopy Studies on Thin Carbon Nitride Films Deposited by Reactive RF Magnetron Sputtering, World J. Nano Sci. Eng. 02 (2012) 92-102

[287] L. Ci, L. Song, C. Jin, D. Jariwala, D. Wu, Y. Li, A. Srivastava, Z.F. Wang, K. Storr, L. Balicas, F. Liu, P.M. Ajayan, Atomic layers of hybridized boron nitride and graphene domains., Nat. Mater. 9 (2010) 430-435

[288] K.M.M.O.W. S. Itoh, Bonding characterization of BC_2N thin films, Appl. Phys. Lett. 68 (1996) 2962

[289] J.F. Moulder, W.F. Stickle, P.E. Sobol, K.D. Bomben, Handbook of X-ray photoelectron spectroscopy: a reference book of standard spectra for identification and interpretation of XPS data, Surf. Interface Anal. (1992) 261

[290] N. kumar, K. Moses, K. Pramoda, S.N. Shirodkar, A.K. Mishra, U. V. Waghmare, A. Sundaresan, C.N.R. Rao, Borocarbonitrides, BxCyNz, J. Mater. Chem. A. 1 (2013) 5806

[291] C.S. Schnohr, M.C. Ridgway, X-Ray Absorption Spectroscopy of Semiconductors, X-Ray Absorpt. Spectrosc. Semicond. 190 (2015) 1-26

[292] S. Bhattacharyya, M. Lbbe, P.R. Bressler, D.R.T. Zahn, F. Richter, Structure of nitrogenated amorphous carbon films from NEXAFS, Diam. Relat. Mater. 11 (2002) 8-15

[293] C. Pallier, J.-M. Leyssale, L.A. Truflandier, A.T. Bui, P. Weisbecker, C. Gervais, H.E. Fischer, F. Sirotti, F. Teyssandier, G. Chollon, Structure of an amorphous boron carbide film: An experimental and computational approach, Chem. Mater. 25 (2013) 2618-2629

[294] I. Jimnez, R. Gago, J. Albella, D. Cceres, I. Vergara, Spectroscopy of bonding in hard graphitic carbon nitride films: Superstructure of basal planes and hardening mechanisms, Phys. Rev. B. 62 (2000) 4261-4264

[295] W. Hua, B. Gao, S. Li, H. gren, Y. Luo, X-ray absorption spectra of graphene from first-principles simulations, Phys. Rev. B - Condens. Matter Mater. Phys. 82 (2010) 1-7

[296] O. Plashkevych, A. Snis, L. Yang, H. gren, S.F. Matar, Near-edge X-ray absorption spectra of carbon-nitride molecules and solids, Phys. Scr. 63 (2001) 70-86

[297] R. Kumar, K. Gopalakrishnan, I. Ahmad, C.N.R. Rao, BN-graphene composites generated by covalent cross-linking with organic linkers, Adv. Funct. Mater. 25 (2015) 5910-5917

[298] S. Reich, C. Thomsen, Raman spectroscopy of graphite, Philos. Trans. R. Soc. A Math. Phys. Eng. Sci. 362 (2004) 2271-2288

[299] A.C. Ferrari, Raman spectroscopy of graphene and graphite: Disorder, electron-phonon coupling, doping and nonadiabatic effects, Solid State Commun. 143 (2007) 47-57

[300] Y.-F.F. Lu, S.-T.T. Lo, J.-C.C. Lin, W. Zhang, J.-Y.Y. Lu, F.-H.H. Liu, C.-M.M. Tseng, Y.-H.H. Lee, C.-T. Te Liang, L.-J.J. Li, Nitrogen-Doped Graphene Sheets Grown by Chemical Vapor Deposition: Synthesis and Influence of Nitrogen Impurities on Carrier Transport., ACS Nano. 7 (2013) 65, 22-32

[301] M. Mohr, J. Maultzsch, C. Thomsen, Splitting of the Raman 2D band of graphene subjected to strain, Phys. Rev. B - Condens. Matter Mater. Phys. 82 (2010) 1-4

[302] Y. Liu, Y. Shen, L. Sun, J. Li, C. Liu, W. Ren, F. Li, L. Gao, J. Chen, F. Liu, Y. Sun, N. Tang, H.M. Cheng, Y. Du, Elemental superdoping of graphene and carbon nanotubes, Nat. Commun. 7 (2016) 1-9

[303] E.H. Lich, on Hubbard model, Phys. Rev. Lett. 62 (1989)

[304] A. Lherbier, S.M.-M. Dubois, X. Declerck, Y.-M. Niquet, S. Roche, J.-C. Charlier, Transport properties of 2D graphene containing structural defects, 075402 (2012) 1-18

[305] A. Lherbier, A.R. Botello-Mndez, J.C. Charlier, Electronic and transport properties of unbalanced sublattice N-doping in graphene, Nano Lett. 13 (2013) 1446-1450

[306] J.-J. Chen, H.-C. Wu, D.-P. Yu, Z.-M. Liao, Magnetic moments in graphene

with vacancies, Nanoscale. 6 (2014) 8814

[307] J. Li, X. Li, P. Zhao, D.Y. Lei, W. Li, J. Bai, Z. Ren, X. Xu, Searching for magnetism in pyrrolic N-doped graphene synthesized via hydrothermal reaction, Carbon N. Y. 84 (2015) 460-468

[308] G.N.Parker,W.M.Saslow, Defect interactions and canting in ferromagnets, Phys. Rev. B 38(1988) 11718

[309] S.N. Mott, Electrons in glass, Rev. Mod. Phys. 50 (1978) 203-208

[310] A.L. Efros, B.I. Shklovskii, Coulomb gap and low temperature conductivity of disordered systems, J. Phys. C Solid State Phys. 8 (1975) L49-L51

[311] D. Joung, S.I. Khondaker, Efros-Shklovskii variable-range hopping in reduced graphene oxide sheets of varying carbon sp^2 fraction, Phys. Rev. B. 86 (2012) 235423

[312] D. Yu, C. Wang, B.L. Wehrenberg, P. Guyot-Sionnest, Variable range hopping conduction in semiconductor nanocrystal solids, Phys. Rev. Lett. 92 (2004) 216802-1

LIST OF PUBLICATIONS

Publications included in this thesis:

1. *Strain-Driven Structure-Ferroelectricity Relationship in hexagonal $TbMnO_3$ Films*
   Rajesh Mandal, Moritz Hirsbrunner, Vladimir Roddatis, R. Gruhl, Leonard Schüler, Ulrich Roß, Sebastian Merten,Philipp Gegenwart and Vasily Moshnyaga. **Physical Review B 102, 104106 (2020)**.

2. *Magneto-dielectric effect in relaxor superparaelectric Tb_2CoMnO_6 Film*
   Rajesh Mandal, Mohit Chandra, Vladimir Roddatis, Philipp Ksoll, Malvika Tripathi, Rajeev Rawat, R.J.Choudhary and Vasily Moshnyaga.
   Physical Review B 101, 094426 (2020).

3. *Interfacial coupling induced enhanced magnetic ordering in 3d-5d based $BaTiO_3$-$SrIrO_3$ hetero-structures*
   Rajesh Mandal, Abhijit Biswas, Supriyo Majumder, Rushikesh Magdum, Ram Janay Choudhary and Satishchandra Ogale. **Manuscript Under Preparation**.

4. *Modulation of Ferromagnetism and transport in $B_xC_yN_z$ thin films via Nitrogen doping and defects*
   Rajesh Mandal, Rohit Babar, Malvika Tripathi, Shouvik Datta, Rajeev Rawat, RJ Choudhary, Mukul Kabir, Satishchandra Ogale.
   Journal of Magnetism and Magnetic Materials 479 (2019), 67-73.

Publications not included in this thesis:

1. *Temperature dependence of the Spin Seebeck effect in a mixed valent manganite*
   Avirup De, Arup Ghosh, **Rajesh Mandal**, Satishchandra Ogale and Sunil Nair.
   Physical Review Letters 124, 017203 (2020).

2. *Enhanced electrocatalytic oxygen evolution activity in geometrically designed $SrRuO_3$ Thin Films*
   Abhijit Biswas, G. Shiva Shanker, Tisita Das, **Rajesh Mandal**, Sudip Chakraborty, and Satishchandra Ogale.
   Applied Surface Science 529 (2020), 147065.

3. *Emergent Double Perovskite Phase at $LaMnO_3/LaNiO_3$ Interfaces: Charge Transfer and Structural Reconstruction*
   Philipp Ksoll, **Rajesh Mandal**, Christoph Meyer, Leonard Schüler, Vladimir Roddatis and Vasily Moshnyaga. **Manuscript Under Preparation**.

Conferences & Talks:

1. **1st Quantum Oxide Research Online Meeting (QUOROM-1)** organized by CNRS/Thales laboratory, Université Paris-Saclay , France. 2020.

2. **26th International Workshop on Oxide Electronics (iWOE26)**, Kyoto University, Kyoto, Japan. 2019. Presented poster *Structure-Ferroelectricity relationship in artificial strain stabilized h- $TbMnO_3$ thin film.*

3. **Guest Talk at The University of Tokyo**, Japan. September 2019. Group of Prof. Shinobu Ohya. Talk Title: *Growth and magneto-electric investigation of Terbium based perovskite and double perovskite thin films.*

4. **25th International Workshop on Oxide Electronics (iWOE25)**, Les Diablerets, Switzerland, 2018. Presented poster *Electrical and Magnetic Properties of Hexagonal $TbMnO_3$-based Heterostructures.*

5. **Talk at Institute Seminar**, I. Physikalisches Institut-Tieftemperaturphysik, Georg-August-Universität Göttingen, Göttingen, Germany. September 2018. Talk Title: *Possible tuning of multiferrocity in rare earth oxide thin film heterostructures.*

6. **International Conference on Nanoscience and Technology (ICONSAT)**, Indian Institute of Science Education and Research (IISER) Pune, India 2016.

7. **Mumbai-Pune Semiconductor Meeting**, Indian Institute of Science Education and Research (IISER) Pune, India 2016.